Study of the causes and eff ects of the Atlantic Meridional Overturning Circulationn

Camille Marini

Thèse présentée pour obtenir le grade de

DOCTEUR DE L'UNIVERSITE PIERRE ET MARIE CURIE

Specialité: Océanographie Physique

(Ecole doctorale 129 : Sciences de l'Environnement d'Ile de France)

par

Camille Marini

Etude des causes et effets de la circulation méridienne de retournement Atlantique

Thèse préparée au LOCEAN, dirigée par Claude FRANKIGNOUL

et soutenue le 28 Novembre 2011 devant le jury composé de

Mme. Pascale Bouruet-Aubertot	*Présidente du jury*	LOCEAN
M. Christophe Cassou	*Rapporteur*	CERFACS (Toulouse)
M. Alain Colin de Verdière	*Rapporteur*	LPO (Brest)
M. Fabio D'Andrea	*Examinateur*	LMD (Paris)
M. Claude Frankignoul	*Directeur de Thèse*	LOCEAN
Mlle Rym Msadek	*Examinateur*	GFDL (Princeton)

Remerciements

Je tiens tout d'abord à remercier Claude pour tout ce qu'il m'a appris pendant ces trois ans. Venant d'un domaine plus statistique, la circulation méridienne de retournement Atlantique était une notion bien éloignée... Merci de m'avoir guidée tout en me faisant confiance. Je tiens aussi à remercier tout particulièrement Juliette pour son son enthousiasme, son dynamisme et pour sa disponibilité à répondre à toute sorte de questions. Merci aussi à Rym pour m'avoir montré un bon exemple. Je remercie aussi l'ensemble du jury, et en particulier Christophe Cassou pour ses nombreuses et enrichissantes questions. Merci aussi à Fabio D'Andréa, membre de mon comité de thèse, pour ses commentaires intéressants.

Merci à toute l'équipe du LOCEAN pour son accueil, à Céline et Dany pour le côté logistique, à l'équipe varclim pour le côté scientifique. Merci en particulier à Guillaume, Pascal, Myriam, Gurvan, Eric, Jérome et Christophe. Merci à Vincent 0 pour m'avoir guidée vers l'océanographie dès mon plus jeune âge. Merci à Pierre Testor pour m'avoir embarquée sur le tethys, afin de voir qu'il y avait de nombreuses aventures, parfois houleuses, derrière de simples fichiers de données de température et salinité. Merci à Fernanda pour sa joie de vivre, à mes co-bureaux Benoît, Manu, Hugo et l'ancêtre Mathieu, ainsi qu'aux autres thésards dont Ghyslaine, Chloé, Anastase.

Je remercie aussi Hanne Sagen, Laurent Bertino et toute l'équipe du NERSC pour leur accueil à Bergen. Merci à M.Renaud pour m'avoir appris à regarder le paysage. Merci aussi au département de mathématiques du palais de la découverte pour ces trois ans de monitorat si agréables.

Je tiens aussi à remercier mes amis, pour m'avoir supportée ces trois ans, Marion, Laura, Alex, Gracian, Sam, et les autres putti. Un 33t de remerciements à Margotte, François, Alex et au jardin du Luxembourg. Merci à Yves, Anaïs, à Louis et à Chantal sans qui je n'aurais pas pu faire cette expérience salée. Enfin, merci à Mattthieu.

Résumé

Dans une première partie de cette thèse, nous étudions l'influence du mode atmosphérique annulaire Sud (SAM) sur la circulation méridienne de retournement Atlantique (AMOC) dans une simulation de contrôle du modèle IPSLCM4. Nous montrons qu'une phase positive du SAM, correspondant à une intensification des vents d'Ouest soufflant au Sud de 45 $^\circ$ S, entraîne après 8 ans une accélération de l'AMOC, via une téléconnection atmosphérique peu réaliste. Nous trouvons aussi un lien entre le SAM et l'AMOC à une échelle de temps multidécennale. Des anomalies positives de sel créées par un SAM positif entrent dans le bassin Atlantique par le Passage de Drake et plus largement par le courant des aiguilles, elles se propagent vers le Nord et atteignent le nord de l'Atlantique Nord, où elles favorisent la convection profonde, entraînant une accélération de l'AMOC.

Dans une seconde partie, nous étudions dans quelle mesure l'Oscillation Multidécennale Atlantique (AMO) reflète les fluctuations de l'AMOC, et quels sont les autres signaux qui l'influencent dans des conditions climatiques de variabilité naturelle, ainsi qu'avec les forçages externes du 20ème siècle. Nous utilisons un filtre dynamique, basé sur un modèle linéaire inverse (LIM) pour décomposer la température de surface de l'océan (SST) Atlantique Nord en une partie liée à la dérive globale, une à El Niño (ENSO), une partie associée à la variabilité de basse fréquence du Pacifique, ainsi qu'un résidu. Dans la simulation historique du modèle IPSLCM5, enlever la dérive globale de l'AMO avec LIM induit de meilleures corrélations avec l'AMOC que lorsque ce signal est soustrait par une dérive linéaire ou par la moyenne de SST globale. De plus, nous trouvons qu'enlever l'influence de ENSO de l'AMO améliore très légérement ses corrélations avec l'AMOC, tandis qu'enlever le signal lié à la variabilité de basse fréquence du Pacifique les dégrade fortement. La robustesse de ces résultats est vérifiée dans des simulations de contrôle avec cinq modèles différents. Cette déconstruction de l'AMO est aussi effectuée dans les observations de SST.

Enfin, nous étudions rapidement l'impact du forçage volcanique sur les liens entre l'AMO et l'AMOC dans une simulation du dernier millénaire avec le modèle IPSLCM4.

Mots clés : Circulation Méridienne de renversement Atlantique, Oscillation Multidécennale Atlantique, El Niño, Variabilité décennale, Variabilité multidécennale, Teleconnections, Oscillation Arctique, Mode Annulaire Sud, Modèle Linéaire Inverse, Eruptions volcaniques.

Abstract Study of the causes and effects of the Atlantic Meridional Overturning Circulation

In the first part of this thesis, we study the influence of the Southern Annular Mode (SAM) onto the Atlantic Meridional Overturning Circulation (AMOC) in a control simulation with the IPSLCM4 model. We show that a positive phase of the SAM, corresponding to an intensification of the Westerlies south of 45 $^\circ$ S, leads to an acceleration of the AMOC after 8 years, via an atmospheric teleconnection, which is likely to be model-dependent. We also find a link between the SAM and the AMOC at a multidecadal time scale. Positive salt anomalies, created by a positive SAM, enter the South Atlantic from the Drake Passage and, more importantly, via the Aghulas leakage; they propagate northward, eventually reaching the northern North Atlantic where they decrease the vertical stratification and thus increase the AMOC.

In the second part of this thesis, we study to what extent the Atlantic Multidecadal Oscillation (AMO) reflects the AMOC fluctuations, and what are the other signals that influence it in natural climate variability conditions and with the external forcings of the 20th century. We use a dynamical filter, based on linear inverse modeling (LIM), to decompose the North Atlantic sea surface temperature (SST) field into a global trend, an El Nino Southern Oscillation-related part (ENSO), a part associated with Pacific decadal variability and a residual. In the historical simulation with the IPSLCM5 climate model, removing the global trend from the AMO with LIM yields to better correlations with the AMOC than removing a linear trend or the global mean SST. We also find that removing the ENSO-related part from the AMO with LIM leads to small changes, and even better correlations with the AMOC. Additionaly removing the signal associated to Pacific decadal variability leads to considerable changes in the AMO, which becomes much less correlated to the AMOC. The robustness of these results is demonstrated by performing the LIM decomposition in control simulations with five different climate models. Besides, the LIM filter is applied to SST observations.

Finally, we briefly study the impact of the volcanic forcing onto the links between the AMO and the AMOC in a simulation of the last millenium with the IPSLCM4 climate model.

Keywords : Atlantic Meridional Overturning Circulation, Atlantic Multidecadal Oscillation, El Niño Southern Oscillation, decadal and multidecadal variability, teleconnections, Arctic Oscillation, Southern Annular Mode, Linear Inverse Modeling, Volcanic eruptions.

Table des matières (Contents)

Chapter 1

Introduction

1.1 The role of the ocean in climate

Climate mainly results from the interactions between oceanic and atmospheric processes and external forcings, such as the solar irradiance, aerosols and greenhouse gases. The last two can have natural (e.g. aerosols from volcanic eruptions) or anthropogenic origins. The climate components vary on a very large spectrum of time and spatial scales. Before considering in more details the oceanic variability at decadal to multidecadal time scales, which is the main topic of this thesis, we show that the ocean plays a key role in climate, in order to then better understand how its variability impacts the climate variability, and how it is influenced by atmospheric and forced variability.

The solar irradiance is the main energy source for the Earth, and it strongly depends on the latitude, as shown in Fig.1.1, with a maximum near the equator where losses due to absorption by the atmosphere is smallest, since the rays arrive vertically. The heat is transported toward the high latitudes by the atmosphere and the ocean, leading to a temperate climate.

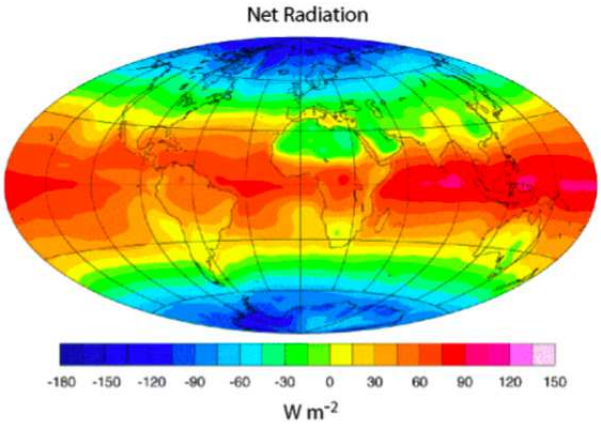

Figure 1.1: Heat flux received at the Earth surface. Source : NASA.

Only 20% of incoming solar radiation are directly absorbed by the atmosphere, while 49% are absorbed by the ocean and land surface, where it is stored as heat, mostly near the surface. As the oceanic heat capacity is larger than the one of the at-

mosphere or the land ($C_{p(oce)} = 4000 J.kg^{-1}.K^{-1}$ versus $C_{p(atm)} = 1000 J.kg^{-1}.K^{-1}$ for air and $C_{p(sol)} = 800 J.kg^{-1}.K^{-1}$ for soil and rocks), the ocean is an important heat reservoir : 3.5 m of water contain as much energy as an entire atmospheric column ([Gill 1982]).

A large amount of the solar energy absorbed by the ocean is transmitted to the atmosphere via radiative and turbulent energy exchange at the sea surface. The latter depends on several atmospheric variables, such as the wind speed, the air humidity and temperature, and the cloud cover, but only on one oceanic variable, the sea surface temperature (SST), which is roughly constant in the surface layer, called the surface mixed layer, where mixing homogenizes water properties. SST thus plays a major role in climate as a key variable of ocean-atmosphere interactions. The climatological SST is shown in Fig.1.2, using the HadISST1 dataset from 1901 to 2008. The HadISST1 data consist of monthly global fields of SST on a 1 $^\circ$ area grid, obtained using data reconstruction techniques based on in situ sea surface measurements since 1871 and satellite derived estimates of SST in recent decades ([Rayner et al. 2003]). As shown in Fig.1.2, the SST distribution is almost zonal with warmest water near the equator, where the net radiation is maximum (Fig.1.1). However, temperatures tend to be cooler in the eastern part of the tropical basin, because of upwelling processes occuring for instance near the Peruvian coast and the western coast of North Africa. The SST is maximum in the equatorial Pacific warm pool, located in the western tropical Pacific and eastern Indian ocean, while lower temperatures due to equatorial upwelling are observed in the eastern equatorial Pacific, referred as the cold-tongue. In the subtropics, temperatures are higher in the western part of oceanic basin, because of western boundary currents advecting heat poleward, such as the Gulf Stream in the North Atlantic and the Kuroshio in the North Pacific. In the subpolar basins, the zonal SST gradient reverses sign, with higher temperatures in the eastern basin and lower in the West, because of the wind-driven cyclonic circulation. In the Southern Ocean, there is a very strong cold thermal front, which is due to the upwelling driven by the Southern

Westerlies. Because of a combination of oceanic and atmospheric processes, SSTs

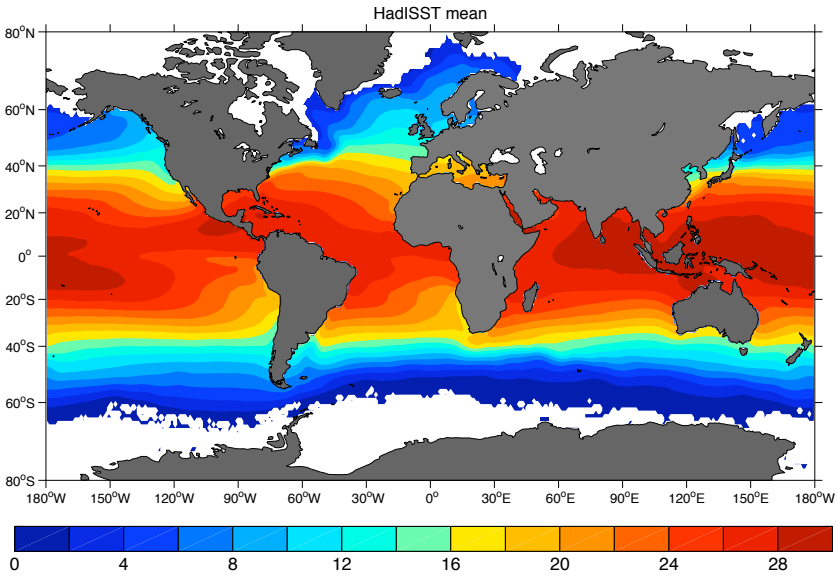

Figure 1.2: Climatological SST (in $^\circ$C) from the HadISST data set (1901-2008).

vary on different time scales. As shown in Fig.1.3, the standard deviations from the annual mean after removing the seasonal cycle are very high in the equatorial eastern Pacific because of the El Niño phenomenon. The variations are also large in the western boundary currents in the North and South Atlantic and the North Pacific, as well as in the area of the Aghulas leakage south of Africa.

The solar energy absorbed by the ocean, which is not transmitted to the atmosphere, is transported by currents, mainly from the equator towards the poles. As shown in Fig.1.4 (left), the northward oceanic heat transport between the equator and 20 $^\circ$N is as large as the atmospheric one, while it is smaller at higher latitudes. Contrary to other basins, the heat transport in the Atlantic is northward at all latitudes (Fig.1.4 right). The heat is largely transported by a slow (a few $mm.s^{-1}$) and large-scale circulation, called the thermohaline circulation or the meridional overturning circulation (MOC). Heat is also carried by ocean eddies and by the wind-driven gyre circulation in the horizontal plane. In particular, intense western boundary currents of the subtropical gyres, such as the Kuroshio and the Gulf Stream, transport warm water poleward.

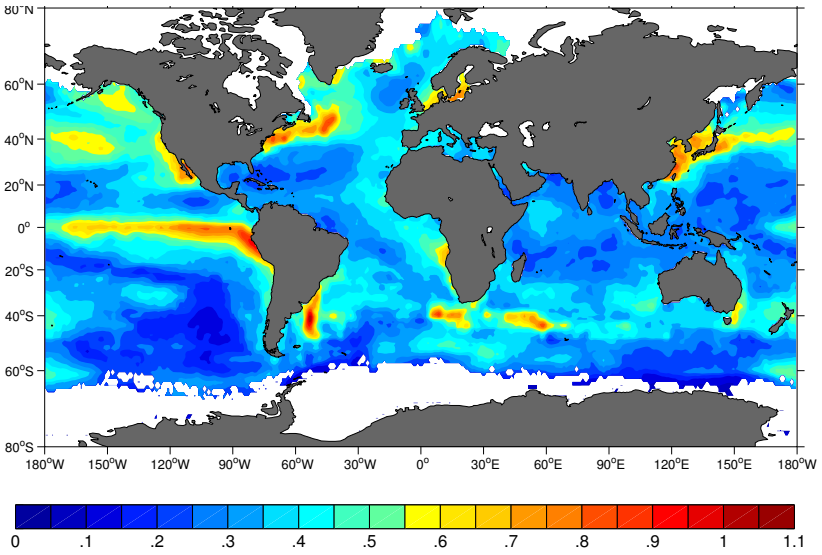

Figure 1.3: Standard deviation (in °C) from the climatological mean SST based on the HadISST data set (1901-2008).

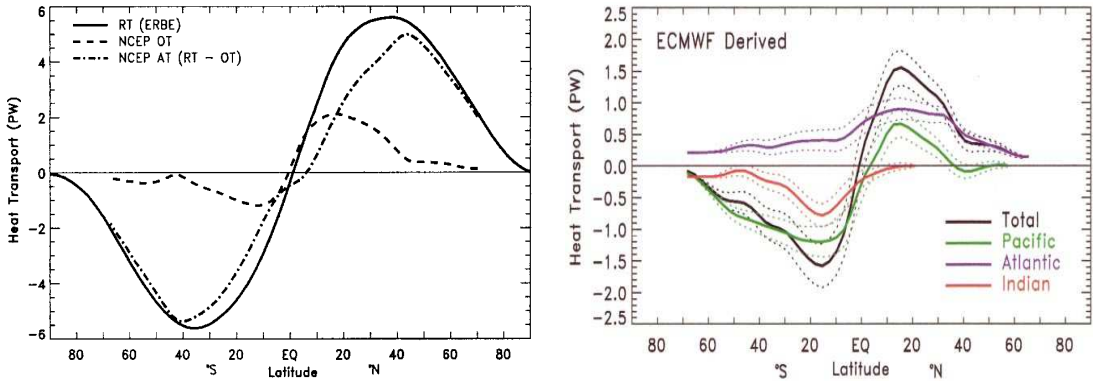

Figure 1.4: Zonally averaged northward heat transport. Left : total (RT), atmospheric (AT) and oceanic (OT), estimations from NCEP. Right : oceanic, total (black), in the Pacific (green), in the Atlantic (blue) and in the Indian ocean (red), estimations from ECMWF. Source : [Trenberth and Caron 2001].

The thermohaline circulation can be viewed as a global conveyor belt that links warm surface waters and deep water flows in the different oceanic basins, as shown by a highly simplified schematic in Fig.1.5. To be rigorous, the thermohaline circulation and the MOC are not exactly equivalent, although they are often used without distinction ([Rahmstorf 2006]), and we focus in this thesis on the MOC.

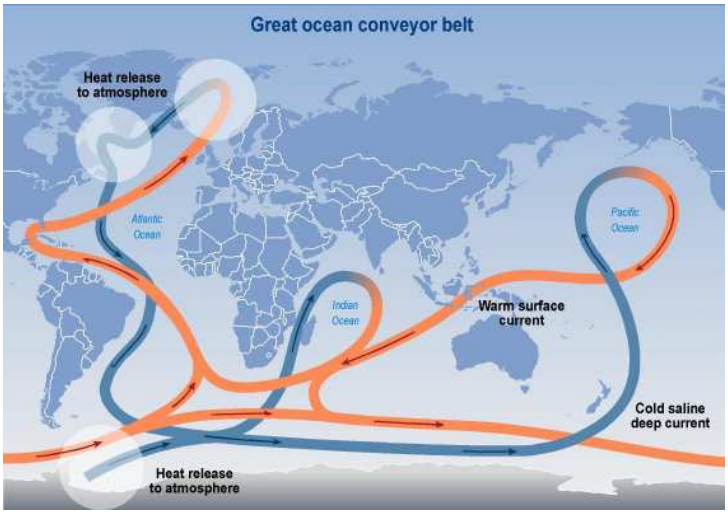

Figure 1.5: Schematic view of the thermohaline circulation. Warm and surface waters are indicated in red, and cold and deep waters in blue. Source : IPCC 2001.

The thermohaline circulation may be contrasted to the wind-driven circulation and is driven by fluxes of heat and freshwater across the sea surface and subsequent mixing of heat and salt in the ocean interior, although it is also affected by the wind. The MOC is generally quantified by the meridional streamfunction, which can be defined globally (MOC) or for the Atlantic only (AMOC). Considering that the meridional transport is non-divergent, i.e. $\frac{\partial V}{\partial y} + \frac{\partial W}{\partial z} = 0$ with V (resp. W) the meridional velocity v (resp. vertical velocity w) integrated along longitudes x ($V = \int v dx$, resp. $W = \int w dx$), there exists a streamfunction $\psi(y, z)$ such as $V = \frac{-\partial \psi}{\partial z}$ and $W = \frac{\partial \psi}{\partial y}$. The MOC corresponds to a meridional flow field, and includes thus wind-driven parts, in particular the Ekman cells. There are various estimates of the mean MOC. For instance, [Ganachaud and Wunsch 2000] used hydrographic sections from 1990 to 1996 gathered by the World Ocean Circulation Experiment (WOCE) to obtain an estimate of the global oceanic transport, shown in Fig.1.6, suggesting that the overturning in the North Atlantic is about 15 Sv. [Talley et al. 2003] computed the meridional overturning circulation from absolute geostrophic velocity estimates based on hydrographic data and from climatological

Ekman transports, and found an overturning in the North Atlantic of 18 Sv +/-3Sv.

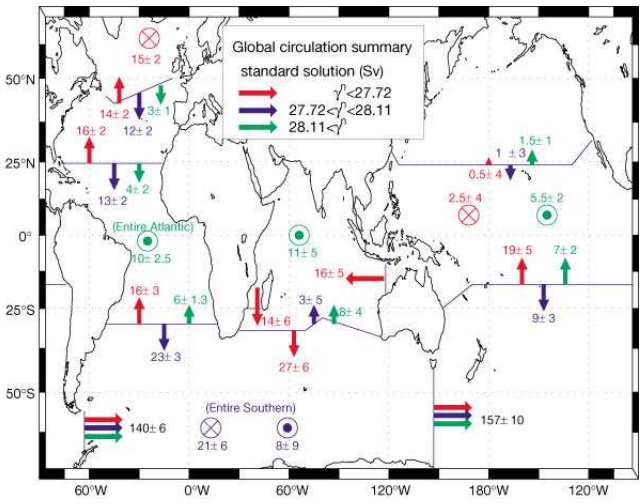

Figure 1.6: Global ocean circulation averaged along longitudes. Estimations obtained with WOCE hydrographic data by [Ganachaud and Wunsch 2000]. Colors indicate the density class of the estimated water mass.

Among the various oceanic processes carrying heat cited above, the dominant one in the North Atlantic is the overturning circulation ([Hall and Bryden 1982]). In the Atlantic, the MOC is made of two main overturning cells : one related to North Atlantic Deep Water (NADW), and one to Antarctic Botom Water (AABW), as sketched in Fig.1.7. There are also Ekman cells, which are wind-driven and do not extend below 500 m. The different cells can be observed in Fig.1.8 showing the mean AMOC streamfunction based on a model constrained by observational data (GECCO model, from [Köhl and Stammer 2008]). The AABW cell is associated to deep waters formed by convection around Antarctica in the Wedell sea and is limited to the deep ocean (below 3000 m). It has a much smaller amplitude than the NADW cell. The NADW cell spans the whole Atlantic basin above 3500 m. Warm waters are carried near the surface northward, in particular via the Gulf Stream in the subtropical gyre. When entering the subpolar region, the surface branch of

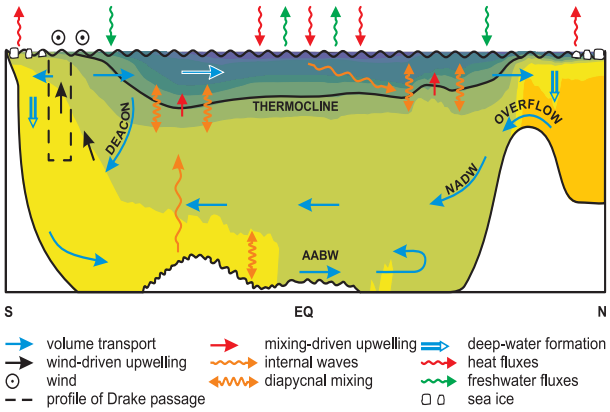

Figure 1.7: Side view of the circulation in the Atlantic, showing various flow components and mechanisms. Color shading shows the observed density stratification, with lightest waters in blue and densest in orange. From [Kuhlbrodt et al. 2007].

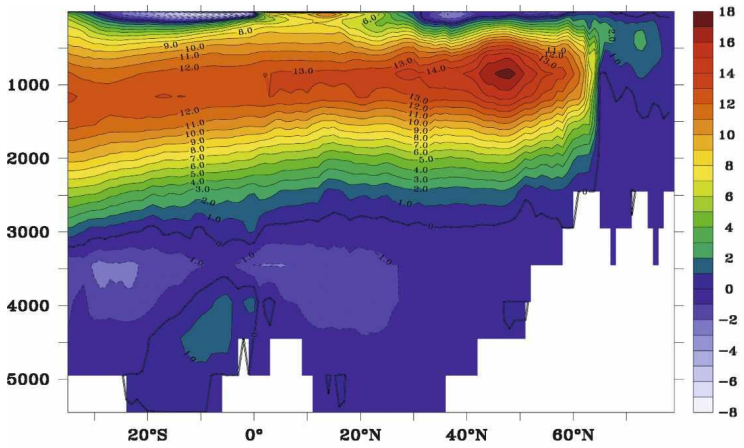

Figure 1.8: AMOC streamfunction based on a model constrained by observational data (GECCO model from 1952-2001). From [Köhl and Stammer 2008].

NADW get colder because of heat loss to the atmosphere, in particular in winter. The cooling is associated with a deepening of the mixed layer depth, reaching more than 1000 m in the main deep convective zones, located in the Labrador Sea, in the Greenland-Norwegian Sea, and near the continental shelves. There exist

two types of mechanism leading to the formation of the NADW : the open ocean convection and the overflows ([Kuhlbrodt et al. 2007]). Deep convection mainly occurs in the Labrador Sea, when the water column has been preconditioned by a buoyancy loss, enhanced cyclonicity, and a weakening of the vertical stratification. If a strong heat loss occurs, the remaining weak density stratification diseappears and vigorous vertical mixing leads to a sinking of cold surface waters and a rising of warmer deep waters. The resulting deep waters can reach depths of 1000 m in the Irminger Sea ([Bacon et al. 2003]), 2000 m in the Labrador Sea, and 3000 m in the Greenland Sea ([Kuhlbrodt et al. 2007]). The other deepwater mass formation occurs via the overflows. In the Nordic Seas, convection at depths of 600 to 800 m is sufficient to create deepwater masses, since the flow has to pass over the sills of the Greenland-Iceland-Scotland ridge. These intermediate depths are regularly ventilated by wintertime mixed layer deepening, contributing to the water masses carried by the overflows. About half of the 15-18 Sv of estimated NADW results from these deepwater masses (2.4-2.9 Sv and 2.4-2.7 Sv from the overflows over the Greenland-Iceland sill in Denmark Strait and over the Iceland-Scotland sill, and 2-4Sv from deep water formed in the Labrador Sea), and related entrainment of waters along the currents paths ([Kuhlbrodt et al. 2007]).

The dense NADW then flows at depth towards the South, in part along the deep western boundary current. It is then upwelled towards the surface through vertical diffusion in the global ocean, and also by the Ekman pumping driven by the strong Westerlies blowing around Antarctica. It has long been considered that the deep convection in the northern North Atlantic was the main driver of the AMOC, but as suggested by [Toggweiler and Samuels 1995], the Southern Ocean may also play a driving role, as discussed below.

1.2 AMOC variability

This circulation, extending from the southern to the northern hemisphere and from the surface to the ocean floor, is hard to fully monitor. Estimations such as that shown in Fig.1.6 only provides mean values of the AMOC, and their uncertainty is too large to document its interannual variability. Since 2004, the RAPID project has deployed moorings along 26.5 $^{\circ}$N to measure the AMOC variability nearly continuously ([Cunningham et al. 2007]). The array design combines cable voltage measurements of the Gulf Stream flowing through the Florida strait at this latitude, estimations of Ekman transport from QuickScat satellite-based wind observations, and measurements of the mid-ocean flow by moored instruments, and it was shown that the total overturning can be estimated as the sum of these components ([Baehr et al. 2004]). It reveals an annual mean overturning of 18.7 Sv +/- 2.1 Sv, but larger fluctuations since it ranges between 4 to 35 Sv (Fig.1.9). All components show a large variability, and the mid-ocean and Gulf Stream components were shown to dominate the seasonnal variability ([Kanzow et al. 2010]). However, the data are limited to one latitude and remain too short to assess the AMOC low-frequency variability. As discussed below, several studies suggest that an index of the low-frequency variability of the North Atlantic SST, named the Atlantic Multidecadal Oscillation (AMO), could be used as an observable proxy of the AMOC over longer periods. In this thesis, we attempt to clarify to what extent it can be indeed done.

Global coupled climate models are useful to investigate the AMOC variability, since they simulate the evolution of the ocean, the atmosphere, the cryosphere, and the land surface, as well as the interactions between these components. Although the ability of models to represent the climate has been considerably improved in recent years, there are still sources of uncertainties arising for instance from the non-representation or the too coarse parameterization of some processes. It is therefore important to consider several models to assess the robustness of a result, since each

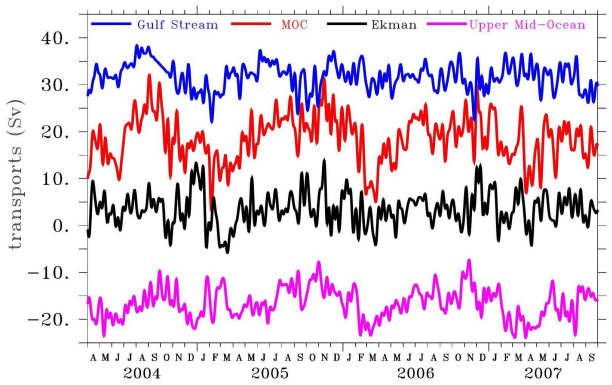

Figure 1.9: Transport time series estimated from the RAPID moorings deployed at 26.5 ° N in the Atlantic basins. The total overturning is shown in red, the blue curve corresponds to the Gulf Stream contribution, the black curve to the Ekman transport contribution, and the pink curve to the upper mid-ocean contribution. Source : RAPID-MOC website.

model has its own bias.

In most climate models, the mean AMOC shows a circulation cell spanning the whole basin, with deep convection occuring at high latitudes, consistent with the observations. However, they show much diversity in their mean value and internal variability, as indicated in Fig.1.10 (left, source : [Gregory et al. 2005]), which shows the AMOC maximum excluding the shallow wind-driven overturning simulated in six coupled models and five Earth system models of intermediate complexity. The latter describe the dynamics of the components of the climate system in less detail than global climate models, but they are more sophisticated than conceptual models ([Claussen et al. 2002]). When integrated with increasing greenhouse gases and aerosol concentrations that simulate the observed and projected anthropogenic forcing, all models show a weakening of the AMOC (Fig.1.10 right from [Gregory et al. 2005], [Schmittner et al. 2005]), which would have large impacts on the global mean climate and on its variability.

In most climate models, the AMOC undergoes multidecadal fluctuations that

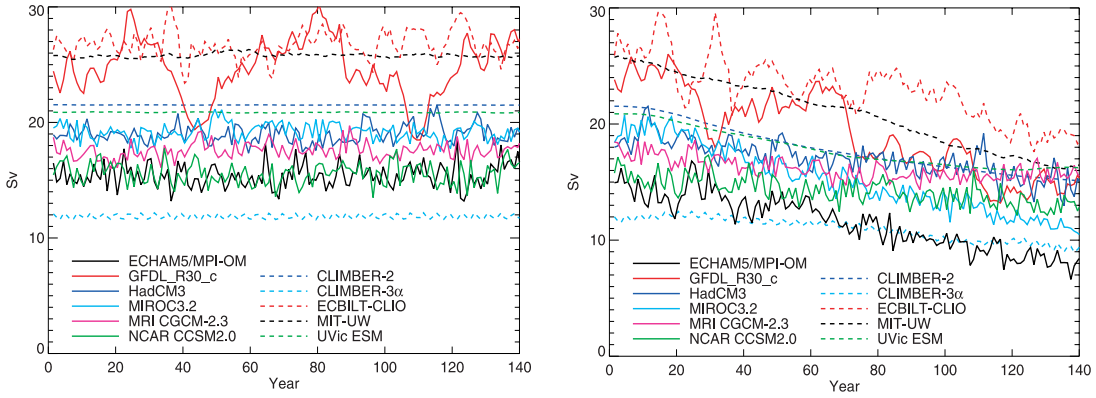

Figure 1.10: Annual time series of AMOC maximum in six coupled climate models and five Earth system models of intermediate complexity. Left : Simulations in control conditions. Right : Simulations with increasing CO_2 concentration bringing it to four times its values in 140 yr. Source : [Gregory et al. 2005].

are closely associated with oceanic heat transport changes ([Dong and Sutton 2001], [Latif et al. 2004]), as illustrated by the common evolution of the time series of 1st empirical orthogonal function (EOF) of Atlantic oceanic transport and AMOC anomalies in a climate model (Fig.1.11 from [Dong and Sutton 2005]). Several

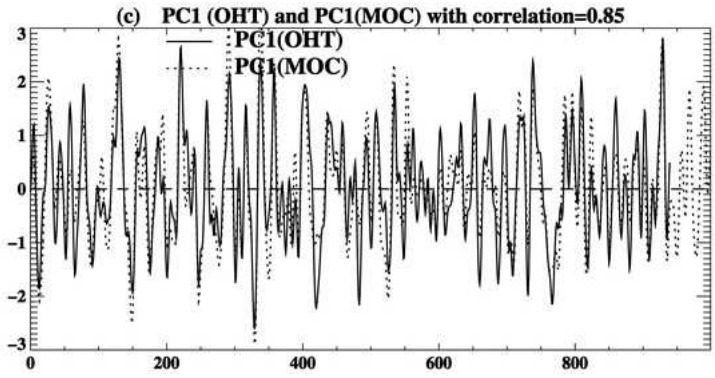

Figure 1.11: From [Dong and Sutton 2005]. Time series of the 1st EOF of Atlantic oceanic heat transport (OHT) and AMOC (here denoted as MOC) from a control simulation of the HadCM3 climate model.

studies indicate that the low-frequency AMOC variability is triggered by changes

in deep convection at high latitudes, which are often caused by the main mode of atmospheric variability in the North Atlantic sector, named the North Atlantic Oscillation (NAO) (e.g. [Delworth et al. 1993], [Eden and Willebrand 2001], [Dong and Sutton 2005], [Deshayes and Frankignoul 2008]). The NAO can be defined as the 1st EOF of Sea Level Pressure (SLP) anomalies in the North Atlantic. A positive NAO phase corresponds to a simultaneous strengthening of the Iceland low and weakening of the Azores high (Fig.1.12), and it is associated with changes in wind, storminess, air temperature, and precipitation across the North Atlantic, as well as over Europe and eastern North America ([Hurrell and Deser 2010]). The NAO frequency spectrum is almost white. A positive NAO phase is associated with

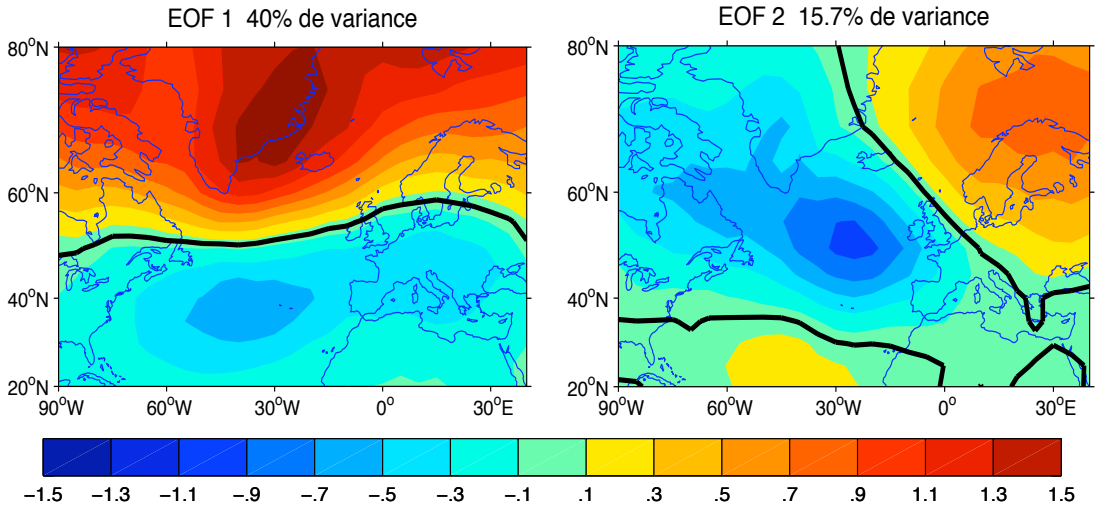

Figure 1.12: NAO and EAP computed as the 1st and 2nd EOF of annual North Atlantic SLP (HadSLP2, 1901-2008).

a cyclonic anomalous circulation in the high latitudes, leading to an intensification of the subpolar gyre, and thus to an increase in the advection of salty water near the deep convection sites. It also forces the convection more directly through anomalous Ekman pumping and anomalous heat fluxes. There is a large concensus on the atmospheric processes forcing the AMOC, although in the low resolution IPSL model (IPSL-CM4), [Msadek and Frankignoul 2008] showed that the 2nd mode of

atmospheric variability in the North Atlantic (East Atlantic Pattern, EAP), shown in Fig.1.12 (right), primarily forces the AMOC, rather than the NAO.

The time scale of the oceanic adjustement strongly depends on the model (e.g. [Eden and Willebrand 2001], [Dong and Sutton 2005]). In an oceanic model forced by the observed surface fluxes from NCEP, [Eden and Willebrand 2001] found an intensification of the subpolar gyre 3 years (yr) after a positive NAO phase, and an increase of the AMOC starting then and reaching a maximum after 8 yr. These time scales are similar to those found by [Dong and Sutton 2005] using a coupled model. On the other hand, [Deshayes and Frankignoul 2008] found a faster AMOC response lagging by 2 yr a positive NAO phase using a realistic hindcast simulation, while [Msadek and Frankignoul 2008] found a slower response of IPSL-CM4 with a maximum AMOC intensification 10 yr after the EAP.

Several studies indicate that the Southern Hemisphere may also play a driving role for the AMOC. An intense oceanic current flows around Antarctica, named the Antarctic Circumpolar Current (ACC). It extends from the surface to the ocean floor. Surface currents are shown in Fig.1.13, based on the OSCAR (Ocean Surface Current Analysis Real-time) data set from 1993 to 2005. Although the mean vertically-integrated velocity is small (between 0.1 and 0.5 $cm.s^{-1}$), the ACC transports a large amount of water (about 125 to 135 Sv, [Cunningham et al. 2003]). As the ACC circumnavigates the Southern Ocean, it redistributes waters from one basin to another one, as sketched in Fig. 1.14 and it thus plays a crucial role in the large-scale oceanic circulation. This intense circulation is driven by the strong Westerlies blowing between 40 and 60 $^{\circ}$ S, in the latitude band of the Drake passage, with a mean wind speed ranging between 7.5 to 12 $m.s^{-1}$. The zonal fluctuations of these winds are well represented by the main mode of atmospheric variability in the Southern Hemisphere. The latter is called Southern Annular Mode (SAM), since its pattern is almost annular. It can be computed as the 1st EOF of SLP anomalies. An upward trend of the SAM, corresponding to an intensication of the Westerlies, as well as a southward shift of the latter have been observed during the past two to three

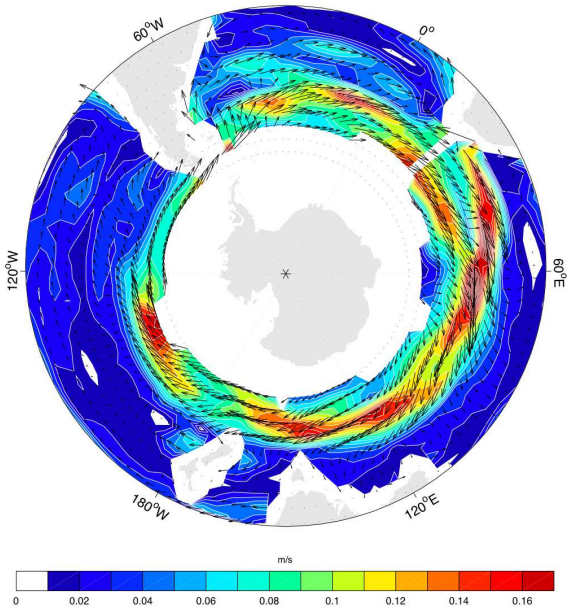

Figure 1.13: Surface currents in the Southern ocean based on the OSCAR data set from 1993 to 2005. Arrows indicate the current direction and colors its intensity.

decade, and these changes are attributed to anthropogenic forcing ([Cai 2006]). Using a model sensitivity experiment, [Toggweiler and Samuels 1995] showed that stronger Westerlies can induce more deep water formation in the North Atlantic and more deep outflow through the South Atlantic. Indeed, the stronger winds generate more upwelling and an intensified northward Ekman transport around Antarctica. The equatoward flow must be compensated by water flowing poleward, but passing where the topography allows a zonal pressure gradient, because a net meridional geostrophic flow is only possible in the presence of zonal boundaries. This return flow must thus pass below the sill of the Drake Passage, and such a deep water flow can only be formed where the stratification is weak enough, namely in the northern North Atlantic. Using a climate model, [Sijp and England 2009] showed that a northward shift of the Westerlies leads to a weakening of the AMOC, but also to a strengthening of the thermohaline sinking in the North Pacific, since the position of the Westerlies controls both the amount of relatively fresh water coming

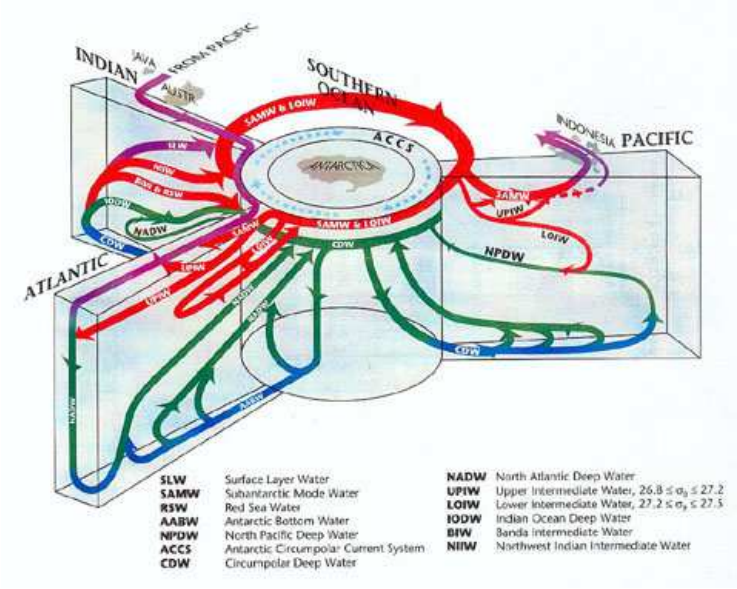

Figure 1.14: From [Schmitz 1996]. Schematic meridional sections of interbasin flow for each ocean with their global linkage. Surface layer circulations are shown in purple, intermediate circulations in red, deep circulations in green, and bottom circulations in blue.

from the Drake Passage into the Atlantic basin and the inflow of salty water coming from the Indian Ocean through the Agulhas leakage. Based on climate models, [Toggweiler and Russell 2008] argued that the predicted increase and poleward shift of the Westerlies in the 21th century should in part counterbalance the weakening of the AMOC predicted by climate models in a warmer climate ([Gregory et al. 2005]). Indeed, these stronger and southward shifted winds should bring more deep water from the Southern Ocean interior to the surface, and thus lead to more sinking and a stronger AMOC. Similarly, [Biastoch et al. 2009] used a high-resolution oceanic model forced by the observed winds to show that the poleward shift of the Westerlies leads to an increase of salt entering the Atlantic basin through the Aghulas leakage, which may lead to a strengthening of the AMOC when these saltier water reach the northern North Atlantic. All these studies focused on the equilibrium response to different wind configurations, the transient behavior was only briefly

discussed by [Sijp and England 2009], who showed that the AMOC adjustment was taking at least 30 yr. It is thus crucial to investigate the processes governing the Southern Hemisphere variability and to understand its impact on the AMOC.

As mentionned above, the multidecadal fluctuations of the AMOC are closely related to oceanic heat transport changes. The AMOC variability is also associated with basin-scale SST anomaly that are often an interhemispheric dipole ([Latif et al. 2004], [Vellinga and Wu 2004], [Knight et al. 2005], [Mignot et al. 2007]), as illustrated in Fig.1.15. This pattern is very similar to

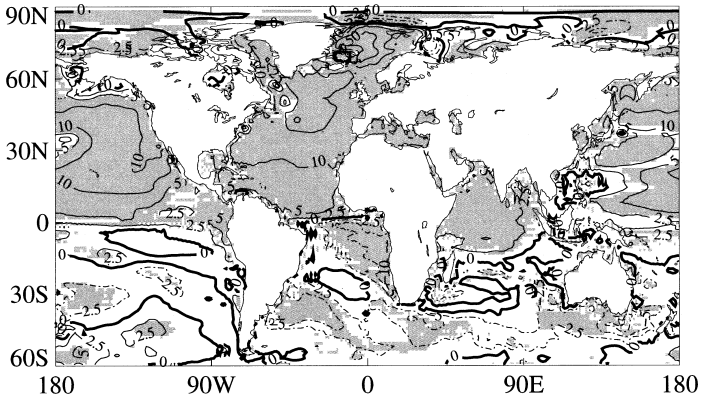

Figure 1.15: Regression of decadally averaged SST anomalies onto the AMOC maximum (units 0.01 $^\circ C.Sv^{-1}$, contours values at +/- 50, 25, 10, 5, 2.5, and 0). Solid contours indicate positive values and dash-dotted contours correspond to negative values. The shaded area indicates that the regression is 5% significant. Source : [Vellinga and Wu 2004].

the one associated with multidecadal fluctuations of North Atlantic SST, often represented by the AMO, as shown in Fig.1.16. The latter is commonly defined as the time series of low-pass filtered (with a cut-off period of $T_c = 10$ yr) SST anomalies averaged in the North Atlantic basin (0-60 $^\circ$N, 75-7.5 $^\circ$W) and linearly detrended to remove the long-term changes ([Enfield et al. 2001], [Sutton and Hodson 2005]). Using a control simulation of a global climate model, [Latif et al. 2004] found a high correlation between low-pass filtered North Atlantic SST anomalies (averaged

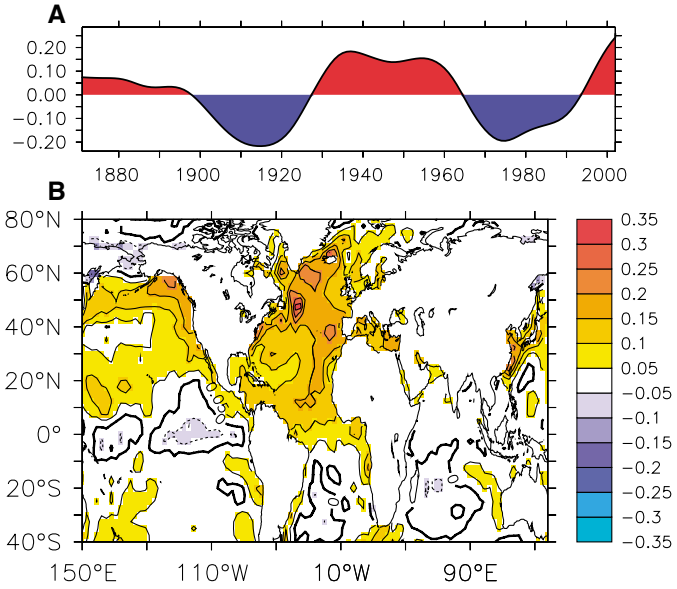

Figure 1.16: From [Sutton and Hodson 2005]. (Top) AMO time series defined as the time series of SST anomalies averaged over the North Atlantic (0-60 ° N, 75-7.5 ° W), low-pass filterd with a 37-point Henderson filter that also removes the long term mean. (Bottom) SSTs (in ° C) associated with the normalized AMO index.

between 40-60 ° N and 50-10 ° W) and the AMOC maximum at 30 ° N, suggesting that the AMOC variations could perhaps be reconstructed from surface observations. They also showed that, in greenhouse warming simulations, the low-frequency AMOC variability was well reflected in the SST difference between North and South Atlantic. Similarly, [Knight et al. 2005] found a strong correlation between the AMOC maximum at 30 ° N and the AMO in a control simulation of the HadCM3 climate model, suggesting that the AMO may be a good predictor of the AMOC. Hence, they reconstructed the past AMOC variability from the observed SST fields ([Rayner et al. 2003]).

The high correlation found in most climate models between the AMO and the AMOC when the latter leads by a few years suggests indeed that the AMO may be an observable proxy of the AMOC variability, since SSTs are easily measur-

able contrary to the AMOC. However, although the AMO in part reflects the AMOC multidecadal variability, it is influenced by external forcings (volcanic activity, solar forcing) and anthropogenic changes. Since there is no reason to assume that the resulting SST changes can be removed by simply substracting a linear trend, [Trenberth and Shea 2006] argued that the global changes could be more efficiently removed by substracting the global mean SST, while [Ting et al. 2009] constructed a model-based estimate of the forced component of North Atlantic SST variability using several coupled model simulations with multiple ensemble members and a signal-to-noise maximizing empirical orthogonal function analysis. In addition, the Atlantic SST is influenced by short time scales atmospheric forcing and ocean dynamics. It is also affected by the SST changes in the Tropical Pacific linked to ENSO via an atmospheric bridge described below ([Alexander et al. 2002], [Brönnimann 2007]). Moreover, there are links at low frequencies between the North Atlantic SST and the Pacific Decadal Oscillation (PDO) [Enfield et al. 2001], [Orgeville and Peltier 2007], [Müller et al. 2008]), and [Enfield and Mestas-Nunez 1999] and [Mestas-Nunez and Enfield 1999] mentionned a linkage between the eastern North Pacific and the North Atlantic SST on decadal to multidecadal time scales. It is thus of interest to try removing these various influences from the SST field in order to better single out the SST signature of the AMOC.

1.3 Global modes of SST variability

To understand the relation between the AMOC and the AMO and establish to what extent the latter can be used as an indicator of the former, it is useful to briefly review what controls the SST variability. The SST depends on atmospheric processes governing the heat flux at sea surface, but also on oceanic processes, such as heat transport by currents, vertical and horizontal mixing, and the mixed layer depth. The oceanic upper layer is observed to be well mixed by turbulent motions,

with an almost uniform distribution of temperature, salinity, and horizontal velocity within a detph h. The temperature equation can thus be integrated over the mixed layer to give an equation of the SST evolution ([Frankignoul 1985])

$$h\frac{\partial T}{\partial t} + h\mathbf{u}.\nabla T + \mathbf{w_e}(T - T_b) - \kappa h\nabla^2 T + \frac{Q_{net} - Q_b}{\rho C_p} = 0 \tag{1.1}$$

with T the temperature of water in the mixed layer, ρ its density, C_p its heat capacity, Q_{net} is the net heat flux across the air-sea interface (positive upward), Q_b the heat flux at the mixed layer base, $\mathbf{u}$ the horizontal current velocity, $\mathbf{w_e}$ the entrainment velocity, T_b the temperature of entrained water, and κ the horizontal diffusivity parameterizing the horizontal mixing. The term $\mathbf{w_e}(T - T_b)$ indicates changes induced by water entrained in the mixed layer, and $\mathbf{u}.\nabla T$ corresponds to the temperature advection by horizontal currents. The horizontal velocity can be decomposed into a part related to quasi-geostrophic currents $\mathbf{u_{geo}}$ and a part associated with Ekman transport $\mathbf{u_{ek}}$. Q_b mainly represents vertical mixing at the mixed layer base and the part of solar radiation absorbed at larger depth. It can generally be neglected, since most of the solar radiation is absorbed in the mixed layer (except when the mixed layer is shallow, as in the eastern tropical Pacific). The surface heat flux is defined by $Q_{net} = Q_s + Q_l + Q_{sw} + Q_{lw}$ with Q_s and Q_l sensible and latent heat fluxes, Q_{sw} is the short wave radiation, and Q_{lw} the net flux of infrared radiation from the sea.

As mentionned above, the SST varies on different time scales and these variations depend on the geographical location (Fig.1.3). In this thesis, we are interested in interannuel to multidecadal time scales. To understand the mechanism governing SST varibility, we decompose each variable into a seasonaly varying mean (denoted by an overbar) and an anomaly (denoted by a prime), the equation (1.1) becomes

$$\begin{array}{rcll} \frac{dT'}{dt} & = & -\frac{Q'_{net}}{\rho C_p \overline{h}} & \text{A} \\ & & -\frac{(h\mathbf{u})'.\nabla(\overline{T}+T')}{\overline{h}} & \text{B} \\ & & -\frac{h'}{\overline{h}}\frac{\partial \overline{T}}{\partial t} & \text{C} \\ & & -\frac{(\overline{\mathbf{w_e}}-\mathbf{w_e}')(T'-T'_b)}{\overline{h}} - \mathbf{w_e}'\frac{(\overline{T}-\overline{T_b})}{\overline{h}} & \text{D} \\ & & +\kappa h\nabla^2 T' & \text{E} \end{array} \tag{1.2}$$

where $\frac{d}{dt} = \frac{\partial}{\partial t} + \overline{\mathbf{u}}.\nabla$ is the time derivative following the mean motion, and contains thus advection by mean currents. Note that, in equation (1.2), mean products of anomalies have been neglected, as well as some mixing contribution, and $\frac{\partial T'}{\partial t}$ as compared to $\frac{\partial \overline{T}}{\partial T}$ in the term related mixed layer depth changes (C). The terms participating to the evolution of SST anomaly can be divided into 3 types ([Frankignoul 1985]). The first type corresponds to the effect of atmospheric forcing on SST via surface heat flux (A), wind-driven currents (B), mixed-layer depth changes (C), and entrainment (D). The second type is related to the effect of the ocean interior variability, mainly via quasi-geostrophic motions that alter the upper layer by horizontal advection and vertical motion near the mixed layer base (C and D). The third type is associated with the damping of SST anomaly, made by atmospheric feedback mainly via (A), by oceanic feedback (D), by horizontal mixing (F), and by vertical mixing if Q_b were not neglected.

Global averaged SSTs have been observed to increase by 0.74 °C in the last century (between 1906 and 2005), mainly due to anthropogenic forcing ([Trenberth et al. 2007]). This warming is not steady and depends on the season and on the location, as indicated in Fig.1.17 (from [Ting et al. 2009] 2009) showing the ratio of externally forced variance and the total variance averaged for the six IPCC AR4 coupled models with at least four ensemble members for the twentieth century. The forced warming is much weaker over the North Atlantic, the North Pacific, and in the Southern Hemisphere near 60 °S, which is probably due to local ocean dynamics and/or uneven distribution of clouds and aerosols effects ([Ting et al. 2009] 2009). Concerning natural variability, at period larger than a month or so, except for the ENSO teleconnections (as discussed below), the atmospheric signal can be considered in a first approximation as a white noise forcing the ocean variability, and the ocean integrates the atmospheric forcing, as shown in the stochastic model of climate variability of [Hasselmann 1976] and [Frankignoul and Hasselmann 1977]. At low frequencies, however, the term associated with the advection of mean SST anomalies by geostrophic currents anomalies

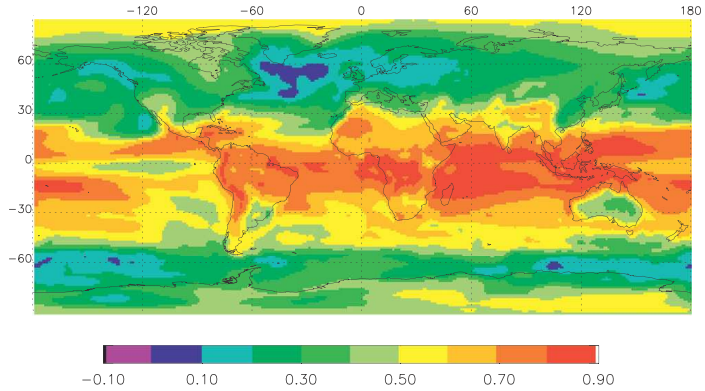

Figure 1.17: From [Ting et al. 2009]. Ratio of externally forced variance and the total variance averaged for the six IPCC AR4 coupled models with at least four ensemble members for the twentieth century

($\mathbf{u_{geo}}'.\nabla\overline{T}$ in eq.(1.2)) plays an increasing role. For instance, the low frequency fluctuations of the AMOC are associated with anomalous, geostrophic currents, which distort the mean SST gradient, mainly resulting in the pattern shown in Fig.1.15.

SST variations at one location are generally related to those at another in the surroundings, reflecting the large spatial scale of both the atmospheric forcing and the oceanic variations. Eigentechniques such as EOF analysis and Principal Oscillation Patterns are useful tools to objectively define patterns of variability. For instance, in the EOF analysis, the 1st eignemode corresponds to a spatio-temporal pattern of variability that maximizes the variance.

The main mode of global SST natural variability result from coupled ocean-atmosphere interactions linked to the El Niño Southern Oscillation (ENSO, Fig.1.18). During an El Niño, which occurs every 3-5 yr, the eastern Pacific equatorial SSTs undergoes a large warming. It is strongly linked to the atmosphere, with an El Niño event being associated with a reduced Walker circulation, measured by a low Southern Oscillation Index (SOI) and corresponding to a low sea-saw in SLP between the East and the West Pacific. In this study, we do not focus on ENSO mechanisms, but on its impact on remote oceanic conditions. As shown in

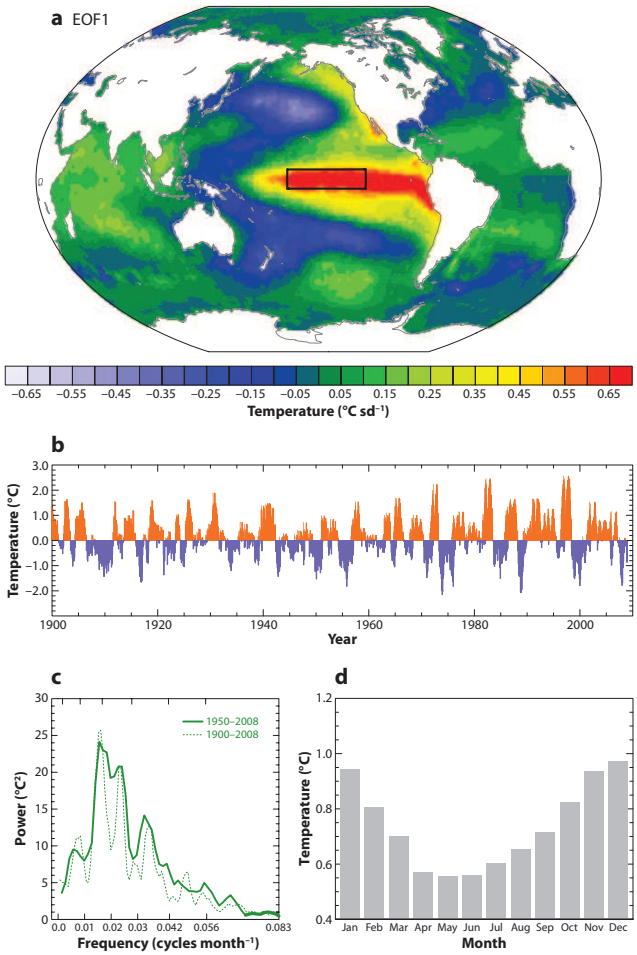

Figure 1.18: From [Deser et al. 2010]. (a) First EOF of detrended monthly global SST anomalies based on the HadISST data set (1900-2008), accounting for 19% of the variance and representing the ENSO. (b) Time series of monthly SST anomalies in the Niño 3.4 region, which is indicated in the EOF pattern by the rectangle. (c) Power spectrum of the Niño 3.4 index based on 1950-2008 (solid curve) and 1900-2008 (dashed curve). (d) Monthly std of the Niño 3.4 index.

Fig.1.19, SST anomalies are associated with El Niño in the North Pacific, the north tropical Atlantic and Indian oceans during winter and spring ([Klein et al. 1999], [Alexander et al. 2002], [Brönnimann 2007]). This connection is established via an "atmospheric bridge" mechanism sketched in Fig.1.20 : the SST warming in

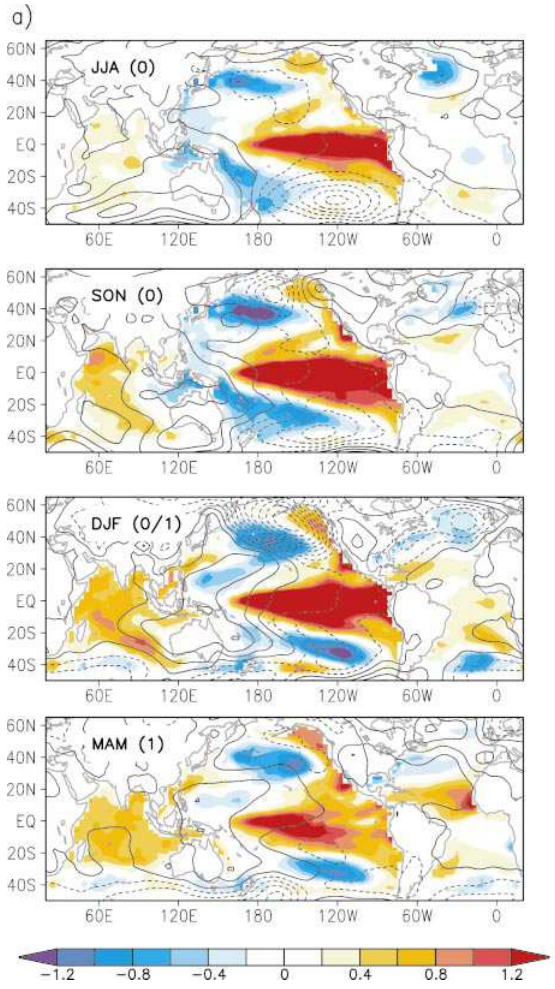

Figure 1.19: From [Alexander et al. 2002]. El Niño- La Niña composite of SLP (contour of 1 mb) and SST (color shading of 0.2 ° C) for June to August (JJA(0)), September to November (SON(0)) of the ENSO year, December of the ENSO year to February of 1 yr after (DJF(0/1)), and March to May of 1 yr after.

the equatorial Pacific alters the deep convective zone, which changes the Hadley and Walker cells, generates Rossby waves, and affects the interactions between the quasi-stationary flow and storm tracks ([Trenberth et al. 1998]). This generates anomalous heat, freshwater, and momentum fluxes outside the equatorial Pacific. The ocean then responds to these flux anomalies, leading to changes in mixed layer depth, salinity, and SST. ENSO also leads to a warming in the whole Trop-

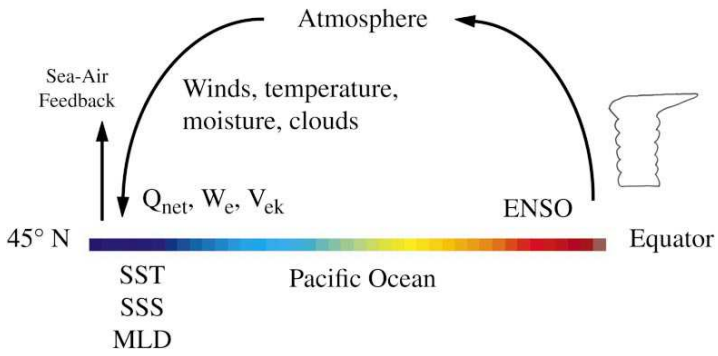

Figure 1.20: From [Alexander et al. 2002]. Schematic of the atmospheric bridge mechanism between the tropical and North Pacific Oceans, this mechanism is also valid for the South Pacific, Atlantic, Indian Oceans. Q_{net} is the net surface heat flux, $\mathbf{W_e}$ the entrainment rate into the mixed layer, mainly driven by surface fluxes, SSS the sea surface salinity, and MLD the mixed layer depth.

ics, through the "tropospheric temperature mechanism" ([Chiang and Sobel 2002], [Chiang and Lintner 2005]) : the troposphere is warmed by the heat released by ENSO, and this warming is rapidly propagated to the remote Tropics by Kevin waves, and then transmitted to the ocean.

In the North Pacific, the main mode of SST variability results from the ENSO teleconnections, but also from the local atmospheric forcing and the advection by geostrophic currents. This mode is the PDO, defined as the leading EOF of annual North Pacific SST (20 ° N-60 ° N, 120 ° E-100 ° W) ([Mantua et al. 1997]). It has a horseshoe pattern, with positive anomalies along the American coast and negative anomalies in the central North Pacific in a positive phase (Fig.1.21). In the observations, the PDO is associated with SLP changes corresponding to a Pacific North American Pattern (PNA) ([Wallace and Gutzler 1981]), with positive SLP anomalies over Hawaï, negative anomalies south of the Aleutian Islands, and positive anomalies over the intermountain region of North America. Note that the PNA is a natural mode of atmospheric variability, which is reflected in the 2nd EOF of the

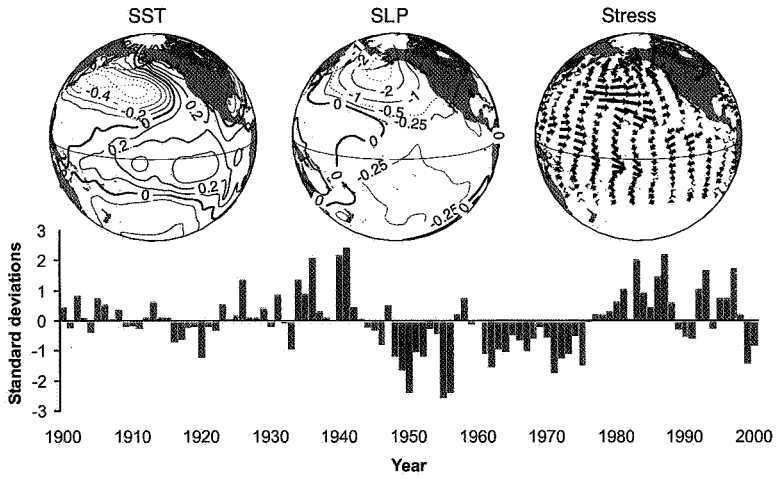

Figure 1.21: From [Mantua and Hare 2002]. SST (top left) in $^\circ$C, SLP (top middle) in mbar, and wind stress (top right) associated with November-March averaged values of the PDO index (Bottom). The longest wind vectors represent a pseudo stress of 10 $m^2.s^{-2}$.

Northern Hemisphere extratropical SLP. The PDO was shown to be well modelled by a 1st order auto-regressive process forced by the natural variability of the Aleutian low, the ENSO via the atmospheric bridge, as well as oceanic advection in the Kuroshio-Oyashio Extension ([Schneider and Cornuelle 2005]). It is also influenced by the reemergence of North Pacific SST ([Newman et al. 2003]).

In the North Atlantic, the dominant mode at interannual to decadal scale is the North Atlantic tripole, which is largely driven by the NAO via surface energy flux and Ekman currents, but also influence by SST anomaly reemergence ([de Coëtlogon and Frankignoul 2003]). At lower frequency, the SST is dominated by another mode of variability first discussed by [Bjerknes 1964], [Kushnir 1994], and later referred to as the AMO ([Kerr 2000]). The mode does not seem to be related to direct atmospheric forcing but was suspected to reflect the variability of oceanic circulation ([Delworth and Mann 2000]), as discussed above.

1.4 Objectives of this thesis

This thesis has two different goals. The first objective is to investigate the influence of the Southern Ocean onto the AMOC at interannual to multidecadal time scales, using 500 yr of a control simulation with the IPSL-CM4 climate model. This is done in Chapter 2, which is an article published in Journal of Climate.

The second objective, which is the main topic of this thesis, is to understand the relation between the AMOC and the AMO, and to establish to what extent the latter can be used as an observable proxy of the former. In particular, we investigate the impact of removing the ENSO teleconnections, the influence the Pacific decadal variability, and the trend related to global warming in the last century. This AMO deconstruction is made using a dynamical filter, based on linear inverse modeling (LIM). First, we describe the LIM theory in Chapter 3. Then, in Chapter 4, the LIM approach is applied to the observed global SST anomalies (north of 20 $^\circ$ S where data coverage is best), and used to decompose the North Atlantic SST field into a signal linked to the global trend, a part that is related to ENSO, one to decadal variability in the Pacific, and a residual. To determine which "filtered" AMO is expected to best reflect the AMOC variability, the decomposition is also applied to an historical simulation and several control simulations of global climate models, where the AMOC is known.

The AMO deconstruction is also made in a simulation of the last millennium climate in Chapter 5, representing the volcanic eruptions, since the latter, and in particular explosive tropical eruptions, strongly impact SST and the oceanic variability (e.g. [Robock 2000], [Jones et al. 2005], [Otterå et al. 2010], [Mignot et al. 2011]).

Chapter 2

Influence of the Southern Annular Mode onto the Atlantic Meridional Overturning Circulation

624 JOURNAL OF CLIMATE VOLUME 24

Links between the Southern Annular Mode and the Atlantic Meridional Overturning Circulation in a Climate Model

CAMILLE MARINI, CLAUDE FRANKIGNOUL, AND JULIETTE MIGNOT

LOCEAN, Université Pierre et Marie Curie, Paris, France

(Manuscript received 15 December 2009, in final form 6 September 2010)

ABSTRACT

The links between the atmospheric southern annular mode (SAM), the Southern Ocean, and the Atlantic meridional overturning circulation (AMOC) at interannual to multidecadal time scales are investigated in a 500-yr control integration of the L'Institut Pierre-Simon Laplace Coupled Model, version 4 (IPSL CM4) climate model. The Antarctic Circumpolar Current, as described by its transport through the Drake Passage, is well correlated with the SAM at the yearly time scale, reflecting that an intensification of the westerlies south of 45°S leads to its acceleration. Also in phase with a positive SAM, the global meridional overturning circulation is modified in the Southern Hemisphere, primarily reflecting a forced barotropic response. In the model, the AMOC and the SAM are linked at several time scales. An intensification of the AMOC lags a positive SAM by about 8 yr. This is due to a correlation between the SAM and the atmospheric circulation in the northern North Atlantic that reflects a symmetric ENSO influence on the two hemispheres, as well as an independent, delayed interhemispheric link driven by the SAM. Both effects lead to an intensification of the subpolar gyre and, by salinity advection, increased deep convection and a stronger AMOC. A slower oceanic link between the SAM and the AMOC is found at a multidecadal time scale. Salinity anomalies generated by the SAM enter the South Atlantic from the Drake Passage and, more importantly, the Indian Ocean; they propagate northward, eventually reaching the northern North Atlantic where, for a positive SAM, they decrease the vertical stratification and thus increase the AMOC.

1. Introduction

The Southern Ocean is a key component of the climate system. Its circulation is dominated by the Antarctic Circumpolar Current (ACC) that transports about 125–135 Sv (1 Sv $\equiv 10^6$ m^3 s^{-1}) of water around Antarctica (Cunningham et al. 2003) and links the Atlantic, Indian, and Pacific Oceans, redistributing water masses from one basin to another, thus playing a fundamental role in the global oceanic circulation. The ACC is largely driven by the strong southern westerlies, primarily reflecting the balance between surface wind stress and bottom stress due to the pressure gradient across topographic features on the ocean floor (Munk and Palmen 1951; Olbers et al. 2004). It may also be influenced by the wind stress curl (Stommel 1957) and buoyancy forcing (Gnanadesikan and Hallberg 2000). The atmospheric variability in the Southern Hemisphere is strongly dominated by the southern annular mode (SAM; Thompson and Wallace 2000). A positive phase of the SAM corresponds to an intensification and southward shift of the westerlies. Using low-resolution coupled ocean–atmosphere models, several studies (e.g., Hall and Visbeck 2002; Sen Gupta and England 2006) show that the intensification of the westerlies creates an anomalous northward Ekman drift. Through mass continuity, this enhances the upwelling around Antarctica, leading to a large vertical tilt of the isopycnals in the Southern Ocean and thus an increase of the ACC transport.

The southern ocean–atmosphere system may play a driving role in the global meridional overturning circulation (MOC). Based on sensitivity studies with an ocean circulation model forced by annual mean boundary conditions at the surface, Toggweiler and Samuels (1995) found that stronger winds blowing in the latitude band of the Drake Passage increase deep-water formation in the North Atlantic and the deep outflow through the South Atlantic. Indeed, a stronger zonal wind stress increases the northward Ekman transport around Antarctica. As

Corresponding author address: Camille Marini, LOCEAN, Université Pierre et Marie Curie, 4 place Jussieu, 75252 Paris CEDEX 05, France.
E-mail: camille.marini@locean-ipsl.upmc.fr

DOI: 10.1175/2010JCLI3576.1

a net meridional geostrophic flow is only possible in the presence of zonal boundaries, they argued that the return flow must pass below the sill of the Drake Passage (at about 2500 m), where topography allows a zonal pressure gradient. Such a deep-water flow can only be formed where the stratification is weak enough, namely in the northern North Atlantic. Sijp and England (2009) examined the influence of the position of the Southern Hemisphere westerlies on the global MOC in a global ocean–ice circulation model coupled to a simplified atmosphere. The latitude of the zero-wind stress curl was shown to control both the amount of relatively fresh water coming from the Drake Passage into the Atlantic basin and the inflow of salty water coming from the Indian Ocean through the Agulhas leakage, so that a northward shift of the westerlies reduced the Atlantic MOC (AMOC) but enhanced the thermohaline sinking in the North Pacific; the opposite occurred for a southward shift. Toggweiler and Russell (2008) argued that the predicted increase and poleward shift of the westerlies in the twenty-first century should bring more deep water from the Southern Ocean interior to the surface, leading to more sinking and a stronger AMOC. This would oppose the weakening of the AMOC predicted by climate models in a warmer climate (Gregory et al. 2005) so that it is important to better understand the relation between the Southern Hemisphere winds and the AMOC. All these studies were based on coarse-resolution ocean models and focused on the equilibrium response to different wind configurations; the transient behavior was only briefly discussed in Sijp and England (2009), who showed that the AMOC adjustment was taking at least 30 yr.

Meredith et al. (2004) found observational evidence that the seasonality of the transport through Drake Passage is well correlated with that of the SAM, but Böning et al. (2008) detected no increase in the tilt of the isopycnals between the 1960s and recent years, as would be expected from the positive trend in the SAM during recent decades, or as simulated by coarse-resolution models. They thus concluded that the ACC transport and the meridional overturning in the Southern Ocean were insensitive to decadal changes in the wind stress, and they argued that mesoscale eddies play an integral role in stabilizing the oceanic response. Although it may seem debatable to solely link the ACC transport to the SAM in the changing environment of the last few decades, this suggests that mesoscale eddies need to be resolved to study the Southern Ocean response to changing winds. Screen et al. (2009) investigated the response of the Southern Ocean temperature to the SAM in a forced oceanic model at resolutions ranging from coarse (with a Gent and McWilliams parameterization; Gent and McWilliams 1990) to eddy resolving. The fast response was similar, but the high-resolution version showed an increase in the Southern Ocean mesoscale eddy kinetic energy 2–3 yr after a positive SAM, which resulted in a warming of the upper layers south of the polar front, in part compensating the initial increase in northward Ekman transport. Using an eddy-permitting oceanic model forced by the atmospheric variability of the last decades, Biastoch et al. (2009) showed that the observed poleward shift of the westerlies in the past two to three decades was associated with an increase of the Agulhas leakage. Consequently, more salty Indian Ocean waters have entered the Atlantic basin and begun to invade the North Atlantic, which may influence the future evolution of the AMOC. On the other hand, Treguier et al. (2010) found with an eddy-permitting oceanic hindcast that the MOC in the Southern Hemisphere was well correlated with the SAM at interannual and decadal time scales, while the eddy contribution to the MOC was chaotic in nature and uncorrelated with the SAM, so the model behavior was similar to that of coarse-resolution models. Hence, although eddy-resolving climate models will ultimately be needed to capture realistically the effect of the SAM on the Southern Ocean and the AMOC, the role of oceanic eddies is still debated and it remains of interest to understand the behavior of the present generation of climate models, in particular those that parameterize the eddy effects.

The aim of this study is to investigate the main features of the natural variability of the austral region and the links between the Southern Hemisphere winds, the ACC, and the AMOC on different time scales. As the observations are too sparse and eddy-resolving climate models are not yet available, we use a control simulation of the IPSL CM4 climate model. The model was used with a rather coarse atmospheric resolution (LoRes version, to follow Marti et al. 2010) for the Intergovernmental Panel on Climate Change (IPCC) Fourth Assessment Report (AR4). As its representation of the Southern Ocean circulation was poor (Russell et al. 2006), we use a higher-resolution version (HiRes; Marti et al. 2010) that compares better with the observations, as described in section 2. Section 3 discusses the relations between the ACC, the SAM, and the global MOC in the Southern Hemisphere at the interannual time scale. In section 4, we focus on the AMOC and discuss a SAM impact at the decadal time scales, while the link between the SAM and the AMOC at longer time scales is discussed in section 5 and conclusions are given in section 6.

2. Model description

A control simulation with version HiRes of the IPSL CM4 model is used for this study. The atmospheric component of the model is Laboratoire de Météorologie

Dynamique Zoomé (LMDZ; (Hourdin et al. 2006) with 144 longitudinal and 97 latitudinal grid points. As described by Marti et al. (2010), this is higher than the version LoRes (96 × 72) that was used for the IPCC AR4 and phase 3 of the Coupled Model Intercomparison Project (CMIP3) and rates poorly in its ability to simulate the Southern Ocean (Russell et al. 2006). This ability is largely improved in the present version of the model. There are 19 vertical levels in the atmosphere with hybrid σ-p coordinates. Other components are identical to the LoRes version. The oceanic model is Océan Parallélisé 8 (OPA8; Madec et al. 1998) with a horizontal resolution based on a 2° mesh and 31 vertical levels, with 10 levels in the top 100 m. Mesoscale eddies that are crucial for representing the ACC (e.g., Marshall and Radko 2006; Treguier et al. 2007) are taken into account by a Gent and McWilliams parameterization, which similarly flattens the isopycnals using a coefficient that depends on the growth rate of baroclinic instabilities (usually varying from 15 to 3000 $m^2\ s^{-1}$). Iudicone et al. (2008) argued that this parameterization led to a realistic representation of the ACC dynamics in the ocean component of the model. The land surface model is the Organizing Carbon and Hydrology in Dynamic Ecosystems (ORCHIDEE) model (Krinner et al. 2005) and the dynamic and thermodynamic sea ice model is the Louvain-la-Neuve Sea Ice Model (LIM; Fichefet and Morales-Maqueda 1999). The Ocean Atmosphere Sea Ice Soil (OASIS; Valcke 2006) coupler is used to synchronize the different components of the coupled model. The last 500 years of a 650-yr control run using constant 1860-level greenhouse forcing are to a reasonable approximation in a statistically stationary state and are used in this study.

The key features of the Southern Hemisphere climatology are well reproduced. As shown in Fig. 1, the mean surface wind stress is rather realistic but shifted toward the equator by about 5° compared to the 40-yr European Centre for Medium-Range Weather Forecasts (ECMWF) Re-Analysis (ERA-40). It is a general caveat of the IPSL model to represent the major atmospheric structures shifted equatorward (Marti et al. 2010). The ACC follows the line of maximum wind stress and it thus goes too far north after the Drake Passage. The mean transport across the Drake Passage is 90 Sv. It is weaker than the observed transport (125–135 Sv; see Whitworth 1983; Whitworth and Peterson 1985) but more realistic than the 34 Sv of the LoRes version, where the maximum westerlies were located even further equatorward. The ACC and the wind stress are also too weak in the South Pacific. The zonal SST distribution in the Southern Ocean is quite realistic, except that the meridional temperature gradient is too weak near the ACC. However, there are two major biases in the model salinity (not shown). The surface waters are too fresh in the Pacific sector compared to the Levitus climatology (presumably because of too much sea ice melting during austral summer) and too salty south of Africa [primarily because the evaporation minus precipitation flux is too strong (not shown, but see Marti et al. 2010)]. The mean global MOC (including the parameterized eddy contribution) between 60° and 30°S is shown in Fig. 2. There is a surface-intensified clockwise cell that results from the strong westerlies near 50°S,

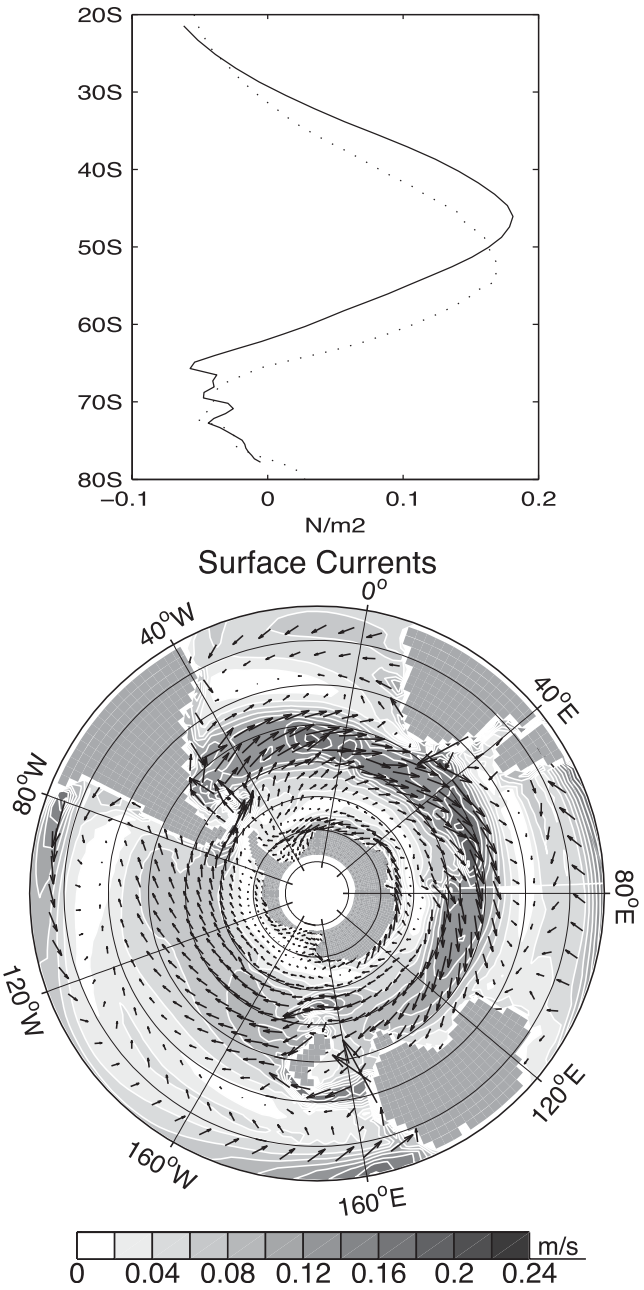

FIG. 1. (top) Climatology of zonally averaged zonal wind stress in the HiRes simulation (solid line) and in the ERA-40 reanalysis (dashed lines). (bottom) Climatology of surface currents and wind stress in the HiRes simulation. The grayscale indicates the norm of the vectors and the arrows their direction.

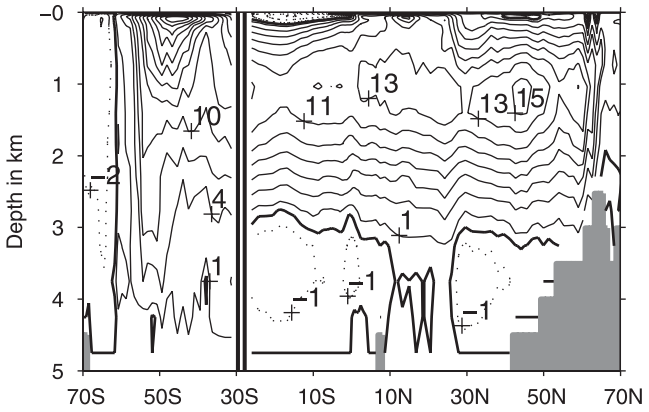

FIG. 2. Climatology of the global MOC south of 30°S and of the AMOC north of 30°S from the HiRes simulation. Contour interval is 3 Sv for the MOC and 2 Sv for the AMOC; dashed lines correspond to negative values and the thick line to zero.

which cause upwelling to the south and sinking to the north. Note that this cell would be stronger if the eddies were not taken into account, since they compensate a part of the Ekman transport along the ACC, albeit less than in models that explicitly represent them (Marshall and Radko 2006; Treguier et al. 2007). North of 30°S, Fig. 2 only shows the Atlantic MOC, which is the major contributor to the global MOC. It has a maximum of 15 Sv near 45°N at a depth of 1100 m, which is consistent with the observational estimate of 15 Sv by Ganachaud and Wunsch (2000).

The amount of incoming North Atlantic Deep Water (NADW) at 32°S plays an important role in the dynamics of the Southern Ocean, as this salty water is subject to both upwelling and mixing with the Antarctic Circumpolar Deep Water that circulates around Antarctica (Russell et al. 2006). Following Talley (2003), the amount of incoming NADW at 32°S is quantified by considering that its density is between 27.4 σ_0 and 45.86 σ_4 kg m^{-3} (σ_0 and σ_4 are the potential density at 0 and 4000 m, respectively). It averages to 14 Sv, which is slighty less than the 17 Sv found in the observations (Talley 2003). Because the corresponding southward salt transport is a little too weak, the salinity gradient is too small, contributing to the too-weak zonal transport by the ACC. To summarize, the HiRes version of the IPSL CM4 coupled model shows performances in the Southern Ocean near the average of the other 18 coupled models of the IPCC AR4 (Russell et al. 2006).

3. Interannual variability of the Southern Hemisphere atmosphere and its links with the Southern Ocean

In the Southern Hemisphere, the leading mode of atmospheric variability is the SAM. It is primarily associated with zonally symmetric fluctuations of the strength and position of the westerlies (Thompson and Wallace 2000), and it is well represented by the first empirical orthogonal function (EOF) of the annual fluctuations of the sea level pressure (SLP) south of 20°S (Fig. 4, top). In the model, this mode explains 63% of the total yearly variance and it compares well with the observed one, although it is too zonally symmetric. A positive phase of the SAM corresponds to an intensification of the westerlies south of 45°S and a weakening to the north, so that the maximum zonal wind stress is shifted south. The spectrum of the normalized EOF time series (SAM index) corresponds to a white noise at time scales shorter than 50 yr, but is blue at longer periods (Fig. 3, top). As in the observations (Thompson and Wallace 2000; Hall and Visbeck 2002), the SAM depends little on seasons, although it is slightly stronger during austral summer.

In a positive phase of the SAM, the wind stress generates a northward Ekman transport along the ACC and a southward Ekman transport around 30°S. The Ekman pumping is thus positive south of about 50°S and north of 30°S, and negative in between (Fig. 4, bottom). Along Antarctica, the SAM is associated with an anomalous divergence of the surface currents that increases the isopycnals' slope in the Southern Ocean, resulting in a larger meridional pressure gradient. Since the ACC can be considered to be in geostrophic equilibrium far below the surface (Olbers et al. 2004), this increases the zonal current speed. As an index of the ACC variability, we use the annual time series of transport across the Drake Passage (Fig. 3, middle left). In the model, the transport varies between 80 and 100 Sv, showing much year-to-year variability and strong low-frequency fluctuations. The power spectrum is red at low frequency but is approximately white at time scales shorter than 20 yr (Fig. 3, middle right). Note that, unless otherwise noted, all results of this paper are based on yearly averages.

The SAM index and the ACC are only correlated with no time lag ($r = 0.44$), significant at the 5% level [significance is estimated as in Bretherton et al. (1999), assuming that time series are autoregressive processes of order 1]. This correlation is slightly lower than in the observations ($r = 0.68$; Meredith et al. 2004), or in the coarser-resolution climate model of Hall and Visbeck (2002) ($r = 0.5$) and the high-resolution oceanic hindcast of Hughes et al. (2003) ($r = 0.7$).

In the southern Atlantic basin, shallow salinity anomalies appear in phase with—and 1 yr after—a positive SAM (Fig. 5). The positive anomalies are primarily coming from the Indian and the Pacific basins. South of Africa, they are largely due to salinity advection by anomalous westward geostrophic currents flowing from south of Madagascar into the Atlantic basin. In the Pacific, they are generated

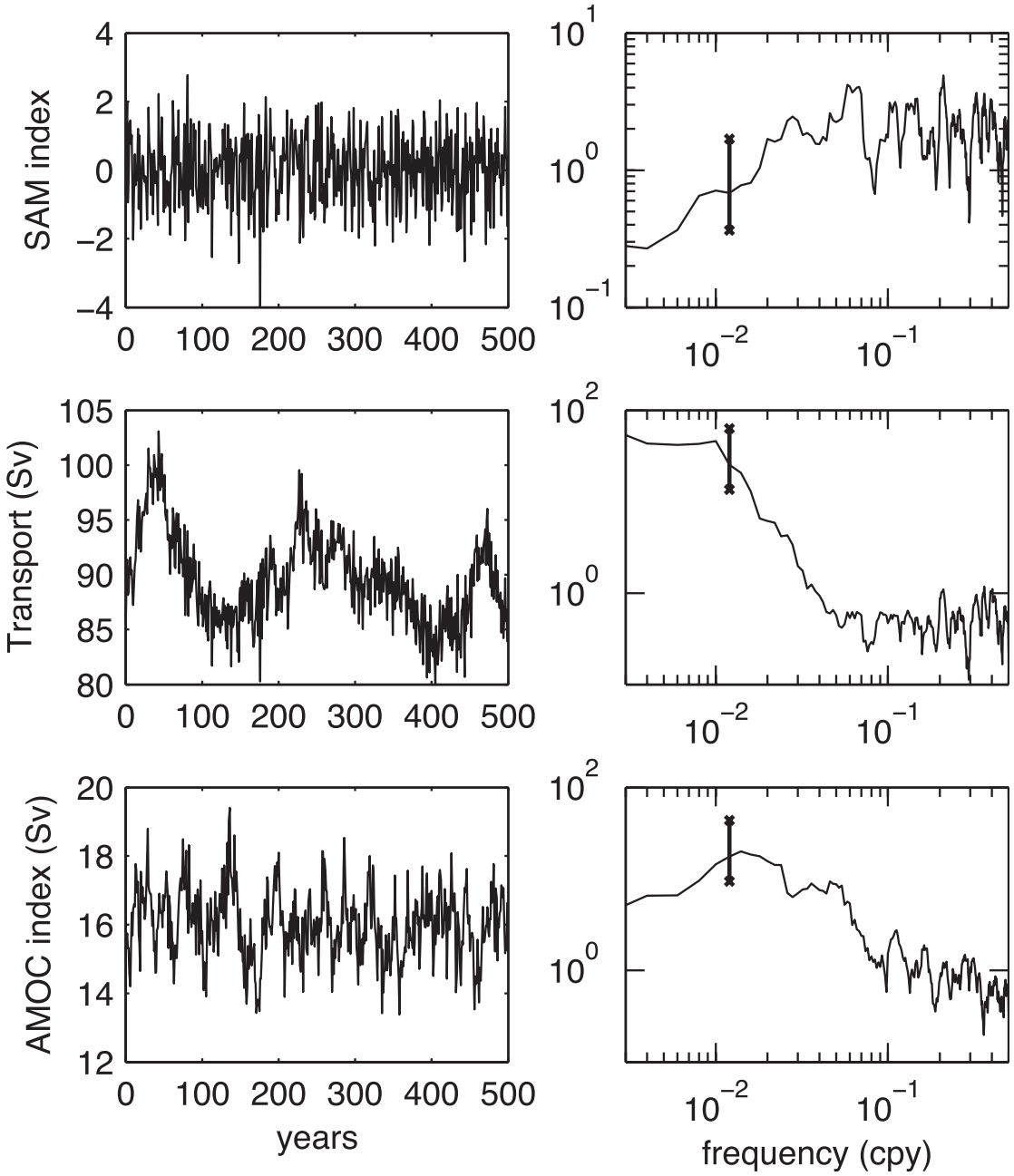

FIG. 3. (left) Time series and (right) power spectrum of, from top to bottom, the SAM index, the mass transport across the Drake Passage (in Sv), and the AMOC maximum below 500 m and between 30° and 60°N (in Sv). Power spectra are estimated with the multitaper method (seven tapers). The 95% confidence interval is indicated.

by anomalous northward Ekman transport and then advected by the mean ACC into the Atlantic through the Drake Passage. These salinity anomalies circulate in the Atlantic basin but do not cross the equator before at least 8 yr. This is consistent with Speich et al. (2001), who found in a global ocean model that the shortest travel time for salinity anomalies from the Drake Passage and the southern tip of Africa to reach 20°N in the Atlantic was 11 yr, and the median travel time 50 yr. The impact of these anomalies onto the AMOC is discussed in section 5.

The strongest response of the Southern Ocean MOC to the SAM variability is fast and found at no lag in the regression in Fig. 6, which shows a nearly barotropic dipole reflecting the downwelling north of 50°S and the upwelling farther south expected from SAM Ekman pumping. The response pattern is very similar to the first EOF of the global MOC (not shown), which explains 43% of the yearly variance. This is consistent with Treguier et al. (2010), who showed that the MOC and the meridional Ekman transport in the Southern Hemisphere were

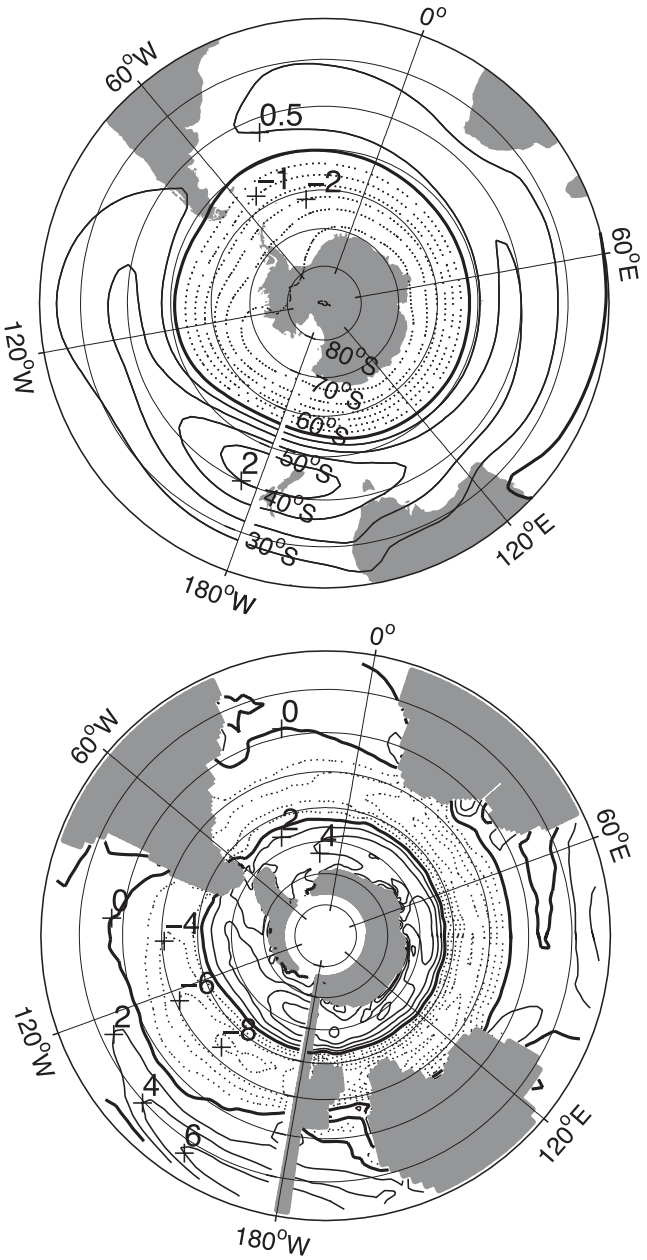

FIG. 4. (top) The SAM pattern, represented by the first EOF of the yearly SLP anomalies south of 20°S. The EOF time series (SAM index) is normalized, and the contour interval is 0.5 hPa. (bottom) Regression of annual anomalies of Ekman pumping on the SAM index. Contour interval is 2 m yr^{-1}. Dashed lines correspond to negative values and the thick lines to zero.

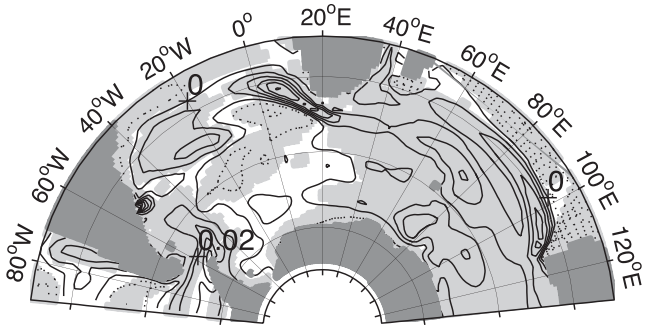

FIG. 5. Regression of annual anomalies of the averaged salinity between 0 and 100 m onto the SAM index when the SAM leads by 1 yr. Contour interval is 0.01 psu; dashed lines correspond to negative values. The shaded areas indicate that the regression is 5% significant.

highly correlated with the SAM index at interannual time scales, using an eddy-permitting oceanic model forced by an atmospheric reanalysis. Near the surface, the eddy contribution to the total MOC tends to counteract the Ekman transport and pumping (Fig. 6, top right), but its amplitude is an order of magnitude smaller. However, the eddy contribution peaks 2 yr after a positive SAM, when it affects the whole water column and—although its amplitude is still low (0.2 Sv)—nearly cancels the MOC response near the ACC (Fig. 6, bottom). Interestingly, such a time lag in the parameterized eddy response to the SAM is broadly consistent with studies based on eddy-resolving models (e.g., Meredith and Hogg 2006; Screen et al. 2009), where the eddy activity lags a positive SAM by 2–3 yr, suggesting that the slow amplification of eddy activity may be linked to mean flow changes. At lower frequencies, the eddy contribution still plays a compensating role near the ACC, which may explain the lack of correlation of the ACC with the SAM discussed in section 5.

North of 30°S, the MOC response to the SAM can be considered separately in each oceanic basin. The fast responses are very similar and concentrated in the Southern Hemisphere, with their contribution to the global MOC at 30°S partly reflecting their different width (55% from the Pacific MOC, 35% for the Indian MOC, and 10% for the AMOC). In the following, we focus on the Atlantic basin.

4. Relation between the AMOC and the SAM

The main mode of atmospheric variability in the Northern Hemisphere—the North Atlantic Oscillation (NAO)—is thought to have a strong influence on the AMOC variability (e.g., Delworth et al. 1993; Eden and Willebrand 2001; Dong and Sutton 2005; Deshayes and Frankignoul 2008), primarily through a rapid adjustment to the wind stress and a slow response to anomalous heat fluxes and wind stress via convection in the northern North Atlantic. In the LoRes version of the IPSL CM4 model, it is primarily the east Atlantic pattern (EAP, which is the second mode of atmospheric variability in the North Atlantic) that forces the delayed AMOC intensification (Msadek and Frankignoul 2009). To single out the influence of the Southern Ocean westerlies on the AMOC, we have performed multiple linear regressions on the SAM, the EAP, and the NAO indices (the latter

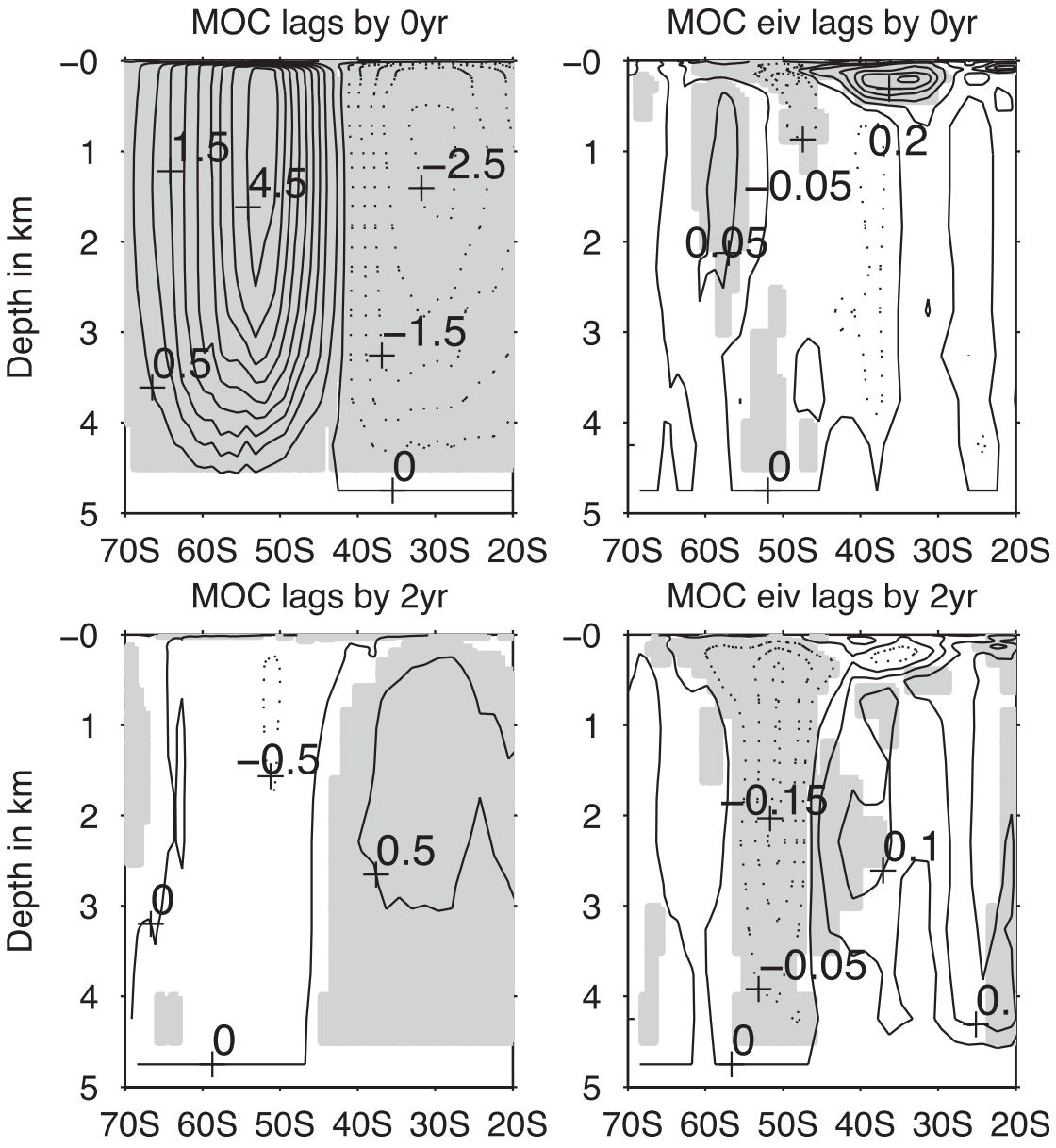

FIG. 6. (left) Regression of annual anomalies of the global MOC and (right) the eddy contribution to it on the SAM index at (top) zero lag and (bottom) 2 yr after. Contour interval is (left) 0.5 Sv and (right) 0.05 Sv. Dashed lines correspond to negative values. The shaded areas indicate that the regression is 5% significant.

two are computed as the first and second principal components of annual SLP anomalies in the area 20°–80°N, 90°W–40°E), as described in appendix A. The SAM and NAO indices are indeed weakly correlated ($r = 0.18$ for yearly values) both in the model and in the National Centers for Environmental Prediction (NCEP) reanalysis, although the correlation is only statistically significant in the former. On the other hand, the EAP is uncorrelated with the SAM and, of course, the NAO, so that the multiple linear regression is nearly equivalent to separate single regressions. As illustrated in Fig. 7 (left and middle), the in-phase AMOC response to the NAO and the EAP forcing is equivalent barotropic, and is larger for the NAO, reflecting the stronger Ekman pumping. When the AMOC lags by 2 yr, anomalies change sign. The response to the NAO becomes very small by 3 yr except at high latitudes, while the response to the EAP continues to evolve. The AMOC anomalies around 50°N keep growing and progressively expand into a basin-scale intensification of the AMOC, which peaks after 7 yr.

The AMOC patterns resulting from the multiple regressions are shown for the SAM index in Fig. 7 (right) at different lags. When the SAM leads by 1 yr, the AMOC anomalies in the Southern Hemisphere also change sign

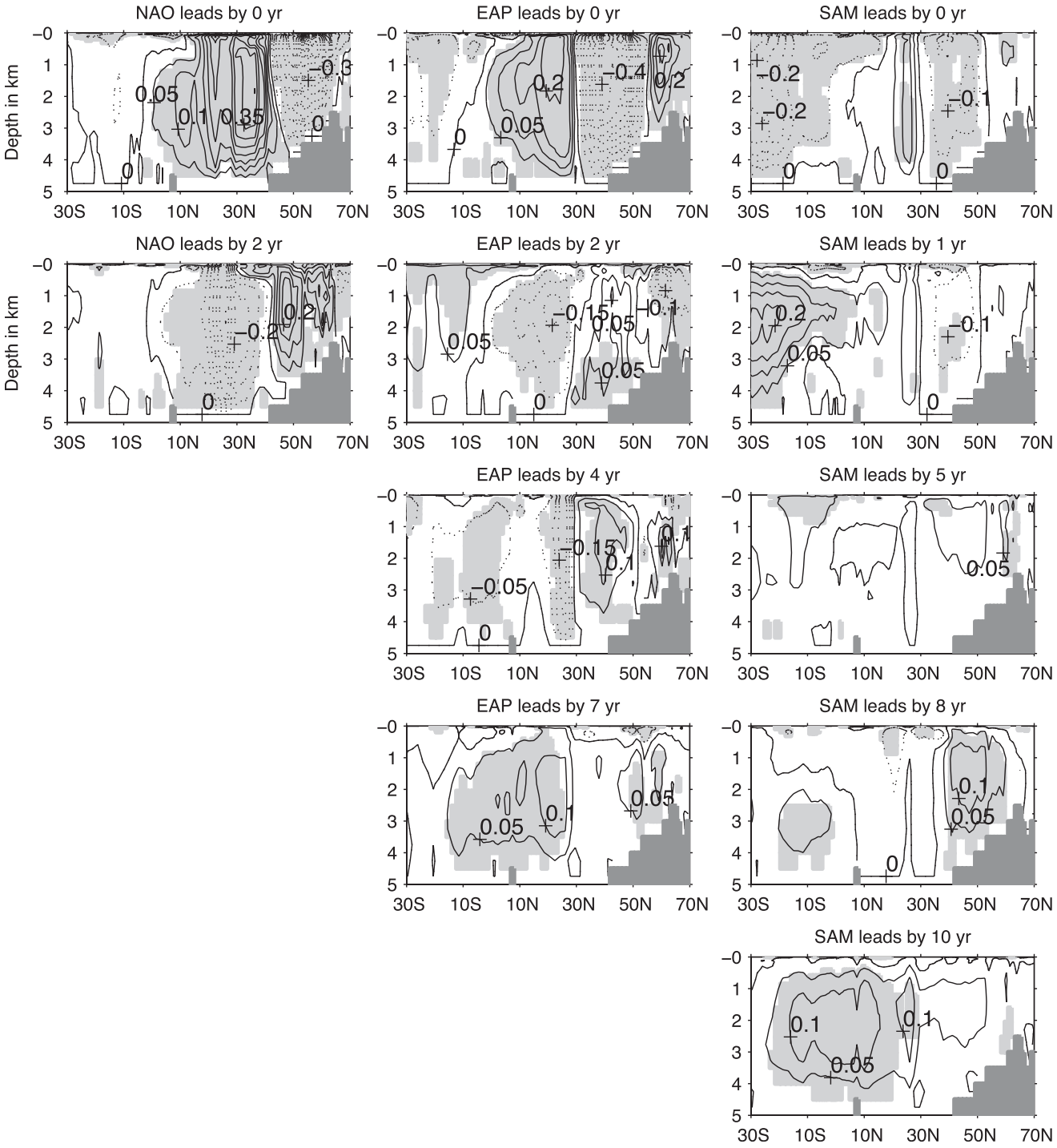

FIG. 7. Multiple linear regression of annual anomalies of the AMOC on the SAM, the NAO, and the EAP at different lags when the SAM leads. Contour interval is 0.05 Sv; dashed lines correspond to negative values. The shaded areas indicate that the regression is 5% significant.

and become baroclinic, disappearing after 2 yr. There is thus a similarity in the direct response of the AMOC to the Southern and Northern Hemisphere atmospheric variability, but the dynamics of the sign reversal have not been elucidated. The lag 1 regression shows that at 30°S the flow below 2500 m is southward. This results in a small but significant correlation ($r = 0.23$) when the SAM leads the incoming NADW at 30°S by 1 yr.

Significant anomalies are also found in the North Atlantic at lag 0, but they decrease rapidly. However, a growing intensification of the AMOC appears in the northern North Atlantic, starting 4 yr after a positive

SAM, but more clearly seen at lag 5 (Fig. 7, right). These remote responses to the SAM cannot be explained by the propagation of oceanic anomalies from the Southern to the Northern Hemisphere, since the time scale is too short. They are, rather, due to atmospheric teleconnections. As the results are unchanged if simple (instead of multiple) regressions are performed, the mechanism is thereafter investigated through simple regressions.

During a positive SAM, there is a significant anomalous SLP low in the northern North Atlantic (Fig. 8, top). The signal is stronger in boreal winter, and it is primarily linked to El Niño–Southern Oscillation (ENSO) teleconnections. Because of a symmetric ENSO forcing of the Northern and Southern Hemispheres, La Niña conditions are associated at no lag with a positive SAM and negative SLP anomalies in the northern North Atlantic. This is shown by the SLP regression mapped onto the ENSO-3.4 index (Fig. 8, middle), which is very similar to the SLP regression mapped onto the SAM index, except for a change of sign and larger anomalies. Consistent with Seager et al. (2003), the observations [NCEP reanalysis for SLP (Kalnay et al. 1996) and Hadley Centre Global Sea Ice and Sea Surface Temperature (HadISST) for SST (Rayner et al. 2003)] similarly show that a negative SAM, albeit much less zonally symmetric than in the model, is associated with El Niño (Fig. 8, bottom). Negative SLP anomalies in the North Atlantic are also seen in the observations, but they extend farther north than in the model, which is linked to a general bias of coupled models (Brönnimann 2007), and the high over Greenland is much weaker. In the model, the wind stress associated with these SLP anomalies in the northern North Atlantic induces local Ekman pumping that reaches -1.5 m yr^{-1} around 30°N and 1.5 m yr^{-1} around 50°N (not shown). This generates the strong AMOC response between about 30° and 50°N seen in the unlagged regression of the AMOC onto the SAM (Fig. 7, top right). The AMOC regression onto a "filtered" SAM index where the ENSO signal has been removed (as described in appendix B) shows at no lag a negligible signal north of 15°N (not shown), thereby confirming the role of ENSO in this teleconnection.

To explain the longer-term (lag 4 and later) response of the AMOC seen on Fig. 7 (right), one must take into account the fact that the ENSO influence is not the only mechanism that links the SAM to the North Atlantic signal. Indeed, a regression of the North Atlantic atmospheric fields onto the "ENSO-filtered" SAM index shows significant (albeit smaller) SLP anomalies centered on the west coast of Greenland (not shown) and, more importantly, substantial easterlies appearing 6–12 months after a positive SAM (1 yr after a positive SAM for annual anomalies; Fig. 9). Such a relatively long time lag suggests that the interhemispheric link involves the ocean.

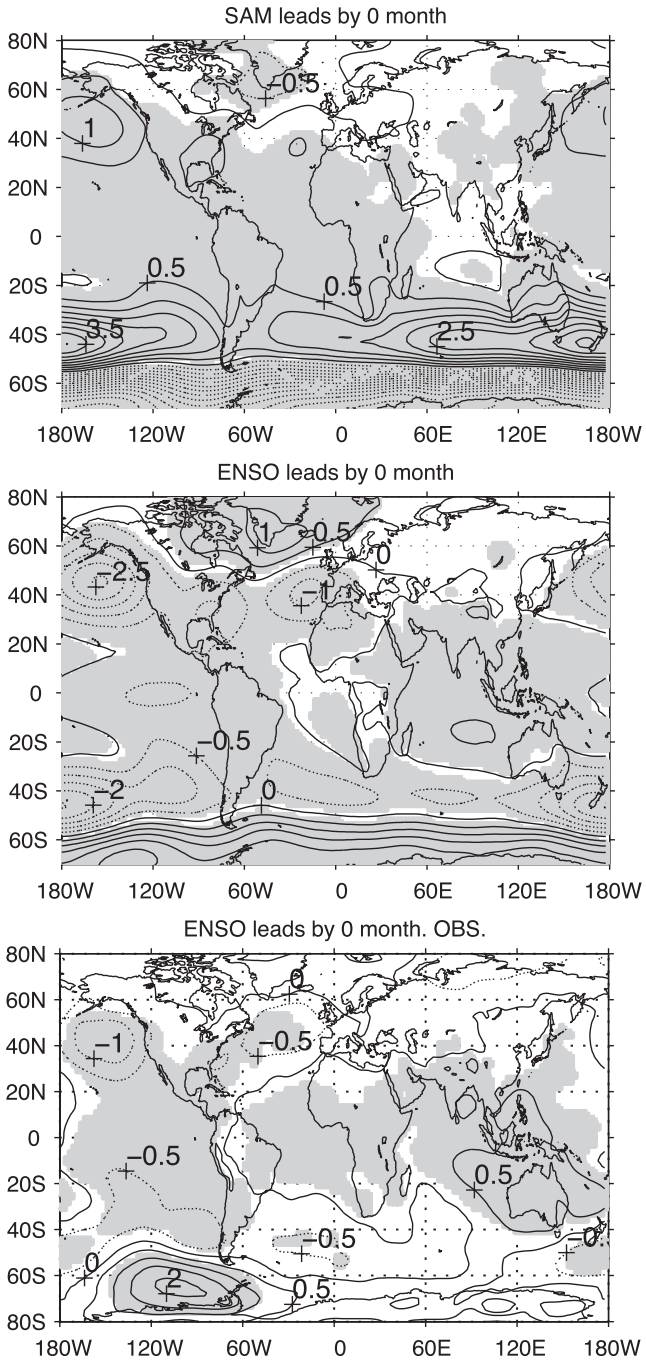

FIG. 8. Regression of monthly anomalies of the SLP mapped onto (top) the SAM index in the model, (middle) ENSO in the model, and (bottom) ENSO in the observations during 1993–2008. Contour interval is 0.5 hPa. Dashed lines correspond to negative values. The shaded areas indicate that the regression is 5% significant.

Thompson and Lorenz (2004) showed that the SAM has a significant signature in the tropics and the subtropics of both hemispheres during the cold season, after about 2 weeks. We speculate that this atmospheric teleconnection modifies the tropical and subtropical SST, which introduces an additional delay. The resulting SST anomalies should

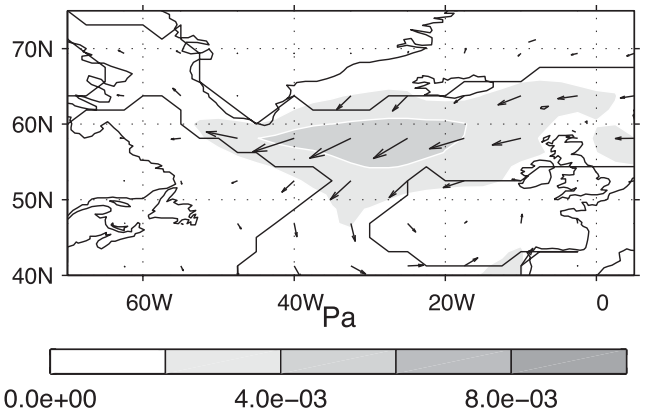

FIG. 9. Regression of annual anomalies of ENSO-filtered surface wind stress onto ENSO-filtered SAM index when it leads by 1 yr. Arrows indicate the direction and gray shadings the norm of wind stress anomalies. The solid line indicates the limit of 5% significant regression.

then affect the high northern latitudes via an atmospheric teleconnection, introducing a further 1- or 2-month delay (Liu and Alexander 2007). Whether this scenario is plausible, however, remains to be established.

In any case, wind stress anomalies reflecting this interhemispheric teleconnection (Fig. 9) as well as ENSO forcing both drive anomalous currents, in particular in the Irminger Sea (Fig. 10, top). A positive salinity anomaly reaching up to 500-m depth then rapidly appears between the tip of Greenland and Iceland, primarily resulting from anomalous salinity advection and mean salinity advection along the East Greenland Current and the North Atlantic Current (Fig. 10, middle). Evaporation and precipitation play a lesser role, since their regression onto the SAM is not significant. It can be shown that the salinity anomalies associated with the ENSO index are not very persistent, changing sign 2 yr later, probably because of the 3-yr period of ENSO in the model. By contrast, salinity anomalies associated with the ENSO-filtered SAM index are quite persistent, remaining significant in the regression up to 7 yr after the SAM. Note that because of the integrating aspect of the oceanic response, such regressions cannot truly separate the contribution of the two forcings, yet the close similarity (not shown) between the regressions on the ENSO-filtered and that on the raw SAM indices suggests that the direct ENSO forcing plays a lesser role at larger lags. The associated density anomalies, which have a similar regression pattern on the SAM index (not shown), lead to a deepening of the winter mixed layer in the model deep convection area between the tip of Greenland and Iceland (thick contour in Fig. 10), peaking 4 yr after a positive SAM (Fig. 10, bottom). As a result, significant clockwise AMOC anomalies appear near 50°N about 4 yr after a positive SAM, and they grow—slowly expanding and moving southward with increasing lags. By lag 8, the

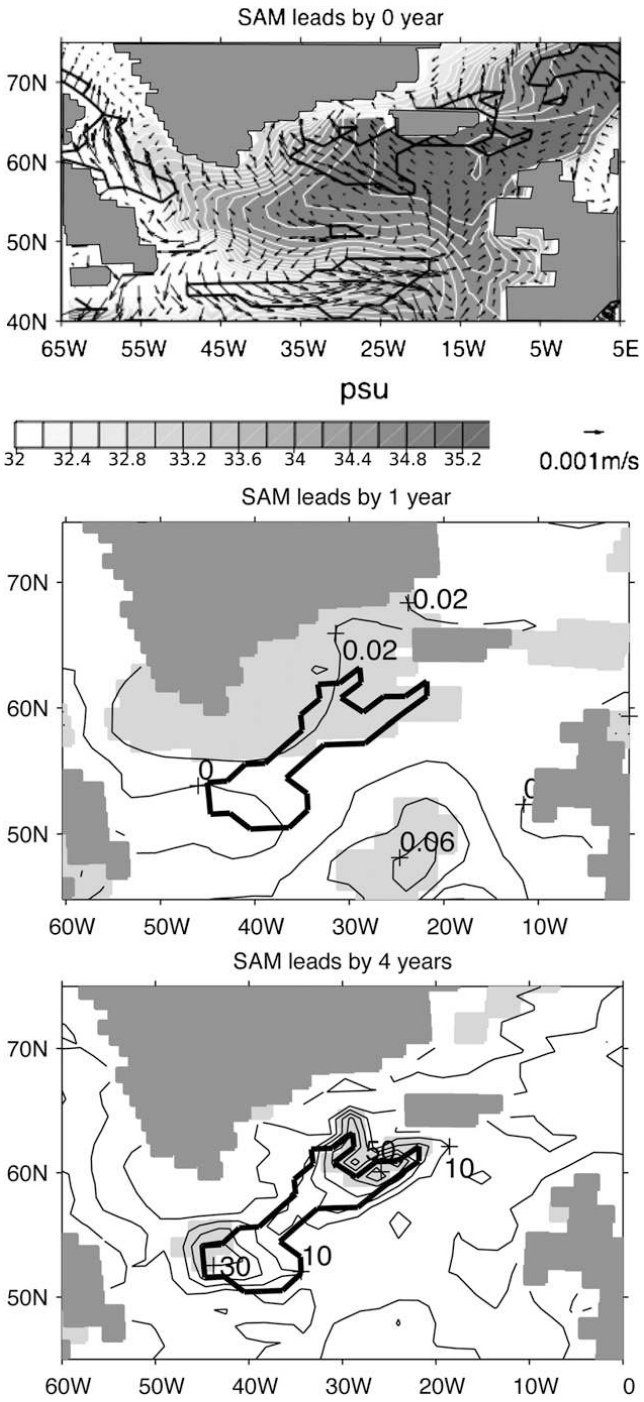

FIG. 10. (top) Linear regression onto the SAM index of surface currents superposed on the mean surface salinity field with no time lag. Thick lines indicate the limit of significant areas. (middle) Surface salinity 1 yr later (contour interval 0.02 psu). The shaded areas indicate that the regression is 5% significant. (bottom) Winter mixed-layer depth 4 yr later (contour interval 10 m). The shaded areas indicate that the regression is 5% significant. The thick contour in bottom two panels indicates the mean convective area of the model.

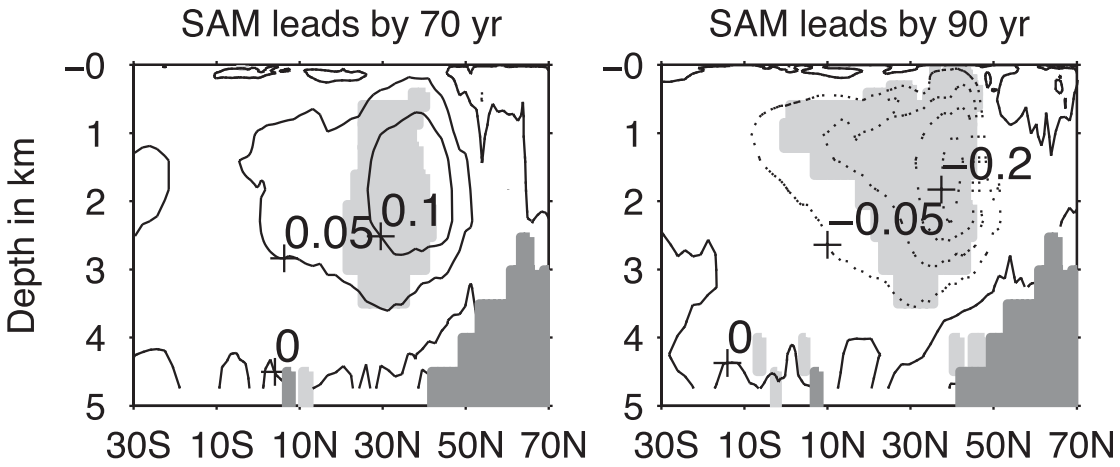

FIG. 11. Regression of anomalies of low-pass-filtered (T_c = 10 yr) AMOC on the SAM index, when the latter leads by 70 and 90 yr. Contour interval is 0.05 Sv; dashed lines correspond to negative values. The shaded areas indicate that the regression is 10% significant.

clockwise circulation cell has expanded but remains centered at 50°N, whereas it is shifted south and reaches 30°S by lag 10 (Fig. 7, right) before slowly disappearing. The signal is weak (~0.15 Sv) yet it corresponds to 15% of the maximum standard deviation of the AMOC variability, and it is similar to the AMOC response to the EAP (Fig. 7, middle). Its statistical significance was confirmed by a Monte Carlo test, where the regression was repeated 500 times, linking the original AMOC anomalies with randomly permuted SAM based on blocks of 2 and 4 successive years.

5. Links between the southern circulation and the AMOC at multidecadal scale

Since the salinity anomalies generated in the Southern Ocean by the SAM variability (see Fig. 5) only slowly propagate northward in the Atlantic, as discussed in section 3, their impact on the AMOC is best investigated by considering low-pass-filtered data. We first use a low-pass Butterworth filter with a cutoff period of T_c = 10 yr. As shown by the regression in Fig. 11 (left), the AMOC is accelerated about 70 yr after a positive SAM phase. The signal is weak, ~0.1 Sv for a typical SAM fluctuation, yet it corresponds to about 12.5% of the maximum standard deviation of the low-pass AMOC variability. Statistical significance was estimated by a Student's t test with $T/(T_c/2)$ degrees of freedom (T being the length of the time series), consistent with the effective Nyquist frequency, and its robustness was confirmed by a Monte Carlo method, where the regression was repeated 500 times, linking the filtered AMOC anomalies with randomly permuted SAM based on blocks of 25 and 50 successive years. In the figures, we use for clarity the 10% significance level, as the number of number of freedom is smaller, but the main features are 5% significant, albeit in a smaller area.

The delayed intensification of the AMOC appears to be due to the interhemispheric propagation of the salinity anomalies driven by the SAM. Indeed, the positive salinity anomalies in Fig. 5 propagate northward in the Atlantic Ocean, cross the equator after a decade (not shown), and spread into the northern subtropical gyre about 10 yr later (Fig. 12). The signal becomes too noisy at longer time lag to be traced farther north, although it appears in the Hovmöller diagram in Fig. 13, where a slightly stronger low-pass filter (T_c = 20 yr) has been used to more clearly show the salinity propagation up to the subtropical gyre. We suggest that the salinity anomalies

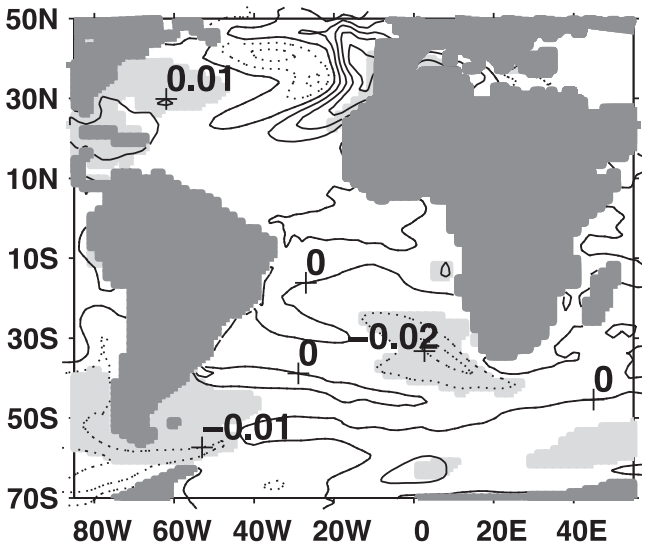

FIG. 12. Regression of low-pass-filtered (T_c = 10 yr) salinity anomalies averaged between 0 and 100 m onto the SAM index, when the latter leads by 20 yr. Contour interval is 0.01 psu; dashed lines correspond to negative values. The shaded areas indicate that the regression is 10% significant.

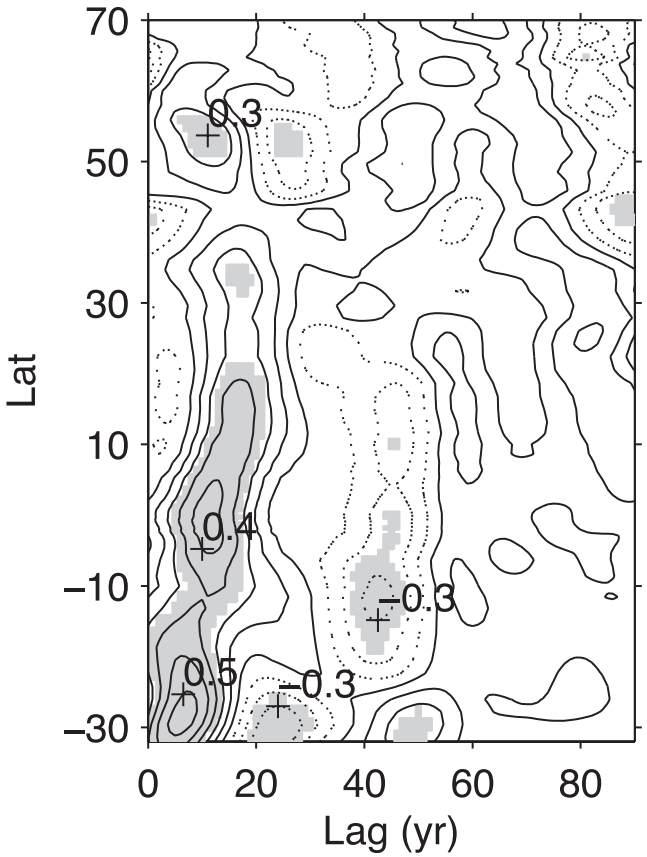

FIG. 13. Correlation between low-pass-filtered (T_c = 20 yr) zonally averaged salinity in the Atlantic (0–100 m) and the SAM index. Contour interval is 0.1; dashed lines correspond to negative values. The shaded areas indicate that the regression is 10% significant.

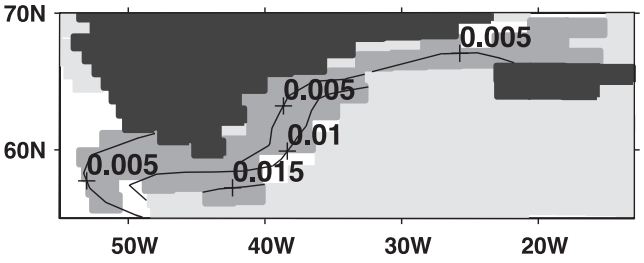

FIG. 14. Regression of low-pass-filtered (T_c = 10 yr) salinity anomalies on the isopycnal surface $27\sigma_0$ onto the SAM index, when the latter leads by 65 yr. Contour interval is 0.005 psu. The gray shaded areas indicate that the regression is 10% significant. The light shading indicates grid points where the regression is not computed, as the density of $27\sigma_0$ is reached less than 60% of the year.

circulate in the subtropical gyre and subduct in its center before being advected northward in the subsurface along the North Atlantic Current. Indeed, 65 yr after a positive SAM, positive anomalies are found southeast of Greenland between 200- and 300-m depth (isopycnals $26.4\sigma_0$–$27.2\sigma_0$; Fig. 14). The arrival of the more salty waters in the northern North Atlantic leads to an anomalous deepening of the mixed layer in the convective area south of Greenland about 70 yr after a positive SAM (not shown), and it thus intensifies the AMOC.

To verify that the implied northward advection time is consistent with the model circulation, we launched about 25 000 fictitious Lagrangian floats in the upper 100 m of the Drake Passage and near the tip of Africa (section at 16°E between 40° and 50°S) where positive salinity anomalies enter the Atlantic basin in a positive phase of the SAM (Fig. 5). The float trajectories are computed by the Ariane tool (Blanke and Raynaud 1997) using the model climatological monthly tridimensional currents. Among particles launched in the Drake Passage, 21% reach the 40°N section: 19% below the 100-m depth with a median travel time (T_m) of 120 yr and 2% in the upper 100 m with T_m = 70 yr. Most of the remaining particles complete one revolution around Antarctica (74%) with T_m = 30 yr. A much larger percentage of the particles launched near the tip of Africa reach the 40°N section: 55% below 100-m depth with T_m = 44 yr and 6% in the upper 100 m with T_m = 21 yr. Hence, as shown by Friocourt et al. (2005), the bulk of the water reaching the North Atlantic comes from the Indian Ocean by the Agulhas Current. A few float trajectories that reach the North Atlantic are shown in Fig. 15 (top). Although there is much dispersion, they generally reach the North Hemisphere subtropical gyre in 20–40 yr. After subduction and recirculation in the gyre, they travel north toward the tip of Greenland. They reach the convective area of the subpolar gyre with a median travel time of 65 yr, sink, and then travel back southward in the deep ocean. We also launched fictitious drifters in the northwestern tropics, where the salinity signal was seen about 20 yr after a positive SAM. Three trajectories are illustrated in Fig. 15 (bottom), where the color coding indicates their depth. The drifters reach the northern North Atlantic after 30–50 yr and sink. These traveling times are thus broadly consistent with the lagged correlation between the SAM and the AMOC, and they are also comparable to the travel time found by Mignot and Frankignoul (2005, 2009).

The regression in Fig. 11 (right) shows that the AMOC intensification at lag 70 is followed by a slowdown 20 yr later. This seems to be due to the same advective process as above but for salinity anomalies of opposite sign. Indeed, negative salinity anomalies enter in the South Atlantic from both the Indian and the Pacific basins about 20 yr after a positive SAM and thus 20 yr after the positive salinity anomalies that eventually lead to the AMOC acceleration discussed above (Figs. 12 and 13). In the Indian basin, the freshening is primarily generated by

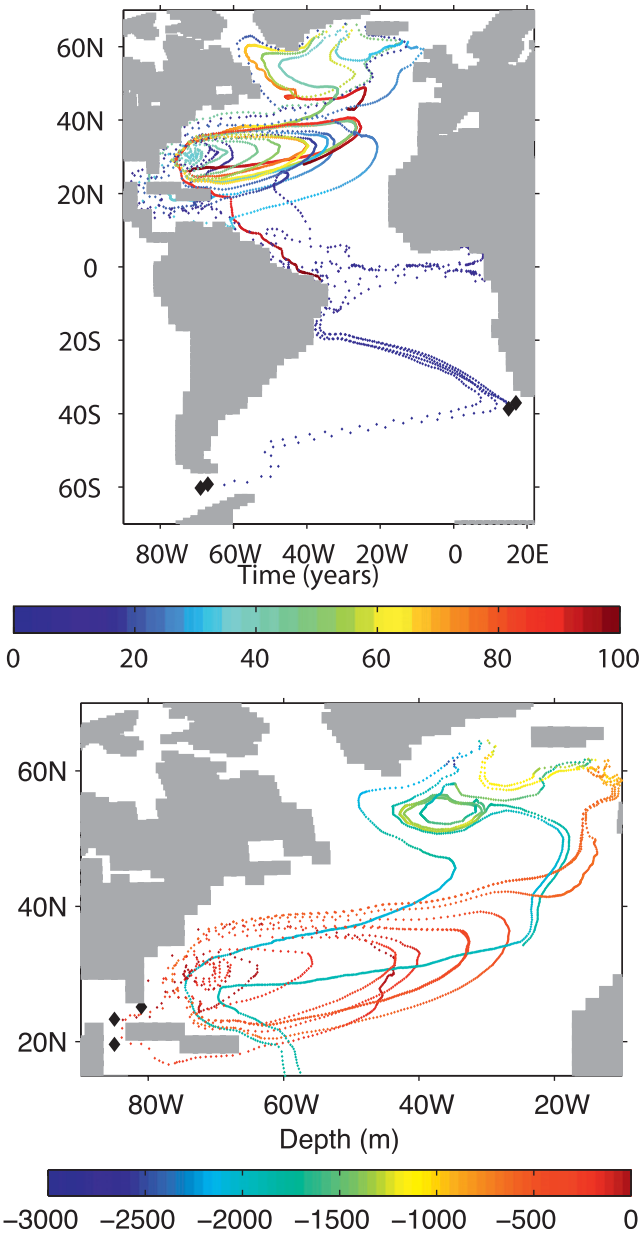

FIG. 15. Lagrangian trajectories of the fictitious drifters advected by mean currents for 100 yr. (top) Drifters launched (black diamonds) in the Drake Passage and near the tip of Africa; they reach the northern North Atlantic after about 40 yr. The colors indicate the travel time of the drifters. (bottom) Drifters launched in the tropics; they reach the northern North Atlantic after about 30 yr. The colors indicate the depth of the drifters.

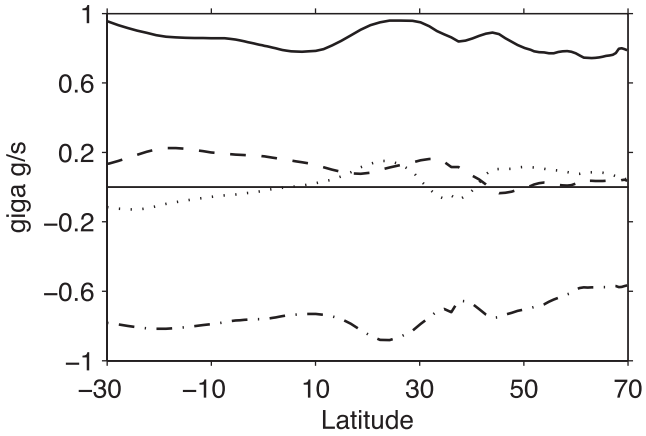

FIG. 16. Regression of low-pass-filtered (T_c = 10 yr) meridional salt transport (in Gg s^{-1}) onto the low-pass-filtered SAM index when the SAM leads by 5 yr (solid line), by 15 yr (dashed), by 25 yr (dashed–dotted), and by 35 yr (dotted). Note that it is computed from 150 yr of data.

anomalous southward advection of the mean salinity field due to SAM-driven currents near the west coast of Australia (Fig. 5). The negative salinity anomalies are then advected by the mean currents toward Madagascar and then into the Atlantic basin by the Agulhas Current. In the Pacific basin, strong negative salinity anomalies appear about 10 yr after a positive SAM near Antarctica between 150°E and 180° (not shown). They are linked to salinity advection by anomalous eastward currents that are particularly strong at lag 10 and to ice melting (not shown). These negative salinity anomalies are then advected by the ACC, entering in the Atlantic by the Drake Passage. Hence, 20 yr after a positive SAM, the salinity anomalies entering the Atlantic basin are opposite to those in Fig. 5 and they should correspondingly reduce the AMOC 20 yr after it has intensified, as seen in Fig. 12. The 20-yr reversal is also clearly seen in the regression of the meridional salt transport onto the SAM index (Fig. 16), which suggests an oscillatory behavior. Note that the meridional salt transport could only be estimated in a 150-yr sequence in which the data had been saved, so this calculation has to be considered with caution.

Although the control simulation is too short (500 yr) to investigate the longer time scales with much confidence, the AMOC seems to be almost adjusted to the SAM changes in time scales longer than 100 yr, consistent with the simulation of Toggweiler and Samuels (1995), Sijp and England (2009), and others, supporting that stronger westerlies lead to a stronger AMOC. This is suggested by Fig. 17, which shows that the AMOC index (maximum of the AMOC below 500-m depth and between 30° and 60°N) and the SAM evolve approximately in phase when low-pass filtered with a cutoff period of 60 yr. This is also suggested by the significant coherency between the AMOC and the SAM at periods longer than about 100 yr, with the SAM leading the AMOC by a decade or two (not shown). Whether such a small lag results from a mixture of the processes discussed in sections 4 and 5 can only be speculated upon.

On the other hand, we found no link between the SAM (or the AMOC) and the ACC at the centennial time scale, suggesting that the large centennial variability of

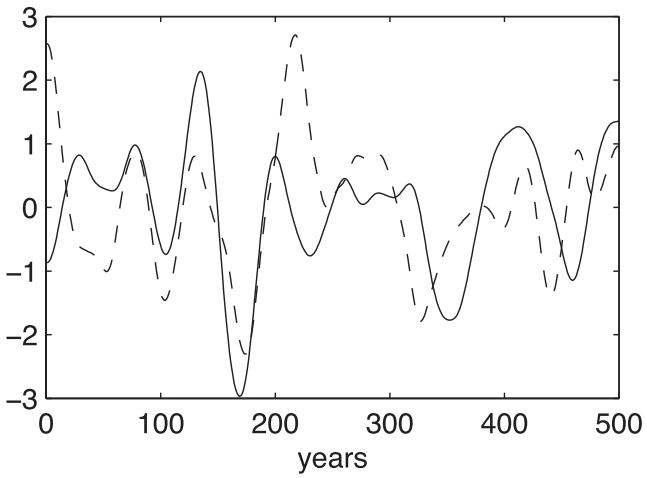

FIG. 17. Normalized time series of the SAM index (dashed line) and of AMOC index (solid line) filtered with a cutoff period of 60 yr.

the Drake Passage transport seen in Fig. 3 reflects slow changes in the hydrography of the Southern Ocean in the Indian and Pacific basins. These changes are, however, beyond the scope of a study that focuses on the influence of the southern winds on the AMOC.

The lack of link between the SAM and the ACC is likely to result from the fact that, at this long time scale, the sloping of the isopycnals in the Southern Ocean associated with westerly enhancement is compensated by an increase in the eddies' activity that flattens the isopycnals' slope, as discussed in section 3.

6. Summary and conclusions

The links between the SAM, the ACC, and the AMOC have been investigated in a 500-yr control run of the HiRes version of the IPSL climate model. Although this version is more realistic than the LoRes version discussed by Russell et al. (2006), it has some limitations: the Southern Hemisphere westerlies are located too far north; the amount of incoming NADW at 30°S in the Atlantic is slightly underestimated; and the ACC, transporting about 90 Sv, is too weak compared to the observations. Nonetheless, the main features of the Southern Ocean circulation are sufficiently well represented to investigate its variability on the annual-to-multidecadal time scales. Eddies are not resolved, but the Gent and McWilliams parameterization with a coefficient depending on the growth rate of baroclinic instabilities seems to represent them acceptably, as suggested by Iudicone et al. (2008). In particular, the parameterized eddy response to the SAM is maximum with a time lag of 2 yr, consistent with the eddy-resolving simulations of Meredith and Hogg (2006) and Screen et al. (2009).

The positive Ekman pumping south of 45°S associated with a positive SAM phase creates a divergence of water masses around Antarctica that increases the isopycnals' slope in the ACC, leading to a rapid intensification of its zonal transport, consistent with Sen Gupta and England (2006), Hall and Visbeck (2002), and Meredith et al. (2004). The Ekman pumping also generates an equivalent barotropic dipolar circulation cell in the MOC in the Southern Hemisphere. One year after a positive SAM phase, this circulation cell reverses, leading in the South Atlantic to an increase in the incoming NADW at 30°S. In the model, the fast response of the Southern Ocean to the SAM is very zonally symmetric. However, the observations suggest more dependence on longitude. Using hydrographic and Argo profiles, Sallée et al. (2008) found that the ACC fronts could be displaced either poleward or equatorward, or simply intensified by the SAM, depending on the ocean basins. The discrepancy results from the SAM pattern being much too zonal in the IPSL CM4 model.

The AMOC was shown to intensify about 8 yr after a positive SAM, although the signal is weak, typically reaching only 0.15 Sv. It results from a correlation between the SAM and wind stress in the northern North Atlantic atmosphere, which was shown to reflect both a SAM-forced atmospheric teleconnection to the northern North Atlantic and a hemispherically symmetric influence of ENSO. Both mechanisms lead to anomalous salinity advection toward the main area of deep convection in the model, which progressively erodes the vertical stratification after a positive SAM, enhances the deep convection, and then accelerates the AMOC. The observations also suggest interhemispheric links related to ENSO (Seager et al. 2003), albeit less pronounced in the northern North Atlantic, but we found no significant correlations between the SAM and the North Atlantic SLP in the reanalysis. Although this may be due to the more limited sample, the interhemispheric teleconnections are likely to be too strong in the model. Hence, the link between the AMOC and the SAM at the decadal scale may be model specific and requires further investigation.

At the multidecadal scale, the SAM alters the AMOC through salinity advection from the Southern Hemisphere into the northern North Atlantic. A positive phase of the SAM creates positive salinity anomalies that enter in the Atlantic basin from the Drake Passage and, more importantly, from the Indian Ocean by Agulhas leakage. These anomalies are slowly advected northward, crossing the equator and spreading in the northern subtropics in about 20 yr. Although we could not trace their circulation further, we showed some evidence based on Lagrangian tracers that they circulate and subduct in the subtropical gyre, and are then advected northward along the North Atlantic Current, reaching the northern North Atlantic

about 65 yr after a positive SAM. This enhances the deep convection, so that the AMOC is intensified 70 yr after a positive SAM. A deceleration of the AMOC is found 20 yr later. It was shown that this phase reversal is due to the same mechanism, as negative salinity anomalies coming from the Indian and Pacific basin enter in the Atlantic basin about 20 yr after a positive SAM. This freshening was generated earlier by SAM-driven anomalous advection in the Pacific and the Indian basins and then advected into the Atlantic basin. Note that these AMOC changes are weak, typically reaching 0.2 Sv, but that typical low-frequency fluctuations are only 4 times larger.

The spreading of oceanic anomalies from the Southern Ocean to the northern North Atlantic has been observed in hosing experiments using climate models (Seidov et al. 2005; Stouffer et al. 2007; Swingedouw et al. 2008). In sensitivity experiments where freshwater was added south of 60°S for 100 yr, Swingedouw et al. (2008) found that one of the main processes affecting the response of the AMOC was the spread of salinity anomalies from the Southern Ocean toward the North Atlantic convection sites, where they weakened the production of deep water and reduced the AMOC in about 50 yr. This time scale is broadly consistent with the time lag found here.

On the centennial time scale, the AMOC seems to be lagging the SAM forcing by a decade or two, with a stronger AMOC corresponding to a positive SAM phase. This is consistent with the steady-state simulation of Toggweiler and Samuels (1995), Sijp and England (2009), and others, supporting that stronger westerlies lead to a stronger AMOC. On the other hand, no relation to the AMOC or the SAM could be found for the strong centennial fluctuations undergone by the ACC in the model. Clearly, much longer simulations are needed to assess the processes controlling the low-frequency response of the World Ocean to the variability of the SAM. This would be of much interest, since observations and models indicate a positive trend in the SAM index over the past few decades and predict its continuation in the twenty-first century (Marshall 2003; Yin 2005). As a positive SAM should enhance the Atlantic Overturning circulation, it could mitigate the expected decrease of the AMOC in global warming conditions.

Acknowledgments. We thank G. Madec for helpful discussions, R. Msadek, C. Cassou, and F. D'Andréa for useful comments, and Bruno Blanke for making available the Lagragian tool and helping us to use it. We also thank the reviewers, whose insightful comments greatly improved the paper. The research leading to these results has received funding from the European Community's Seventh Framework Programme (FP7/2007–2013) under Grant Agreement GA212643 (THOR: ''Thermohaline Overturning—at Risk?,'' 2008–2012). CF was supported in part by the Institut Universitaire de France.

APPENDIX A

Multiple Linear Regression

Our multiple linear regression model assumes that a zero-mean variable $y(t)$ can be expressed as an error term plus a linear combination of three other zero-mean variables $[x_1(t), x_2(t), x_3(t)]$, that is,

$$y(t) = \sum_{i=1}^{3} a_i x_i(t) + \epsilon(t), \tag{A1}$$

where $\epsilon(t)$ is the error term, also called noise, and the a_i are the regression coefficients. Let $\mathbf{A}$ be the vector column of these coefficients, $\mathbf{X}$ the matrix whose the element at the ith row and jth column is $x_j(t = i)$, and $\mathbf{Y} = [y(t = i)]_{i=1...t}$. The regression coefficients are determined by an ordinary least squares estimation:

$$\mathbf{A} = (\mathbf{X}\mathbf{X}^{\mathrm{T}})^{-1}\mathbf{X}^{\mathrm{T}}\mathbf{Y}, \tag{A2}$$

where the index T denotes transpose. This is equivalent to an orthogonal projection of the variable y onto the space made of the $\{x_j\}_{j=1...3}$ vectors. Statistical significance is tested on each regression coefficient by a Student's t test. For more details, see von Storch and Zwiers (1999).

APPENDIX B

Removing ENSO

The ENSO signal is well characterized by the first two EOFs and principal components (PCs) of the SST in the tropical Pacific between 15°S and 15°N. In the model, the first PC is highly correlated with the ENSO-3.4 index ($r = 0.99$) and the two PC have a spectral peak at a period of 3 yr. To subtract the ENSO signal from the atmospheric fields, we use a linear regression onto the two PCs, assuming a fast atmospheric response. For monthly anomalies, a regression with one or two months' lag gives very similar results. Removing the ENSO signal from oceanic data was not attempted, as the ocean acts as an integrator of the ENSO forcing—removing its influence would require a more sophisticated model of the response of the ocean.

REFERENCES

Biastoch, A., C. W. Böning, F. U. Schwarzkopf, and J. R. E. Lutjeharms, 2009: Increase in Agulhas leakage due to poleward shift of Southern Hemisphere westerlies. *Nature,* **462,** 495–499.

Blanke, B., and S. Raynaud, 1997: Kinematics of the Pacific Equatorial Undercurrent: An Eulerian and Lagrangian approach from GCM results. *J. Phys. Oceanogr.,* **27,** 1038–1053.

Böning, C. W., A. Dispert, M. Visbeck, S. R. Rintoul, and F. U. Schwarzkopf, 2008: The response of the Antarctic Circumpolar Current to recent climate change. *Nat. Geosci.,* **1,** 864–869.

Bretherton, C. S., M. Widmann, V. P. Dynmnikov, J. M. Wallace, and I. Bladé, 1999: The effective number of spatial degrees of freedom of a time-varying field. *J. Climate,* **12,** 1990–2009.

Brönnimann, S., 2007: Impact of El Niño–Southern Oscillation on European climate. *Rev. Geophys.,* **45,** RG3003, doi:10.1029/2006RG000199.

Cunningham, S. A., S. G. Alderson, B. A. King, and M. A. Brandon, 2003: Transport and variability of the Antarctic Circumpolar Current in Drake Passage. *J. Geophys. Res.,* **108,** 8084, doi:10.1029/2001JC001147.

Delworth, T., S. Manabe, and R. J. Stouffer, 1993: Interdecadal variations of the thermohaline circulation in a coupled ocean–atmosphere model. *J. Climate,* **6,** 1993–2011.

Deshayes, J., and C. Frankignoul, 2008: Simulated variability of the circulation in the North Atlantic from 1953 to 2003. *J. Climate,* **21,** 4919–4933.

Dong, B., and R. T. Sutton, 2005: Mechanism of interdecadal thermohaline circulation variability in a coupled ocean–atmosphere GCM. *J. Climate,* **18,** 1117–1135.

Eden, C., and J. Willebrand, 2001: Mechanism of interannual to decadal variability of the North Atlantic circulation. *J. Climate,* **14,** 2266–2280.

Fichefet, T., and A. M. Morales-Maqueda, 1999: Modelling the influence of snow accumulation and snow-ice formation on the seasonal cycle of the Antarctic sea-ice cover. *Climate Dyn.,* **15,** 251–268.

Friocourt, Y., S. Drijfhout, B. Blanke, and S. Speich, 2005: Water mass export from Drake Passage to the Atlantic, Indian, and Pacific Oceans: A Lagrangian model analysis. *J. Phys. Oceanogr.,* **35,** 1206–1222.

Ganachaud, A., and C. Wunsch, 2000: Improved estimates of global ocean circulation, heat transport and mixing from hydrographic data. *Nature,* **408,** 453–457.

Gent, P. R., and J. C. McWilliams, 1990: Isopycnal mixing in ocean circulation models. *J. Phys. Oceanogr.,* **20,** 150–155.

Gnanadesikan, A., and R. W. Hallberg, 2000: On the relationship of the Circumpolar Current to Southern Hemisphere winds in coarse-resolution ocean models. *J. Phys. Oceanogr.,* **30,** 2013–2034.

Gregory, J. M., and Coauthors, 2005: A model intercomparison of changes in the Atlantic thermohaline circulation in response to increasing atmospheric CO_2 concentration. *Geophys. Res. Lett.,* **32,** L12703, doi:10.1029/2005GL023209.

Hall, A., and M. Visbeck, 2002: Synchronous variability in the Southern Hemisphere atmosphere, sea ice, and ocean resulting from the annular mode. *J. Climate,* **15,** 3043–3057.

Hourdin, F., and Coauthors, 2006: The LMDZ4 general circulation model: Climate performance and sensitivity to parametrized physics with emphasis on tropical convection. *Climate Dyn.,* **27,** 787–813.

Hughes, C. W., P. L. Woodworth, M. P. Meredith, V. Stepanov, T. Whitworth, and A. R. Pyne, 2003: Coherence of Antarctic sea levels, Southern Hemisphere Annular Mode, and flow through Drake Passage. *Geophys. Res. Lett.,* **30,** 1464, doi:10.1029/2003GL017240.

Iudicone, D., G. Madec, B. Blanke, and S. Speich, 2008: The role of Southern Ocean surface forcings and mixing in the global conveyor. *J. Phys. Oceanogr.,* **38,** 1377–1400.

Kalnay, E., and Coauthors, 1996: The NCEP/NCAR 40-Year Reanalysis Project. *Bull. Amer. Meteor. Soc.,* **77,** 437–471.

Krinner, G., and Coauthors, 2005: A dynamic global vegetation model for studies of the coupled atmosphere-biosphere system. *Global Biogeochem. Cycles,* **19,** GB1015, doi:10.1029/2003GB002199.

Liu, Z., and M. Alexander, 2007: Atmospheric bridge, oceanic tunnel, and global climatic teleconnections. *Rev. Geophys.,* **45,** RG2005, doi:10.1029/2005RG000172.

Madec, G., P. Delecluse, M. Imbard, and C. Lévy, 1998: OPA Version 8.1 Ocean General Circulation Model reference manual. LODYC/IPSL Tech Rep. 11, 91 pp.

Marshall, G. J., 2003: Trends in the southern annular mode from observations and reanalyses. *J. Climate,* **16,** 4134–4143.

Marshall, J., and T. Radko, 2006: A model of the upper branch of the meridional overturning of the Southern Ocean. *Prog. Oceanogr.,* **70,** 331–345.

Marti, O., and Coauthors, 2010: Key features of the IPSL ocean atmosphere model and its sensitivity to atmospheric resolution. *Climate Dyn.,* **34,** 1–26.

Meredith, M. P., and A. M. Hogg, 2006: Circumpolar response of Southern Ocean eddy activity to a change in the southern annular mode. *Geophys. Res. Lett.,* **33,** L16608, doi:10.1029/2006GL026499.

——, P. L. Woodworth, C. W. Hughes, and V. Stepanov, 2004: Changes in the ocean transport through Drake Passage during the 1980s and 1990s, forced by changes in the southern annular mode. *Geophys. Res. Lett.,* **31,** L21305, doi:10.1029/2004GL021169.

Mignot, J., and C. Frankignoul, 2005: The variability of the Atlantic meridional overturning circulation, the North Atlantic Oscillation, and the El Niño–Southern Oscillation in the Bergen Climate Model. *J. Climate,* **18,** 2361–2375.

——, and ——, 2009: Local and remote impacts of a tropical Atlantic salinity anomaly. *Climate Dyn.,* **35,** 1133–1147. doi:10.1007/s00382-009-0621-9.

Msadek, R., and C. Frankignoul, 2009: Atlantic multidecadal oceanic variability and its influence on the atmosphere in a climate model. *Climate Dyn.,* **33,** 45–62.

Munk, W. H., and E. Palmen, 1951: Note on the dynamics of the Antarctic Circumpolar Current. *Tellus,* **3,** 53–55.

Olbers, D., D. Borowski, C. Völker, and J.-O. Wölff, 2004: The dynamical balance, transport and circulation of the Antarctic Circumpolar Current. *Antarct. Sci.,* **16,** 439–470.

Rayner, N. A., D. E. Parker, E. B. Horton, C. K. Folland, L. V. Alexander, D. P. Rowell, E. C. Kent, and A. Kaplan, 2003: Global analyses of sea surface temperature, sea ice, and night marine air temperature since the late nineteenth century. *J. Geophys. Res.,* **108,** 4407, doi:10.1029/2002JD002670.

Russell, J. L., R. J. Stouffer, and K. W. Dixon, 2006: Intercomparison of the Southern Ocean circulations in IPCC coupled model control simulations. *J. Climate,* **19,** 4560–4575.

Sallée, J. B., K. Speer, and R. Morrow, 2008: Response of the Antarctic Circumpolar Current to atmospheric variability. *J. Climate,* **21,** 3020–3039.

Screen, J. A., N. P. Gillett, D. P. Stevens, G. J. Marshall, and H. K. Roscoe, 2009: The role of eddies in the Southern Ocean temperature response to the southern annular mode. *J. Climate,* **22,** 806–818.

Seager, R., N. Harnik, Y. Kushnir, W. Robinson, and J. Miller, 2003: Mechanisms of hemispherically symmetric climate variability. *J. Climate,* **16,** 2960–2978.

Seidov, D., R. J. Stouffer, and B. J. Haupt, 2005: Is there a simple bi-polar ocean seesaw? *Global Planet. Change,* **49,** 19–27.

Sen Gupta, A., and M. H. England, 2006: Coupled ocean–atmosphere–ice response to variations in the southern annular mode. *J. Climate,* **19,** 4457–4486.

Sijp, W. P., and M. H. England, 2009: Southern Hemisphere westerly wind control over the ocean's thermohaline circulation. *J. Climate,* **22,** 1277–1286.

Speich, S., B. Blanke, and G. Madec, 2001: Warm and cold water routes of an O.G.C.M. thermohaline conveyor belt. *Geophys. Res. Lett.,* **28,** 311–314.

Stommel, H., 1957: A survey of ocean current theory. *Deep-Sea Res.,* **4,** 149–184.

Stouffer, R., D. Seidov, and B. J. Haupt, 2007: Climate response to external sources of freshwater: North Atlantic versus the Southern Ocean. *J. Climate,* **20,** 436–448.

Swingedouw, D., T. Fichefet, H. Goose, and M. F. Loutre, 2008: Impact of transient freshwater releases in the Southern Ocean on the AMOC and climate. *Climate Dyn.,* **33,** 365–381.

Talley, L. D., 2003: Shallow, intermediate, and deep overturning components of the global heat budget. *J. Phys. Oceanogr.,* **33,** 530–560.

Thompson, D. W. J., and J. M. Wallace, 2000: Annular mode in the extratropical circulation. Part I: Month-to-month variability. *J. Climate,* **13,** 1000–1016.

——, and D. J. Lorenz, 2004: The signature of the annular modes in the tropical troposphere. *J. Climate,* **17,** 4330–4342.

Toggweiler, J. R., and B. Samuels, 1995: Effect of Drake Passage on the global thermohaline circulation. *Deep-Sea Res. I,* **42,** 477–500.

——, and J. Russell, 2008: Ocean circulation in a warming climate. *Nature,* **451,** 286–288.

Treguier, A. M., M. H. England, S. R. Rintoul, G. Madec, J. Le Sommer, and J.-M. Molines, 2007: Southern Ocean overturning across streamlines in a eddying simulation of the Antarctic Circumpolar Current. *Ocean Sci.,* **3,** 491–507.

——, J. Le Sommer, J. M. Molines, and B. de Cuevas, 2010: Response of the Southern Ocean to the southern annular mode: Interannual variability and multidecadal trend. *J. Phys. Oceanogr.,* **40,** 1659–1668.

Valcke, S., Ed., 2006: OASIS3 user guide. PRISM–Support Initiative Tech. Rep. 3, 64 pp. [Available online at http://www.prism.enes.org/Publications/Reports/oasis3_UserGuide_T3.pdf.]

von Storch, H., and F. W. Zwiers, 1999: *Statistical Analysis in Climate Research*. Cambridge University Press, 494 pp.

Whitworth, T., III, 1983: Monitoring the transport of the Antarctic Circumpolar Current at Drake Passage. *J. Phys. Oceanogr.,* **13,** 2045–2057.

——, and R. G. Peterson, 1985: Volume transport of the Antarctic Circumpolar Current from bottom pressure measurements. *J. Phys. Oceanogr.,* **15,** 810–816.

Yin, J. H., 2005: A consistent poleward shift of the storm tracks in the simulations of 21st century climate. *Geophys. Res. Lett.,* **32,** L18701, doi:10.1029/2005GL023684.

Chapter 3

Linear Inverse Modeling

Contents

This chapter sums up the LIM theory, based on [Risken 1996], [Penland 1989], [Penland and Matrosova 1994], [Penland and Sardeshmukh 1995], [Farrell and Ioannou 1996], and [Penland 1996], among others.

3.1 Model

Any autonomous dynamical system may be written as :

$$\frac{d\chi}{dt} = \beta\chi + \eta(\chi) + \mathbf{f} \tag{3.1}$$

where χ is the state vector, β the deterministic feedback matrix, η represents the nonlinear terms, and $\mathbf{f}$ the external forcing. For instance, if χ contained all relevant variables representing the coupled global ocean-atmosphere system, the dynamical system (3.1) would model the evolution of the oceanic and atmospheric dynamics. This would be a system of tremendous dimension and require to know the equations governing the evolution of the system. It is of interest to focus on the evolution of a subset $\mathbf{x}$ of the system, such as the evolution of SST.

A Linear Inverse Model states that the evolution of the subset $\mathbf{x}$ is well approximated by a multivariate linear Markov process

$$\frac{d\mathbf{x}}{dt} = \mathbf{B}\mathbf{x} + \mathbf{F} \tag{3.2}$$

where $\mathbf{B}$ is a linear operator and $\mathbf{F}$ a white noise, which represents the short time scale atmospheric forcing, as well as nonlinear processes. F_i is assumed to be a Gaussian white noise at position i with constant covariance matrix $\mathbf{Q} =< \mathbf{F}^T.\mathbf{F} >$, where the subscript T indicates transpose.

[Penland and Sardeshmukh 1995] showed that LIM is a good approximation of the evolution of the seasonal anomalies of tropical SST. Note that the dimensionality of the system can be conveniently reduced by working in a truncated Empirical Orthogonal Function (EOF) space, meaning that $\mathbf{x}$ contains the main principal components of tropical SST anomalies.

Let $\mathbf{x}(t_0) = \mathbf{x}_0$ be the initial condition of eq.(3.2). Let $\mathbf{R}(t) = \mathbf{R}_{t_0}^t$ be the resolvent of the associated homogeneous equation, ie the linear application that associates $\mathbf{x}(t_0)$ to $\mathbf{x}(t)$. As $\mathbf{B}$ does not depend on time, $\mathbf{R}(t) = \mathbf{R}_{t_0}^t = e^{(t-t_0)\mathbf{B}}$. We set $\mathbf{y}(t) = \mathbf{R}(t)^{-1}\mathbf{x}(t)$, ie $\mathbf{x}(t) = \mathbf{R}(t)\mathbf{y}(t)$. Eq.(3.2) can be rewritten as

$$\begin{cases} \frac{d\mathbf{R}(t)}{dt}\mathbf{y}(t) + \mathbf{R}(t)\frac{d\mathbf{y}(t)}{dt} = \mathbf{B}\mathbf{R}(t)\mathbf{y}(t) + \mathbf{F}(t) \\ \mathbf{y}(t_0) = \mathbf{x}_0 \end{cases} \tag{3.3}$$

As $\frac{dR(t)}{dt} = BR(t)$, (3.3) becomes :

$$\begin{cases} \frac{d\mathbf{y}(t)}{dt} = \mathbf{R}(t)^{-1}\mathbf{F}(t) \\ \mathbf{y}(t_0) = \mathbf{x}_0 \end{cases} \tag{3.4}$$

whose solution is $\mathbf{y}(t) = \mathbf{x}_0 + \int_{t_0}^{t} \mathbf{R}(s)^{-1}\mathbf{F}(s)ds$. Thus, the solution to (3.2) is

$$\mathbf{x(t)} = \mathbf{e^{(t-t_0)B}x_0} + \int_{\mathbf{t_0}}^{\mathbf{t}} \mathbf{e^{(t-s)B}F(s)ds} \tag{3.5}$$

The coefficient i, j of the correlation matrix $\mathbf{C}$ of $\mathbf{x}$ at a lag τ is given by $C_{ij}(\tau) =< x_i(t+\tau)x_j(t) >$. When inserting (3.5) in the correlation function, the forcing term drops out resulting in

$$\mathbf{C}(\tau) = e^{\tau\mathbf{B}}\mathbf{C}(0) = \mathbf{G}(\tau)\mathbf{C}(0) \tag{3.6}$$

where $\mathbf{G}(\tau)$ is a Green matrix called the linear propagator. Using (3.6), the matrix $\mathbf{B}$ can be empirically derived from

$$\mathbf{B} = \tau^{-1}\ln(\mathbf{C}(\tau)\mathbf{C}(0)^{-1}) \tag{3.7}$$

The transition probability $p(\mathbf{x}, t+\tau/\mathbf{x}', t)$ that the pattern $\mathbf{x}'$ at time t will be followed by $\mathbf{x}$ at $t+\tau$ obeys a Fokker-Plank equation :

$$\frac{dp(\mathbf{x}, t+\tau/\mathbf{x}', t)}{d\tau} = \sum_{i,j}\Big\{-B_{i,j}\frac{\partial}{\partial x_i}(x_j p(\mathbf{x}, t+\tau/\mathbf{x}', t)) + \frac{1}{2}Q_{ij}\frac{\partial^2}{\partial x_i x_j}p(\mathbf{x}, t+\tau/\mathbf{x}', t)\Big\} \tag{3.8}$$

with the initial condition $p(\mathbf{x}, t/\mathbf{x}', t) = \delta(\mathbf{x} - \mathbf{x}')$. Multiplying (3.8) by $x_m x_n$, integrating by parts, and assuming the stationarity of $\mathbf{x}$ ($\frac{d<\mathbf{x}_m\mathbf{x}_n>}{dt} = 0$) leads to :

$$\mathbf{Q} + \mathbf{BC}(0) + \mathbf{C}(0)\mathbf{B}^T = 0 \tag{3.9}$$

which is called the Fluctuation-Dissipation relation and can be used to compute the covariance matrix $\mathbf{Q}$ of the noise.

Using (3.7) and (3.9) and choosing an appropriate lag τ, the matrices $\mathbf{B}$ and $\mathbf{Q}$ can be empirically derived, determining the linear system (3.2) associated to the data $\widetilde{\mathbf{x}}$, provided that the latter is known in a period long enough to compute its covariance. Note that $\mathbf{B}$ should not depend on the lag τ_0 if the LIM hypothesis is

verified, except that τ_0 has to be shorter than half of the shortest oscillatory period of data (referred as the "Nyquist problem").

Relation (3.5) can be written as

$$\mathbf{x}(t) = e^{\tau \mathbf{B}} \mathbf{x}_0 + \boldsymbol{\varepsilon}(t) \tag{3.10}$$

and used to make predictions at a lead time t with a prediction error $\boldsymbol{\varepsilon}$, whose covariance matrix equals $< \boldsymbol{\varepsilon}(\tau)\boldsymbol{\varepsilon}(\tau)^T >= \mathbf{C}(0) - \mathbf{G}(\tau)\mathbf{C}(0)\mathbf{G}(\tau)^T$.

3.2 Normal modes

Using the deterministic part of (3.5), an eigenanalysis of $\mathbf{B}$ leads to writing $\mathbf{x}(\mathbf{t})$ as a sum of empirical normal modes,

$$\mathbf{x} = \sum_i \mathbf{u}_i \exp(\lambda_i t) c_i = \sum_i \{\mathbf{a}_i \cos(\omega_i t) + \mathbf{b}_i \sin(\omega_i t)\} \exp(\sigma_i t) \tag{3.11}$$

where $\mathbf{u}_i$ is the ith eigenvector of $\mathbf{B}$ and λ_i the corresponding eigenvalue, c_i an arbitrary complex constant, σ_i and ω_i the real and imaginary parts of λ_i, $\mathbf{a}_i$ and $\mathbf{b}_i$ real vectors such as $\mathbf{a}_i^T \mathbf{b}_i = 0$, $\mathbf{a}_i^T \mathbf{a}_i = 1$ and $\mathbf{b}_i^T \mathbf{b}_i \geqslant 1$. As $\mathbf{B}$ is a real but not a symmetric matrix, the eigenmodes are not orthogonal and some eigenvalues can be complex conjugate. Besides, since the system is assumed to be stable, all the $\mathbf{B}$ eigenvalues have negative real part. The ith eigenmode of B is thus either a damped mode (if λ_i is real) or a damped oscillatory mode (if λ_i is complex). Each damped eigenmode is characterized by a pattern, a time series and a decay time $-1/\sigma_i$. Each damped oscillatory mode is described by two patterns and two time series corresponding to the cosinus and sinus phases, a period $2\pi/\omega_i$, and a decay time. The ith $\mathbf{B}$ eigenmode time series $\alpha_i(t)$ corresponding to the realization $\widetilde{\mathbf{x}}$ used to empirically derive $\mathbf{B}$ are computed by projecting $\widetilde{\mathbf{x}}$ onto the corresponding adjoint eigenvector $\mathbf{v}_i$. Thus, our initial data can be written as the sum of the eigenmodes of $\mathbf{B}$

$$\mathbf{x}(\mathbf{t}) = \sum_i \mathbf{u}_i \alpha_i(t) = \sum_i \mathbf{u}_i \mathbf{v}_i^T \mathbf{x}(t) \tag{3.12}$$

By definition, $\mathbf{B}\mathbf{u}_i = \lambda_i \mathbf{u}_i$, ie a mode is invariant by the deterministic system and any solution of the deterministic part of (3.2) can be expressed as a linear combination of normal modes (cf eq. 3.11). Besides, when there is a stochastic resonance or any other transient phenomenon, the dominant mode is the one with the largest decay time (since the real part of its eigenvalue is nearest to 0).

The eigenmodes of the stochastic forcing matrix can also been studied :

$$\mathbf{F} = \sum_i (\mathbf{q}_i \eta_i r_i(t)) \tag{3.13}$$

where $\mathbf{q}_i$ and η_i are the ith eigenvector and eigenvalue of $Q =< \mathbf{F}\mathbf{F}^T > dt$, and $\mathbf{r}_i(t)$ an independent gaussian white noise with unit variance. The efficiency of forcing functions in exciting individual normal modes (B eigenmodes) can be estimated by projecting the forcing pattern $\mathbf{q}_i$ weighted by η_i onto the normal modes adjoint : $|\eta_i \mathbf{v}_i^T \mathbf{q}_i|$ with $\mathbf{v}_i$ the ith eigenmode of B^T.

3.3 Maximum amplification and optimal initial structure

The non-orthogonality of the $\mathbf{B}$ eigenmodes allows a constructive interference of several modes, leading to a transient amplification of the system. If $\mathbf{N}$ is a positive definite hermitian form, then $\|\mathbf{y}\|_N = \mathbf{y}^T\mathbf{N}\mathbf{y}$ is a norm vector and we define the amplification of the system over a time τ by :

$$\mu(\tau) = \frac{\|\mathbf{x}(\tau)\|_N^2}{\|\mathbf{x}(0)\|_L^2} = \frac{\mathbf{x}(\tau)^T\mathbf{N}\mathbf{x}(\tau)}{\mathbf{x}(0)^T\mathbf{L}\mathbf{x}(0)} = \frac{\mathbf{x}(0)^T\mathbf{G}(\tau)^T\mathbf{N}\mathbf{G}(\tau)\mathbf{x}(0)}{\mathbf{x}(0)^T\mathbf{L}\mathbf{x}(0)} \tag{3.14}$$

where $\mathbf{L}$ and $\mathbf{N}$ are the initial and final norm kernels respectively ([Tziperman et al. 2008], [Hawkins and Sutton 2009]).

The optimal initial condition $\mathbf{x}(0)$ that maximizes $\|\mathbf{x}(\tau)\|_N$ subject to $\mathbf{x}(0)$ having unit norm under the initial norm kernel $\mathbf{L}$ (ie $\|\mathbf{x}(0)\|_L = 1$) is given by :

$$\max_{\mathbf{x}(0)} \left\{ \mathbf{x}(0)^T\mathbf{G}(\tau)^T\mathbf{N}\mathbf{G}(\tau)\mathbf{x}(0) + \lambda \mathbf{x}(0)^T\mathbf{L}\mathbf{x}(0) \right\} \tag{3.15}$$

which leads to the generalized eigenvalue problem :

$$\mathbf{G}(\tau)^T\mathbf{N}\mathbf{G}(\tau).\mathbf{x}(0) = \lambda \mathbf{L}\mathbf{x}(0) \tag{3.16}$$

with the optimal initial structure normalized such as $\mathbf{x}(0)^T\mathbf{L}\mathbf{x}(0) = 1$. The eigenvector $\boldsymbol{\phi}_1(\tau)$ of (eq.(3.16)) associated with the largest eigenvalue $\gamma_1(\tau)$ is the initial spatial structure leading to the maximum amplification after a time τ. The function $\gamma_1(\tau)$, called the maximum amplification curve, quantifies the maximum growth possible over an interval τ in the absence of forcing. The optimal initial structure is given by $\mathbf{x}(0) = \boldsymbol{\phi}_1(\tau_m)$ ($\tau_m = argmax(\gamma_1(\tau))$), leading to the maximum amplification $\mathbf{x}(\tau_m) = \mathbf{G}(\tau_m)\mathbf{x}(0) = \mathbf{G}(\tau_m)\boldsymbol{\phi}_1(\tau_m)$ in τ_m months. The contribution from each eigenmode $\mathbf{u}_i$ of $\mathbf{B}$ to the optimal initial structure can be estimated by the magnitude of its projection onto the corresponding modal adjoint, the eigenvector $\mathbf{v}_i$ of $\mathbf{B}^T$, which have the same eigenvalue as $\mathbf{u}_i$.

Depending on what we are looking for, different initial and final norm kernels can be defined. For instance, using 3-mo running mean SST anomalies in the tropical strip, [Penland and Sardeshmukh 1995] showed that the optimal perturbations leading to the maximum amplification of the domain integral of squared SST anomalies (ie the variance) evolved in a "structure strongly reminiscent of an ENSO event" after 7 mo. To filter ENSO in the tropical band, [Penland and Matrosova 2006] selected the empirical normal modes that most significantly contributed to the growth, defined as an increase in the domain variance. In these cases, the initial and final norm kernels are chosen as $\mathbf{N} = \mathbf{L} = Id$ and $\|\mathbf{y}\|_N = \|\mathbf{y}\|_L$ are L_2 norm.
In the next chapter, another norm kernel will be introduced (eq.(4.1))

3.4 Integration of the LIM equation

Given a state vector $\mathbf{x}$ known for a long enough period, the system can be empirically derived, i.e. the deterministic matrix $\mathbf{B}$ and the covariance matrix $\mathbf{Q}$ of the noise $\mathbf{F}$ can be computed from eq.(3.7) and eq.(3.9). The equation (3.2) can then be integrated to generate a new state vector. The appropriate method of integration is a second order Runge-Kutta method for generating continuous Markov models

([Kloeden and Platen 1992]), which consists of a two step process :

$$\begin{cases} y_i(t+\Delta) = y_i(t) + \sum_{j=1}^{d} B_{ij} y_j(t)\Delta + \sum_{k=1}^{d} q_{ik}\sqrt{\eta_k \Delta} R_k \\ x_i(t+\frac{\Delta}{2}) = \frac{1}{2}(y_i(t) + y_i(t+\Delta)) \end{cases} \tag{3.17}$$

where $\mathbf{q_k}$ and η_k are the kth eigenvector and the associated eigenvalue of the matrix $\mathbf{Q}$, $\mathbf{R}$ is a d-dimensional vector of independent Gaussian numbers, each having unit variance. $\mathbf{R}$ must be generated once per time step, and not within the sum over d. If the sample time is one month, then the time step Δ is chosen equal to $\frac{1}{120}$ month, ie 6 hours ([Penland and Matrosova 1994]). The initial condition is chosen at the peak of the probability distribution, here $\mathbf{y}(0) = 0$ (as we work with anomalies).

3.5 Studying the coupling between two variables using LIM

Let $\mathbf{x_1}$ and $\mathbf{x_2}$ be two variables, for instance the Atlantic SST and the AMOC anomalies. If $\mathbf{x} = \begin{bmatrix} \mathbf{x_1} \\ \mathbf{x_2} \end{bmatrix}$ is well approximated by a multivariate Markov process, the LIM framework can be used, and $\mathbf{x}$ follows the equation :

$$\frac{d}{dt}\begin{bmatrix} \mathbf{x_1} \\ \mathbf{x_2} \end{bmatrix} = \mathbf{B}\begin{bmatrix} \mathbf{x_1} \\ \mathbf{x_2} \end{bmatrix} + \mathbf{F} = \begin{pmatrix} \mathbf{B_{11}} & \mathbf{B_{21}} \\ \mathbf{B_{12}} & \mathbf{B_{22}} \end{pmatrix}\begin{bmatrix} \mathbf{x_1} \\ \mathbf{x_2} \end{bmatrix} + \begin{bmatrix} \mathbf{F_1} \\ \mathbf{F_2} \end{bmatrix} \tag{3.18}$$

where $\mathbf{B}$ refers to the deterministic matrix and $\mathbf{F}$ to the white noise forcing (as described in section 3.1). The sub-matrix $\mathbf{B_{21}}$ (respectively $\mathbf{B_{12}}$) corresponds to the deterministic influence of the variable 2 onto the variable 1 (resp., variable 1 onto the variable 2).

An eigenalysis of $\mathbf{B_{11}}$ and $\mathbf{B_{22}}$ gives informations on the uncoupled dynamics of the variable 1 and 2, respectively, and it is of interest to compare the eigenmodes of $\mathbf{B_{11}}$ and $\mathbf{B_{22}}$ to the ones of $\mathbf{B}$.

To further study the coupling between the two variables, the system (3.18) can be integrated as described in 3.4 but setting the coefficients of some sub-matrices to zero. More precisely, the system can be considered as fully uncoupled by integrating the system with $\mathbf{B_{11}} = \mathbf{B_{22}} = 0$ and $< \mathbf{F_1}\mathbf{F_2}^T >= 0$ (no correlation between the noise eigenmodes). To evaluate the effect of the noise coupling, $\mathbf{B_{11}}$ and $\mathbf{B_{22}}$ can be

set to zero, but not $< \mathbf{F_1 F_2}^T >$. The system can also be integrated with variable 1 (or variable 2) that does not force variable 2 (or variable 1), i.e. $\mathbf{B_{12}} = 0$ (or $\mathbf{B_{21}} = 0$), with correlated noise or not.

3.6 Hypothesis

Different hypothesis can be verified to justify the LIM to approach the system :

- its statistics are Gaussian.

  Note from [Sardeshmukh and Sura 2008] : For the SST variability in the eastern Pacific, it has been shown that the Probability Density Functions are almost gaussian for 3-month averages ([Penland and Sardeshmukh 1995]), but non-gaussian for monthly averages ([Hannachi et al. 2003]).

- the deterministic $\mathbf{B}$ is independent of the lag τ_0 used to determine it (tau test).

- the noise covariance matrix $\mathbf{Q}$ is positive definite (since it is a covariance matrix).

3.6.0.1 Tau test

If LIM is a good approximation of the system, the matrix $\mathbf{B}$ should not depend on the lag τ used to determine it, ie determining $\mathbf{B}$ from $\mathbf{C}(\tau_1) = e^{\tau_1 \mathbf{B}}\mathbf{C}(0)$ or $\mathbf{C}(\tau_2) = e^{\tau_2 \mathbf{B}}\mathbf{C}(0)$, with $\tau_1 \neq \tau_2$, should lead to the same results. Hence, a simple test of the accuracy of the LIM model is to compare $\mathbf{B}$ estimated at different lag (tau test, [Penland and Sardeshmukh 1995]). However, as discussed by [Newman 2007], if $\mathbf{B}$ can only be determined at one lag because of the Nyquist problem, an alternate test is to verify that the empirically derived matrix $\mathbf{B}$ reproduces the observed covariance $\mathbf{C}_{obs}(l) = \frac{1}{nt}\sum_{t=1}^{nt-l} \mathbf{x}(t)\mathbf{x}(t+l)$ of $\mathbf{x}$ (in EOF space) at a longer lag l ([Winkler et al. 2001]). The reconstructed covariance matrix $\mathbf{C}(l) = e^{l\mathbf{B}}\mathbf{C}(0)$ and

$\mathbf{C}_{obs}(l)$ can be compared using :

$$d(l) = \frac{\mathbf{C}_{lim}(l) - \mathbf{C}_{obs}(l)}{\mathbf{C}_{obs}(l)}. \tag{3.19}$$

Chapter 4

Deconstructing the Atlantic Multidecadal Oscillation

Contents

As described in the introduction, the AMO is strongly linked to the AMOC variability. However, it is also influenced by external forcings (volcanic activity, solar forcing) and anthropogenic changes. Local atmospheric forcing and remote oceanic processes, such as ENSO and the Pacific decadal variability may also impact the multidecadal fluctuations of Atlantic SSTs via atmospheric teleconnections.

In most studies, the SST changes associated with anthropogenic and external forcings are removed by a linear trend ([Enfield et al. 2001], [Sutton and Hodson 2005], Fig.4.1 left) or by the global mean SST ([Trenberth and Shea 2006], Fig.4.1 right). Since the SST response to an in-

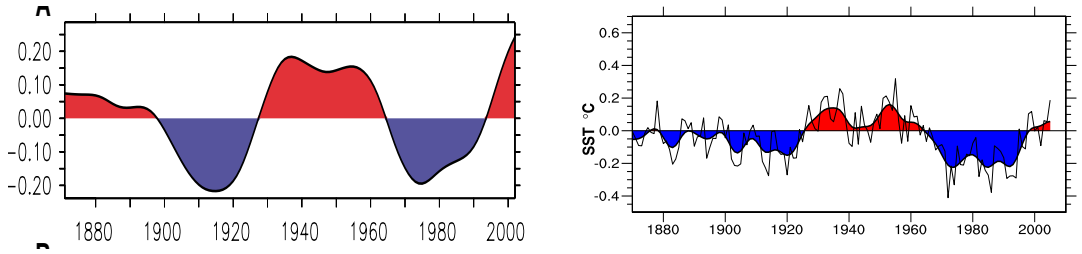

Figure 4.1: AMO time series in the observations, where the anthropogenic and external forcings have been removed by a linear trend (left, from [Sutton and Hodson 2005]) and by the global mean SST (right, from [Trenberth and Shea 2006]).

crease in greenhouse gases and aerosol concentrations may be more complex, [Ting et al. 2009] constructed instead a model-based estimate of the forced component of North Atlantic SST variability using several coupled model simulations with multiple ensemble members and a signal-to-noise maximizing empirical orthogonal function analysis. In this thesis, we use LIM to filter out these global SST signals.

[Penland and Matrosova 2006] have described several statistical methods to remove the ENSO signal, pointing out their limits. A common approach is to use a band-pass filtering between approximately 2 and 6 yr, which corresponds to ENSO periods. This is based on the very strong assumption that all the SST variability in that frequency band is related to ENSO. Another frequently used method is linear regression on one or several ENSO indices (like SST anomalies in the Niño 3.4 area, or the 1st PC of SST anomalies in the Tropical Pacific). However, this also removes ENSO-unrelated signals associated with these indices, and it may not fully represent the dynamics of the ENSO phenomenon. To remove the Pacific influence on the AMO, [Guan and Nigam 2009] generalized this approach

and used a regression of the SSTs onto six PCs of rotated extended empirical orthogonal functions of Pacific SST, which are well adapted to propagating signals. Two of these time series corresponded to the canonical ENSO variability (one for growth and one for decay), one to west-to-east ENSO development, one to biennal variability, and two to decadal variability : a Pan-Pacific mode and a North Pacific mode. Removing the regression on six Pacific PCs from the North Atlantic SST lead to considerable changes in the AMO (Fig.4.2), mostly because the Pan-Pacific decadal mode was correlated with the SST variability in the North Atlantic, in particular the AMO ($r = 0.48$) when it led by 5 seasons, suggesting a Pacific-Atlantic basin connectivity on decadal time scale. Note that the Pacific decadal mode confined to the North Pacific was highly correlated to the PDO ($r = 0.57$) and was leading SST anomalies in the North Atlantic by 3 yr, southeastward of Greenland and near the American coast between 25 and 35 $^\circ$N. However, as [Müller et al. 2008] found a strong coherency at decadal frequencies between the PDO and the North Atlantic Oscillation (NAO), which strongly influences the AMOC variability (e.g. [Delworth et al. 1993], [Eden and Willebrand 2001], [Deshayes and Frankignoul 2008]), it is not clear that the North Pacific decadal signal should be removed from the AMO to extract the part related to the AMOC.

To remove the ENSO signal, [Penland and Matrosova 2006] proposed using instead LIM. They showed that the dynamics of SST anomalies in the tropical strip were well represented by a stable, linear multivariate process driven by stochastic forcing. The SST signal was decomposed into nonnormal modes, and the ENSO modes identified from the optimal growth from an initial condition to a mature ENSO event. As the ENSO modes could be efficiently substracted from the SST field to reveal ENSO-unrelated signals, the LIM approach is used in this chapter to remove the ENSO imprint from the AMO. During the course of this Ph.D, [Compo and Sardeshmukh 2010] also used the LIM approach to remove ENSO-related SST variations from the global SST record, albeit in a slightly different manner, since we define the LIM-based filter from the whole SST field

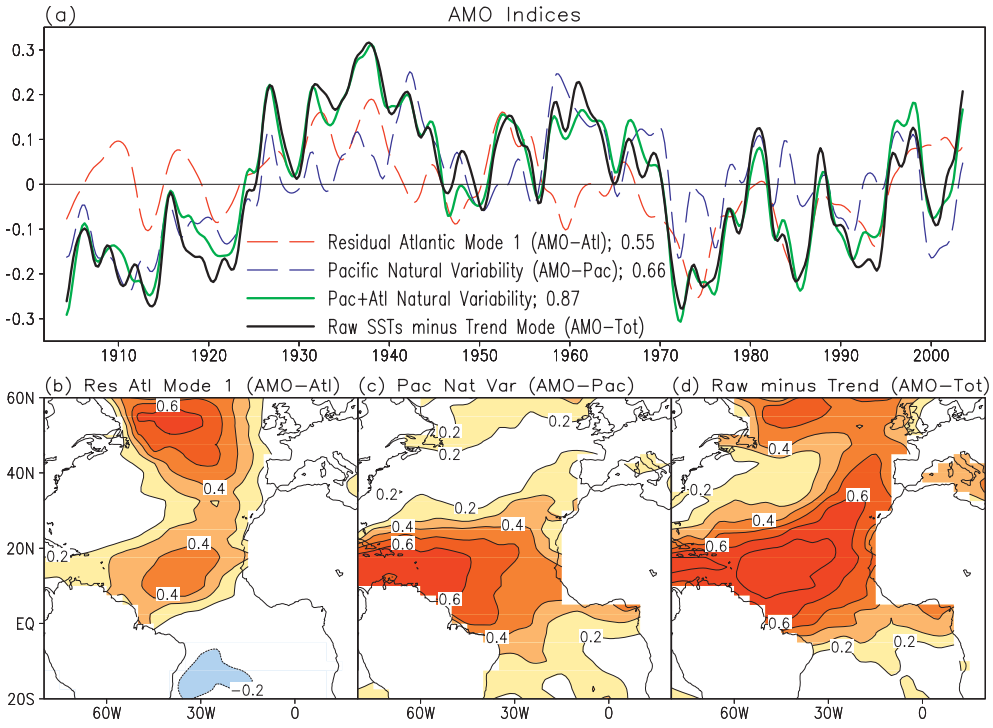

Figure 4.2: From [Guan and Nigam 2009]. Top : AMO indices in HadISST computed as the traditional AMO (AMO-Tot, black curve), from the leading mode of Atlantic SST after removing the regression on six Pacific PCs (AMO-Atl, red curve), from the Atlantic footprint of the Pacific natural variability (AMO-Pac, blue curve), from the sum of the last two indices (green curve). Bottom : Correlations between raw Atlantic SST and AMO-Atl (left), AMO-Pac (middle), and AMO-Tot (right).

while they only define it in the tropical strip and introduce an "atmospheric bridge operator" to remove the ENSO influence from the extratropical SSTs. [Compo and Sardeshmukh 2010] found that the ENSO-unrelated AMO was very close to the traditional AMO, except before about 1900, thus contrasting with the Pacific-unrelated AMO obtained by [Guan and Nigam 2009], where the warm and cool phases did not always coincide with the ones of the traditional AMO.

In this chapter, we use LIM to extract the part of the AMO that is related

to the AMOC variability in observations, a historical simulation of the IPSLCM5 climate model, and control simulations with five different climate models.

This chapter is a more detailed version of an article submitted to Journal of Climate in September 2011.

4.1 Method and data

4.1.1 Using Linear Inverse Modeling to deconstruct the AMO

To extract the part of the AMO that is best related to the AMOC variability, the LIM approach is applied to global SST anomalies (north of 20 °S where data coverage is best in the observations), and used to decompose the North Atlantic SST field into a signal linked to the global trend, a part that is related to ENSO, one to decadal variability in the Pacific, and a residual. Assuming that global SST anomalies, denoted $\mathbf{x}$, are well approximated by eq.(3.2) (which is verified below), LIM is used to write $\mathbf{x}$ as a linear combination of empirical normal modes (section 3.2) and modes corresponding to the global trend signal, to ENSO, and to the decadal Pacific signal are identified.

Similarly to [Penland and Matrosova 2006], we consider as ENSO modes the empirical normal modes that most significantly contribute to the optimal initial structure leading to the maximum amplification of SST variance in the Tropics. Mathematically, the SST variance in the Tropics can be measured by the norm vector $\|\mathbf{y}\|_N = \mathbf{y}^T\mathbf{N}\mathbf{y}$ when $\mathbf{N}$ is a positive definite hermitian form (normalized to have unit determinant) defined by

$$\mathbf{N} = (\mathbf{W}.\mathbf{E})^T(\mathbf{W}.\mathbf{E}) \tag{4.1}$$

where the matrix $\mathbf{E}$ of size (n, p) contains the patterns of the p retained EOF restricted to the n grid points of the Tropics, and $\mathbf{W}$ is a matrix of area weighting, which takes into account the Earth curvature. The amplification μ of the system over a time τ is given by eq.(3.14) and then becomes

$$\mu(\tau) = \frac{\|\mathbf{x}(\tau)\|_N^2}{\|\mathbf{x}(0)\|_{l_2}^2} = \frac{\mathbf{x}(\tau)^T\mathbf{N}\mathbf{x}(\tau)}{\mathbf{x}(0)^T\mathbf{x}(0)} = \frac{\mathbf{x}(0)^T\mathbf{G}(\tau)^T(\mathbf{W}.\mathbf{E})^T(\mathbf{W}.\mathbf{E})\mathbf{G}(\tau)\mathbf{x}(0)}{\mathbf{x}(0)^T\mathbf{x}(0)} \tag{4.2}$$

We thus search for the initial structure with small SST anomaly variance in the entire domain leading to the largest SST anomaly variance in the tropical strip. As explained in section 3.3 the contribution from each eigenmode $\mathbf{u}_i$ of $\mathbf{B}$ to the

optimal initial structure is estimated by the magnitude of its projection onto the corresponding modal adjoint[1]. However, in our case, the eigenmodes corresponding to the global SST changes and Pacific decadal signals may contribute to the optimal initial structure, but cannot be considered as ENSO modes. As most of the ENSO signal is found below a period of 8 yr, modes having a larger period will not be considered as ENSO modes. Similarly, as ENSO may not be predictable after 18-24 mo ([Penland and Sardeshmukh 1995], [Chang et al. 2004]), modes having a decay time larger than 24 mo will not be classified as ENSO modes. As discussed in [Penland and Matrosova 2006], the identification of "ENSO modes" is somewhat subjective. Choosing too many modes may add noise in the North Atlantic SSTs and include signals that are involved in the link between the AMO and the AMOC, while choosing only a few modes may miss a significant part of the ENSO signal. To check its accuracy, the ENSO-related signals can be compared to classical indices, such as Niño 3.4 and Niño 1.2.

As will be shown below, the signal linked to external forcing in the last century will appear in the first damped mode of the LIM decomposition. Modes related to the Pacific decadal variability are chosen as those having a period larger than 10 yr and showing strong anomalies in the Pacific.

Once the global signal, the ENSO modes, and the decadal Pacific signal are identified, the SST field can be decomposed into various parts, which may not be orthogonal. For instance, if E is the subset of ENSO modes, then :

$$\mathbf{X}(t) = \underbrace{\sum_{i \in E} \mathbf{u}_i \alpha_i(t)}_{ENSO\ related} + \underbrace{\sum_{i \notin E} \mathbf{u}_i \alpha_i(t)}_{ENSO\ unrelated} \tag{4.3}$$

Using the second part of the sum, the residual SST anomalies can be reconstructed. The ENSO-unrelated AMO is expected to be a better proxy of the AMOC vari-

[1]It might be more physical not to include the Atlantic in this projection, since the variability arising in this area (via the AMOC for instance) may influence ENSO, and we aim at removing the influence of the ENSO onto the North Atlantic, but not the opposite. However, omitting the Atlantic does not change the order of the 1st contributors to the optimal initial structure.

ability than the traditional AMO index, after possible modes corresponding to anthropogenic and external forcing have also been removed.

4.1.2 Data

The observed SST fields are taken from the HadISST1 data ([Rayner et al. 2003]) during the 1901-2008 period, an historical simulation with the IPSLCM5 model ([Dufresne 2011]), and control simulations of five coupled climate models : IPSLCM4-CTRLA ([Marti et al. 2010]), IPSLCM5-piControl2 ([Dufresne 2011]), HadCM3 ([Gordon et al. 2000]), MPI-ESM ([Jungclaus et al. 2010]), and CCSM3 ([Collins et al. 2006]). For the latter model, we only consider the last 250 years of the simulation, when the AMOC has an irregular, red noise behaviour ([Kwon and Frankignoul 2011]). The different datasets are summarized in Table 4.1. Note that, except CCSM3, models are used in the European project THOR (Thermohaline Circulation at Risk?). IPSLCM4 is the model used in chapter 2, but here a more recent and longer control simulation is used. The IPSLCM5 model is an updated version of IPSLCM4 with a slightly higher atmospheric simulation, and with the oceanic component NEMO/OPA9 instead of NEMO/OP8 that better parameterizes the tidal mixing. Seasonal SST anomalies are considered between 20 $^\circ$ S and 60 $^\circ$ N in HadISST, and between 20 $^\circ$ S and 80 $^\circ$ N in the coupled models, after removing grid points where the averaged sea ice cover in March is higher than 25%. Note that results are only shown up to 70 $^\circ$ N, since the area north of this latitude is mostly covered by sea ice. In the control simulations with the climate models, a quadratic trend is substracted at each grid point to remove possible non-physical trend linked to insufficient spin-up. We work in a truncated EOF space, which is defined separately in 3 different domains : the North Atlantic (20 $^\circ$ N-80 $^\circ$ N, 100 $^\circ$ W-5 $^\circ$ E), the North Pacific (20 $^\circ$ N-80 $^\circ$ N, 120 $^\circ$ E-100 $^\circ$ W), and the tropical strip (20 $^\circ$ S-20 $^\circ$ N). Hence, the state vector $\mathbf{x}$ is composed of three sets of principal components. The number of retained EOFs in each area is given in Table 4.1. In most cases, about 70% of the variance is retained. It was verified that the results

	Type	Period	Resolution		Number of EOFs		
			Ocean	Atmosphere	N.Atl	N.Pac	Tropics
HadISST	Observations	1901-2008 108yr	$1^\circ \times 1^\circ$		7 (74%)	4 (64%)	12 (85%)
CCSM3	Control	450-699 250yr	128×256 40 levels	T85 26 levels	14 (73%)	7 (65%)	7 (60%)
HadCM3	Control	3090-3789 800yr	$1.25^\circ \times 1.25^\circ$ 20 levels	$2.5^\circ \times 3.75^\circ$, 19 levels	14 (69%)	9 (65%)	8 (67%)
MPI-ESM	Control	2800-3799 1000yr	101×120 40 levels	T31 19 levels	17 (70%)	14 (80%)	5 (80%)
IPSLCM4	Control	1200-2199 1000yr	2° Mercator mesh 31 levels	$2.5^\circ \times 3.75^\circ$ 19 levels	12 (75%)	7 (66%)	8 (79%)
IPSLCM5 control	Control	1800-2799 1000yr	2° Mercator mesh 31 levels	$2^\circ \times 3.75^\circ$ 39 levels	8 (71%)	8 (69%)	10 (70%)
IPSLCM5 historical	Historical	1850-2005 156yr	2° Mercator mesh 31 levels	$2^\circ \times 3.75^\circ$ 39 levels	8 (75%)	8 (73%)	8 (79%)

Table 4.1: Summary of the dataset. The percentage of explained variance is indicated in brackets.

depend little on the EOF truncation. In all datasets, classical Niño indices are defined as the time series of detrended seasonal SST anomalies averaged in the Niño 3.4 (120-170 $^\circ$W, 5 $^\circ$S-5 $^\circ$N) and Niño 1.2 (90-80 $^\circ$W, 10 $^\circ$S-0 $^\circ$) regions.

Throughout this study, the statistical significance of correlations or regressions is computed with a student t-test at a level of 5%. For seasonal or annual anomalies, the number of degrees of freedom is estimated as in [Bretherton et al. 1999], assuming that time series are autoregressive processes of order 1. For low-pass filtered data with a cutoff period of T_c, it is estimated by $\frac{T}{T_c/2} - 2$ (T being the length of the time series), assuming for simplicity independent samples at half the filter cut-off period.

4.1.3 Testing the validity of the LIM

To check the accuracy of the LIM to approximate the evolution of seasonal SST between 20 $^\circ$S and 80 $^\circ$N, we use the tau test described in section 3.6.0.1. As tropical SST anomalies were shown to be well represented by LIM

([Penland and Sardeshmukh 1995]), we simply compare $d(l)$ with a distance $d_{ref}(l)$ obtained by applying LIM only in the tropical strip, retaining the same number of tropical EOFs than in the "global" $\mathbf{B}$. This is done for the HadISST data and the IPSLCM5 control simulation, using $l = 1$ to 30 seasons. In the observations, d ranges between -0.8 and 0.1 and d_{ref} between -1 and 0.3. In IPSLCM5, d is in the interval $[-1.3, 1]$ and d_{ref} in $[-1.5, 1.5]$. Thus, in both cases, d and d_{ref} are of the same order of magnitude, showing that the LIM can indeed be used to model the global SST anomalies.

4.2 SST signature of the AMOC

Before applying LIM to extract the part of the AMO that is related to the AMOC variability, we show the relation between the traditional AMO and the AMOC in climate models, where the AMOC is known. To characterize the AMOC variability at low frequencies, we use three indices, namely the low-pass filtered (T_c = 10 yr) AMOC maximum below 500 m between 10 and 60 ° N, that at 30 ° N, and the 1st PC of low-pass filtered AMOC anomalies (hereafter AMOC PC1), whose pattern is a circulation cell spanning the whole Atlantic basin and reaching a maximum between 45 and 55 ° N, depending on models (Fig.4.3). Note that although the std of the

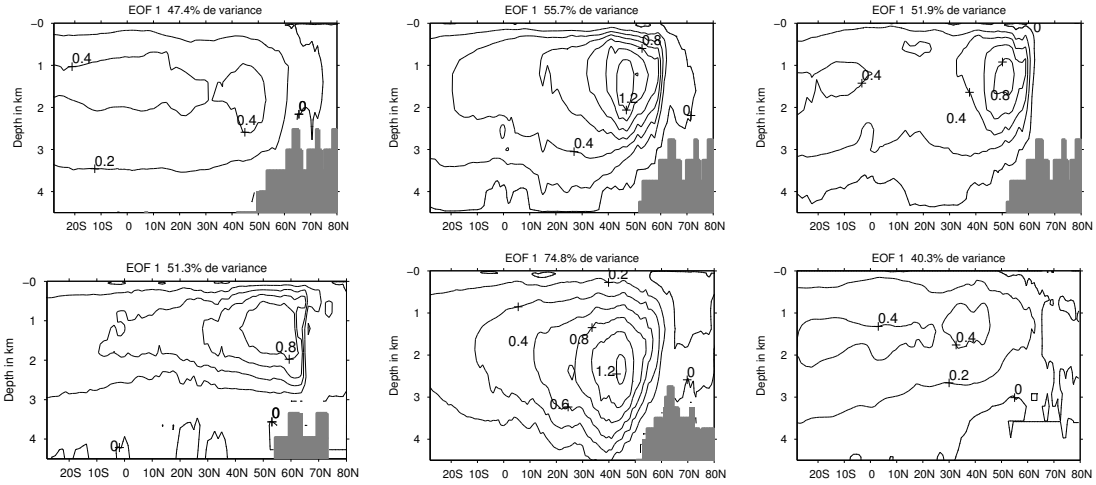

Figure 4.3: First EOF (in Sv) of low-pass filtered (T_c = 10 yr) AMOC anomalies in IPSLCM4 (top left), IPSLCM5 (top middle), historical IPSLCM5 simulation (top right), HadCM3 (bottom left), CCSM (bottom middle), and MPI (bottom right).

AMOC maximum is similar in all models, their mean value differs considerably, with weaker values for the IPSL models and stronger for CCSM3 (Table 4.2). Fig.4.4 shows the power density spectrum of AMOC PC1 in the 6 simulations. Similarly to the associated patterns, differences can be noticed from one model to another. However, in all models, AMOC PC1 shows spectral energy at multidecadal time scales. The discrepancy among models emphasizes the need of considering several

Models	CCSM3	HadCM3	MPI-ESM	IPSLCM4	IPSLCM5
Mean max AMOC 1060N	21.6	18.6	16.6	10.1	10.2
Std AMOC 1060N	1.1	1.1	0.9	1.3	1.2

Table 4.2: Mean and std (in Sv) of the AMOC maximum between 10 and 60 ° N (max AMOC 1060N) in the different models.

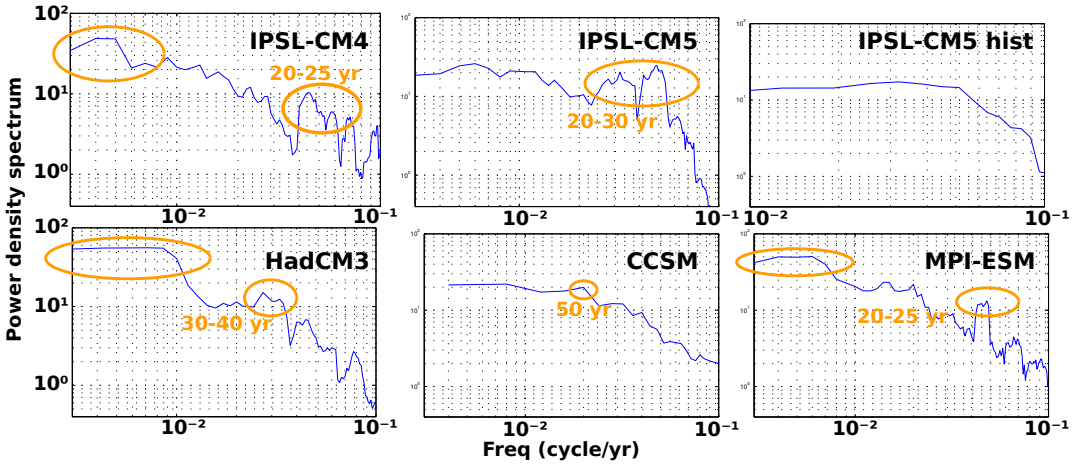

Figure 4.4: Power density spectrum of the first principal component of low-pass filtered (T_c = 10 yr) AMOC anomalies in IPSLCM4 (top left), IPSLCM5 (top middle), historical IPSLCM5 simulation (top right), HadCM3 (bottom left), CCSM (bottom middle), and MPI (bottom right).

models to check whether key signals are found in all models and to validate the use of models to understand the observations.

To illustrate the SST signature of the AMOC, we first consider control simulations, which are not affected by external forcing. Fig.4.5 shows for four models the regression of low-pass filtered SST anomalies onto AMOC PC1 both in phase and when the AMOC leads by a few years. For HadCM3 and CCSM3, a SST anomaly maximum is found along the North Atlantic current. Significant negative anomalies are also seen north of England and southeast of Greenland in CCSM3, but the latter get smaller as the lag increases. Around lag 3, the SST pattern becomes similar to the AMO (shown in Fig.4.20 below), which is also shown by the maximum in the

correlation between AMOC PC1 and the AMO (Table 4.6). The correlation then slowly decreases as the SST signature of the AMOC becomes weaker. For MPI-ESM, the SST pattern associated to the AMOC primarily indicates a warming of the subpolar gyre, and it is similar to the AMO when the AMOC leads by a few years (maximum correlation at a lag of 4 yr). There are more changes with lag in IPSLCM5, where a dipole is observed in phase with the AMOC with negative anomalies in the subpolar gyre and smaller positive anomalies in the subtropical gyre. When the AMOC leads, the latter are progressively intensified and advected northeastward along the North Atlantic current, and by lag 6, the SST structure becomes very similar to the AMO represented in Fig.4.20 below. The maximum correlation between the AMO and the AMOC PC1 occurs at a lag larger than the other models (Table 4.6). Similar patterns are found for IPSLCM4 (not shown). Note that in both models, the North Atlantic ice cover is unrealistically large, as discussed in [Marti et al. 2010].

Although the SST patterns associated with an AMOC intensification may differ substantially, they always show a large warming in the subpolar gyre centered between 45 and 55 $^\circ$N and 40 and 30 $^\circ$W, depending on the model (except for MPI-ESM, where the maximum is located near Newfoundland), a weaker warming in the subtropical gyre, and very small anomalies in the tropical Atlantic. Note that SSTs associated with the AMO also differ considerably from one model to another (Fig.4.20), as well as the temporal characteristics of the AMO, as shown in Fig.4.6. Despite the discrepancy among models, a positive AMO phase thus follows an AMOC intensification by a few years in all models, as shown in Fig.4.7, consistently with earlier studies (e.g. [Vellinga and Wu 2004], [Msadek and Frankignoul 2009]).

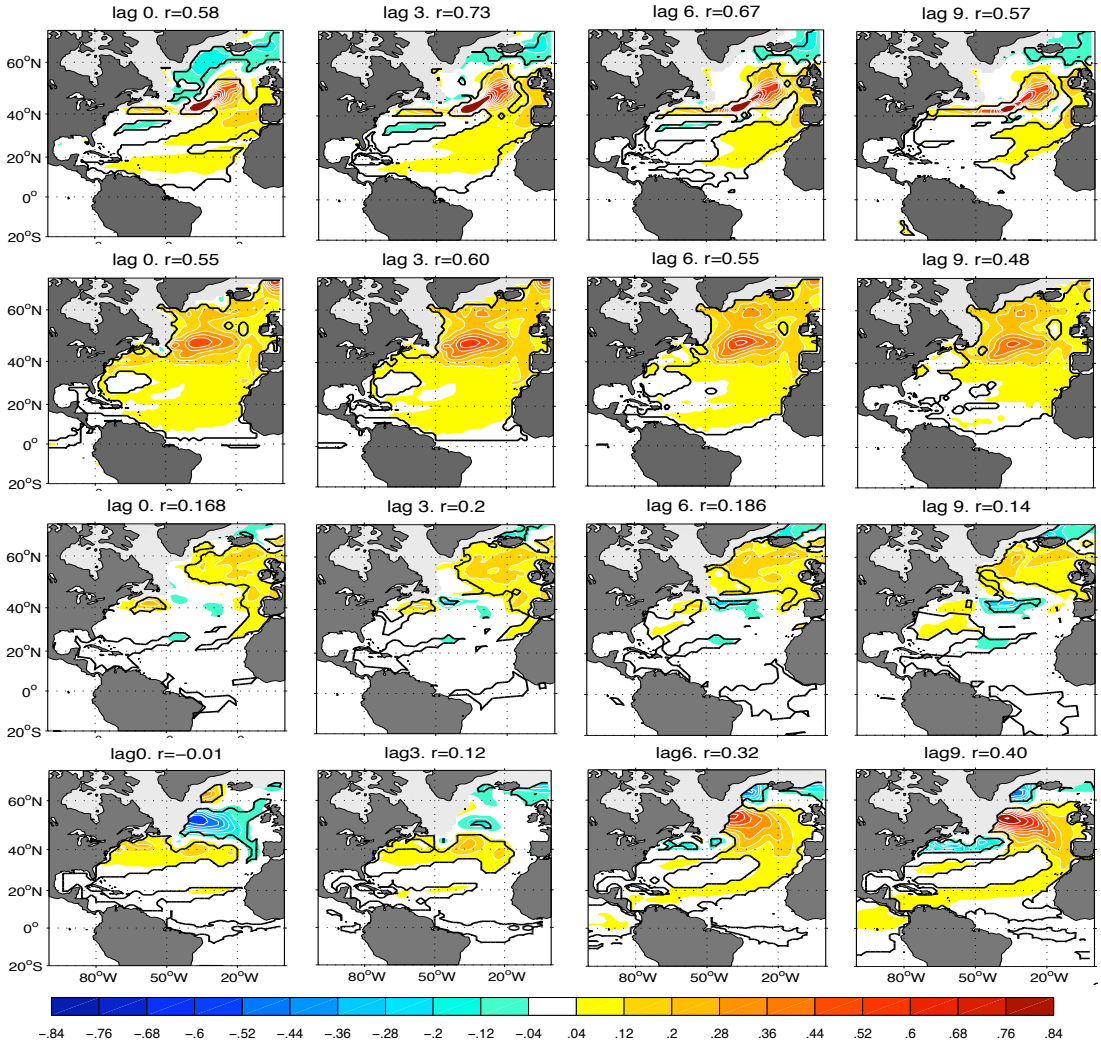

Figure 4.5: Regression of low-pass filtered SST onto AMOC PC1 in phase and when the AMOC leads (lag in yr) for CCSM3 (top), HadCM3 (2nd row), MPI-ESM (3rd row), and IPSLCM5 (bottom). The black contour indicates 5% significance and r is the correlation between the 1st AMOC PC and the traditional AMO. Light gray shading indicates where the sea ice cover in March is higher than 25%.

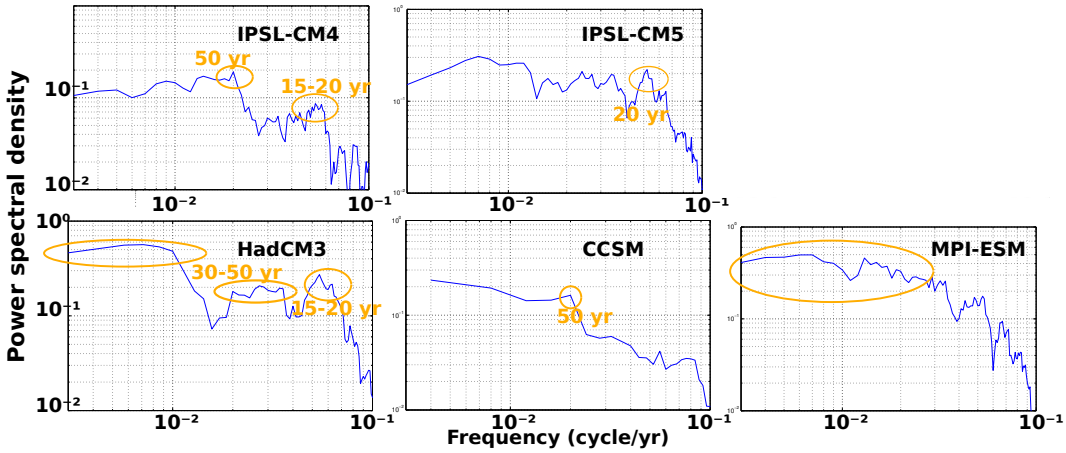

Figure 4.6: Power density spectrum of the AMO in IPSLCM4 (top left), IPSLCM5 (top middle), HadCM3 (bottom left), CCSM (bottom middle), and MPI (bottom right).

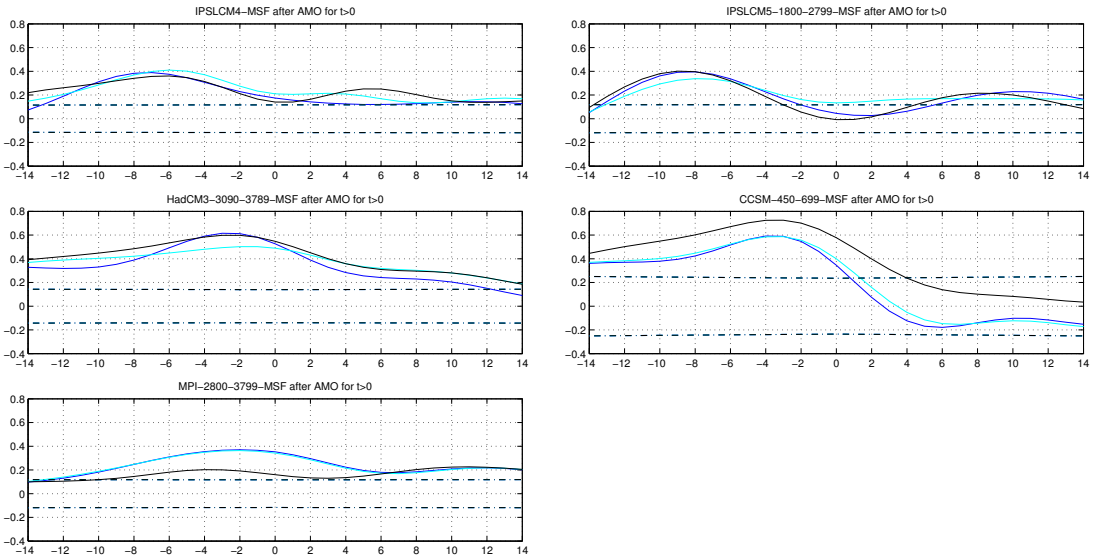

Figure 4.7: Correlation between the traditional AMO and AMOC PC1 (black), the low-pass filtered AMOC maximum between 10 and 60 ° N (blue), and the low-pass filtered AMOC maximum at 30 ° N (cyan). The AMOC leads for negative lags. Top left : IPSLCM4, top right : IPSLCM5, middle left : HadCM3, middle right : CCSM3, and bottom left : MPI-ESM.

4.3 A Historical simulation with the IPSLCM5 model

The historical simulation with IPSLCM5 better corresponds to the observations than control simulations. It starts with initial conditions from the 50th year of the control simulation, and it is forced by the "observed" solar forcing and the atmospheric composition due to both anthropogenic and volcanic influences during 1850-2005, following the CMIP5 protocol described in [Taylor et al. 2011]. Note that the volcanic radiative forcing is simply simulated by an additional change to the solar constant (Fig.4.8, [Dufresne 2011]), contrary to the last millennium simulation with IPSLCM4 used in the next chapter, where it is implemented by a radiative module (Kohdri et al, in prep).

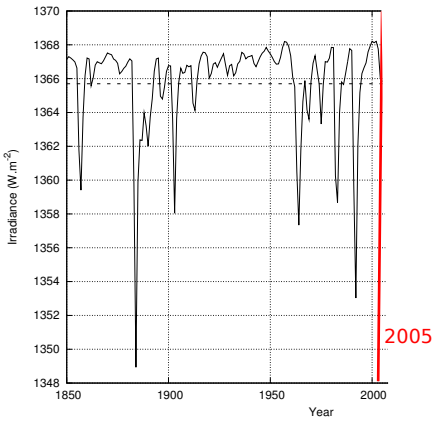

Figure 4.8: Time evolution of the total solar irradiance ($W.m^{-2}$) with volcanic eruptions in the historical simulation with IPSLCM5. Strong peaks correspond to the forcing due to volcanic eruptions. From [Dufresne 2011].

In this simulation, the correlation between the AMOC indices and the traditionally defined AMO (Fig.4.10) is weaker than in the control simulations. It peaks when the AMO lags by about a decade, but it is not significant (Table 4.4). As shown in Fig.4.9 (bottom), the regression of low-pass filtered SST anomalies onto AMOC PC1 first shows a strong cooling in the subpolar gyre, but by lag 5 they are replaced by a growing warming, while the Gulf Stream region becomes colder. As

the lag increases, the SST pattern associated to the AMOC starts resembling that in the control simulation, with a maximum correlation, albeit not significant between the AMO and AMOC PC1 at lag 12. However, the global SST pattern associated with the traditional AMO (Fig.4.11 top left) mostly contains positive anomalies, suggesting that the global changes are not well removed by linear detrending.

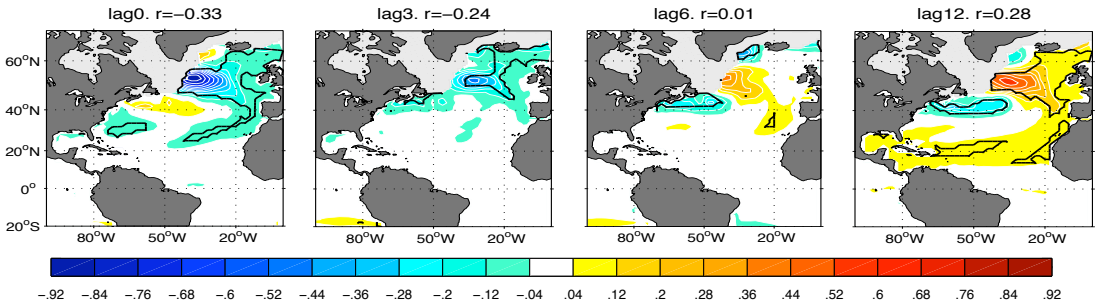

Figure 4.9: Regression of low-pass filtered SST onto AMOC PC1 in phase and when the AMOC leads (lag in yr) for the historical IPSLCM5 simulation. The black contour indicates 5% significance and r is the correlation between the 1st AMOC PC and the traditional AMO. Light gray shading indicates where the sea ice cover in March is higher than 25%.

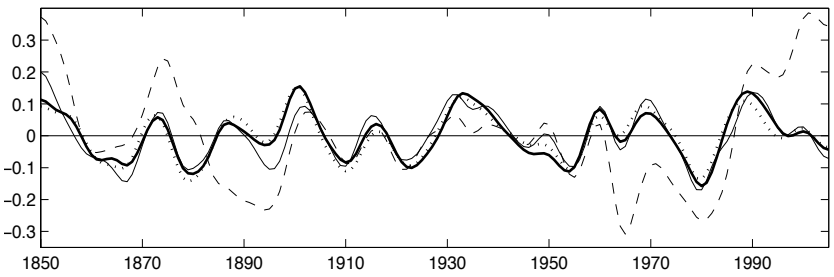

Figure 4.10: Time series in $^\circ$C of the traditional AMO (dashed line), the AMO-GT (continuous line), the AMO-GT/EN (thick line), and the AMO-GT/EN/PD (dotted). LIM made from the historical IPSLCM5 simulation.

To deconstruct the AMO, we apply the LIM filter. The dimension of $\mathbf{x}$ is 24 (Table 4.1), 8 PCs being considered in each area. The first 3 EOFs and their

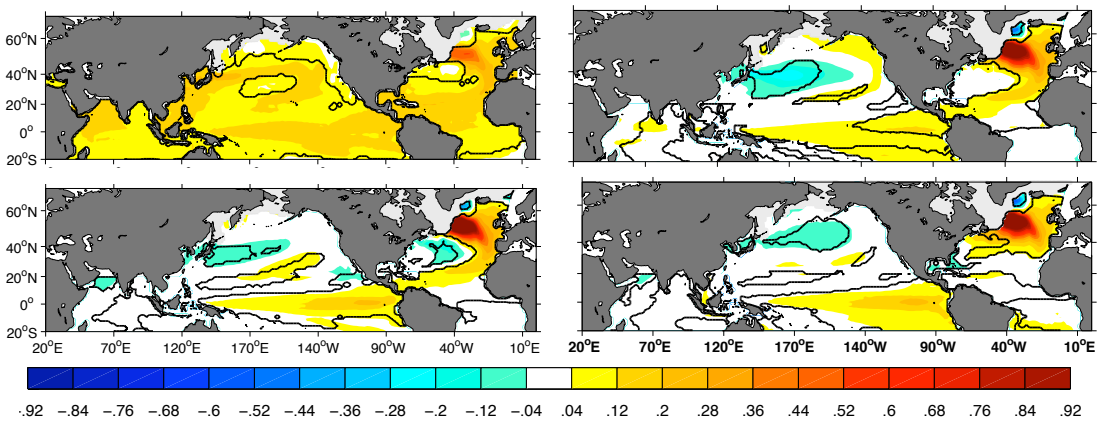

Figure 4.11: SST pattern (in ˚C) associated with the AMO time series in Fig.4.10. Top left : traditional AMO, Top right : AMO-GT, Bottom left : AMO-GT/EN, Bottom right : AMO-GT/EN/PD. LIM made from the historical IPSLCM5 simulation. The black contour indicates 5% significance.

associated PCs of each area are shown in Fig.4.12-4.14. The eigenmodes of **B** are

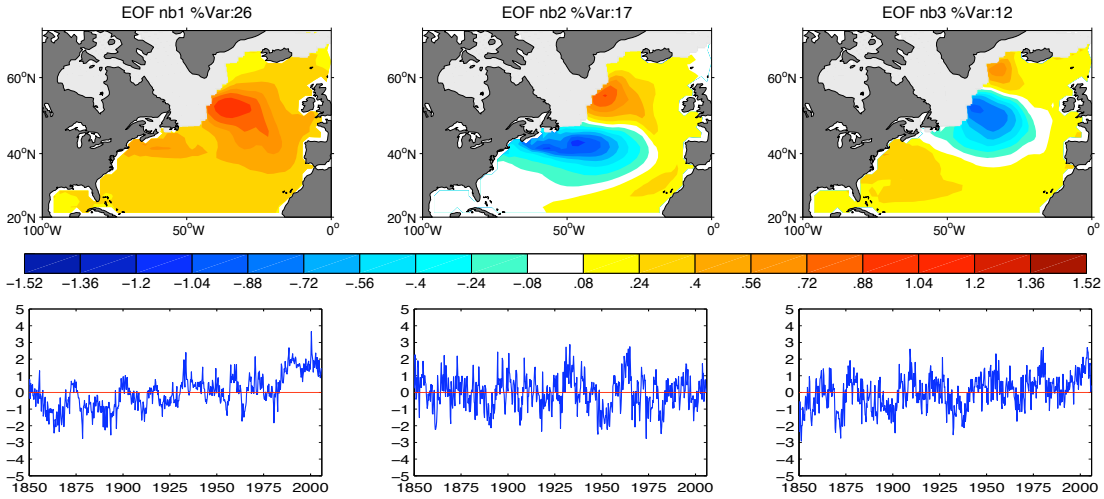

Figure 4.12: EOFs (top) and the associated PCs (bottom) of seasonal SST anomalies in the North Atlantic. The percentage indicates the explained variance. Light gray shaded area indicates where the sea ice cover in March is higher than 25%.

listed in Table 4.3 (right) and the main ones shown in Fig.4.15. The 1st mode is a

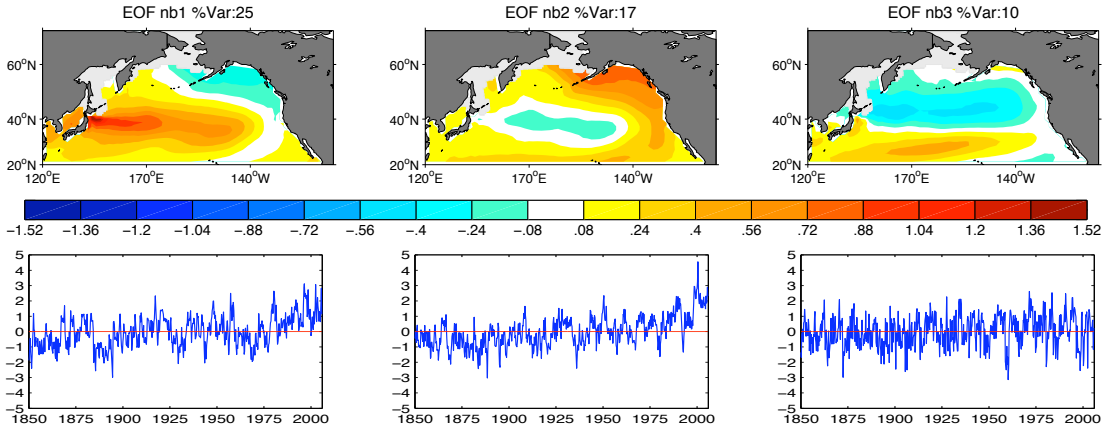

Figure 4.13: EOFs (top) and the associated PCs (bottom) of seasonal SST anomalies in the North Pacific. The percentage indicates the explained variance. Light gray shaded area indicates where the sea ice cover in March is higher than 25%.

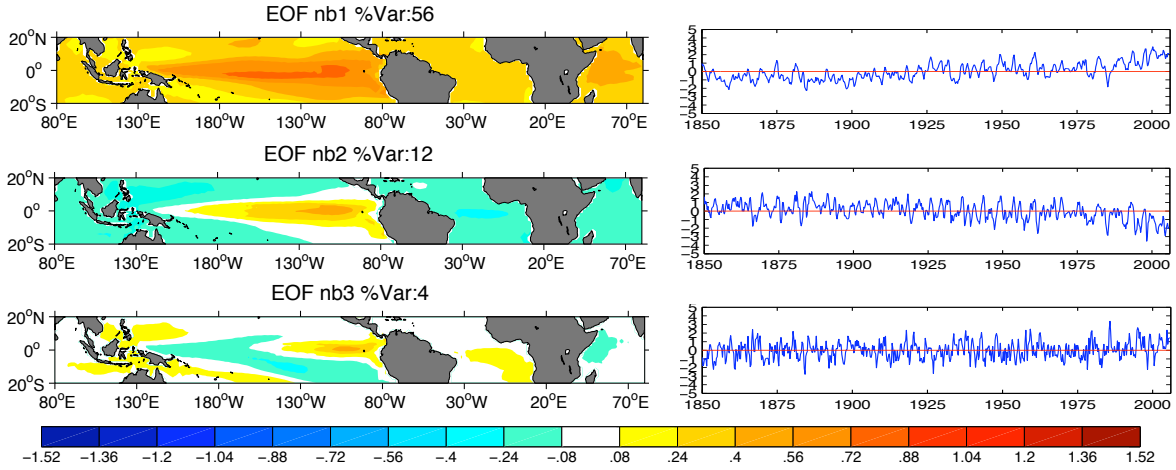

Figure 4.14: EOFs (top) and the associated PCs (bottom) of seasonal SST anomalies in the Tropics. The percentage indicates the explained variance.

damped mode that corresponds to a global warming, and the associated time series has a strong positive trend (Fig.4.15), it is likely to represent the SST response to external and anthropogenic forcing. Indeed, its correlation with the global SST average is 0.95. Several abrupt cooling episodes are observed after some volcanic eruptions (Krakatoa in 1883, Agung in 1963, and Pinatubo in 1991) but not after

Modes	Decay time DT	Period T
1	10.3 yr	∞
2	1.3 yr	∞
3/4	**11 mo**	**5 yr**
5	9 mo	∞
6/7	*7 mo*	*13.8 yr*
8	6 mo	∞
9/10	6 mo	6.6 yr
11/12	5 mo	20 yr
13/14	5 mo	2.4 yr
15/16	4 mo	5.1 yr
17	4 mo	∞
18/19	4 mo	5.7 yr
20/21	3 mo	10.8 yr
22/23	**3 mo**	**2.8 yr**

Table 4.3: Decay time and period of the main eigenmodes of $\mathbf{B}$ in the historical IPSLCM5 simulation. The ENSO modes are indicated in bold characters, and the Pacific decadal modes in italics.

all volcanic eruptions taken into account in the simulation (4.8). The pattern of this mode shows a weaker warming in the North Pacific, which might be attributed to aerosols effects, as [Ting et al. 2009] (2009) indicated that the forced component of surface temperatures estimated from six IPCC AR4 coupled models shows a patch of weaker warming in the North Pacific (Fig.1.17), which is likely to be caused by aerosols forcing. The second eigenmode is also a damped mode, showing regular oscillations with strong spectral peaks around 80 yr and 4 yr. It has a tripolar pattern in the North Atlantic with a main lobe centered around 50 $^\circ$N, 30 $^\circ$W, and a weaker signal in the North Pacific. Interestingly, the AMO derived from this mode, i.e. using $\sum_{i=2} \mathbf{u}_i \alpha_i(t)$, is significantly correlated with the traditional AMO ($r = 41$) and to the AMOC, in fact more so than our deconstructed AMO, as discussed in section 4.7.

Since only the 1st eigenmode seems to correspond to the global trend mode, a filtered AMO index, referred to as AMO-GT, is computed by removing it, using $\sum_{i\neq 1} \mathbf{u}_i \alpha_i(t)$. It is of interest to compare the traditional AMO index (low-pass

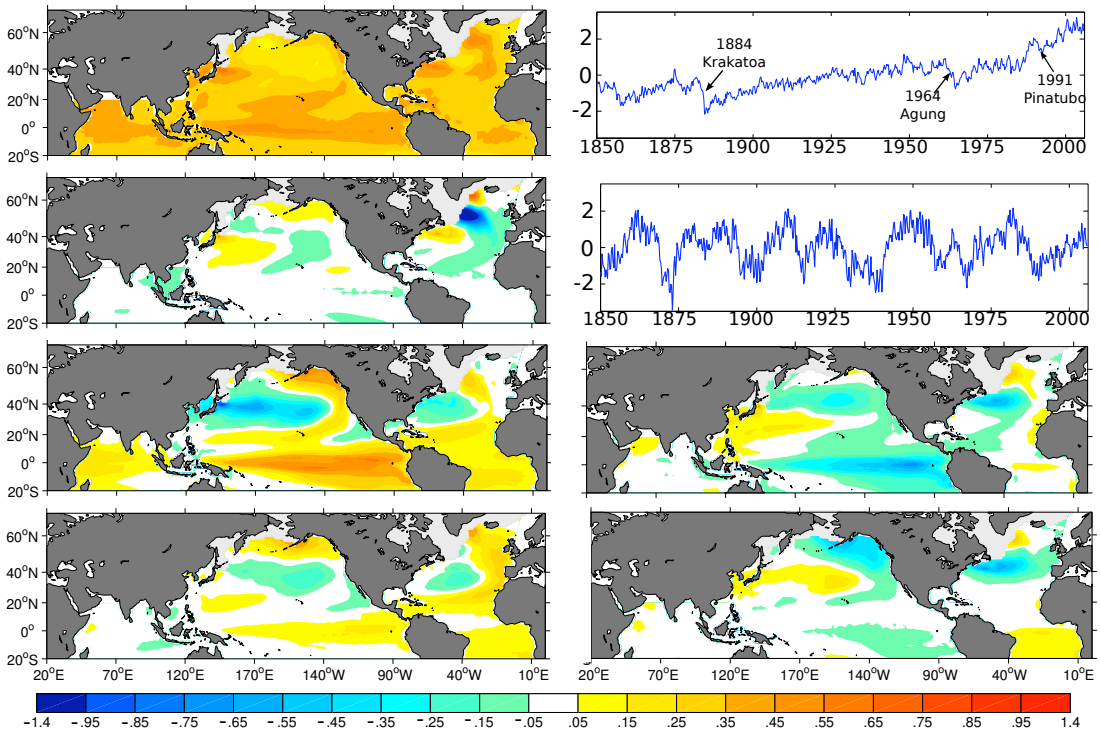

Figure 4.15: Normal modes of the deterministic matrix B number 1 (top), 2 (2nd row), 3/4 (3rd row), and 6/7 (bottom). LIM made from the historical IPSLCM5 simulation.

filtered SST in the grid points space with a cutoff period of 10 yr in the North Atlantic, 0 °-60 °N, 75 °W-7.5 °E, after linear detrending) to AMO-GT. As shown in Fig.4.10, its low-frequency variability is strongly reduced (std = 0.08 °C versus 0.16 °C for the traditional one). The associated SST pattern (Fig.4.11, top right) indicates less warming, except in the North Atlantic where the positive SST anomaly is much larger. In addition, negative anomalies appear in the central North Pacific. The SST anomaly has thus become more similar to the traditional AMO of the IPSLCM5 control simulation (Fig.4.20 1st row of bottom right panel). Whereas correlations were not 5% significant when the AMO lags the AMOC indices , they increase considerably for AMO-GT (Table 4.4) and become significant, reaching 0.37 for AMOC PC1. Note that removing the global mean SST before computing the AMO as in [Trenberth and Shea 2006] improves the correlation with AMOC

PC1 to $r = 0.28$, but it remains not significant. This suggests that the LIM-based filter is a more appropriate way to remove the global warming than linear detrending or removing the global mean.

Model	AMO	AMOC max 30N	AMOC max 10-60N	1st AMOC PC
IPSLCM5 historical	**raw data**	***0.21 (lag10)***	***0.23 (lag10)***	***0.22 (lag12)***
	AMO-GT	0.24 (+16%)	0.35 (+51%)	0.37 (+69%)
	AMO-GT/EN	0.34 (+61%)	0.45 (+94%)	0.51 (+130%)
	AMO-GT/EN/PDO	0.25 (+20%)	0.37 (+61%)	0.45 (+103%)

Table 4.4: Correlation between the various AMO and AMOC indices in the IPSLCM5 historical simulation. The percentages indicate the increase in correlations when using modified AMO indices. Italic indicates that the correlation is not 5% significant.

To remove the ENSO contribution to the AMO, we use the maximum amplification of SST variance in the tropical strip [2]. The optimal initial structure (Fig.4.16 2nd row) shows anomalies of the same sign in the whole area with strong anomalies in the eastern Pacific, North Pacific with a PDO-like pattern, and North Atlantic. The optimal growth (Fig.4.16 bottom) corresponds to a mature ENSO event and occurs 9 mo after the optimal initial structure, as shown by the maximum amplification curve (Fig.4.16 top left). The 1st two modes contributing most to the optimal initial structure are modes 3/4 and 1 (Fig.4.16 top right), and the next one having a period shorter than 8 yr is mode 22/23. These modes are used to filter ENSO and the global trend signal, and their sum has indeed a significant correlation with the raw Niño 1.2 and Niño 3.4 indices (respectively $r = 0.76$ and $r = 0.84$). As shown in Fig.4.10, the ENSO-unrelated AMO, referred to as AMO-GT/EN, computed from $\sum_{i \notin \{1,3/4,22/23\}} \mathbf{u}_i \alpha_i(t)$ is rather similar to AMO-GT ($r = 0.9$), but the associated pattern is somewhat different, with a stronger cooling in the subtropical gyre (Fig.4.11, bottom left). Despite the relative closeness between AMO-GT and AMO-GT/EN, the correlation between AMO-GT/EN and all the AMOC indices

[2] Similar results were obtained by considering the maximum amplification in the tropical Indopacific, the tropical Pacific, or even the whole domain.

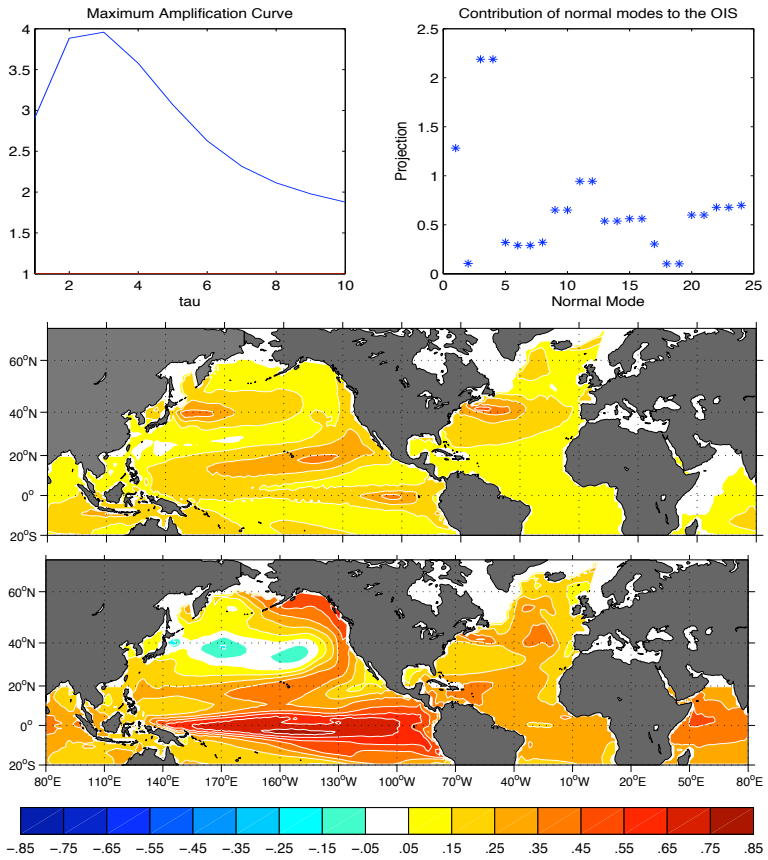

Figure 4.16: Maximum Amplification curve (top left) and projection of normal modes onto the optimal initial structure (top right). Optimal initial structure (middle) leading to maximum amplification (bottom) of SST variance in the tropical strip. LIM made from IPSLCM5 (historical simulation).

strongly increases, reaching $r = 0.51$ for AMOC PC1 (Table 4.4).

Mode 6/7 is a decadal mode with a strong signal in the North Pacific. It is associated to the PDO ($r = 0.33$), but a good representation of the model PDO is only obtained by adding the ENSO mode 3/4 ($r = 0.76$), consistently with [Newman 2007] who showed that the PDO represents not a single phenomenon but rather the superposition of several processes with different time scales. Nonetheless, the usefulness of removing from the AMO the signal linked to the decadal variability of the North Pacific as in [Guan and Nigam 2009] can be tested by removing

this additional mode ($\sum_{i\notin\{1,3/4,6/7,22/23\}} \mathbf{u}_i\alpha_i(t)$). As shown in Table 4.4, AMO-GT/EN/PD leads to substancially smaller correlation with the AMOC indices, as well as changes in the SST pattern, which looses the negative anomalies in the subtropical gyre and has positive anomalies in the South Atlantic (Fig.4.11).

This suggests that LIM is indeed a good filter to eliminate the global change signal, and that the ENSO influence should be removed to extract the part of the AMO that is best related to the AMOC variability. On the other hand, filtering the signal associated with the Pacific decadal variability deteriorates the AMO-AMOC correlations. To assess the robustness of the latter results, we now apply the LIM filter to control simulations of several climate models, where no external forcing needs to be eliminated.

4.4 Control simulations

4.4.1 LIM-based ENSO filter

As previously, the analysis is made in a truncated EOF space, retaining a total of 26 to 36 EOFs, depending on the model (Table 4.1). Note that the first EOFs used to apply LIM in CTRLA are shown in Fig.5.2-5.4 in the next chapter. The temporal characteristics of the main **B** normal modes are listed in Table 4.5. The modes differ between models, but there are also similarities, in particular there is always a multidecadal oscillatory mode showing strong anomalies in the subpolar North Atlantic and a PDO-like pattern in the North Pacific.

Fig.4.17 and Fig.4.18 show some empirical normal modes obtained in HadCM3 and IPSLCM5. The first modes obtained in IPSLCM4 are shown in Fig.5.5 in the next chapter. In both HadCM3 and IPSLCM5, the first mode has a centennial period and shows strong positive anomalies north of 20 °N in the Atlantic, and a PDO-like pattern in the North Pacific. The SST anomalies in the Atlantic are similar to those associated with multidecadal oscillations of the AMOC shown in Fig.4.5, and, as it is discussed in section 4.5 below, the AMOs computed from these modes are strongly correlated with the AMOC. A similar mode with a long period and showing strong anomalies in both Pacific and Atlantic is found in the other control simulations, as more deeply discussed in section 4.5. The other modes that are shown correspond to ENSO-related modes and Pacific decadal modes, and are described below.

As in the historical IPSLCM5 simulation, the maximum amplification in SST variance in the tropical strip is used to identify the ENSO modes. The optimal initial structures leading to maximum amplification show in each model strong SST anomalies around the equator in the eastern Pacific with a maximum generally found between 110 °W and 130 °W (Fig.4.19), while it was along the South American coast in the observations. These structures lead to an optimal growth after 6 to 9 mo, depending on the model, which corresponds in each case to very large

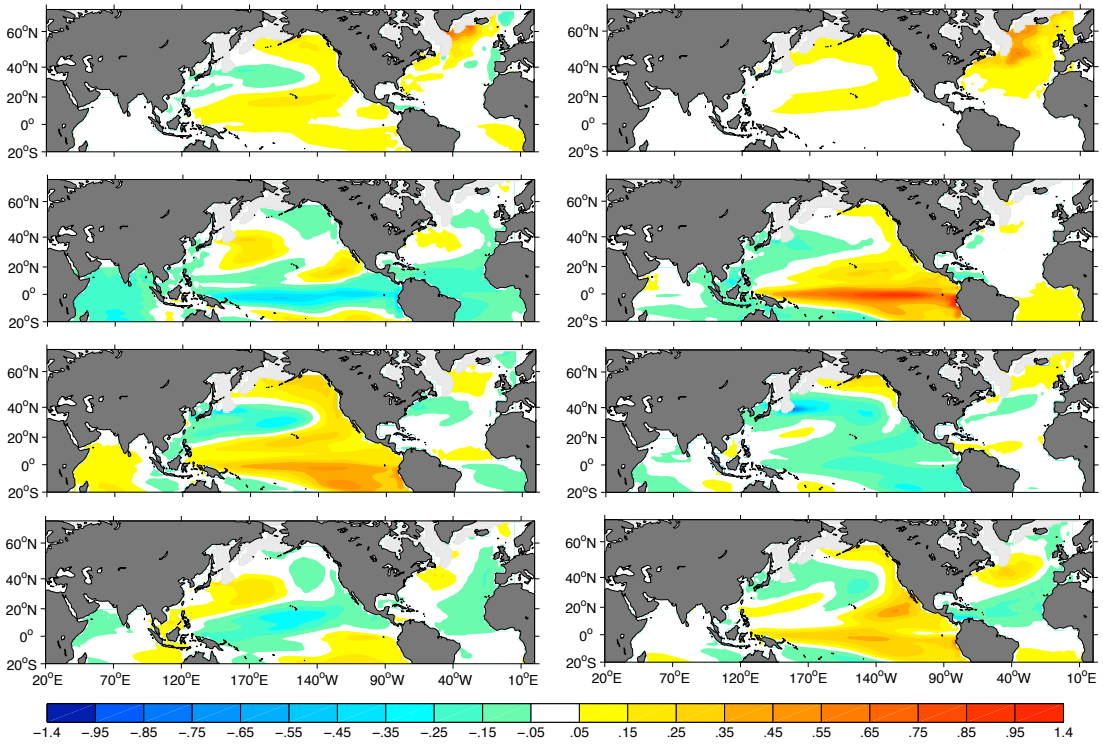

Figure 4.17: Normal modes (in °C) of the deterministic matrix **B**. Mode 1/2 (1st row), 5/6 (2nd row), 7/8 (3rd row), and 14/15 (bottom). LIM made from HadCM3.

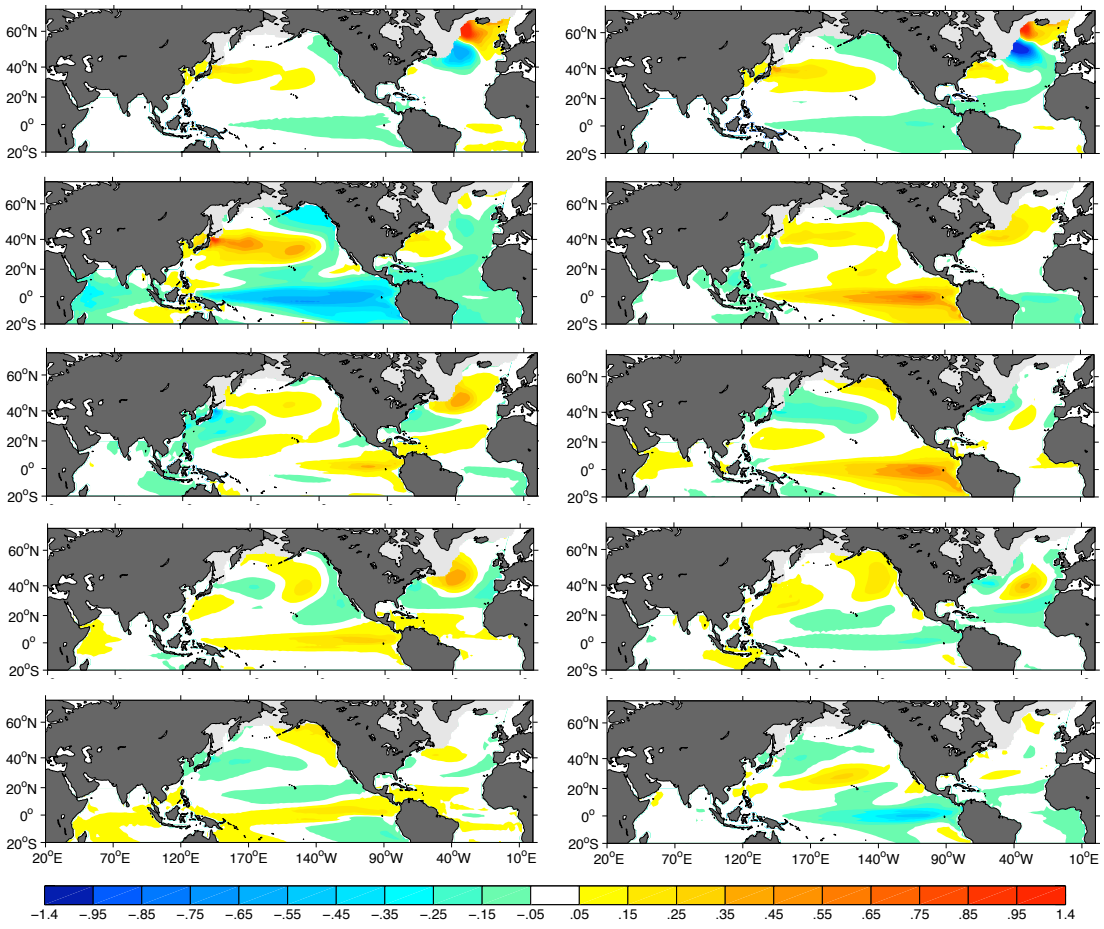

Figure 4.18: Normal modes (in °C) of the deterministic matrix **B**. Mode 1/2 (1st row), 3/4 (2nd row), 12/13 (3rd row), 17/18 (4th row), and 20/21 (bottom). LIM made from IPSLCM5 (control).

IPSLCM4			IPSLCM5 Control			CCSM3		
Mode	DT (mo)	T (yr)	Mode	DT (mo)	T (yr)	Mode	DT (mo)	T (yr)
1/2	**17**	**3**	1/2	16	105	1/2	19	54
3/4	*17*	*32*	**3/4**	**13.6**	**5.3**	*3/4*	*16*	*17.8*
5/6	**13**	**3.1**	5	8.8	∞	**5/6**	**11.8**	**2.3**
7	12	∞	6/7	7.6	34.9	7/8	9.8	10.5
8/9	**10**	**1.8**	8/9	6.1	36.7	9/10	9	50.9
10	10	∞	10/11	5.5	18.8	11/12	7.9	19.9
11	9	∞	**12/13**	**4.9**	**3.6**	**13/14**	**6.9**	**7.1**
12/13	**9**	**7.8**	14/15	4.8	11	**15/16**	**6.7**	**5.2**
14/15	8	10	16	4.5	∞	17	6.4	∞
16/17	7	35.2	**17/18**	**4.5**	**4.7**	18/19	5.2	13
18	6	∞	19	4.1	∞	20/21	4.9	4.7
19/20	5	5.1	**20/21**	**3.9**	**1.8**	22	4.5	∞

HadCM3			MPI-ESM		
Mode	DT (mo)	T (yr)	Mode	DT (mo)	T (yr)
1/2	31.2	102	**1/2**	**48**	**3.4**
3/4	19.2	15.6	*3/4*	*28.8*	*64.4*
5/6	**16.8**	**2.9**	5	22.8	∞
7/8	*13.2*	*36.4*	6/7	18	23.8
9/10	12	9.9	8/9	16.8	10.5
11	10.8	∞	*10/11*	*12*	*33.2*
12/13	10.4	23.3	12/13	12	16.1
14/15	**8.8**	**6**	14/15	10.7	4.1
16	7.9	∞	16/17	10	11
17/18	7.7	2.7	18	10	∞
19/20	6.8	3.4	**19/20**	**7.8**	**1.5**
21/22	6.6	9	21	7.8	∞

Table 4.5: Decay times (DT) and periods (T) of the first **B** eigenmodes for the different control simulations. The ENSO modes are indicated in bold characters, and the Pacific decadal modes in italics.

SST anomalies spanning the tropical Pacific and a horseshoe pattern in the North Pacific, reminiscent of a mature ENSO event.

As before, we consider as ENSO modes those having the largest contribution to the optimal initial structure, a period smaller than 8 yr, and strong anomalies in the tropical Pacific (bold letters in Table 4.5). Their relevance can be verified

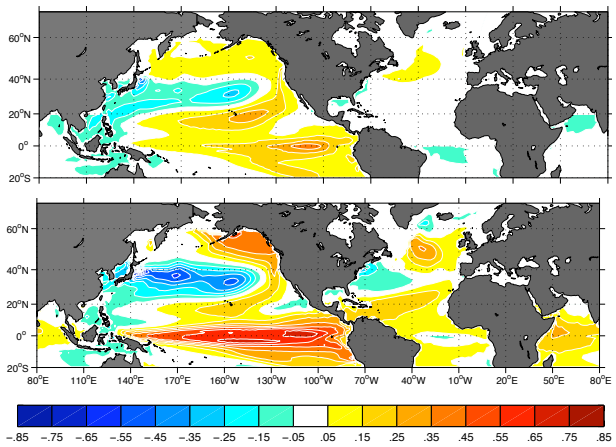

Figure 4.19: Optimal initial structure (top) leading to maximum amplification (bottom) of SST variance in the Tropical Strip. LIM made from IPSLCM5 (control).

by computing Niño 1.2 and Niño 3.4 indices from $\sum_{i\in E} \mathbf{u}_i \alpha_i(t)$. The correlation with the original indices is generally good, ranging between about 0.8 and 0.9, and the associated SST patterns are very similar. The standard deviation of the reconstructed indices is too large, except in MPI-ESM. Adding more oscillatory modes fitting our criteria to the subset E leads to more realistic standard deviation, but more noisy patterns. It was found that using too many ENSO modes actually deteriorates the link between the ENSO-unrelated AMO and the AMOC, which supports our choice of a limited number of ENSO modes in the observations and the historical simulation.

Using $\sum_{i\notin E} \mathbf{u}_i \alpha_i(t)$, ENSO-unrelated SSTs are used to define an AMO-EN index in the different simulations. The standard deviation of AMO-EN is only slightly smaller than that of traditional AMO and the correlation between the two indices is very high in HadCM3 and MPI-ESM ($r = 0.98$) and high in CCSM3 ($r = 0.93$). On the other hand, the ENSO removal has a strong impact in IPSLCM4 ($r = 0.79$) and IPSLCM5 ($r = 0.85$). Although the associated SSTs remain similar in the northern North Atlantic, some differences are noticed, as illustrated in Fig.4.20 (2nd row for each model). For instance, the almost interhemispheric pattern in the

Atlantic is reinforced in IPSLCM5 and HadCM3 as the negative anomalies in the South Atlantic are stronger and more significant. There are also significant changes in the Pacific, in particular for HadCM3 and IPSLCM5. It can be shown that the warming of the eastern equatorial Pacific seen in IPSLCM5 tends to lag the AMO by up to 5 yr, which suggests that the AMO (or the AMOC) has a significant impact on SST in the tropical Pacific. However, this warming is not seen in the historical IPSLCM5 simulation (Fig.4.11 lower left), where the equatorial Pacific is slightly but not significantly colder than average. Whether the difference reflects a change in regime or statistical incertainties is not known. On the other hand, in the Atlantic basin, the signature of the AMO is very similar in the control and, at large lag, in the historical simulation, and the SST evolution when it lags the AMOC are nearly indistinguishable after ENSO and global trend removal (not shown), reflecting the efficiency of the LIM filter.

Model	AMO	AMOC max 30N	AMOC max 10-60N	1st AMOC PC
IPSLCM4	**raw data**	**0.41 (lag6)**	**0.39 (lag7)**	**0.36 (lag6)**
	AMO-EN	0.43 (+5%)	0.43 (+10%)	0%
	AMO-EN/PDO	0.39 (-5%)	0.45 (+15%)	0.34 (-6%)
IPSLCM5 Control	**raw data**	**0.34 (lag8)**	**0.40 (lag8)**	**0.40 (lag9)**
	AMO-EN	0.39 (+14%)	0.42 (+5%)	0.43 (+7%)
CCSM3	**raw data**	**0.59 (lag3)**	**0.59 (lag3)**	**0.73 (lag3)**
	AMO-EN	0.58 (-2%)	0%	0.72 (-2%)
	AMO-EN/PDO	0.55 (-7%)	0.56 (-5%)	0.67 (-8%)
HadCM3	**raw data**	**0.50 (lag2)**	**0.62 (lag2)**	**0.60 (lag3)**
	AMO-EN	0%	0.63 (+2%)	0.61 (+2%)
	AMO-EN/PDO	0.39 (-22%)	0.52 (-16%)	0.46 (-24%)
MPI-ESM	**raw data**	**0.37 (lag2)**	**0.37 (lag2)**	**0.20 (lag4)**
	AMO-EN	0.41 (+10%)	0.41 (+10%)	0.23 (+13%)
	AMO-EN/PDO	0.39 (+6%)	0.39 (+6%)	0.21 (+5%)

Table 4.6: Correlation between the various AMO and AMOC indices in the different model simulations. The percentages indicate the increase in correlations when using modified AMO indices. Italic indicates that the correlation is not 5% significant.

As shown in Table 4.6, the impact of ENSO removal onto the AMO-AMOC

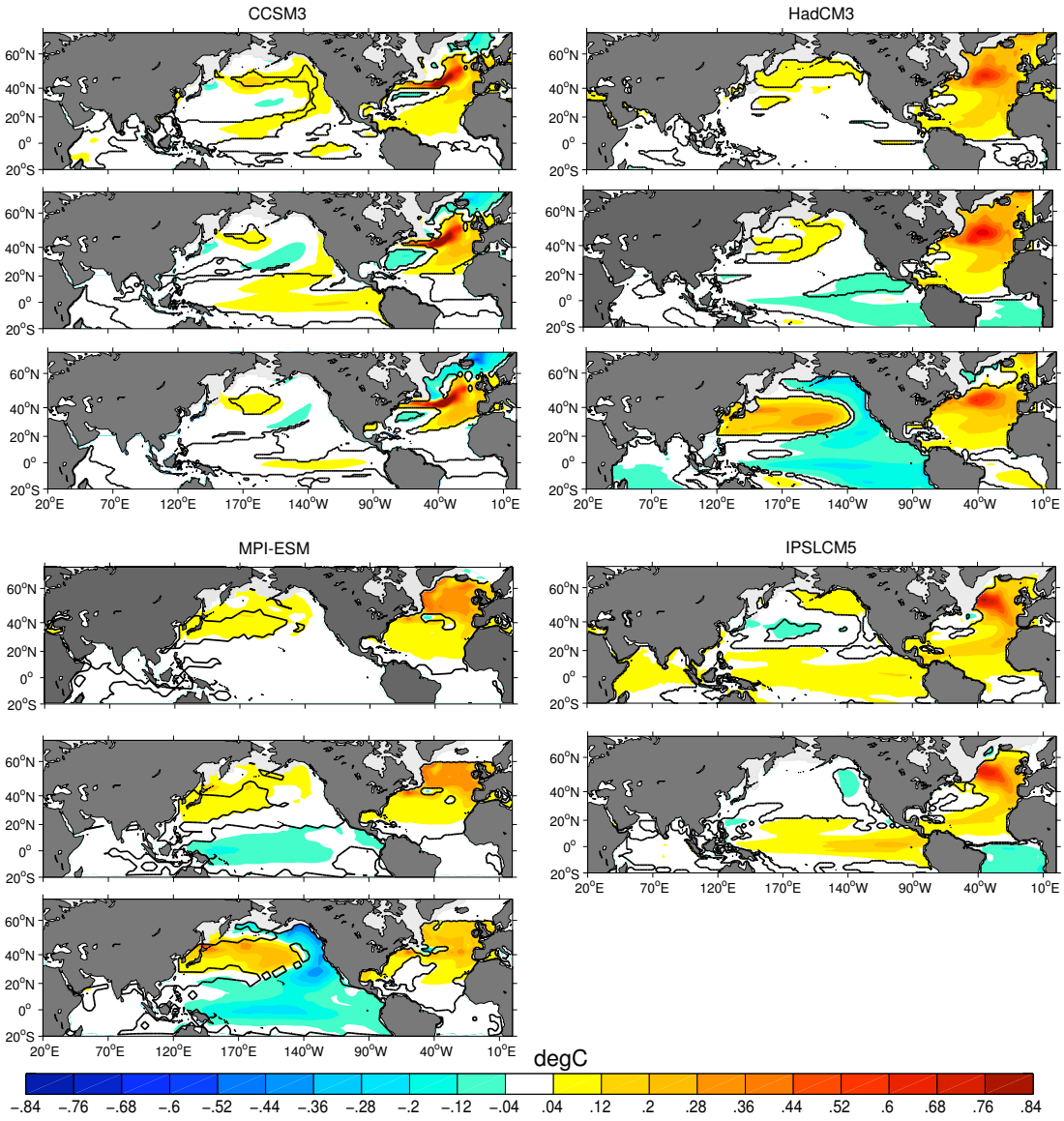

Figure 4.20: SST pattern (in °C) associated with the traditional AMO (1st row), the AMO-EN (2nd row), and the AMO-EN/PD (3rd row) in CCSM3 (top left), HadCM3 (top right), MPI-ESM (bottom left), and IPSLCM5 (bottom right). The black contour indicates 5% significance.

correlations is rather weak and depends on the model. It increases the correlations by about 10% in IPSLCM4, IPSLCM5, and MPI-ESM, while the correlations are almost unaffected for HadCM3 and CCSM3. However, LIM is more successful at

enhancing the AMO-AMOC correlations than when a linear regression is used to removed the ENSO, as discussed in the next section (section 4.4.2). To understand why the ENSO removal does not improve the correlation between the AMOC and the AMO in the last two models, it is of interest to consider the links between the tropical Pacific and the Atlantic sector.

The ENSO first affects the Atlantic sector through the "atmospheric bridge" ([Alexander et al. 2002], [Klein et al. 1999]), corresponding to changes in the atmospheric circulation acting on surface fluxes. More precisely, a weakening of trade winds in the tropical North Atlantic is observed during ENSO, leading to a decrease of surface evaporation and a subsequent warming in about 3 to 6 months ([Klein et al. 1999]). Several mechanisms may explain the reduced trade winds, involving negative SLP anomalies located over the south-east United States that are associated with changes in the Pacific-North American (PNA) pattern ([Wallace and Gutzler 1981]), and the reduction in the strength of the Atlantic Hadley cell that results from the modification of the Walker circulation by the shift in the tropical Pacific convection. In addition, [Chiang and Lintner 2005] and [Chiang and Sobel 2002] showed that ENSO may affect the whole Tropics through the "tropospheric temperature mechanism". The heat released by ENSO from the ocean to the atmosphere leads to a tropospheric warming, that is propagated to the remote Tropics by Kelvin waves forced by the anomalous convection in the tropical Pacific, leading to a remote tropical ocean warming 2 to 3 months after the peak of ENSO .

Consistently with the above studies, a significant correlation ($r \sim 0.4$) is found in the observations between the 1st PC of yearly SST in the tropical Pacific and SST anomalies in the tropical North Atlantic between 10 and 25 $^\circ$N (Fig.4.21 top left). In the North Atlantic sector, the associated SLP is a broad low centered around 50 $^\circ$N, 25 $^\circ$W, extending up to the south-east United States. Note that, the PNA pattern is not apparent with yearly data (not shown). As shown in the other panels of Fig.4.21, in all control simulations but CCSM3, this correlation is

stronger (∼0.55). However, the maximum correlation is not found in the same area (between 0 and 30 ° N in IPSLCM5 and IPSLCM4, between 30 ° S and 20 ° N in MPI-ESM, and between 30 ° S and 10 ° N in HadCM3). This warming may be in part due to the negative SLP anomalies observed in almost all models but MPI-ESM south-east of the United States. A low is observed in the North Pacific that resembles the Aleutian low but shifted southward in all models (and southeastward in CCSM3) and evokes the PNA pattern, although too strong anomalies are observed in the North Atlantic especially in the IPSL models and MPI. The high meridional pressure gradient centered around 40-50 ° N in the Atlantic may weaken the Westerlies, reducing the heat fluxes and thus leading to the warming observed in midlatitudes. In MPI-ESM, ENSO imprint on SST is also found at midlatitudes, but it cannot be explained by the anomalous SLP, which are much stronger and very different from the other models and from the observations. In HadCM3, although the correlations between ENSO and the tropical Atlantic are strong, they are more equatorially confined than in IPSL simulations or in MPI-ESM. In addition, there is less ENSO imprint at midlatitude. This might explain the much smaller increase in AMO-AMOC correlations when the ENSO is removed in this model. In CCSM3, the SST, wind stress, precipitation, and thermocline depth reponses to ENSO are too narrowly confined to the equator in the Pacific ([Deser et al. 2006]), and the correlations between SSTs and ENSO (Fig.4.21 top middle) are much smaller in the tropical North Atlantic than in the other models. This may explain why the correlations between AMO and AMOC are not improved in this model when the ENSO signal is removed.

Although Fig.4.21 might suggest that removing ENSO with LIM in the observations would increase the AMO-AMOC correlations, but not as much as in the IPSL models or in MPI-ESM, the interpretation of this figure requires more caution, since connections between the Atlantic and ENSO are not stationary in the observations ([Sutton and Hodson 2003], [Greatbatch et al. 2004]). Besides, discussing the impact of ENSO onto the Atlantic using regressions may be inadequate

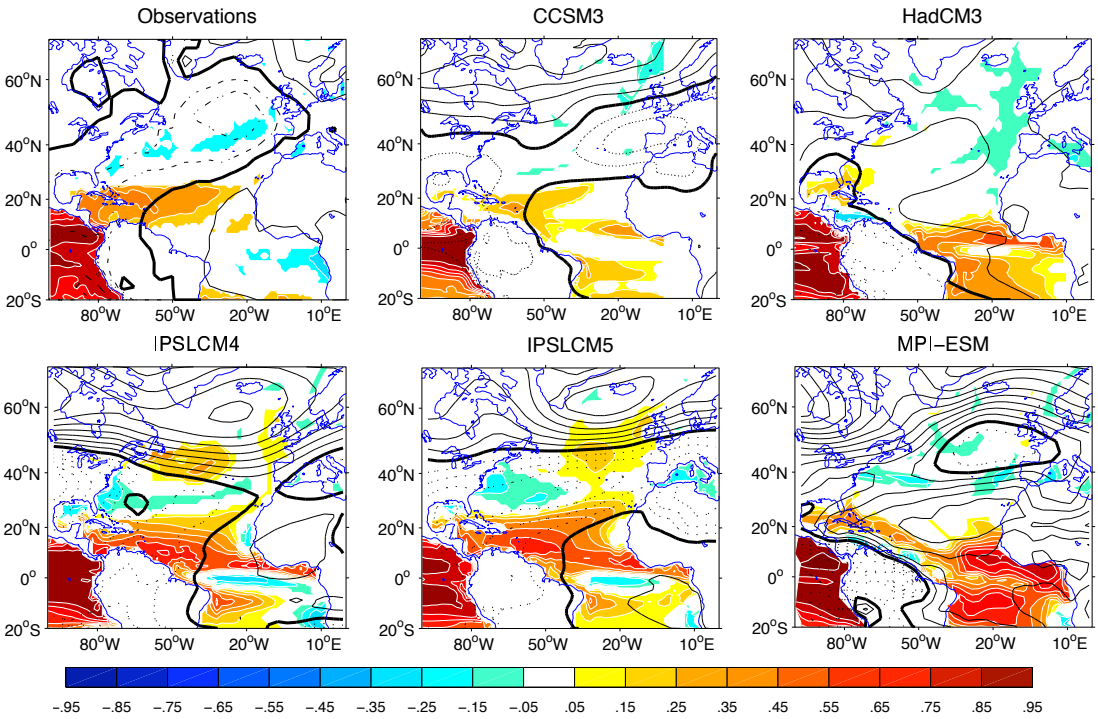

Figure 4.21: Correlation between annual SST (colors) anomalies and the first PC of annual SST anomalies in the Tropical Pacific, and regression of SLP (contours) anomalies onto the latter. Results are shown only for significant correlations at the 10% level. Contour interval is 0.1 hPa, dashed lines correspond to negative values. Top left : observations, Top middle : CCSM3, Top right : HadCM3, Bottom left : IPSLCM4, Bottom middle : IPSLCM5 (control), Bottom left : MPI-ESM.

([Penland and Matrosova 2006], [Compo and Sardeshmukh 2010]).

4.4.2 Removing ENSO by regression

A common procedure to remove ENSO effects is to use a linear regression on one or several ENSO indices. For comparison with the LIM approach, we assume that the ENSO signal is well characterized by the first two EOFs and PCs of the yearly SST anomalies in the tropical Pacific between 20°S and 20°N, and compute a new AMO index. Compared to the traditional AMO, its correlations with the AMOC indices increases in the control simulations by 7 to 14% in IPSLCM4, depending on the

AMOC index, 0 to 5% in MPI-ESM, while it decreases by 3 to 5% in IPSLCM5, 0 to 2% in HadCM3 and by 2 to 5% in CCSM3. A comparison with Table 4.6 shows that, except in IPSLCM4 , removing the ENSO signature from the AMO by regression analysis is much less successful than by LIM at extracting the part of the AMO that is related to the AMOC variability. This agrees with [Penland and Matrosova 2006] and [Compo and Sardeshmukh 2010], who argued that the ENSO signal must be removed using a dynamical filter such as the LIM and not by regression.

4.4.3 Should we remove the link with the decadal variability in the Pacific?

In the historical IPSLCM5 simulation, filtering the signal linked to the North Pacific decadal variability from the AMO degraded the relation to the AMOC. To investigate whether removing the decadal Pacific-linked signal from the AMO similarly degrades its relation to the AMOC in the control simulations, we attempted to identify PDO-like normal modes with low frequency variability in the models. The decadal Pacific modes P are indicated in Table 4.5 in italic letters. Using $\sum_{i\in P} \mathbf{u}_i\alpha_i(t)$, a PDO index was computed for the different models. It correlates with the raw PDO at $r = 0.54$ in IPSLCM4, $r = 0.81$ in CCSM3, and $r = 0.6$ in HadCM3. To significantly reconstruct the PDO in MPI-ESM ($r = 0.6$), the ENSO mode 1/2 was also taken into account. In IPSLCM5, the only mode leading to a reasonable reconstruction of the PDO signal is mode 3/4 ($r = 0.6$), which has a 5.3 yr period and was selected as an ENSO mode, and there was no other decadal mode with a strong signal in the Pacific, as it was the case in the historical simulation. The decadal Pacific modes in the control runs have strong anomalies in the North Atlantic, but it is only in IPSLCM4 that the mode is significantly related to the AMO ($r = 0.62$). The impact on the AMO of removing the decadal teleconnections with the Pacific is illustrated for 3 models in Fig.4.20 (3rd row of the different panels). In CCSM3 and HadCM3, significant negative SST anomalies are now found south of Greenland, while the subpolar warming decreases in HadCM3

and MPI-ESM. Note also the appearance of a strong PDO-like signal in HadCM3, as in the observations (Fig.4.27).

Except for IPSLCM5, the decadal Pacific modes were added to the subset E of ENSO modes and a filtered AMO was computed, referred to as AMO-EN/PD. As shown in Table 4.6, the correlations with the AMOC indices are degraded in nearly all cases, most strongly so in HadCM3. Hence, the control simulations confirm that a Pacific decadal signal should not be substracted from the AMO if its relation to the AMOC is to be optimized.

Since removing the signal linked to decadal Pacific changes clearly degrades the relation between the AMO and the AMOC, the links between the two basins should reflect a dynamical coupling, or more likely a common forcing of the two basins. Evidence for the latter was given by [Müller et al. 2008], who showed that there was a significant coherence in the observations at periods between 10 and 20 yr between the North Atlantic Oscillation (NAO), ENSO, the Aleutian low, and the PDO, suggesting global teleconnections. As the NAO is a main driver of the AMOC, removing such teleconnections from the AMO would indeed degrades its relation to the AMOC. As shown in Fig.4.22, the low-pass filtered (T_c = 5 yr) PDO is associated with the Aleutian low in each model, as in the observations (e.g. [Schneider and Cornuelle 2005]). However, there is always an Arctic high that is not seen in the observations. In the Atlantic, a pattern resembling a negative phase of the NAO is observed for all models but MPI-ESM and HadCM3. In the latter, such a pattern is associated to the yearly PDO (not shown), probably reflecting a different time scale than other models. In the observations, negative SLP anomalies centered around 45 $^\circ$ N, 30 $^\circ$ W are associated with the low-pass filtered PDO in the Atlantic, similarly to the negative pole of a negative NAO phase, but the positive pole is centered over northern Europe instead of southeast of Greenland.

Further investigations are needed to understand if this interbasin connection arises from the North Pacific, from the North Atlantic, or simply results from an hemispheric mode of atmospheric circulation. [Orgeville and Peltier 2007] found

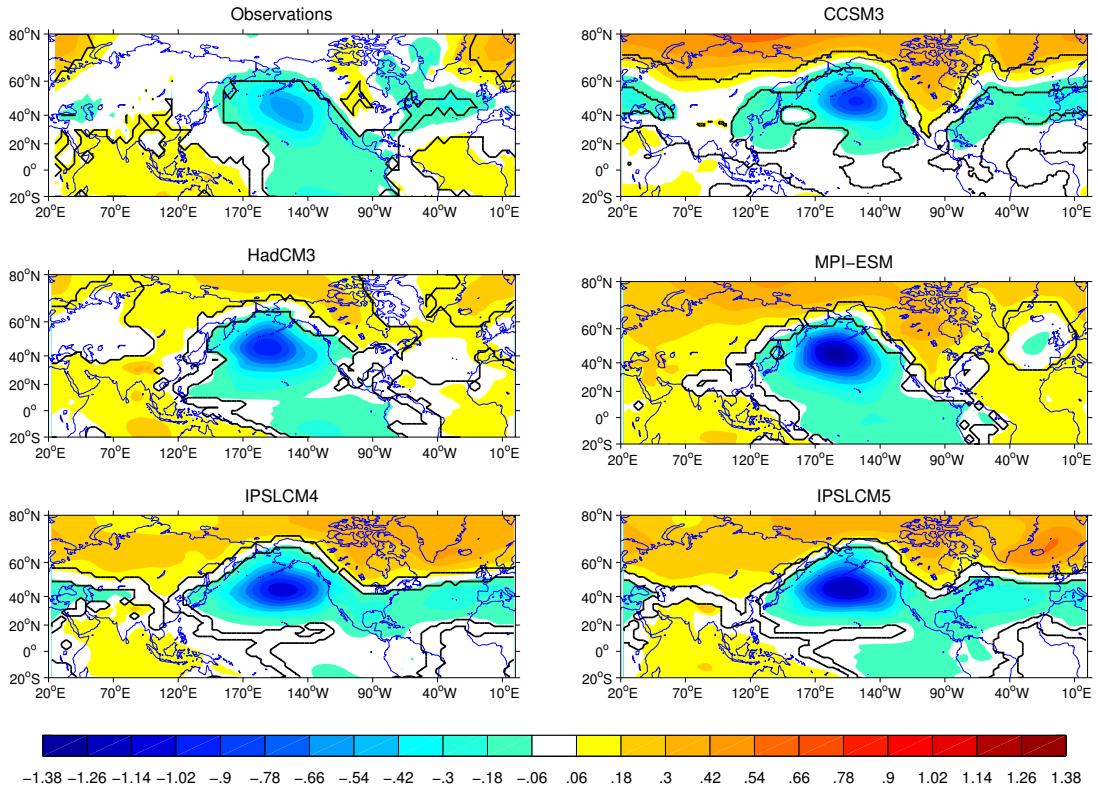

Figure 4.22: regression of low-pass filtered ($T_c = 5$ yr) SLP (in hPa) anomalies onto the low-pass filtered PDO. The black contour indicates 10% significance. Top left : observations, Top right : CCSM3, Middle left : HadCM3, Middle right : MPI-ESM, Bottom left : IPSLCM4, Bottom right : IPSLCM5 (control).

in the observations a strong correlation between the AMO and the low-frequency component ($\sim$ 60 yr) of the PDO when the AMO leads by 13 yr, but also when the PDO leads by 13 yr. They argued that these signals were the 2 components in phase quadrature of a unique oscillation cycle, and give two possible explanations. The first one states that the Atlantic and Pacific basins collectively produce variability at a 60 yr time scale, with teleconnections acting in both directions. In the second explanation, the AMO plays the dominant role: being forced by the multidecadal fluctuations of the AMOC, it impacts the global northern hemisphere atmospheric circulation, leading to an oceanic adjustement in the North Pacific, as discussed by

[Zhang and Delworth 2007]. Indeed, based on observations, the latter also found a lagged response to the AMO of the component of the PDO, which is independent of ENSO and associated to multidecadal fluctuations. They used a hybrid coupled model to demonstrate that the AMO leads to a weakening of the mid-latitude winter storm track, shifting poleward the westerly winds. This results in a reduced Aleutian low, associated to a negative wind stress curl anomaly that shifts northward the Kuroshio current, leading to warm SST anomalies in the central and western North Pacific, especially in the Kuroshio-Oyashio extension (KOE) region. These warm SST anomalies in the KOE region further weaken the Aleutian low, resulting in a positive air-sea feedback. In this study, only the Atlantic was found to impact the Pacific, however [Li et al. 2009] showed that the North Pacific and the North Atlantic interactions were intimately coupled through an inter-basin atmospheric teleconnection dominated by the leading mode of extratropical atmospheric variability (AO for Arctic Oscillation). This study was based on a climate model with an idealized oceanic temperature anomaly initiated over the Gulf Stream and the Kuroshio extension regions.

As shown in Fig.4.23, we also find lead-lag correlations between the AMO and the PDO in the observations, consistently with [Orgeville and Peltier 2007]. However, similar correlations are not seen in the control simulations and no common behavior is found among models. This does not help understanding the origin of the link between a NAO-like pattern and the PDO at low-frequency shown in Fig.4.22 and found in all control simulations. However, this emphasizes that the times scales and mechanisms involved in the interconnection between the Pacific decadal variability, the AMO and the AMOC is likely to be model-dependent.

4.5 Further deconstructing the AMO?

Our LIM deconstruction of the AMO increases its correlation with the AMOC when the ENSO signal is removed. However, it could be optimized further. Indeed, it

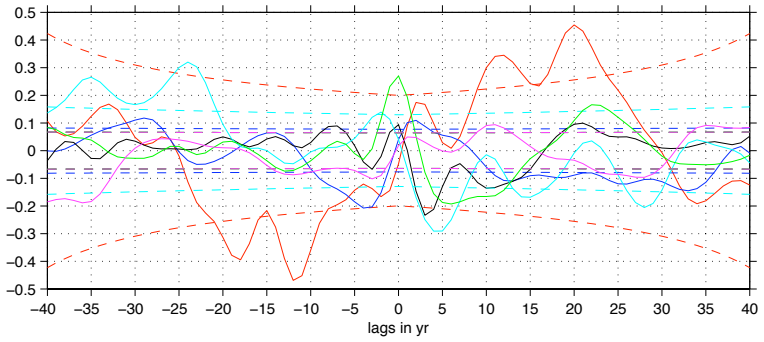

Figure 4.23: Correlation between low-pass filtered (T_c = 5 yr) PDO and AMO indices in the observations (red curve), in HadCM3 (blue), in CCSM3 (cyan), in IPSLCM4 (black), in IPSLCM5 (green), and in MPI-ESM (magenta). Dashed lines indicate 5% significance.

was found in some models that a single normal mode was better correlated with the AMOC than AMO-GT/EN. In the historical IPSLCM5 simulation, the second mode was a damped mode, but it showed strong oscillations with a spectral peak around 80 yr. The AMO based on this mode turned out to be highly correlated to the AMOC, reaching $r = 0.6$ when the AMOC leads by 9 yr, which is larger than when the AMO was computed after removing the global trend signal and the ENSO modes. The regression of low-pass filtered SST onto this AMO index is shown in Fig.4.24. The SST maximum in the North Atlantic reaches 4 $^\circ$ C and is much larger than for the traditional AMO and the other AMOs obtained with LIM.

In HadCM3 and IPSLCM5 control simulations, the 1st mode was oscillatory with a period of about 100 yr and it showed large SST anomalies in the North Atlantic (Fig.4.17 and 4.18). Again, the AMO derived from it is better correlated with the AMOC than AMO-EN, the increase in correlation compared to the traditional AMO reaching 46% in IPSLCM5, and of 16% in HadCM3. The latter result is consistent with [Vellinga and Wu 2004], who found that the strong centennial fluctuations of the AMOC in HadCM3 impacted the surface climate.

A mode with a multidecadal period, and strong anomalies in both the North

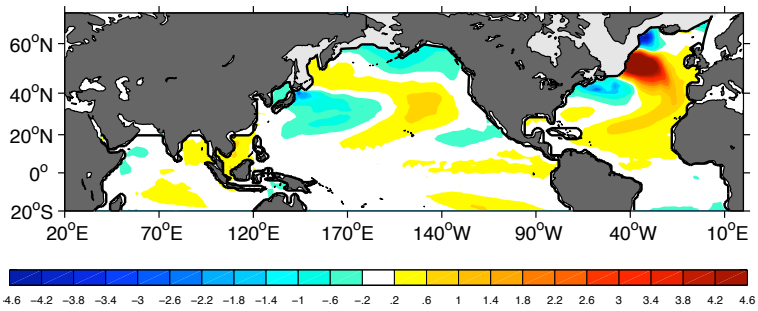

Figure 4.24: Regression of low-pass filtered SST (in °C) anomalies onto the AMO index computed from $\sum_{i=2} \mathbf{u}_i \alpha_i(t)$

Atlantic and North Pacific, is also found in the other control simulations (mode 3/4 in IPSLCM4, 1/2 in CCSM3, and 3/4 in MPI-ESM). However the AMOs computed from these modes do not improve the correlations with the AMOC indices (and slightly degrade it), except for the correlation with the AMOC maximum between 10 and 60 °N in IPSLCM4, which is increased by 21% compared to the traditional AMO.

This also emphasizes that other signals than the global trend and ENSO have to be removed from the AMO to optimize its correlation with the AMOC. The local atmospheric forcing mostly generates the seasonal and interannual SST variations, but because of SST re-emergence and other dynamical processes it may also affect the lower frequencies. In principle, removing the local SST response might be attempted using LIM, since the local atmospheric forcing should enter the white noise forcing $\mathbf{F}$ in eq.(3.2). However, as the latter is dominated by the NAO and the East Atlantic Pattern, which are also important driver of the AMOC (e.g. [Eden and Willebrand 2001] 2001, [Deshayes and Frankignoul 2008] 2008, [Msadek and Frankignoul 2009] 2009), removing the local SST response without altering the AMOC-driven one may be difficult.

4.6 The AMO in the observations

Although our LIM deconstruction could be further improved to find the best proxy of the AMOC variability, we apply it to the observations. Based on previous results, we expect that removing the global trend and the ENSO from the AMO using LIM would increase its correlation with the AMOC, while removing a signal of Pacific decadal variability would degrade it.

For the observed SST, the dimension of $\mathbf{x}$ is 23 (Table 4.1). As was also the case for each model simulation, the matrix $\mathbf{B}$ could only be determined at a lag of one season, probably because of the Nyquist problem at larger lags [3]. The $\mathbf{B}$ eigenmodes are listed in Table 4.7 in order of decreasing decay time, and the first 8 patterns are shown in Fig.4.25.

Mode	Decay time DT	Period T
1	4.3yr	∞
2/3	*1.6yr*	*47.7yr*
4	1.1yr	∞
5/6	**10mo**	**7.2yr**
7/8	**7mo**	**3.1yr**
9/10	6mo	13.1yr
11	6mo	∞
12/13	5mo	4.7yr
14/15	4mo	14.4yr
16/17	4mo	3.4yr
18	3mo	∞
19/20	3mo	3.1yr
21	3mo	∞
22/23	3mo	7.9yr

Table 4.7: Decay time and period of the main eigenmodes of $\mathbf{B}$ in observed SST. The ENSO modes are indicated in bold characters, and the Pacific decadal modes in italics.

As was the case in the historical IPSLCM5 simulation, the 1st mode is damped and corresponds to a global warming ($r = 0.95$ with the global SST average), but its amplitude is much smaller and its decay time more than halved, suggesting

[3] If 3-mo running mean anomalies had been used, lags from 1 to 4 mo could be used

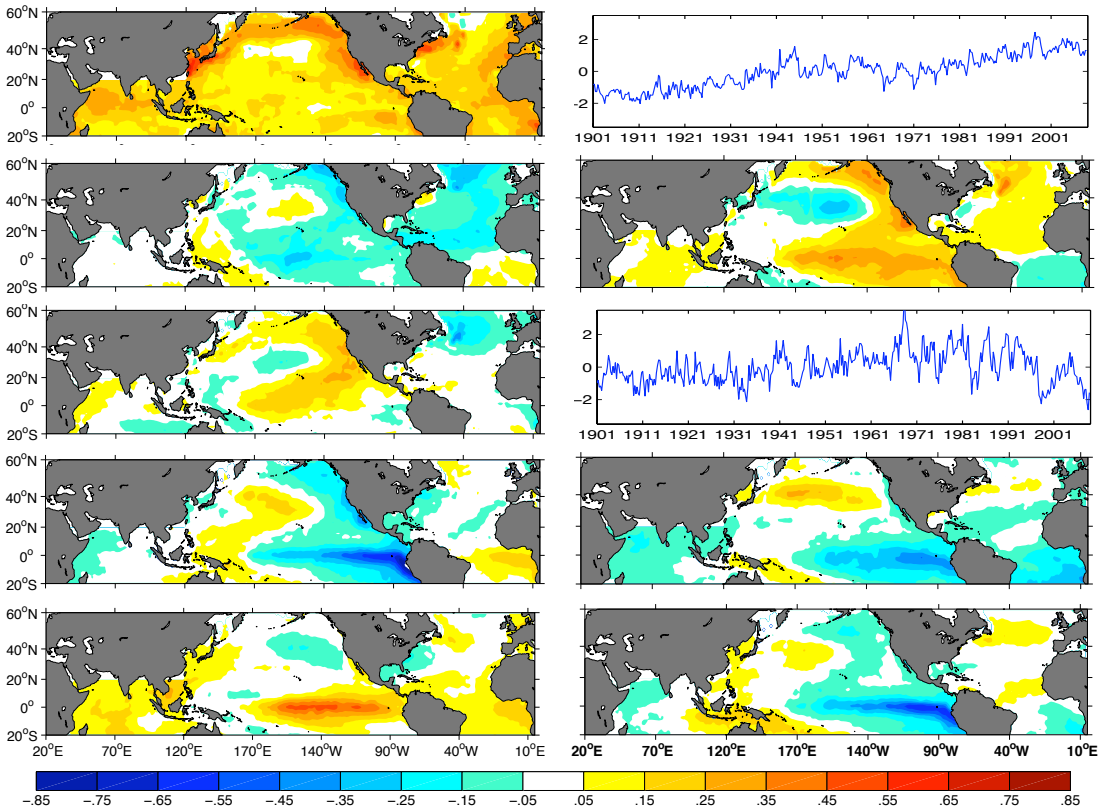

Figure 4.25: Normal modes (in °C) of the deterministic matrix **B**. Mode 1 with its time series (top), 2/3 (2nd row), 4 with its time series (3rd row), 5/6 (4th row), and 7/8 (bottom). LIM made from observed SST.

that the IPSLCM5 model overestimates the response to external and anthropogenic forcing. Note that the warming is weaker in the North Pacific and in the northern North Atlantic (Fig.4.25 top left), similarly to the forced component of the surface temperature variance estimated from six IPCC AR4 models by [Ting et al. 2009] (Fig.1.17). Note also that the time series of this mode shows a small cooling after 1963 and after 1991, which might be linked to the volcanic eruptions of Mount Agung and Pinatubo. It is of interest to compare the traditional AMO index to "the filtered" AMO computed using $\sum_{i\neq 1} \mathbf{u}_i \alpha_i(t)$, then applying the low-pass filter, and referred to as AMO-GT. As shown in Fig.4.26, there are significant differences, although the warm and cold phases are identical and the correlation is high ($r =$

0.91). The standard deviation of AMO-GT is smaller than that of the traditional AMO (0.11 ° C versus 0.14 ° C), and the recent warming is less pronounced. The period estimated from zero-crossings of the autocorrelation function is ∼ 48 yr versus ∼ 60 yr for the traditional AMO. The associated SST patterns obtained by regression are similar, but AMO-GT has a small area of negative anomalies south of Newfoundland, and weaker anomalies in the subtropical gyre (Fig.4.27 top panels). The revised AMO index of [Trenberth and Shea 2006], where external forcings were removed by substracting the global SST mean, also had a smaller range than the traditional index and lower anomalies in the subtropical gyre. The recent warming in the 20th century was even less pronounced (less than 0.1 ° C versus 0.15 ° C for AMO-GT).

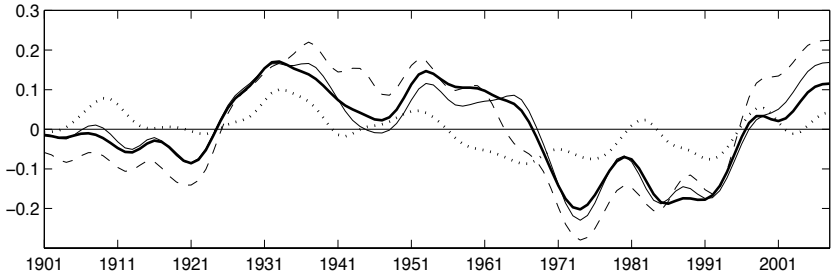

Figure 4.26: Time series in ° C of the traditional AMO (dashed line), the AMO-GT (continuous line), the AMO-GT/EN (thick line), and the AMO-GT/EN/PD (dotted). LIM made from observed SST.

As for climate models, the ENSO modes were estimated from the maximum amplifications of SST variance in the tropical strip, which occurs after 9 mo. The optimal initial structure and that of maximum amplification (Fig.4.28) have smaller positive anomalies than in the the historical IPSLCM5 simulation, consistently with the stronger model response to external forcing. The optimal growth structure shows a developped El Niño phenomenon with a tongue of positive anomalies in the eastern Pacific and local maxima around the equator at 115 ° W and 160 ° W, anomalies of opposite sign in the western tropical Pacific, and positive anomalies

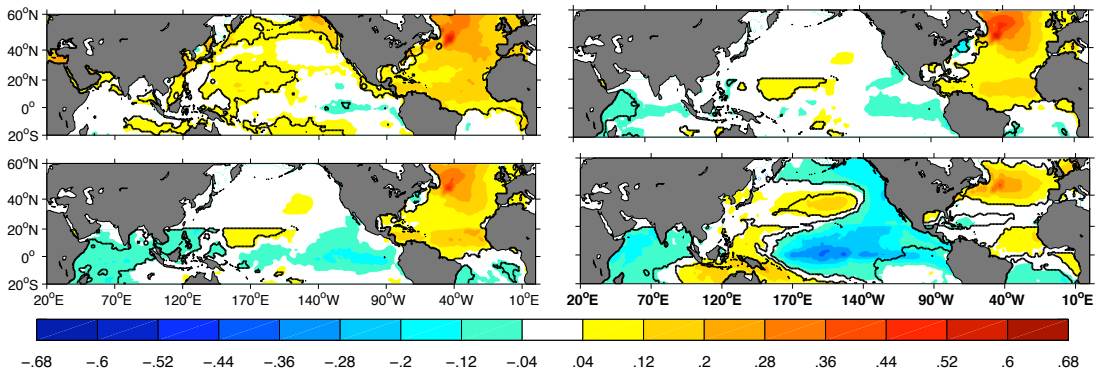

Figure 4.27: SST pattern (in °C) associated with the AMO time series in Fig.4.26. Top left : traditional AMO, Top right : AMO-GT, Bottom left : AMO-GT/EN, Bottom right : AMO-GT/EN/PD. LIM made from observed SST. The black contour indicates 5% significance.

in the Indian ocean and the tropical Atlantic, combined with a warm phase of the PDO. Considering only the tropical strip, [Penland and Matrosova 2006] obtained very similar structures, except that there was a longitudinal dipole in the tropical Atlantic at the maximum amplification. However, note that the North Pacific part of the initial structure also resembles the PDO. Modes 7/8, 1, 5/6, and 2/3 strongly contribute to the optimal initial structure (Fig.4.28 top right), and they all have prominent anomalies in the Tropical Pacific. However, only two of them qualify as ENSO modes, as shown by Table 4.7. The oscillatory mode 7/8 ($T = 3.1$ yr) has a cosinus phase showing strong anomalies along the western coast of South America and evoking the Niño 1.2 pattern, and a sinus phase resembling a mature Niño event (Fig.4.25). The oscillatory mode 5/6 ($T = 7.2$ yr) is similar, but for stronger anomalies in the North Pacific. As discussed above, mode 1 represents the global SST changes. It strongly contributes to the optimal initial structure and the optimal growth structure, since the data were not detrended before computing the maximum amplification. Mode 2/3 has a too large period ($T = 47.7$ yr) to correspond to ENSO and it resembles the PDO pattern in the North Pacific. The

correlation between the raw PDO and the one computed with $\sum_{i\in\{2/3\}} \mathbf{u}_i\alpha_i(t)$ is indeed significant ($r = 0.52$), and they have similar spectra at low frequencies.

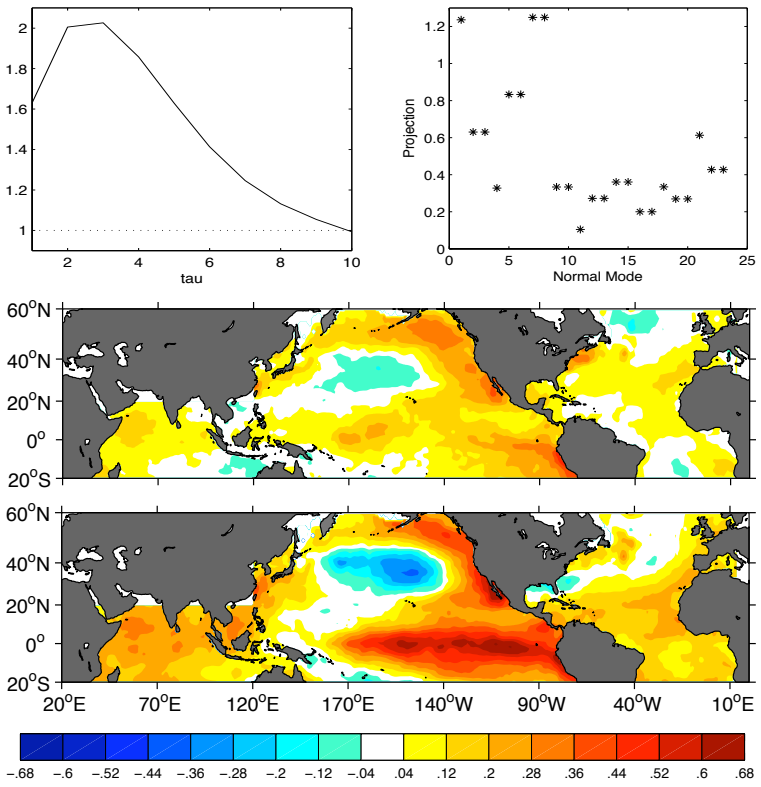

Figure 4.28: Maximum Amplification curve (top left) and projection of normal modes onto the optimal initial structure (top right). Optimal initial structure (middle) leading to maximum amplification (bottom) of SST variance in the tropical strip. LIM made from observed SST.

The SST field reconstructed using $\sum_{i\in E} \mathbf{u}_i\alpha_i(t)$ with $E = \{1, 5/6, 7/8\}$ is expected to contain much of the ENSO signal and the global trend, and the reconstructed ENSO indices indeed correlate well with the original ones ($r = 0.78$ for Niño 3.4 and $r = 0.85$ for Niño 1.2). The associated spatial patterns are very similar to those obtained from the raw data (spatial correlation $r_s = 0.92$ for Niño 3.4 and $r_s = 0.91$ for Niño 1.2). However, the amplitude of the two reconstructed indices is too high (standard deviation $std = 1.85\ ^\circ$ C versus $0.72\ ^\circ$ C for Niño 3.4 and $2.18\ ^\circ$ C

versus 0.8 °C for Niño 1.2). Adding the decadal Pacific mode (mode 2/3) increases the correlation with the Niño 3.4 index ($r = 0.83$) but only slightly decreases the amplitude of the ENSO indices ($std = 1.56$ °C for Niño 3.4 and $std = 1.74$ °C for Niño 1.2). Comparable amplitudes are only obtained by adding higher modes, but the latter are noisy outside the tropical Pacific and were not retained, consistent with the model results discussed in section 4.4. Note that the comparison between the raw and the reconstructed ENSO indices is of limited interest to quantify LIM success at modeling the ENSO, since linear regression on these indices work poorly to remove the ENSO impact onto the AMO (see section 4.4.2).

After substraction of the global and ENSO modes, the SST field was reconstructed, yielding a new AMO index referred to as AMO-GT/EN. Removing the ENSO modes affected little the AMO amplitude ($std = 0.10$ °C) but slightly increased its estimated period (~ 55 yr). The associated SST pattern (Fig.4.27 bottom left) shows more pronounced cooling anomalies in the South Atlantic and the tropical Pacific. Based on results obtained with climate models, AMO-GT/EN should be better correlated to the AMOC than the traditional AMO and than AMO-GT. If the in-phase correlation between Atlantic SSTs and ENSO were a trustable indicator of the ENSO impact on the Atlantic, we could infer from Fig.4.21 that the increase in AMO-AMOC correlations would be within the range between the worst and the best value found in climate models.

[Guan and Nigam 2009] obtained a very different AMO index by also removing the signals linked to the decadal variability of the Pacific, primarily because their Pan-Pacific decadal mode lead the AMO by 5 seasons. And, in climate models, removing such a signal was found to degrade the AMO-AMOC correlations. To investigate this effect in the observations, we add the Pacific decadal oscillatory mode 2/3 to the subset of removed modes ($P = \{1, 2/3, 5/6, 7/8\}$). Although this PDO-like mode represents low frequency variability in the Pacific, it also shows strong anomalies in the Atlantic with a pattern evoking the AMO. Indeed, the AMO computed from $\sum_{i \in 2/3} \mathbf{u}_i \alpha_i(t)$ is highly correlated with the traditional AMO

($r = 0.83$). Mode 2/3 thus reflects a strong linkage between low frequencies in the Pacific and in the Atlantic, consistently with [Orgeville and Peltier 2007], who showed that the AMO and the low-frequency component of the PDO were signatures of the same oscillation cycle. Note that, in control simulations, PDO-like modes also show strong anomalies in the North Atlantic, as was discussed in 4.4.3.

The AMO index obtained by removing this additional mode, referred as AMO-GT/EN/PD, has a different behaviour (Fig.4.27 bottom right) and much smaller amplitude ($std = 0.05\,^{\circ}$C). As in the other cases, the associated SST pattern shows an almost interhemispheric signal in the Atlantic basin, but the positive anomalies in the western subtropical gyre are much weaker and less significant, and the negative pole south of Newfoundland has disappeared. This structure is very similar to the one obtained by [Guan and Nigam 2009]. However, Fig.4.27 reveals that there is a large signal in the tropical Pacific, which resembles a La Nina event and a negative phase of the PDO. Hence, after removing the low frequency North Pacific mode, the AMO is associated to SST anomalies having a negative PDO-like pattern. Whereas the traditional PDO and AMO do not correlate without lag, these indices have a correlation of $r = -0.32$, which persists when the AMO leads, when estimated from $\sum_{i \notin P} \mathbf{u}_i \alpha_i(t)$. Note that removing the mode 2/3 does not remove the whole PDO signal, but only its low frequencies variability. Indeed, the 1st EOF of the residual North Pacific SST also resembles the PDO, but has much less variability at low frequencies.

4.7 Summary

In this chapter, a dynamical filter based on LIM is used to deconstruct the AMO and to extract the part that is best related to the AMOC variability. Assuming that the seasonal SST anomalies between 20 $^{\circ}$S and 80 $^{\circ}$N are well approximated by a multivariate linear markov process, the SST field can be decomposed into a sum of empirical normal modes, which can be split into a part related to the global

trend (in the observations or in historical simulations), a ENSO-related part, one linked to decadal variability in the Pacific, and a residual. The LIM filter was used to deconstruct the AMO in the observations, the historical IPSLCM5 simulations, and control simulations with 5 climate models.

In the observations and in the historical IPSLCM5 simulation, the empirical normal mode having the largest decay time is non-oscillatory, and its time series reflects a warming tendency in almost the whole domain. When the mode is removed from the SST field in the historical IPSLCM5 simulation, the AMO index is substantially altered, and it is found to better correlate with the AMOC than traditional AMO indices where the global signal is removed by a linear trend or by the global mean SST. This suggests that LIM is a superior method for removing the global warming signal from the SST field.

ENSO-related empirical normal modes were chosen as modes having a period shorter than 8 yr, showing large anomalies in the tropical Pacific, and strongly contributing to the optimal initial structure leading to the maximum amplification in the SST variance in the tropical strip. Removing these modes leads to a small increase in the correlations between the AMO and the AMOC indices. Note that, as shown in section 4.4.2, LIM is more successfull at removing the ENSO than a regression, consistently with [Penland and Matrosova 2006] and [Compo and Sardeshmukh 2010]. The increase strongly depends on the model, probably reflecting differences in the representation of the atmospheric bridge between the tropical Pacific and the Atlantic sector. The increase is largest in all the IPSL simulations and MPI-ESM, but it is negligible in HadCM3 and CCSM3. However, the ENSO influence on SLP and SST in the Atlantic is much stronger and somewhat different in the IPSL models and in MPI-ESM than in the observations, where little links is found in the North Atlantic. On the other hand, when the ENSO links are removed from the SST in CCSM3, the AMO-AMOC correlations remain unchanged or become slightly smaller, depending on the AMOC index, since the correlation between ENSO and the tropical Atlantic

SST is weaker than in the observation, suggesting that the ENSO links to the AMO are underestimated in this model. This suggests that removing ENSO with LIM in the observations would increase the AMO-AMOC correlations, but not as much as in the IPSL models or in MPI-ESM, with the caveat that discussing the impact of ENSO onto the Atlantic using regressions may be inadequate ([Penland and Matrosova 2006], [Compo and Sardeshmukh 2010]), even more so because connections between the Atlantic and ENSO are not stationary in the observations ([Sutton and Hodson 2003], [Greatbatch et al. 2004]).

We also find that in nearly all cases removing the Pacific decadal variability from the SST field as in [Guan and Nigam 2009] degrades the correlation between the AMOC indices and the AMO, suggesting a link between the decadal variability in the Pacific, the AMO, and the AMOC. This may be due to their forcing by coherent atmospheric patterns. Indeed, [Müller et al. 2008] showed that on decadal time scales, the PDO and the NAO were strongly coherent. As the AMOC is largely driven by the NAO in most models, removing the Pacific decadal variability from the AMO may remove part of the signal induced by the AMOC. The close links between the AMO and the PDO in the observations was discussed by [Orgeville and Peltier 2007], who found that the PDO contained a quasi-periodic oscillation at 20 yr and a lower frequency (60 yr) signal, which were linked to the AMO in both lead and lag conditions. They argued that the AMO and the PDO were two components in phase quadrature of a same oscillation. We found indeed that the mode having the largest period in the observations was related to both the AMO and the PDO. In the climate models, the decadal Pacific modes also show strong anomalies in the North Atlantic, but a close link to the AMO was anly found in IPSLCM4.

If the analogy with the climate models may be trusted, the AMO-GT/EN index and pattern derived from the observations should be better related than the traditional AMO to the AMOC intensity a few years earlier. The optimal lag was, however, model dependent, ranging between 2 and about 10 years, so

that further studies are needed to establish the most realistic value. Using 6 yr as the averaged delay, our study tentatively suggests that, in recent time, the AMOC was weakest in the late 60s, remained low until the mid-eighties, and then intensified until the late 90s. There are no fully trustable model-based reconstruction of the AMOC, but oceanic hindcast or reanalysis can be tentatively used for comparison. The 50-yr (1952-2001) GECCO estimates for the AMOC maximum at 48 ° N ([Köhl and Stammer 2008], [Grist et al. 2009]) suggests that it was weakest in the early 60s, increased until the Nineties, and remained strong until at least 2001, consistently with model hindcasts ([Biastoch et al. 2008], [Deshayes and Frankignoul 2008]). Fig.4.29 shows the traditional AMO and AMO-GT/EN based on HadISST (1953-2008) and the 1st PC of yearly AMOC in the realistic hindcast simulation used by [Deshayes and Frankignoul 2008]. This shows some similarities with we inferred from the AMO, but a more qualitative estate remains to be established.

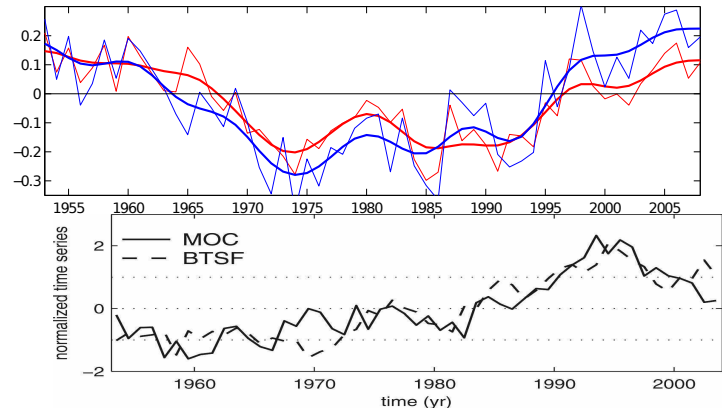

Figure 4.29: Top : Traditional AMO (blue) and AMO-GT/EN (red) time series based on HadISST (1953-2008), thin curves correspond to unfiltered time series. Bottom : from [Deshayes and Frankignoul 2008], 1st PC of yearly AMOC (plain line) and barotropic streamfunction (dashed line) in a realistic hindcast simulation from 1953 to 2003.

Chapter 5

Volcanic impact on oceanic variability over the last millennium

Contents

Volcanic explosive eruptions can have a broad impact on climate variability, depending on the amount of volatiles reaching the stratosphere and the latitudes of the eruptions ([Thompson et al. 2009]). Volatiles reaching the troposphere diseappear

within a few months, and eruptions occuring at high latitudes remain in the eruption hemisphere because of the Brewer-Dobson circulation in the midldle-latitude stratosphere. In this chapter, we focus on explosive stratospheric volcanism occuring in the Tropics. It induces a climate response at two time scales : first a rapid radiative effect in the first 3 yr, and a longer lasting dynamical effect induced by this cooling ([Robock 2000], [Stenchikov et al. 2009], [Mignot et al. 2011]). Indeed, during an eruption, sulfur gases are injected into the stratosphere, where they are converted in several weeks to sulfate aerosols with an e-folding residence time of about 1 yr ([Robock 2000]). The stratospheric sulfate aerosols scatter some solar radiation back to space, leading to a strong cooling at the surface.

In the Tropics, this cooling is first associated with a La Niña-like signal (except for some eruptions that were concomitant with an El Niño event such as the Pinatubo eruption in 1991), but it might then induce an El Niño event ([Adams et al. 2003], [McGregor and Timmermann 2011]), or at least increase the likehood and the amplitude of an event ([Emile-Geay et al. 2008]), based on the thermostat mechanism ([Clement et al. 1996]). Indeed, as in the Western Pacific the thermocline is deeper and the surface divergence small, the SST is more easily affected by the radiative cooling compared to the eastern equatorial Pacific SST, which is largely controlled by dynamical processes. The SST cooling is thus faster in the western part of the basin, resulting in a reduced zonal SST gradient. The trade winds then weaken, reducing further the SST gradient, leading to El Niño conditions. As mentionned above, some eruptions occur during a positive ENSO, the climatic signal of volcanic eruptions and ENSO have the same amplitude, it is then necessary to separate the volcanic forcing from that of ENSO ([Robock 2000], [Thompson et al. 2009]).

Stratospheric explosive volcanic activity also affects the extratropics. Indeed, as the stratospheric heating is larger in the Tropics than in the high latitudes for a tropical eruption, the pole-to-equator temperature gradient is increased, especially in winter, resulting in a stronger jet stream in the northern hemisphere and mod-

ifying the atmospheric circulation. Volcanic activity may thus impact the AMOC, which is largerly driven by heat, freshwater, and momentum fluxes. Using a climate model simulating the response to a super eruption with 100 times the amount of sulfur gases released in the atmosphere during the Pinatubo eruption (1991), [Jones et al. 2005] found an atmospheric response with a positive Arctic Oscillation pattern, leading to a doubling of the AMOC about 9 yr after the eruption. Similarly, using models forced by solar irradiance and volcanic aerosols, [Otterå et al. 2010] and [Mignot et al. 2011] found a NAO-like atmospheric response to volcanic forcing, leading to an increase in the AMOC within 10 yr. However, such a response was only found when considering the last 500-600 yr of the past millennium when the volcanic activity was moderate, as emphasized by [Mignot et al. 2011].

In this chapter, we consider the same simulation as [Mignot et al. 2011] and use LIM to test whether it is efficient at isolating the volcanic signal and investigate the influence of volcanic activity on oceanic variability. It is indeed of interest to try to filter out the strong and rapid radiative cooling induced by volcanic eruptions, since it may mask dynamical impacts of smaller amplitude.

5.1 Simulation of the last millennium climate with the IPSLCM4 climate model

In this chapter, a control and a forced simulation of the IPSLCM4 v2 climate model ([Marti et al. 2010]) are used to study the volcanic impact on the oceanic variability. The control simulation was also used in the previous chapter and was referred to as IPSLCM4 (section 4.1.2), but it will be referred to here as CTRLA to distinguish it from the forced simulation LM2SV, referred to as MILL. Recall that the oceanic component of the model is OPA8.2 ([Madec et al. 1998]), with a horizontal resolution of 2 ° x 2 ° refined to 0.5 ° near the equator, and 31 vertical levels. The atmosphere is represented by the LMDz4 atmospheric model ([Hourdin et al. 2006]) with a resolution of 3.75 ° in longitude and 2.5 ° in latitude, and 19 vertical levels. The land surface model is ORCHIDEE 1.9.1 ([Krinner et al. 2005]), and the sea ice is modeled by the the LIM2 sea-ice model ([Fichefet and Morales-Maqueda 1999]). These components interact via the OASIS coupler ([Valcke 2006]).

The simulation MILL aims at simulating the last millennium climate from 850 to 2000. It is forced with reconstructions of the Total Solar Irradiance (TSI), greenhouse gases concentrations, changes in orbital parameters, and radiative effect of volcanic eruptions. The TSI reconstruction is from [Vieira and Solanki 2009] and follows the scaling recommended for the 3rd phase of the paleoclimate modeling intercomparison (PMIP III, [Schmidt et al. 2010]), with a decrease of the total irradiance during the 17th century Maunder minimum of 0.1% of the contemporary value. The solar radiative forcing is shown in Fig.5.1 (top). The radiative effect of volcanoes is implemented by a new radiative module developped by Kohdri et al (in prep) that mimics the effect of sulfate aerosols. The input is the time series of stratospheric volcanic aerosol optical depth (AOD, Fig.5.1 bottom) based on monthly mean optical thickness latitudinal reconstruction by [Ammann et al. 2003] and [Gao et al. 2008]. An increase in the global mean optical depth of 0.1 corresponds to a radiave forcing of $-3Wm^{-2}$. A caveat of this radiative module is the

overestimation of the radiative effect of the mega eruptions, as discussed in Kohdri et al (in prep) and [Timmreck et al. 2009]. The greenhouse gas concentrations are

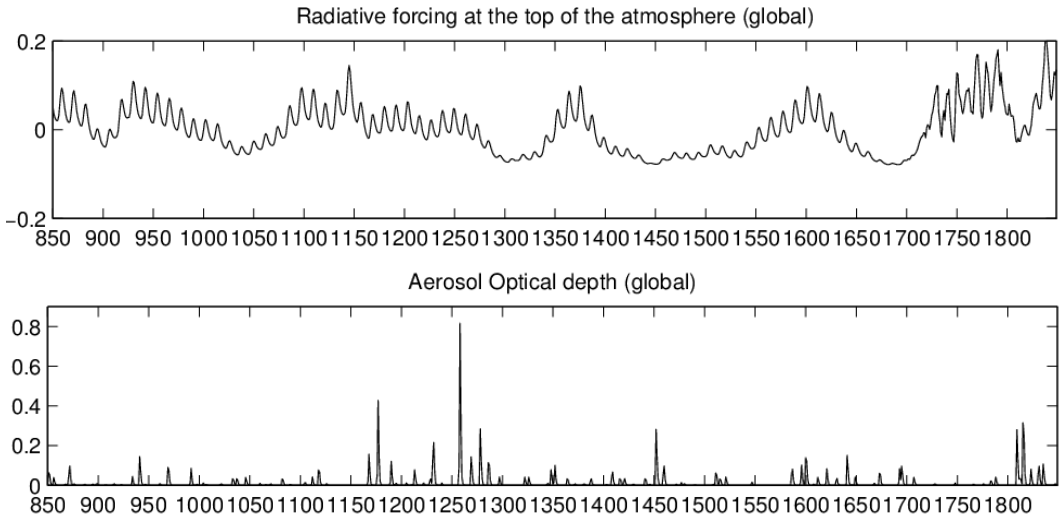

Figure 5.1: Time series of anomalous short wave input at the top of the atmosphere (in Wm^{-2}), taken as an estimation of variations of the TSI (top) and imposed optical depth of volcanic aerosol (bottom) (a change of 0.1 corresponds to a global anomalous radiative forcing of about $-3Wm^{-2}$).

those used in the 4th assessment report of intergouvernmental panel on climate change ([Jansen et al. 2007]). Note that the simulation does not include the forcing by anthropic aerosols, leading to an overestimated global warming over the 20th century. However we do not consider this period, but only the simulation from 850 to 1849, since we focus on external natural variability.

In MILL, [Mignot et al. 2011] found a strong and long lasting thermal and dynamical oceanic reponse to the volcanic forcing, while the solar forcing was not significant, probably because this simulation underestimates it and overestimates the volcanic activity. The thermal response consisted of a fast tropical cooling, a penetration of this cooling in the subtropical ocean interior within 1 to 5 yr, and a further propagation towards high latitudes. The dynamical response strongly depended on the volcanic eruption. For the period after 1400, associated with moderate volcanism and eruptions mainly occuring in the warm season, a positive

NAO-like pattern was found and resulted in a strengthening of the AMOC 5 to 10 yr after the eruptions. On the other hand, for the period 1100-1300, which is associated with a very intense volcanic activity and eruptions occuring mostly in the cold season, no AMOC intensification was found, but rather a strong reduction after 10 yr, as well as a large expansion of sea-ice.

We first apply LIM to the whole period 850-1849, and then separately to the period of intense volcanism (1150-1300) and of moderate volcanism (1350-1849).

5.2 Use of LIM to study the volcanic impact on SST variability

The LIM was applied to seasonal SST anomalies between 20 ° S and 80 ° N. As in the previous chapter, we work in a truncated EOF space to lower the dimensionality of the system and compute EOF separately for the tropical strip, the North Atlantic, and the North Pacific. The first 3 EOFs are shown for the period 1200-2199 in CTRLA and 850-1849 in MILL in fig.5.2-5.4. In the tropical strip, the

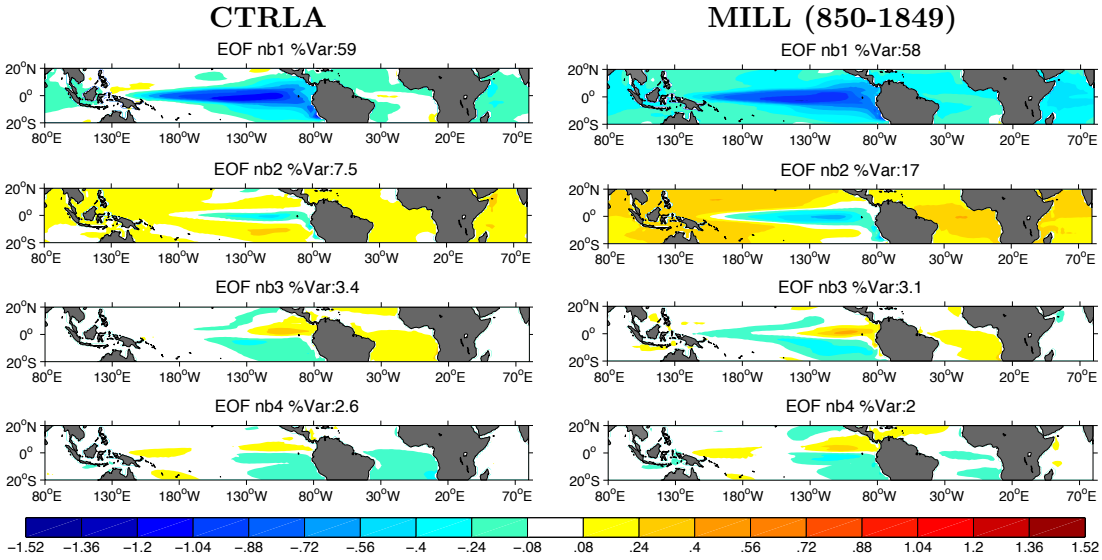

Figure 5.2: EOFs of seasonal SST anomalies in the tropical strip. The percentage indicates the explained variance.

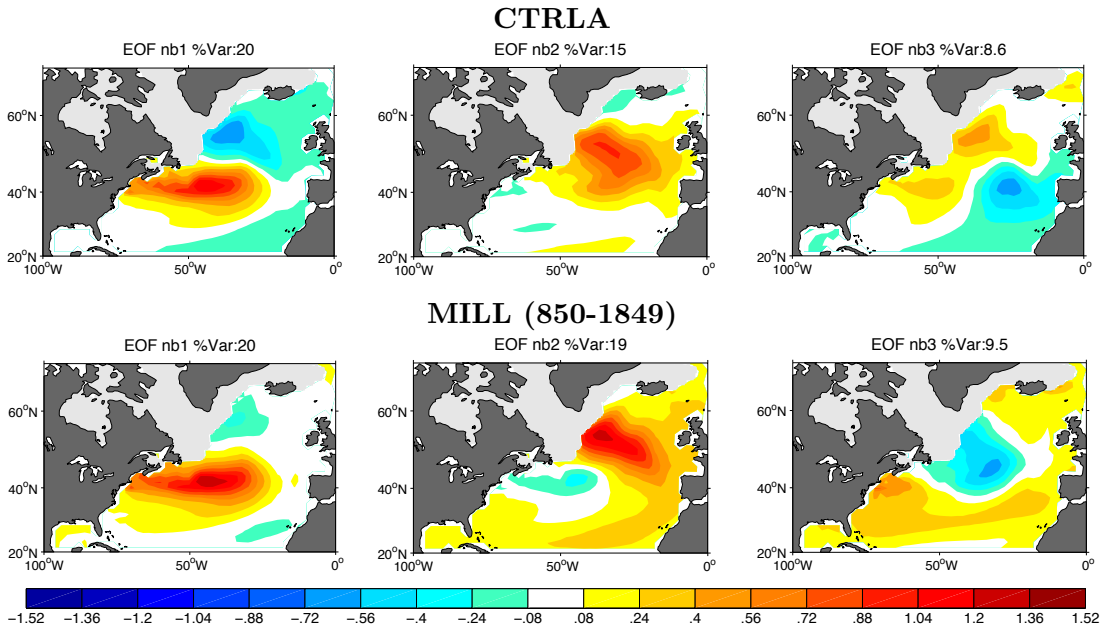

Figure 5.3: EOFs of seasonal SST anomalies in the North Atlantic. The percentage indicates the explained variance. Light gray shaded area indicates where the sea ice cover in March is higher than 25%.

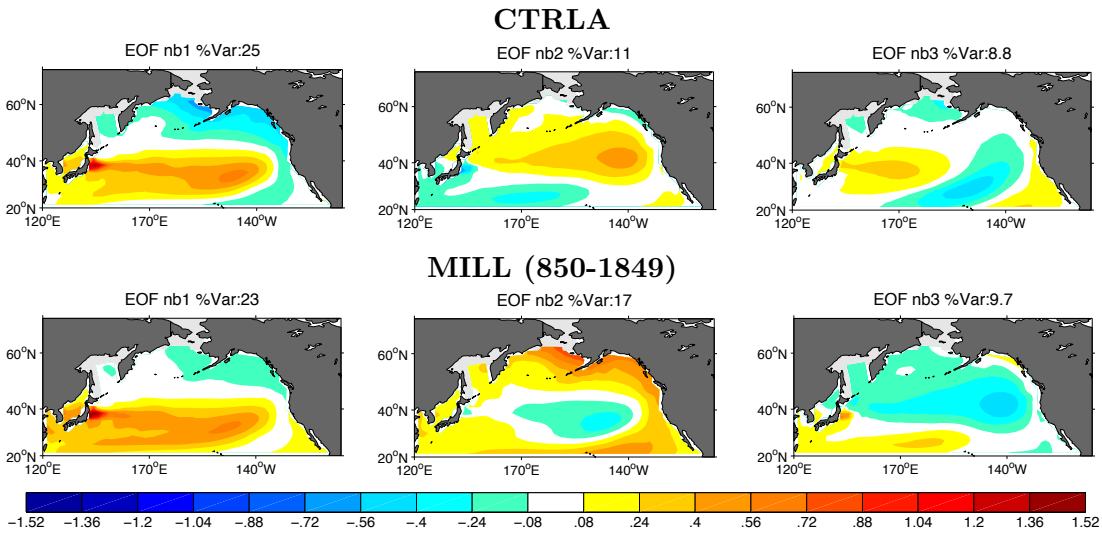

Figure 5.4: EOFs of seasonal SST anomalies in the North Pacific. The percentage indicates the explained variance. Light gray shaded area indicates where the sea ice cover in March is higher than 25%.

first EOF is somewhat different in MILL compared to CTRLA, showing a global warming/cooling with stronger anomalies in the equatorial and eastern Pacific, which probably reflects the strong tropical cooling caused by volcanic eruptions in the Tropics ([Emile-Geay et al. 2008], [McGregor and Timmermann 2011]). In the North Atlantic and North Pacific, the main EOFs are more similar. To constitute the LIM state vector, the same number of EOFs in CTRLA and MILL are taken in the North Pacific and North Atlantic, but one more tropical EOF is considered in MILL (Table 5.1), to take into account the possibility that the tropical cooling following an eruption may need more EOFs to be propoerly represented.

Simulation	Period	Number of EOFs		
		N.Atl	N.Pac	Tropics
CTRLA	1200-2199	12	7	8
		75%	66%	79%
MILL		12	7	9
	850-1849	78%	70%	86%
	1350-1849	79%	69%	85%
	1100-1349	79%	74%	88%

Table 5.1: Number of EOFs and corresponding variance taken into account in the LIM analysis.

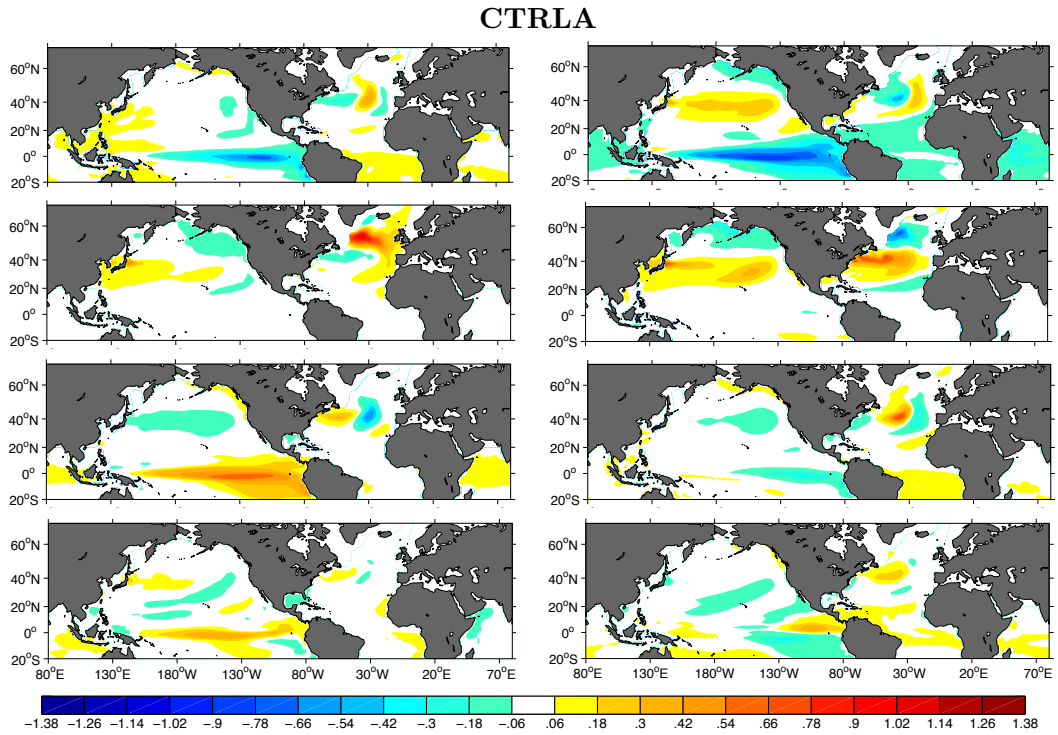

Figure 5.5: Normal modes (in °C) of the deterministic matrix **B**. Mode 1/2 (1st row), 3/4 (2nd row), 5/6 (3rd row), 8/9 (bottom). LIM made from CTRLA.

5.2.1 Comparison between LIM results obtained with CTRLA and MILL (850-1849)

As was the case in the previous chapter, the matrix **B** could only be determined at a lag of one season, reflecting the Nyquist problem. The first few empirical normal modes are shown in Fig.5.5 for CTRLA and Fig.5.6 for MILL (850-1849), and their decay time and period are indicated in Table 5.2. Contrary to CTRLA, the first mode of MILL is damped with a large decay time of 4.4 yr, and it corresponds to a cooling in the whole domain with larger anomalies in the tropical strip. Its time series shows strong peaks at the dates of volcanic eruptions, and its correlation with the global AOD is $r = 0.7$. Note that this mode is not significantly correlated to the TSI, probably because of the too weak variations of the TSI reconstruction used in MILL and the overtestimated volcanic radiative effect ([Mignot et al. 2011]).

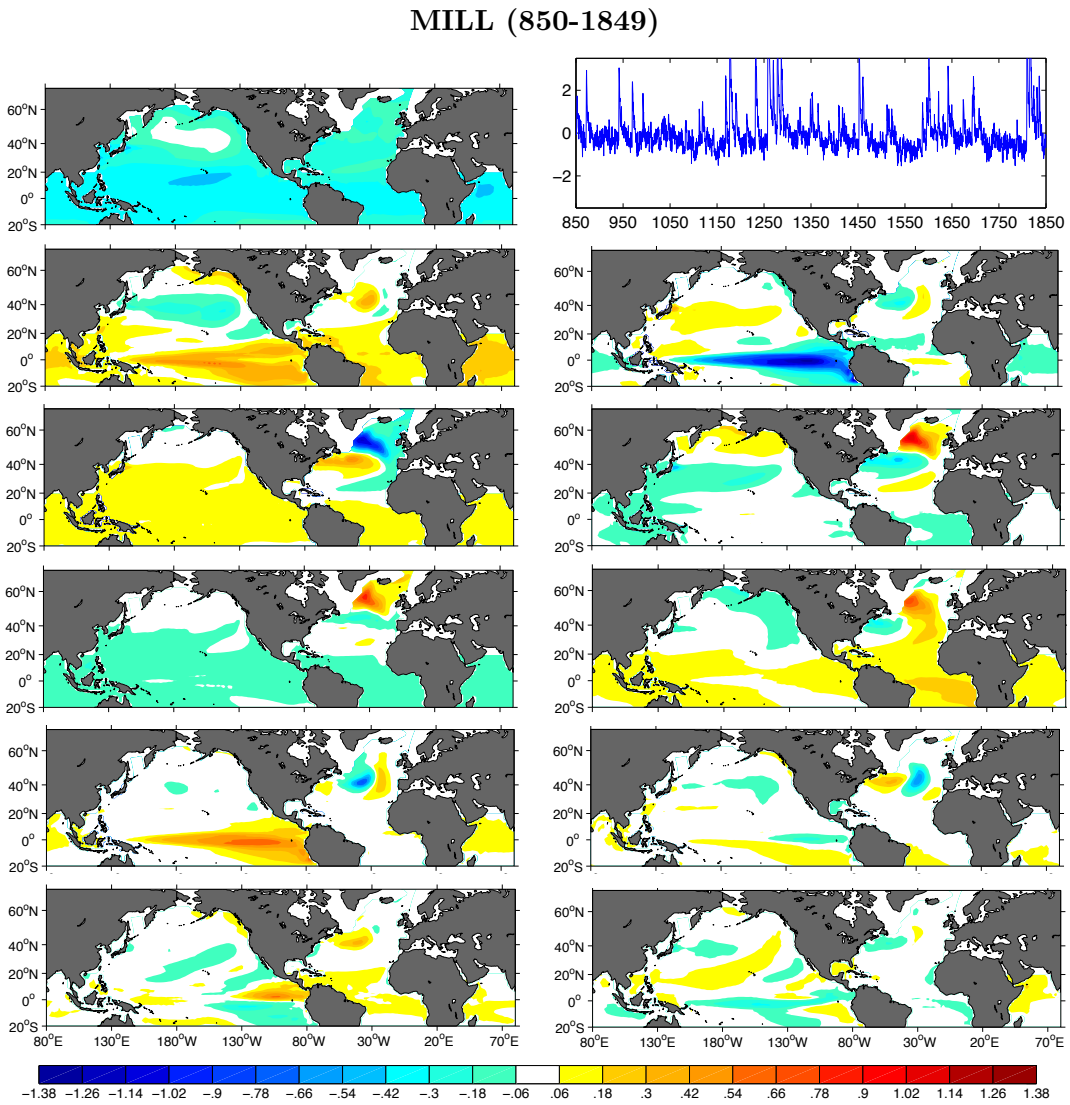

Figure 5.6: Normal modes (in °C) of the deterministic matrix **B**. Mode 1 and its associated time series (1st row), 2/3 (2nd row), 4/5 (3rd row), 6/7 (4th row), 8/9 (5th row), and 11/12 (bottom). LIM made from MILL (850-1849).

Using Northern Hemisphere temperature inferred from tree-ring reconstructions and composites of 50 volcanic eruptions between 1400-1940 with their timing inferred from records of ice-core AOD, [Hegerl et al. 2003] found a significant cooling in the first 3 yr of the eruption, which disappears after about 5 yr, consistenly with the decay time of 4.4 yr of the first LIM mode. Similarly, [Thompson et al. 2009] found

a recovery time scale of 7 yr, inferred from the composite response of the observed SST (HadISST2) to the volcanic eruptions of the 20th century, after removing the ENSO signal.

The first mode of CTRLA is oscillatory with a period of 3 yr, and it shows strong anomalies in the tropical strip, evoking ENSO. It is very similar to mode 2/3 of MILL (850-1849). Mode 5/6 of CTRLA also evokes the ENSO signal and is very similar to mode 3/4 of MILL. Similarly, both mode 8/9 of CTRLA and mode 11/12 of MILL show a North/South SST tripole in the eastern equatorial Pacific and have similar period and decay time (Table 5.2).

In CTRLA, mode 3/4 was found to be related to the PDO and to the AMO (see section 4.4.3). Modes 4/5 and 6/7 in MILL similarly have a long period (resp. 41.4 yr and 28.2 yr) and strong anomalies in the North Atlantic and North Pacific, and they resemble mode 3/4 of CTRLA. However, contrary to the latter, they also have nearly uniform anomalies south of 40 $^\circ$ N in the Pacific and of 20 $^\circ$ N in the Atlantic, which suggests that a part of the volcanic signal is contained in these modes. Indeed, the correlations between the AOD and the cosinus phase of mode 4/5 and mode 6/7 are respectively -0.3 and 0.4. The fact that these modes reflect both the volcanic response and the multidecadal variability in the northern hemisphere could suggest a dynamical link between these signals. However, such modes are not found when LIM is applied separately to the periods 1350-1849 and 1150-1300, reflecting instead that the simulation contains two different regimes, one of very intense volcanism (1150-1300, Fig.5.1) and one of more moderate volcanic activity (1350-1849), as discussed by [Mignot et al. 2011]. For the following, we consider the two periods separately.

CTRLA			MILL (850-1849)			MILL (1350-1849)			MILL (1150-1300)		
Mode	DT (mo)	T (yr)	Mode	DT (mo)	T (yr)	Mode	DT (mo)	T (yr)	Mode	DT (mo)	T (yr)
			1	4.4yr	∞	1	5yr	∞			
1/2	1.4yr	3	2/3	1.6yr	3	2/3	1.7yr	26	1/2	2.1yr	24
3/4	1.4yr	32	4/5	1.4yr	41.4	4/5	1.3yr	2.9	3/4	1.6yr	3
5/6	1.1yr	3.1	6/7	1.1yr	28.2	6/7	1.1yr	2.9	5	1.5yr	∞
7	1yr	∞	8/9	1.1yr	3	8/9	11	1.8	6	1.2yr	∞
8/9	10	1.8	10	1yr	∞	10	11	∞	7/8	1yr	16
10	10	∞	11/12	11	1.7	11/12	11	27	9/10	1yr	3
11	10	∞	13	9	∞	13/14	9	9	11/12	10	8
12/13	9	7.8	14/15	8	11.8	15/16	8	15	13/14	9	1.6
14/15	8	10	16/17	7	11.2	17/18	7	82	15/16	8	28
16/17	7	35	18/19	7	37.1	19/20	7	7	17/18	8	6
18	6	∞	20/21	6	8.4	21	5	∞	19/20	5	19
19/20	6	5.1	22/23	6	33.5	22	5	∞	21/22	5	10
21	5	∞	24	5	∞	23/24	5	12	23/24	5	5
22/23	5	9	25/26	5	12.3	25/26	4	7	25/26	4	3
24	5	∞	27/28	4	4.1	27/28	4	8	27/28	3	9
25/26	4	6.3									
27	4	∞									

Table 5.2: Decay time (DT) and period (T) of **B** normal modes for the different simulations.

5.2.2 LIM results for the moderate volcanic period (1350-1849)

The normal modes of the matrix **B** are listed in Table 5.2 (third column) and the first ones are shown in Fig.5.7. As for the whole period, the first mode is damped

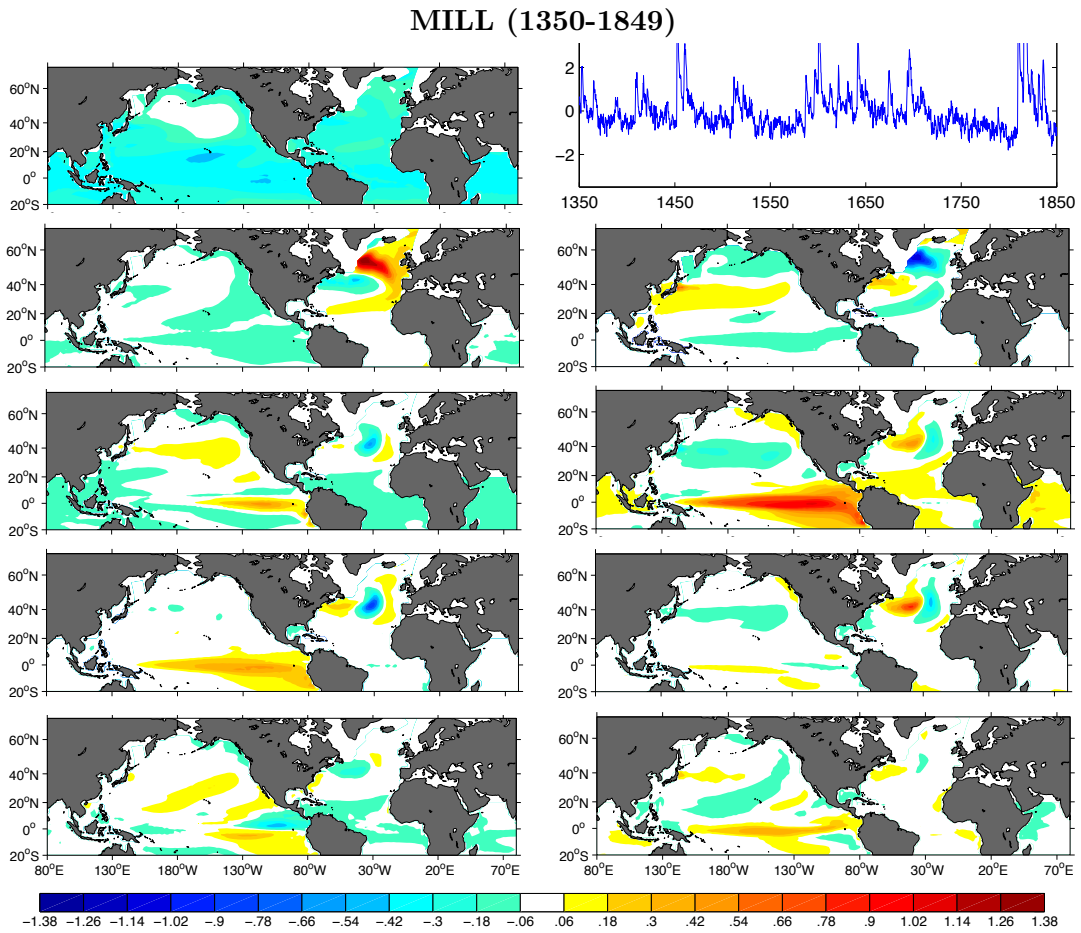

Figure 5.7: Normal modes (in °C) of the deterministic matrix **B**. Mode 1 and its associated time series (1st row), 2/3 (2nd row), 4/5 (3rd row), 6/7 (4th row), 8/9 (bottom). LIM made from MILL (1350-1849).

with a decay time of 5 yr, and it corresponds to a global cooling, more pronounced in the Tropics. Its time series shows strong peaks at the time of volcanic eruptions, and its correlation with the global AOD is 0.7. This mode thus represents the radiative cooling associated with a volcanic eruption. Although low frequency variability evoking the solar forcing of Fig.5.1 might be observed in the time series of this first

mode, more investigations would be required to state whether this mode also contain the SST response to solar forcing. The oscillatory mode 2/3 has a long period of 26 yr and is very similar to mode 3/4 of CTRLA, except that anomalies in the North Pacific are smaller and the decay time is slightly larger. This mode also resembles mode 4/5 and 6/7 of the whole period, but there is little SST anomaly in the Tropics, suggesting that LIM does not mix northern hemisphere multidecadal variability and volcanic response when the volcanic activity is moderate. The oscillatory mode 4/5 shows strong ENSO-like SST anomalies in the tropical Pacific, with a period of 2.9 yr. It is broadly similar to mode 1/2 of CTRLA. Mode 6/7 also has a 2.9-yr period and SST anomalies evoking ENSO, and it strongly resembles mode 5/6 of CTRLA. Mode 8/9 is almost identical to mode 8/9 of CTRLA. Both have a period of 1.8 yr and a cosinus/sinus phase showing a north/south SST dipole in the eastern tropical Pacific, and a cosinus/sinus phase associated with SST anomalies in the center equatorial Pacific.

Except mode 1, the first modes strongly ressemble the modes of CTRLA, showing that LIM is efficient at isolating the radiative forcing signal from the intrinsic oceanic ones in this period of moderate volcanism. We will thus use LIM to decontrust the AMO in this period, as in the previous chapter. However, we first briefly discuss the period of intense volcanism.

5.2.3 LIM results for the intense volcanic period (1150-1300)

When LIM is applied to this period, the results strongly differ from the previous ones. The temporal characteristic of the normal modes of **B** are indicated in Table 5.2 (fourth column) and the patterns of the first modes are shown in Fig.5.8. Unlike during 1350-1849, the first mode is not damped but oscillatory, although it reflects the volcanic activity. The latter also affects other modes. Modes 1/2, 5, 7/8 show an almost global cooling and their time series show strong peaks at periods of volcanic eruptions. The oscillatory nature of modes reflecting a global cooling and thus the volcanic radiative forcing may be explained by the fact that eruptions are very frequent during this period. The strongest eruptions occur in 1168, 1177, 1231, 1258, and 1278, and 2 moderate eruptions are noticed between 1177 and 1231, one between 1258 and 1278, and one after 1278. There is thus a mean time lag between two super eruptions of 25 yr, and a mean time lag of 16 yr when considering all eruptions, which is roughly consistent with the periods of modes 1/2 ($T = 24$ yr) and 7/8 ($T = 16$ yr). The volcanic influence seems so large that even the ENSO modes (modes 3/4 and 9/10) show SST anomalies spanning the whole Tropics and evoke a volcanic influence. Hence, there was no point in trying to isolate the intrinsic oceanic variability and the LIM filter was not applied to this period.

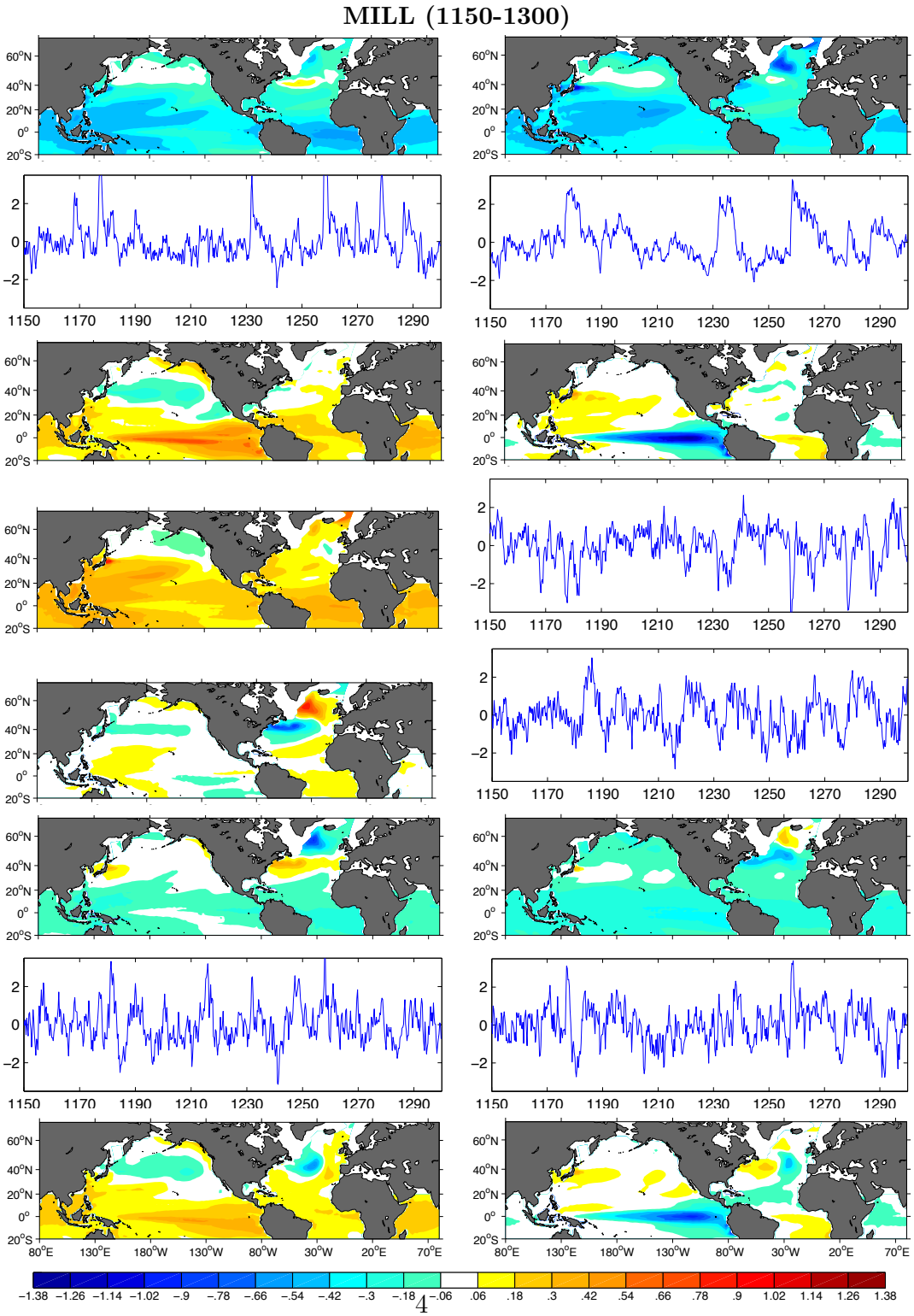

Figure 5.8: Normal modes (in °C) of the deterministic matrix **B**. Mode 1/2 (1st row), and its associated time series (2nd row), 3/4 (3rd row), 5 and its associated time series (4th row), 6 and its associated time series (5th row), 7/8 (6th row), 9/10 (bottom). LIM made from MILL (1150-1300).

5.3 Deconstructing the AMO in the period of moderate volcanic activity (1350-1849)

5.3.1 The traditional AMO and AMOC indices

The traditional AMO index, linearly detrended mean SST in the North Atlantic, is shown in Fig.5.9 (bottom left). Stong negative peaks are observed after the volcanic eruptions, as also indicated by the negative correlation ($r = -0.48$) when the AMO lags by 2 yr the global AOD. Relatively small negative peaks are noticed in 1516, 1676, and 1696, and several small eruptions precede these peaks (Fig.5.1). A moderate peak is observed in 1454, followed by a stronger one in 1461, presumably associated with the super eruption of 1452 and the smaller eruption occuring just after, which may have cumulative impacts. In 1601 a moderate negative peak in the AMO can be linked to the 3 medium eruptions at this period. The moderate peak in 1643 follows the super eruption of 1641. The strongest negative peak in the AMO is observed in 1817, and it is likely linked to the two mega eruptions occuring in 1809 and 1815, again supporting the idea of a cumulative impact of volcanoes. The SSTs associated with the AMO show a global warming, except in the central North Pacific, with a maximum in the northern North Atlantic (Fig.5.9 top left). This pattern strongly differs from traditional AMO patterns (e.g. [Vellinga and Wu 2004], [Knight et al. 2005]), which is shown for CTRLA in Fig.5.9 (top right). Note however that the location of the SST maximum in the North Atlantic is similar in MILL and CTRLA.

As shown in Fig.5.10, this AMO index shows stronger variations than the AMO computed with temperature reconstruction of [Mann et al. 2009], suggesting an overestimated volcanic forcing in MILL. The surface temperature reconstruction of [Mann et al. 2009] is based on a diverse multiproxy network, comprising tree-ring, ice core, coral, sediment, and other proxy records spanning the ocean and land regions over the past 1500 yr. The AMO from [Mann et al. 2009] is negative from 1400 to 1800, period containing the Little Ice Age (1400-1700), when established

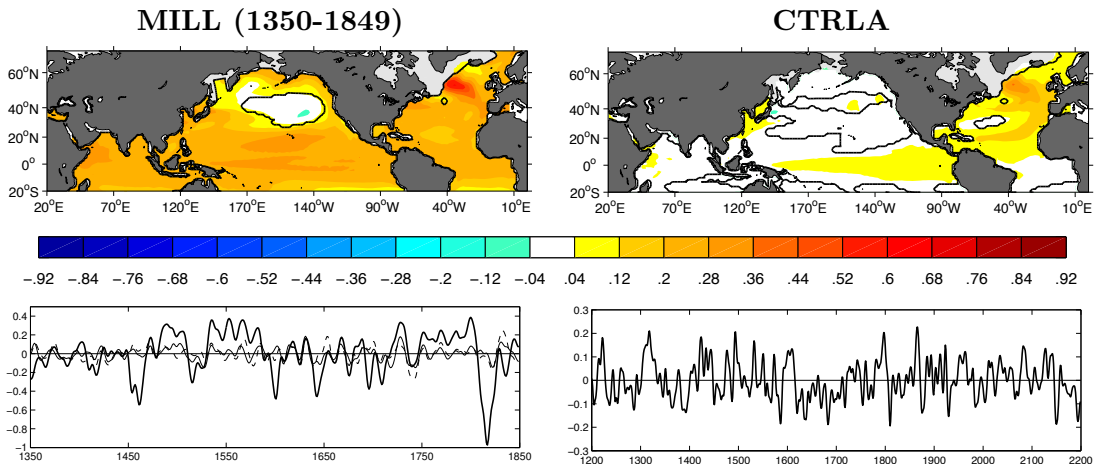

Figure 5.9: Top : SSTs (in °C) associated with the traditional AMO in MILL (1350-1849) (left) and in CTRLA (right). Bottom left: Traditional AMO (in °C, thick line), AMO-Vol (solid line) and AMO-Vol/EN (dashed line) in MILL (1350-1849). Bottom right : Traditional AMO in CTRLA; note the change of scale. The black contour indicates 5% significance.

from the 500-2000 period. However, for comparison with MILL, the climatology must be removed over the period under study.

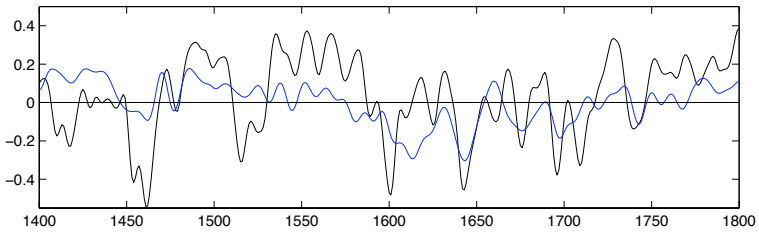

Figure 5.10: Traditional AMO (in °C) in MILL (black curve) and based on temperature reconstruction of [Mann et al. 2009] (blue) from 1400 to 1800.

The 1st EOF of low-pass filtered (T_c = 10 yr) AMOC anomalies is shown in Fig.5.11, as well as its associated time series referred to as AMOC-PC1. As before, a quadratic trend has been removed prior to computing EOFs in order to remove possible non-physical trend linked to insufficient spin-up of the deep ocean. Consistently with CTRLA (see Fig.4.3 of section 4.2), it shows an acceleration cell

spanning the whole Atlantic basin, with a maximum located around 45-50 ° N and 1500-2000 m. The value of this maximum is stronger in MILL (0.8 Sv versus 0.5 Sv). Another index of the AMOC variability is the time series of the AMOC max-

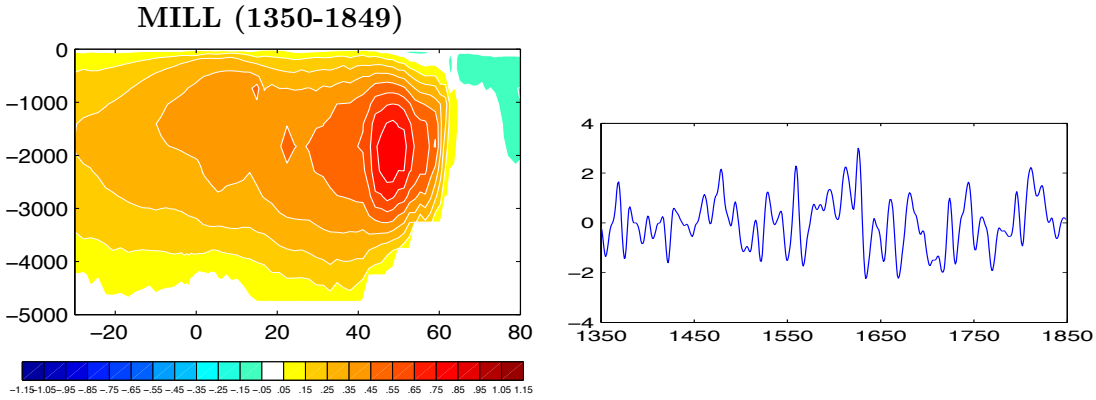

Figure 5.11: 1st EOF of low-pass filtered (T_c = 10 yr) AMOC anomalies (in Sv) (left) and its associated time series (right).

imum between 10 and 60 ° N below 500 m, its mean value equals 11 Sv, which is similar to CTRLA (10.1 Sv). The AMOC maximum at 30 ° N below 500 m also has comparable ranges. Fig.5.12 (left) shows the power spectrum of these low-pass filtered (T_c = 10 yr) normalized indices, and the one of the normalized AMO. In MILL, a spectral peak is found around 18 yr for the 3 AMOC indices, but not for the AMO. In CTRLA, such a spectral peak is also found for the AMOC maximum between 10 and 60 ° N (Fig.5.12 right), and to a lesser extent, for the AMO, but not for the other AMOC indices.

Contrary to CTRLA (see Table 4.6 in section 4.2 of the previous chapter), no really significant correlation is found when the AMO lags the AMOC by a few years, as shown in Fig.5.13. However, a negative correlation is found between the AMO and AMOC-PC1 at zero-lag, which is more persistent when the AMOC lags, probably reflecting an AMOC increase associated with a cooling of the North Atlantic. This correlation function between the AMO and the AMOC differs from the one obtained by [Otterå et al. 2010], who found, in a simulation of the last 600 yr with the Bergen Climate Model (BCM), higher correlations, suggesting again that

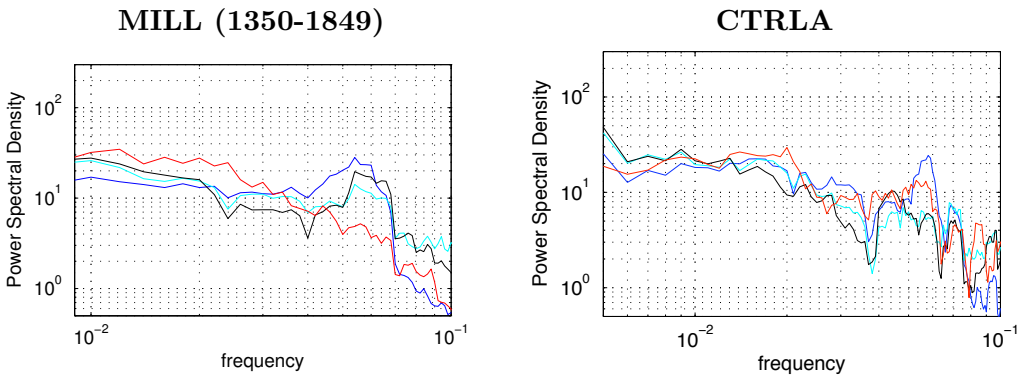

Figure 5.12: Power spectral density of low-pass filtered AMOC maximum between 10 and 60 ° N (blue), AMOC maximum at 30 ° N (cyan), AMOC-PC1 (black), and AMO (red) in MILL (1350-1849) (left) and in CTRLA (right).

the volcanic forcing in MILL may be overestimated. Besides, these correlations occur at larger lags (a negative correlation when the AMO lead by 10 yr and a positive correlation when it lagged by about 30 yr), reflecting longer time scales in BCM.

The link between the AMOC and the AMO is thus strongly perturbed by the

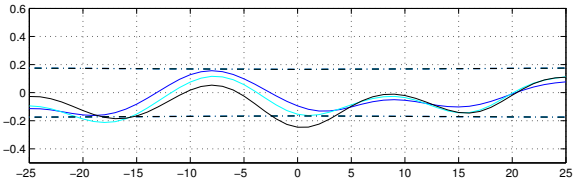

Figure 5.13: Correlation between the traditional AMO and low-pass filtered AMOC maximum between 10 and 60 ° N (blue), AMOC maximum at 30 ° N (cyan), and AMOC-PC1 (black) in MILL (1350-1849). The AMOC leads for negative lags (in yr).

volcanic signal in MILL. We use LIM to remove this signal from the AMO.

5.3.2 LIM-based filter to remove the volcanic signal

To remove the radiative impact of volcanic activity using LIM, we remove the first mode of the matrix **B**, since it is strongly linked to this signal (see section 5.2.2). A new AMO index is then computed from $\sum_{i\neq 1} \mathbf{u}_i \alpha_i(t)$, referred to as AMO-Vol. As shown in Fig.5.9 (bottom left), the strong negative values associated with volcanic eruptions have disappeared. The SSTs associated with AMO-Vol are shown in Fig.5.14 (left), and they are more similar to those associated with the traditional AMO of CTRLA (Fig.5.9), except for a cooling in the subtropical gyre and the subtropical North Pacific in AMO-Vol. The SST maximum in the northern

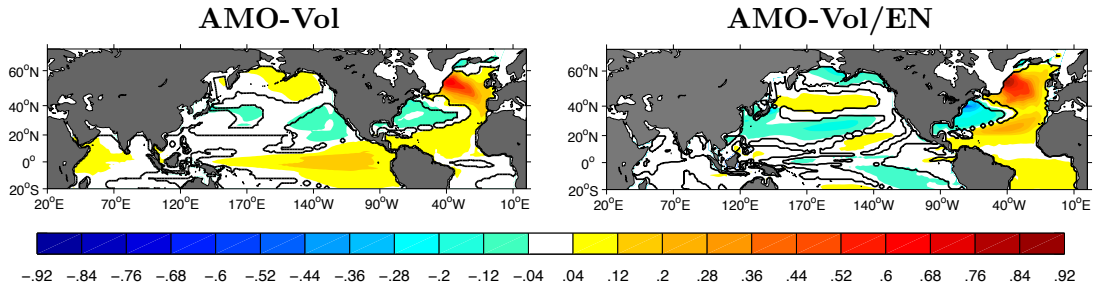

Figure 5.14: SSTs (in °C) associated with the AMO-Vol (left) and AMO-Vol/EN (right). The black contour indicates 5% significance. LIM made from MILL (1350-1849)

North Atlantic is larger in AMO-Vol than in the traditional AMO of CTRLA. Both patterns show a warming in the equatorial Pacific.

As was the case in CTRLA, a positive AMO-Vol phase is found 6 to 7 yr after an AMOC acceleration, as indicated in Fig.5.15. The maximum correlation between AMO-Vol and the AMOC indices ranges between 0.5 and 0.6, depending on the AMOC index, which is higher than in CTRLA (r between 0.36 and 0.41). Note that a negative correlation is found when the AMOC lags by a few years, reflecting that the strong cooling following volcanic eruptions favors deep convection and thus enhances the AMOC. Indeed, using a regression of low-pass filtered AMOC anomalies onto the 1st normal mode of the matrix **B** assumed to represent the

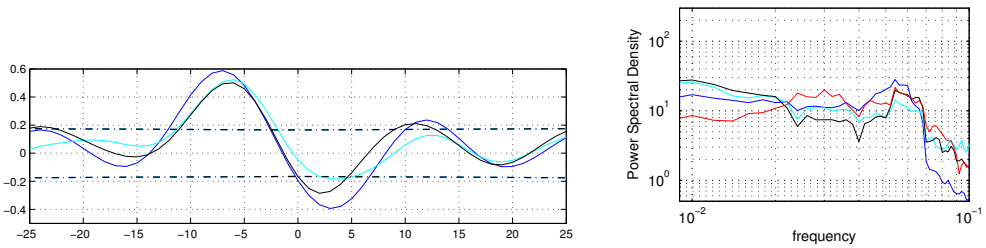

Figure 5.15: Left : Correlation between AMO-Vol and low-pass filtered AMOC maximum between 10 and 60 ° N (blue), AMOC maximum at 30 ° N (cyan), and AMOC-PC1 (black) in MILL (1350-1849). The AMOC leads for negative lags (in yr). Right : Power spectral density of low-pass filtered AMOC maximum between 10 and 60 ° N (blue), AMOC maximum at 30 ° N (cyan), AMOC-PC1 (black), and AMO-Vol (red).

radiative impact of volcanoes (Fig.5.16), an AMOC intensification limited to 10-30 ° N is observed in phase with the 1st LIM mode. This anomalous cell persists up to lag 2. Then, an AMOC acceleration starts at lag 6 in the northern North Atlantic (around 50 ° N), but is significant only from lag 10, extends to span the whole basin by lag 14, and moves then South to disappear at lag 20. Using a composite analysis in the same period of the same simulation, [Mignot et al. 2011] also found a global AMOC acceleration in response to a volcanic eruption, but it lasts shorter, since it disappears after about 10 yr.

The two-way link between AMO and AMOC may explain why, contrary to the traditional AMO, AMO-Vol shows a spectral peak at a period of about 18 yr, as the AMOC indices (Fig.5.15). The comparison with Fig.5.13 suggests that the radiative cooling associated with volcanic eruptions is so strong in MILL that it largely hides the AMO-AMOC link.

As mentionned above, [Otterå et al. 2010] also found such a two-way relationship between the AMO and the AMOC in BCM while they did not remove the volcanic signal. It would be of interest to apply LIM to the BCM simulation to see whether the first mode is also a damped mode reflecting a similarly strong radiative volcanic

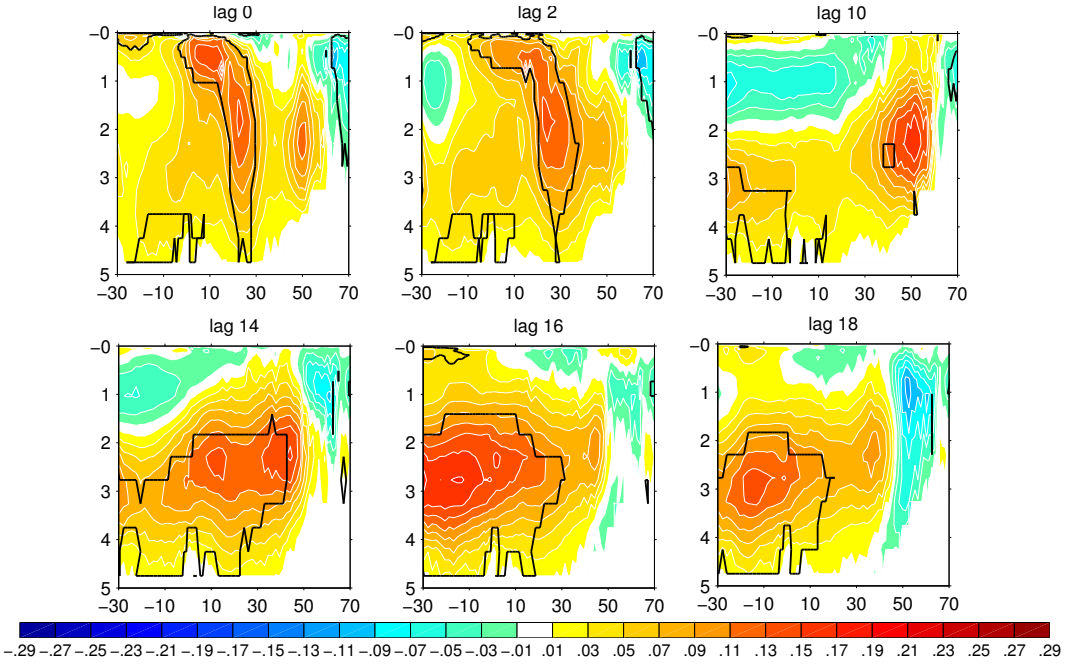

Figure 5.16: Regression of low-pass filtered AMOC anomalies onto the 1st normal mode of the matrix **B** when the latter leads by the lag (in yr) indicated on top of each panel. The black contour indicates 5% significance. LIM made from MILL (1350-1849).

cooling, and, if it is the case, whether removing it increases the AMO-AMOC correlations.

5.3.3 Can we remove ENSO effects?

As in the previous chapter, ENSO modes in MILL are selected as empirical normal modes having a period shorter than 8 yr, showing large anomalies in the tropical Pacific, and strongly contributing to the optimal initial structure leading to the maximum amplification of the SST variance in the Tropics. The optimal initial structure is shown in Fig.5.17 (top), and it leads after 3 seasons to the maximum amplification shown in Fig.5.17 (bottom). The maximum amplification pattern is

reminiscent of an El Niño event, but it also shows an almost global warming, probably linked to the volcanic signal, which was not removed prior to this computation. As previously, the contribution of the normal modes to the optimal initial structure

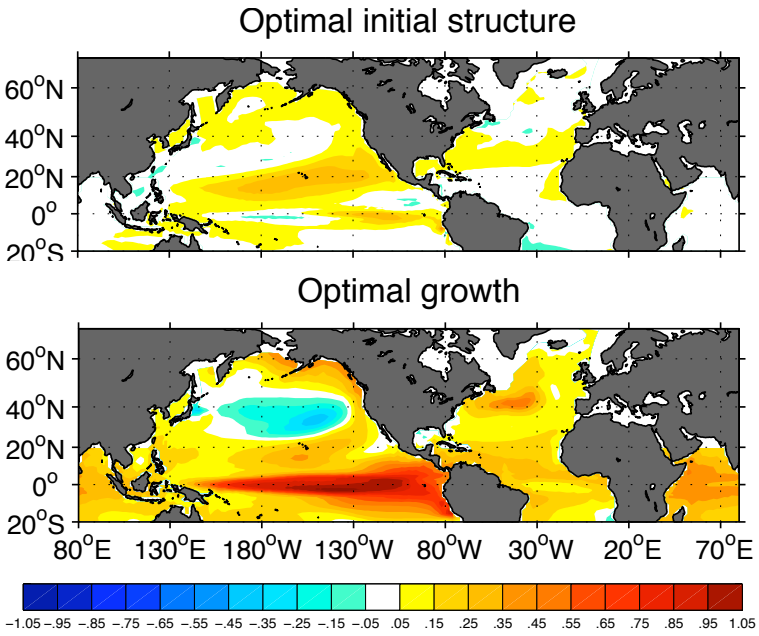

Figure 5.17: Optimal initial structure (top) leading to maximum amplification (bottom) of SST variance in the Tropical Strip. LIM made from MILL (1350-1849).

is estimated as the magnitude of their projection onto the corresponding modal adjoints (see section 3.3). The main contributors are, in decreasing order, mode 4/5, 13/14, 1, 22, 11/12, 25/26, and 6/7. Among these modes, only mode 4/5, 6/7, 13/14, and 25/26 can be considered as ENSO modes, since the others have a too long period or do not show SST anomalies in the equatorial Pacific.

A "filtered" AMO is computed from $\sum_{i \notin \{1,E\}} \mathbf{u}_i \alpha_i(t)$, with $E = \{4/5, 6/7, 13/14, 25/26\}$, to remove the volcanic signal and ENSO. It is referred to as AMO-Vol/EN. Its time series is shown in Fig.5.9 (bottom left) and its associated pattern in Fig.5.14 (right). There is now a warming in the South Atlantic, and the North Atlantic maximum is more spread than in AMO-Vol. A positive correlation is found when the AMO-Vol/EN lags AMOC indices by 7 yr, but it

is smaller than for AMO-Vol (between 0.32 and 0.4 depending on the AMOC index). Hence, removing the ENSO teleconnections reduces the correlation between AMO-Vol and the AMOC, unlike in CTRLA and the other control or historical simulations investigated in the previous chapter (see 4.4.1 and 4.3).

Although this point remains to be elucidated, the smaller correlation when ENSO is removed could occur because volcanic eruptions affect not only the AMOC (as shown above), but also El Niño events, either by altering the atmospheric bridge linking the tropical Pacific and the Atlantic, or by initiating an ENSO event. Removing a signal associated to ENSO from the AMO would thus also remove an indirect forcing of volcanic eruptions, which is involved in the AMOC signal, leading to a decrease in AMO-AMOC correlation.

As discussed earlier, several studies indicate a link between ENSO and the volcanic activity, suggesting that the volcanic radiative forcing may first cause a La Niña-like signal, and then favor an El Niño event ([Adams et al. 2003], [McGregor and Timmermann 2011]). However, this point remains controversial, as discussed by [Robock 2000] and [Emile-Geay et al. 2008]. The latter showed that only outsized volcanic eruptions (larger than that of Mt Pinatubo in 1991) may induce an El Niño event with a probability of 50%, using estimates of volcanic forcing over the past millennium and a climate model of intermediate complexity. Besides, Khodri (personal communication) emphasizes that an El Niño response to volcanic activity is likely to depend on the season.

If we use the 1st normal mode to represent the radiative impact of volcanism and the ENSO modes ($E = \{4/5, 6/7, 13/14, 25/26\}$) to compute the traditional Niño 1.2 and Niño 3.4 indices, we find that Niño 3.4 is negatively correlated in phase with a volcanic eruption ($r = -0.12$), consistenly with the literature. But then we do not find that the correlation becomes positive after a volcanic eruption, so that there is no indication of an El Niño event. This is probably due to the fact that such a response strongly depends on the seasonality and strength of the eruption. This indicates a limitation of the LIM due to its linearity. Moderate and strong

eruptions, as well as eruptions occuring in different seasons should be considered separately, but lack of time has prevented us to do it.

The volcanic forcing may also modify the atmospheric circulation and thus the ENSO teleconnections. A volcanic eruption enhances the pole-to-north temperature gradient in the stratosphere, as well as the geopotential height gradient in the lower stratopshere and troposphere ([Robock 2000], [Otterå et al. 2010]). As illustrated in Fig.5.18, the first EOF of annual geopotential heights at 200 mB in MILL clearly displays an equator-to-pole gradient, with lower anomalies near the equator, as well as smaller anomalies of the Aleutian low and the Islandic low. Its associated time series shows strong peaks after volcanic eruptions. The 2nd EOF in MILL resembles the 1st EOF of CTRLA, and corresponds to the Arctic Oscillation. The 3rd EOF in MILL shows similarities with the 2nd EOF of CTRLA, and evokes the PNA, which is involved in ENSO teleconnections. It explains less percentage of variance in MILL than in CTRLA. Interestingly, contrary to CTRLA, the anomalies located south-east of the USA span the whole Atlantic basin between 20 $^\circ$N and 40 $^\circ$N, and these anomalies are strongly involved in the impact of ENSO onto Atlantic SSTs ([Klein et al. 1999], [Alexander et al. 2002]). This should be investigated further.

5.3.4 The AMO reconstructed from mode 2/3

As discussed in section 5.2.2, the oscillatory mode 2/3 has a long period and shows strong positive anomalies in the North Atlantic and in the North Pacific. Interestingly, the AMO computed from $\sum_{i\in\{2/3\}} \mathbf{u}_i\alpha_i(t)$ is highly correlated with AMOC indices, slightly more than AMO-Vol. Indeed, its correlation equals 0.61 with the AMOC maximum between 10-60 $^\circ$N at lag 6 (versus 0.6), 0.55 with AMOC-PC1 (versus 0.5), and 0.45 with the AMOC maximum at 30 $^\circ$N (versus 0.5). The SSTs associated with this AMO index are shown in Fig.5.19. In the Atlantic, there is an interhemispheric SST dipole, except for the presence of negative anomalies in the subtropical gyre. Also, the SST maximum in the North Atlantic is much stronger

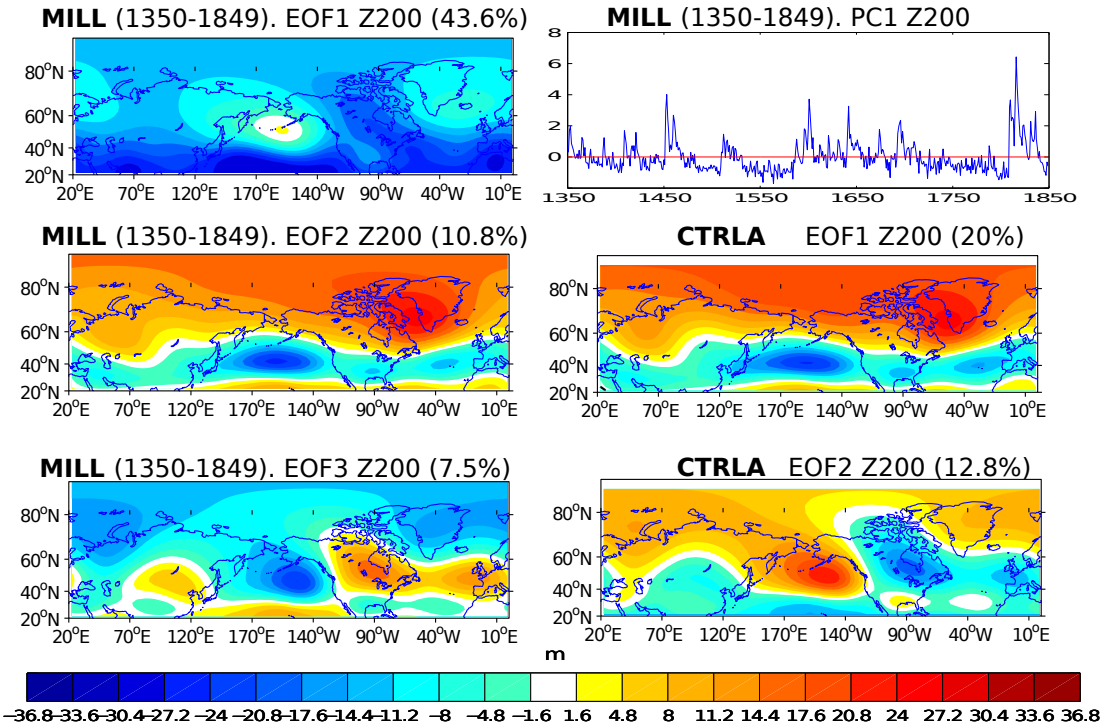

Figure 5.18: EOFs of annual geopotential heights anomalies at 200 mB in MILL (1350-1849) and in CTRLA. The percentage indicates the explained variance by each EOF.

than in AMO-Vol. As discussed above, mode 2/3 of MILL is very similar to mode 3/4 of CTRLA, except the smallest anomalies in the North Pacific in MILL. However, the correlation between the AMO computed from mode 3/4 in CTRLA and the AMOC indices was only larger for the AMOC maximum between 10 and 60 ° N (see section 4.5 of the previous chapter), so that this single mode in CTRLA was not a better proxy of the AMO than AMO-EN.

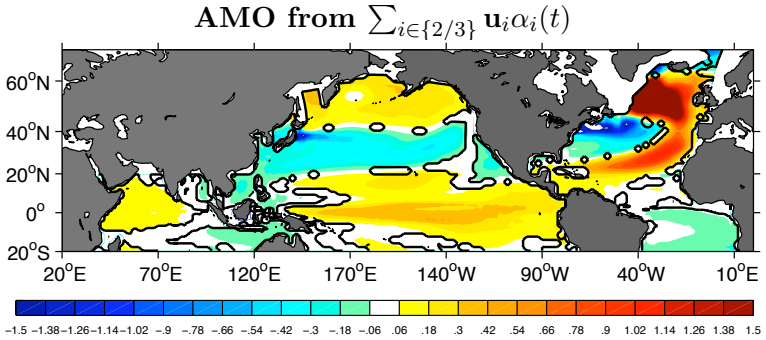

Figure 5.19: SSTs (in °C) associated with the AMO computed from $\sum_{i\in\{2/3\}} \mathbf{u}_i\alpha_i(t)$. The black contour indicates 5% significance. LIM made from MILL (1350-1849)

5.4 Summary

In this chapter, we investigated whether LIM was efficient at isolating in the SST field the radiative forcing associated with volcanic eruptions using a simulation of the last millennium climate. It was shown that this signal could efficiently be isolated in the period of moderate volcanism (1350-1849) of the simulation. Whereas the traditional AMO of the simulation was not found to follow significantly an AMOC intensification, the AMO where the volcanic signal had been removed with LIM was highly correlated with the AMOC when lagging by 6/7 yr, and it was very similar to the AMO of the control simulation. However, contrary to the latter, removing ENSO from the AMO with LIM did not improve its correlation with the AMOC. Further investigations are needed to understand whether this can be explained by a volcanic forcing of both ENSO and the AMOC, or by another mechanism. We first intend to examine the impact of volcanic eruptions on atmospheric variability to understand to what extent ENSO teleconnections are modified. We also want to explore whether the volcanic activity favors El Niño events by considering only moderate eruptions and separating eruptions of different seasons. Besides, we would like to apply LIM to the simulation of the last 600 yr with the BCM model used by [Otterå et al. 2010], where the volcanic forcing is weaker than in MILL. Indeed, it should be emphasized that the volcanic impact in MILL is probably too strong, consistent with the comparison between the AMO in MILL and the AMO based on surface temperature reconstruction of [Mann et al. 2009] (Fig.5.10).

Chapter 6

Conclusions et Perspectives

Dans une première partie de cette thèse, nous nous intéressons aux liens entre les vents de l'hémisphère Sud, l'Océan du Sud et l'AMOC aux échelles de temps interannuelles à multidécennales dans une simulation de contrôle du modèle de climat français IPSLCM4. Nous avons mis en évidence une influence des vents d'Ouest de l'hémisphère Sud, décrit par le SAM, sur l'Océan du Sud à l'échelle de temps annuelle, et sur l'AMOC aux échelles de temps interannuelle/décennale et multidécennale. Lors d'une phase positive du SAM, les vents d'Ouest, intensifiés au sud de 45 °S, créent un transport d'Ekman vers le Nord autour de l'Antarctique, entraînant une divergence des courants de surface. Ceci augmente la pente des isopycnes et donc le gradient méridien de pression, provoquant une intensification de l'ACC, puisque ce dernier peut être considéré comme en équilibre géostrophique loin de la surface. Ce lien avait déjà été trouvé dans les observations et dans des modèles de climat (e.g. [Hall and Visbeck 2002], [Meredith et al. 2004], [Sen Gupta and England 2006]), et valide le comportement du modèle utilisé dans cette étude. L'importance de résoudre les tourbillons méso-échelles dans les simulations de l'Océan du Sud est vivement débatue au sein de la communauté scientifique ([Screen et al. 2009], [Biastoch et al. 2009], [Treguier et al. 2010]), puisque l'activité tourbillonnaire pourrait aussi être modifiée par le SAM à une échelle de temps de 2/3 ans et même contrebalancer le transport d'Ekman vers le Nord et le pompage d'Ekman positif induit en phase d'un SAM positif. Dans la version du modèle IPSLCM4 que nous utilisons, les tourbillons méso-échelles ne sont pas résolus, mais seulement paramétrisés avec une paramétrisation de Gent et McWilliams. Cette dernière aplatit les isopycnes avec un coefficient qui dépend

du taux d'accroissement des instabilités baroclines. Bien que les tourbillons ne soient que paramétrisés, nous trouvons qu'ils répondent au SAM de façon similaire, mais moins marquée que les modèles les résolvant. Nous trouvons une accélération de l'AMOC environ 8 ans après une phase positive du SAM, due à une correlation entre le SAM et la SLP dans le nord de l'Atlantique Nord. Ce lien résulte d'un forçage de ENSO à la fois sur l'hémisphère Sud et l'hémisphère Nord, mais aussi d'une influence directe du SAM sur la SLP dans l'Atlantique Nord. Toutefois, vu qu'une telle influence directe n'est pas trouvée dans les observations, elle apparaît assez irréaliste. Il serait intéressant d'examiner plus en détail cette téléconnection afin de comprendre l'origine de ce biais du modèle.

Une intensification de l'AMOC est aussi trouvée 70 ans après une phase positive du SAM. Elle résulte de l'advection d'anomalies positives de sel, créées dans l'Océan du Sud, qui entrent dans le bassin Atlantique principalement via le courant des Aiguilles, mais aussi par le passage de Drake et circulent vers l'Atlantique Nord. Une vingtaine d'années après un SAM positif, ces anomalies de sel atteignent la gyre subtropicale, puis ne peuvent plus être détectées. Toutefois, elles réapparaissent 40 ans plus tard en surface (i.e. 65 ans après un SAM positif) près des régions de convection profonde dans le nord de l'Atlantique Nord. Nous suggérons que ces anomalies subduquent dans la gyre tropicale, où elles recirculent, puis sont advectées vers le Nord le long du courant Nord Atlantique. Cette hypothèse a été vérifiée par des expériences avec le logiciel ARIANE, qui permet de lâcher des particules dans une zone de l'océan et de suivre leurs trajectoires de façon lagrangienne dans le champ de vitesse moyen du modèle. Toutefois, pour valider complètement ce méchanisme, il serait instructif de faire des expériences où différentes quantités d'anomalies de sel seraient artificiellement introduites dans l'Océan du Sud dans le modèle IPSLCM4. Ceci nous permettrait aussi d'estimer la relation entre la quantité d'anomalies de sel provenant de l'hémisphère Sud et la conséquente modification de l'AMOC. Il est primordial de comprendre plus en détail les liens entre le SAM et l'AMOC via l'advection d'anomalies de sel, vu que les observations montrent une intensification

significative des vents d'Ouest de l'hémisphère Sud et donc une tendance positive du SAM depuis quelques décennies, probablement à cause des changements d'origine anthropique ([Thompson and Solomon 2002], [Marshall 2003]). Ceci entraîne une augmentation de la quantité d'eaux salées entrant dans le bassin Atlantique via le courant des aiguilles, comme le démontre [Biastoch et al. 2009] en utilisant un modèle océanique de très haute résolution qui résout les tourbillons et qui est forcé par des réanalyses atmosphériques. Ces eaux salées pourraient avoir un impact plus tard sur l'AMOC, et ainsi atténuer l'affaiblissement de l'AMOC prédit dans des conditions de réchauffement global. Notre étude contribue à valider ce méchanisme dans des conditions de variabilité naturelle dans un modèle de résolution moyenne. Enfin, nous trouvons qu'à des échelles de temps centennales, l'AMOC et le SAM évoluent quasiment en phase, l'AMOC suivant légèrement le SAM. Ce résultat est cohérent avec la théorie de "l'effet du Passage de Drake" de [Toggweiler and Samuels 1995]. Cependant, pour mieux valider ce point et afin de comprendre les méchanismes sous-jacents, il faudrait considérer une simulation beaucoup plus longue. De plus, comme les tourbillons jouent un rôle crucial dans l'Océan du Sud, cette longue simulation devrait aussi provenir d'un modèle haute résolution pour suffisamment bien représenter l'activité tourbillonnaire.

Dans la deuxième partie de cette thèse, l'objectif est d'étudier dans quelle mesure l'AMO reflète les fluctuations multidécennales de l'AMOC, et quels sont les autres signaux climatiques qui l'influencent. Nous nous intéressons principalement à l'influence de ENSO, de la variabilité décennale du Pacifique, et des forçages externes, tels que le forçage d'origine anthropique et les éruptions volcaniques. Ce travail est basé sur des observations du 20ème siècle, mais aussi sur une simulation historique d'un modèle de climat, plusieurs simulations de contrôle et une simulation du dernier millénaire, l'usage de modèles de climat permettant de pallier le manque d'observations de l'AMOC.

Tout d'abord, nous nous concentrons sur la déconstruction du signal AMO dans des conditions climatiques de variabilité naturelle, ainsi qu'avec les forçages

externes du 20ème siècle. Alors que nous avions déjà commencé ce travail, [Guan and Nigam 2009] ont publié une étude dans laquelle l'influence du bassin Pacifique était soustraite de l'AMO. De même, [Compo and Sardeshmukh 2010] ont enlevé les téléconnections ENSO de l'AMO. Toutefois, ces études se basent uniquement sur les observations du siècle passé, et ces auteurs n'ont pas étudié si ceci améliorait le lien entre AMO et AMOC.

Pour déconstruire l'AMO, nous utilisons un filtre dynamique assez innovant, basé sur le LIM, que nous appliquons aux anomalies globales de SST (20 $^\circ$S-80 $^\circ$N). Il avait déjà été prouvé que le LIM modèlisait bien les anomalies saisonnières de SST dans les Tropiques ([Penland and Sardeshmukh 1995], [Penland 1996]). De plus, LIM avait déjà été utilisé pour identifier et soustraire l'impact de ENSO de la SST tropicale par [Penland and Matrosova 2006]. [Compo and Sardeshmukh 2010] ont introduit un opérateur de régression, qualifié d'opérateur "pont atmosphèrique", afin d'enlever l'influence de ENSO sur la SST extratropicale, invoquant implicitement l'hypothèse d'une réponse rapide (en phase) de SST à ENSO. Nous montrons que LIM peut être appliqué directement aux anomalies globales de SST sans donc devoir faire d'hypothèse sur le temps de réponse de la SST.

Nous montrons que LIM apparaît comme une technique plus efficace pour enlever de l'AMO la dérive globale du siècle passé que soustraire une dérive linéaire ou bien la moyenne de SST globale, comme l'avait fait [Trenberth and Shea 2006]. Néanmoins, ce résultat est obtenu à partir d'une seule simulation historique. Pour valider sa robustesse, il faudrait appliquer la même analyse à des ensembles de simulations historiques obtenues à partir de modèles différents, et les modes LIM devraient être comparés avec ceux obtenus dans les simulations de contrôle des modèles considérés.

Nous trouvons qu'enlever ENSO de l'AMO à l'aide du LIM entraîne une légère augmentation des corrélations entre l'AMO et l'AMOC, contrairement à une simple régression, ce qui renforce l'intérêt d'utiliser un filtre dynamique pour représenter le signal ENSO, comme argumenté par [Penland and Matrosova 2006]

ou [Compo and Sardeshmukh 2010]. ENSO perturbe donc le lien entre l'AMO et l'AMOC par son impact sur la SST Atlantique. Ce résultat semble robuste, tout au moins lorsque que l'on considère des variations climatiques naturelles ou bien le climat du 20ème siècle. Cependant, la valeur de l'augmentation des correlations AMO-AMOC dépend fortement du modèle considéré, variant de 0 à 15%. Ceci reflète des différences de représentation du pont atmosphérique reliant les bassins Pacifique et Atlantique. Si la carte des corrélations entre ENSO et la SST dans l'Atlantique était un bon indicateur de l'impact de ENSO sur l'AMO (ce qui ne l'est pas, puisque ENSO n'est pas bien filtré par une régression linéaire), nous pourrions comparer les cartes obtenues dans les observations et dans les modèles, et nous en déduirions que l'augmentation des corrélations AMO-AMOC après avoir enlevé ENSO dans les observations serait entre la moins bonne et la meilleure valeur trouvée dans les modèles.

Enfin, nous montrons qu'enlever de l'AMO le signal lié à la variabilité de basse fréquence du Pacifique Nord, comme l'ont fait [Guan and Nigam 2009], dégrade fortement son lien avec l'AMOC, ce qui suggère une importante interconnection entre l'AMOC et la variabilité décennale et pluridécennale de la SST Nord Atlantique et Nord Pacifique. En effet, les modes LIM liés à la PDO montrent aussi de fortes anomalies dans l'Atlantique Nord, témoignant d'un lien entre l'AMO et la PDO. De plus, dans tous les modèles, ainsi que dans les observations, nous trouvons qu'une phase positive de la PDO est associée à des anomalies de SLP dans l'Atlantique Nord similaires à celles d'une phase négative de la NAO. Or, la NAO est un moteur principal de la variabilité de l'AMOC et affecte fortement la SST Nord Atlantique. Par conséquent, retirer la PDO de l'AMO enleve un signal lié à l'AMOC et dégrade donc les corrélations AMO-AMOC. Il reste à élucider si cette connection provient de l'Atlantique, du Pacifique, ou d'un forçage commun atmosphérique de type AO. On ne trouve pas de concensus sur ce point dans la littérature (e.g. [Zhang and Delworth 2007], [Müller et al. 2008], [Li et al. 2009]), et les correlations entre AMO et PDO montrées dans la section 4.4.3 suggèrent une grande

diversité de représentation de ce lien parmi les modèles.

En moyenne, l'augmentation des correlations AMO-AMOC après avoir enlevé le signal ENSO (et la dérive globale pour la simulation historique) avec le LIM est certes encourageante mais pas extraordinaire. De plus, dans plusieurs simulations, nous trouvons un mode LIM, ayant une longue période et de fortes anomalies dans l'Atlantique Nord, qui est très fortement corrélé à l'AMOC. Ceci suggère que notre déconstruction de l'AMO est loin d'être optimale. Pour tenter de l'améliorer, il serait intéressant d'essayer d'enlever l'effet du forçage atmosphérique local. Pour ce faire, il faudrait travailler avec la matrice de forçage stochastique du LIM. Dans l'état actuel de notre filtre LIM, nous sommes capables d'identifier les modes de forçage, et pour les retirer, il faudrait réintégrer le système en enlevant ces modes (voir section 3.4 dans le chapitre sur le LIM). Cependant, il n'est pas certain qu'enlever de l'AMO le signal de SST résultant du forçage atmosphérique local améliorerait sa corrélation avec l'AMOC, vu que ce forçage influence fortement l'AMOC (e.g. [Eden and Willebrand 2001], [Deshayes and Frankignoul 2008]). Une autre piste pour trouver un meilleur indicateur observable de la variabilité de l'AMOC serait d'étudier dans les modèles les modes de couplage entre la SST Atlantique et l'AMOC à l'aide du LIM (voir section 3.5 du chapitre sur le LIM), comme l'a fait [Newman 2007] lorsqu'il a étudié le couplage entre la SST du Pacifique tropical et du Pacifique Nord.

Dans le dernier chapitre de cette thèse, nous montrons que le LIM isole de façon assez efficace la réponse de la SST au forçage radiatif des volcans dans une simulation du dernier millénaire du modèle IPSLCM4, lorsque que l'on considère une période d'activité volcanique modérée (période post 1350). Ce n'est pas le cas si l'ensemble de la simulation est prise en compte, certainement à cause de la période de volcanisme intense et rapproché entre 1150 et 1300, qui induit une réponse différente de l'océan et introduit des échelles de temps différentes. Il reste à établir dans quelle mesure et quelles conditions le LIM peut être plus systématiquement utilisé pour isoler la réponse radiative au forçage volcanique.

Pour cela, il serait intéressant de considérer des ensembles de simulations basées sur des modèles de climat différents et modélisant différents forçages volcaniques, comme par exemple un forçage modéré, assez espacé dans le temps et quasi-périodique; ou bien un forçage plus irrégulier; ou encore un forçage assez intense et peu fréquent, etc. Enfin, contrairement à ce que l'on trouve dans les simulations de contrôle de différents modèles climatiques et dans la simulation historique de IPSLCM5, enlever ENSO de l'AMO avec le LIM n'améliore pas les corrélations AMO-AMOC. Nous suggèrons que ceci pourrait s'expliquer par une influence commune des volcans sur l'AMOC, les téléconnections ENSO et la dynamique de ENSO, bien que nous n'arrivions pas encore à mettre cette dernière en évidence, comme suggéré par plusieurs études (e.g. [Adams et al. 2003], [Emile-Geay et al. 2008], [McGregor and Timmermann 2011]). Toutefois, ce travail n'est que préliminaire et demande d'être largement plus approfondi. Par exemple, afin d'étudier l'impact des volcans sur ENSO, il faudra prendre en compte la saisonnalité et l'intensité des éruptions volcaniques. L'effet de l'activité volcanique sur l'atmosphère sera examiné en détail en comparant MILL et CTRLA. Il serait aussi intéressant d'appliquer la même analyse à la simulation des derniers 600 ans réalisée avec le modèle norvégien BCM.

Il est néanmoins assez perturbant qu'enlever ENSO de l'AMO avec le LIM n'amèliore pas sa corrélation avec l'AMOC dans MILL, car ceci est contraire aux résultats trouvés en conditions de variabilité naturelle ou avec un forçage semblable à celui du 20ème siècle. Si l'on veut un indicateur de l'AMOC sur le long terme, il faut prendre en compte le forçage volcanique. Toutefois, il faut souligner que la simulation du dernier millénaire du modèle IPSLCM4 surestime le forçage volcanique et qu'il faudrait considérer d'autres simulations afin de pouvoir sérieusement tester la validité de ce point.

Bibliography

[Adams et al. 2003] J.B. Adams, M.E. Mann and C.M. Ammann. *Proxy evidence for an El Nino-like response to volcanic forcing.* Nature, vol. 426, no. 6964, pages 274–278, 2003. 108, 131, 143

[Alexander et al. 2002] M.A. Alexander, I. Bladé, M. Newman, J.R. Lanzante, N.C. Lau and J.D. Scott. *The atmospheric bridge: The influence of ENSO teleconnections on air-sea interaction over the global oceans.* Journal of Climate, vol. 15, no. 16, pages 2205–2232, 2002. 19, 23, 24, 25, 88, 132

[Ammann et al. 2003] C.M. Ammann, G.A. Meehl, W.M. Washington and C.S. Zender. *A monthly and latitudinally varying volcanic forcing dataset in simulations of 20th century climate.* Geophys. Res. Lett, vol. 30, no. 12, page 1657, 2003. 110

[Bacon et al. 2003] S. Bacon, W.J. Gould and Y. Jia. *Open-ocean convection in the Irminger Sea.* Geophysical research letters, vol. 30, no. 5, page 1246, 2003. 9

[Baehr et al. 2004] J. Baehr, J. Hirschi, J.O. Beismann and J. Marotzke. *Monitoring the meridional overturning circulation in the North Atlantic: A model-based array design study.* Journal of Marine Research, vol. 62, no. 3, pages 283–312, 2004. 10

[Biastoch et al. 2008] A. Biastoch, C.W. Böning, J. Getzlaff, J.M. Molines and G. G. Madec. *Causes of interannual-decadal variability in the meridional overturning circulation of the midlatitude North Atlantic Ocean.* Journal of Climate, vol. 21, no. 24, pages 6599–6615, 2008. 106

[Biastoch et al. 2009] A. Biastoch, C.W. Böning, F.U. Scwarzkopf and J.R.E. Lutjeharms. *Increase in Agulhas leakage due to poleward shift of Southern Hemisphere westerlies.* Nature, vol. 462, pages 495–499, 2009. 16, 137, 139

[Bjerknes 1964] J. Bjerknes. *Atlantic air-sea interaction.* Advances in Geophysics, vol. 10, no. 1, page 82, 1964. 26

[Bretherton et al. 1999] C.S. Bretherton, M. Widmann, V.P. Dymnikov, J.M. Wallace and I. Bladé. *The effective number of spatial degrees of freedom of a time-varying field.* Journal of climate, vol. 12, no. 7, pages 1990–2009, 1999. 65

[Brönnimann 2007] S. Brönnimann. *Impact of El Niño–Southern Oscillation on European climate.* Reviews of Geophysics, vol. 45, no. 3, page RG3003, 2007. 19, 23

[Cai 2006] W. Cai. *Antarctic ozone depletion causes an intensification of the Southern Ocean super-gyre circulation.* Geophys. Res. Lett, vol. 33, no. 3, 2006. 15

[Chang et al. 2004] P. Chang, R. Saravanan, T. DelSole and F. Wang. *Predictability of Linear Coupled Systems. Part I: Theoretical Analyses.* Journal of Climate, vol. 17, no. 7, pages 1474–1486, 2004. 63

[Chiang and Lintner 2005] J.C.H. Chiang and B.R. Lintner. *Mechanisms of remote tropical surface warming during El Niño.* Journal of climate, vol. 18, no. 20, pages 4130–4149, 2005. 25, 88

[Chiang and Sobel 2002] J.C.H. Chiang and A.H. Sobel. *Tropical Tropospheric Temperature Variations Caused by ENSO and Their Influence on the Remote Tropical Climate*.* Journal of climate, vol. 15, no. 18, pages 2616–2631, 2002. 25, 88

[Claussen et al. 2002] M. Claussen, L. Mysak, A. Weaver, M. Crucifix, T. Fichefet, M.F. Loutre, S. Weber, J. Alcamo, V. Alexeev, A. Berger*et al. Earth system models of intermediate complexity: closing the gap in the spectrum of climate system models*. Climate Dynamics, vol. 18, no. 7, pages 579–586, 2002. 11

[Clement et al. 1996] A.C. Clement, R. Seager, M.A. Cane and S.E. Zebiak. *An ocean dynamical thermostat*. Journal of Climate, vol. 9, no. 9, pages 2190–2196, 1996. 108

[Collins et al. 2006] W.D. Collins, C.M. Bitz, M.L. Blackmon, G.B. Bonan, C.S. Bretherton, J.A. Carton, P. Chang, S.C. Doney, J.J. Hack, T.B. Hendersonet *al. The community climate system model version 3 (CCSM3)*. Journal of Climate, vol. 19, no. 11, pages 2122–2143, 2006. 64

[Compo and Sardeshmukh 2010] G.P. Compo and P.D. Sardeshmukh. *Removing ENSO-related variations from the climate record*. Journal of Climate, vol. 23, no. 8, pages 1957–1978, 2010. 59, 60, 90, 91, 104, 105, 140, 141

[Cunningham et al. 2003] S. A. Cunningham, S. G. Alderson, B. A. King and M. A. Brandon. *Transport and variability of the Antarctic Circumpolar Current in Drake Passage*. J. Geophys., vol. 108, page 8084, 2003. 14

[Cunningham et al. 2007] S. A. Cunningham, T. Kanzow, D. Rayner, M.O. Baringer, W.E. Johns, J. Marotzke, H.R. Longworth, E.M. Grant, J.J.M Hirschi, L.M. Beal, C.S. Meinen and H.L. Bryden. *Temporal Variability of the Atlantic Meridional Overturning Circulation at 26.5 ° N*. Science, vol. 317, pages 935–, 2007. 10

[de Coëtlogon and Frankignoul 2003] G. de Coëtlogon and C. Frankignoul. *The Persistence of Winter Sea Surface Temperature in the North Atlantic*. Journal of Climate, vol. 16, pages 1364–1377, 2003. 26

[Delworth and Mann 2000] T.L. Delworth and M.E. Mann. *Observed and simulated multidecadal variability in the Northern Hemisphere.* Climate Dynamics, vol. 16, no. 9, pages 661–676, 2000. 26

[Delworth et al. 1993] T. Delworth, S. Manabe and R.J. Stouffer. *Interdecadal Variations of the Thermohaline Circulation in a Coupled Ocean-Atmosphere Model.* Journal Of Climate, vol. 6, pages 1993–2011, 1993. 13, 59

[Deser et al. 2006] C. Deser, A. Capotondi, R. Saravanan and A.S. Phillips. *Tropical Pacific and Atlantic Climate Variability in CCSM3.* Journal of Climate, vol. 19, pages 2451–+, 2006. 89

[Deser et al. 2010] C. Deser, M.A. Alexander, S.P. Xie and A.S. Phillips. *Sea surface temperature variability: patterns and mechanisms.* Annual Review of Marine Science, vol. 2, pages 115–143, 2010. 23

[Deshayes and Frankignoul 2008] J. Deshayes and C. Frankignoul. *Simulated Variability of the Circulation in the North Atlantic from 1953 to 2003.* Journal Of Climate, vol. 21, pages 4919–4933, 2008. 13, 14, 59, 96, 106, 142

[Dong and Sutton 2001] B.W. Dong and RT Sutton. *The dominant mechanisms of variability in Atlantic Ocean Heat Transport in a Coupled Ocean-Atmosphere GCM.* Geophysical Research Letters, vol. 28, no. 12, pages 2445–2448, 2001. 12

[Dong and Sutton 2005] B. Dong and R.T. Sutton. *Mechanism of Interdecadal Thermohaline Circulation Variability in a Coupled Ocean-Atmosphere GCM.* Journal of Climate, vol. 18, pages 1117–1135, 2005. 12, 13, 14

[Dufresne 2011] J.-L. et al Dufresne. *The IPSL-CM5A Earth System Model: general description and climate change projections.* Climate Dynamics, 2011. 64, 72

[Eden and Willebrand 2001] C. Eden and J. Willebrand. *Mechanism of Interannual to Decadal Variability of the North Atlantlic Circulation.* Journal of Climate, vol. 14, pages 2266–2280, 2001. 13, 14, 59, 96, 142

[Emile-Geay et al. 2008] J. Emile-Geay, R. Seager, M.A. Cane, E.R. Cook and G.H. Haug. *Volcanoes and ENSO over the past millennium.* Journal of Climate, vol. 21, no. 13, pages 3134–3148, 2008. 108, 114, 131, 143

[Enfield and Mestas-Nunez 1999] D. B. Enfield and A.M. Mestas-Nunez. *Multiscale Variabilities in Global Sea Surface Temperatures and Their Relationships with Tropospheric Climate Patterns.* Journal of Climate, vol. 12, no. 9, pages 2719–2733, 1999. 19

[Enfield et al. 2001] D.B. Enfield, A.M. Mestas-Nunez, P.J. Trimble*et al. The Atlantic multidecadal oscillation and its relation to rainfall and river flows in the continental U. S.* Geophysical Research Letters, vol. 28, no. 10, pages 2077–2080, 2001. 17, 19, 58

[Farrell and Ioannou 1996] B. F. Farrell and P.J. Ioannou. *Generalized Stability Theory. Part I: Autonomous Operators.* Journal of the Atmospheric Sciences, vol. 53, no. 14, pages 2025–2040, 1996. 47

[Fichefet and Morales-Maqueda 1999] T. Fichefet and AM Morales-Maqueda. *Modelling the influence of snow accumulation and snow-ice formation on the seasonal cycle of the Antarctic sea-ice cover.* Climate Dynamics, vol. 15, pages 251–268, 1999. 110

[Frankignoul and Hasselmann 1977] C. Frankignoul and K. Hasselmann. *Stochastic climate models, part II application to sea-surface temperature anomalies and thermocline variability.* Tellus, vol. 29, no. 4, pages 289–305, 1977. 21

[Frankignoul 1985] C. Frankignoul. *Sea surface temperature anomalies, planetary waves, and air-sea feedback in the middle latitudes.* Reviews of geophysics, vol. 23, no. 4, pages 357–390, 1985. 20, 21

[Ganachaud and Wunsch 2000] A. Ganachaud and C. Wunsch. *Improved estimates of global ocean circulation, heat transport and mixing from hydrographic data.* Nature, vol. 408, pages 453–457, 2000. 6, 7

[Gao et al. 2008] C. Gao, A. Robock and C. Ammann. *Volcanic forcing of climate over the past 1500 years: An improved ice core-based index for climate models.* J. Geophys. Res, vol. 113, 2008. 110

[Gill 1982] A.E. Gill. Atmosphere-ocean dynamics, volume 30. Academic Pr, 1982. 3

[Gordon et al. 2000] C. Gordon, C. Cooper, C.A. Senior, H. Banks, J.M. Gregory, T.C. Johns, J.F.B. Mitchell and R.A. Wood. *The simulation of SST, sea ice extents and ocean heat transports in a version of the Hadley Centre coupled model without flux adjustments.* Climate Dynamics, vol. 16, pages 147–168, 2000. 64

[Greatbatch et al. 2004] R.J. Greatbatch, J. Lu and K.A. Peterson. *Nonstationary impact of ENSO on Euro-Atlantic winter climate.* Geophysical research letters, vol. 31, no. 2, page L02208, 2004. 89, 105

[Gregory et al. 2005] J.M. Gregory, K. W. Dixon, R. J. Stouffer, A. J. Weaver, E. Driesschaert, M. Eby, T. Fichefet, H. Hasumi, A. Hu, J. H. Jungclaus, I. V. Kamenkovich, A. Levermann, M. Montoya, S. Murakami, S. Nawrath, A. Oka, A. P. Sokolov and R. B. Thorpe. *A model intercomparison of changes in the Atlantic thermohaline circulation in response to increasing atmospheric CO2 concentration.* Geophysical Research Letters, vol. 32, 2005. 11, 12, 16

[Grist et al. 2009] J.P. Grist, R. Marsh and S.A. Josey. *On the relationship between the North Atlantic Meridional Overturning Circulation and the surface-forced overturning streamfunction.* Journal of Climate, vol. 22, no. 19, pages 4989–5002, 2009. 106

[Guan and Nigam 2009] B. Guan and S. Nigam. *Analysis of Atlantic SST Variability Factoring Interbasin Links and the Secular Trend : Clarified Structure of the Atlantic Multidecadal Oscillation.* Journal of Climate, vol. 22, pages 4228–4240, 2009. 58, 60, 79, 102, 103, 105, 140, 141

[Hall and Bryden 1982] M.M. Hall and H.L. Bryden. *Direct estimates and mechanisms of ocean heat transport.* Deep Sea Research Part A. Oceanographic Research Papers, vol. 29, no. 3, pages 339–359, 1982. 7

[Hall and Visbeck 2002] Alex Hall and M. Visbeck. *Synchronous variability in the Southern Hemisphere Atmosphere, Sea Ice, and Ocean Resulting from the Annular Mode.* Journal of Climate, vol. 15, 2002. 137

[Hannachi et al. 2003] A. Hannachi, D.B. Stephenson and K.R. Sperber. *Probability-based methods for quantifying nonlinearity in the ENSO.* Climate Dynamics, vol. 20, pages 241–256, 2003. 54

[Hasselmann 1976] K. Hasselmann. *Stochastic climate models part I. Theory.* Tellus, vol. 28, no. 6, pages 473–485, 1976. 21

[Hawkins and Sutton 2009] E. Hawkins and R. Sutton. *Decadal Predictability of the Atlantic Ocean in a Coupled GCM: Forecast Skill and Optimal Perturbations Using Linear Inverse Modeling.* Journal of Climate, vol. 22, pages 3960–+, 2009. 51

[Hegerl et al. 2003] G.C. Hegerl, T.J. Crowley, S.K. Baum, K.Y. Kim and W.T. Hyde. *Detection of volcanic, solar and greenhouse gas signals in paleo-*

reconstructions of Northern Hemispheric temperature. Geophys. Res. Lett, vol. 30, no. 5, page 1242, 2003. 116

[Hourdin et al. 2006] F. Hourdin, I. Musat, S. Bony, P. Braconnot, F. Codron, J.L. Dufresne, L. Fairhead, M.A. Filiberti, P. Friedlingstein, J.Y. Grandpeix, G. Krinner, P. LeVan, Z.X Li and F. Lott. *The LMDZ4 general circulation model : climate performance and sensitivity to parametrized physics with emphasis on tropical convection.* Climate Dynamics, vol. 27, pages 787–813, 2006. 110

[Hurrell and Deser 2010] J.W. Hurrell and C. Deser. *North Atlantic climate variability: the role of the North Atlantic Oscillation.* Journal of Marine Systems, vol. 79, no. 3-4, pages 231–244, 2010. 13

[Jansen et al. 2007] E. Jansen, J. Overpeck, KR Briffa, JC Duplessy, F. Joos, V. Masson-Delmotte, D. Olago, B. Otto-Bliesner, WR Peltier, S. Rahmstorf*et al. Palaeoclimate. Climate change 2007: the physical science basis. contribution of Working Group I to the Fourth Assessment Report of the Intergovernmental Panel on Climate Change*, 2007. 111

[Jones et al. 2005] G.S. Jones, J.M. Gregory, P.A. Stott, S.F.B. Tett and R.B. Thorpe. *An AOGCM simulation of the climate response to a volcanic super-eruption.* Climate dynamics, vol. 25, no. 7, pages 725–738, 2005. 27, 109

[Jungclaus et al. 2010] JH Jungclaus, SJ Lorenz, C. Timmreck, CH Reick, V. Brovkin, K. Six, J. Segschneider, MA Giorgetta, TJ Crowley, J. Pongratz*et al. Climate and carbon-cycle variability over the last millennium.* Climate of the Past Discussions, vol. 6, pages 1009–1044, 2010. 64

[Kanzow et al. 2010] T. Kanzow, SA Cunningham, WE Johns, J.J.M. Hirschi, J. Marotzke, MO Baringer, CS Meinen, MP Chidichimo, C. Atkinson, C. Beal*et al. Seasonal variability of the Atlantic meridional overturning circulation at 26.5 N.* Journal of Climate, 2010. 10

[Kerr 2000] R.A. Kerr. *A North Atlantic climate pacemaker for the centuries.* Science, vol. 288, no. 5473, page 1984, 2000. 26

[Klein et al. 1999] S.A. Klein, B.J. Soden and N.C. Lau. *Remote sea surface temperature variations during ENSO: Evidence for a tropical atmospheric bridge.* Journal of Climate, vol. 12, no. 4, pages 917–932, 1999. 23, 88, 132

[Kloeden and Platen 1992] P.E. Kloeden and E. Platen. Numerical solution of stochastic differential equations. Springer Verlag, 1992. 53

[Knight et al. 2005] J.R. Knight, R.J. Allan, C.K. Folland, M. Vellinga and M.E. Mann. *A signature of persistent natural thermohaline circulation cycles in observed climate.* Geophysical Research Letters, vol. 32, 2005. 17, 18, 123

[Köhl and Stammer 2008] A. Köhl and D. Stammer. *Variability of the meridional overturning in the North Atlantic from the 50-year GECCO state estimation.* Journal of Physical Oceanography, vol. 38, no. 9, pages 1913–1930, 2008. 7, 8, 106

[Krinner et al. 2005] G. Krinner, N. Viovy, N. de Noblet-DucoudrÂ, J. Ogée, J. Polcher, P. Friedlingstein, P. Ciais, S. Sitch and I.C. Prentice. *A dynamic global vegetation model for studies of the coupled atmosphere-biosphere system.* Global Biogeochemical Cycles, vol. 19, 2005. 110

[Kuhlbrodt et al. 2007] T. Kuhlbrodt, A. Griesel, M. Montoya, A. Levermann, M. Hofmann and S. Rahmstorf. *On the driving processes of the Atlantic meridional overturning circulation.* Reviews of Geophysics, vol. 45, no. 2, page RG2001, 2007. 8, 9

[Kushnir 1994] Y. Kushnir. *Interdecadal variations in North Atlantic sea surface temperature and associated atmospheric conditions.* Journal of Climate, vol. 7, no. 1, 1994. 26

[Kwon and Frankignoul 2011] Y.O. Kwon and C. Frankignoul. *Stochastically-driven multidecadal variability of the Atlantic meridional overturning circulation in CCSM3.* Climate Dynamics, pages 1–18, 2011. 64

[Latif et al. 2004] M. Latif, E. Roeckner, M. Botzet, M. Esch, H. Haak, S. Hagemann, J. Jungclaus, S. Legutke, S. Marsland and U. Mikolajewicz. *Reconstructing, monitoring, and predicting multidecadal-scale changes in the North Atlantic thermohaline circulation with the sea surface temperature.* Journal of Climate, vol. 17, pages 1605–1614, 2004. 12, 17

[Li et al. 2009] C. Li, L. Wu, Q. Wang, L. Qu and L. Zhang. *An intimate coupling of ocean–atmospheric interaction over the extratropical North Atlantic and Pacific.* Climate dynamics, vol. 32, no. 6, pages 753–765, 2009. 94, 141

[Madec et al. 1998] G. Madec, P. Delecluse, M. Imbard and C. Lévy. *OPA 8.1 Ocean General Circulation Model reference manual.* Rapport technique, Note du pole de modelisation de l'Institut Pierre Simon Laplace, nb 11, 1998. 110

[Mann et al. 2009] M.E. Mann, Z. Zhang, S. Rutherford, R.S. Bradley, M.K. Hughes, D. Shindell, C. Ammann, G. Faluvegi and F. Ni. *Global signatures and dynamical origins of the Little Ice Age and Medieval Climate Anomaly.* Science, vol. 326, no. 5957, page 1256, 2009. 123, 124, 135

[Mantua and Hare 2002] N.J. Mantua and S.R. Hare. *The Pacific decadal oscillation.* Journal of Oceanography, vol. 58, no. 1, pages 35–44, 2002. 26

[Mantua et al. 1997] N.J. Mantua, S.R. Hare, Y. Zhang, J.M. Wallace, R.C. Francis*et al. A Pacific interdecadal climate oscillation with impacts on salmon production.* Bulletin of the American Meteorological Society, vol. 78, no. 6, pages 1069–1080, 1997. 25

[Marshall 2003] G.J. Marshall. *Trends in the Southern Annular Mode from observations and reanalyses.* Journal of Climate, vol. 16, 2003. 139

[Marti et al. 2010] Olivier Marti, P. Braconnot, J.-L. Dufresne, J. Bellier, R. Benshila, S. Bony, P. Brockmann, P. Cadule, A. Caubel, F. Codron, N. de Noblet, S. Denvil, L. Fairhead, T. Fichefet, M.-A. Foujols, P. Friedlingstein, H. Goosse, J.-Y. Grandpeix, E. Guilyardi, F. Hourdin, A. Idelkadi, M. Kageyama, G. Krinner, C. Lévy, G. Madec, J. Mignot, I. Musat, D. Swingedouw and C. Talandier. *Key features of the IPSL ocean atmosphere model and its sensitivity to atmospheric resolution.* Climate Dynamics, vol. 34, pages 1–26, 2010. 64, 69, 110

[McGregor and Timmermann 2011] S. McGregor and A. Timmermann. *The Effect of Explosive Tropical Volcanism on ENSO.* Journal of climate, vol. 24, no. 8, pages 2178–2191, 2011. 108, 114, 131, 143

[Meredith et al. 2004] M. P. Meredith, P.L. Woodworth, C.W. Hughes and V. Stepanov. *Changes in the ocean transport through Drake Passage during the 1980s and 1990s, forced by changes in the Southern Annular Mode.* Geophysical Research Letters, vol. 31, 2004. 137

[Mestas-Nunez and Enfield 1999] A. M. Mestas-Nunez and D.B. Enfield. *Rotated Global Modes of Non-ENSO Sea Surface Temperature Variability.* Journal of Climate, vol. 12, no. 9, pages 2734–2746, 1999. 19

[Mignot et al. 2007] J. Mignot, A. Ganopolski and A. Levermann. *Atlantic subsurface temperatures: Response to a shutdown of the overturning circulation and consequences for its recovery.* Journal of Climate, vol. 20, no. 19, pages 4884–4898, 2007. 17

[Mignot et al. 2011] J. Mignot, M. Khodri, C. Frankignoul and J. Servonnat. *Volcanic impact on the Atlantic ocean over the last millennium.* Climate of the

Past Discussions, vol. 7, no. 4, pages 2511–2554, 2011. 27, 108, 109, 111, 115, 117, 128

[Msadek and Frankignoul 2008] Rym Msadek and Claude Frankignoul. *Atlantic multidecadal oceanic variability and its influence on the atmosphere in a climate model*. Climate Dynamics, 2008. 13, 14

[Msadek and Frankignoul 2009] R. Msadek and C. Frankignoul. *Atlantic multidecadal oceanic variability and its influence on the atmosphere in a climate model*. Climate dynamics, vol. 33, no. 1, pages 45–62, 2009. 69, 96

[Müller et al. 2008] WA Müller, C. Frankignoul and N. Chouaib. *Observed decadal tropical Pacific–North Atlantic teleconnections*. Geophysical Research Letters, vol. 35, no. 24, page L24810, 2008. 19, 59, 92, 105, 141

[Newman et al. 2003] M. Newman, G.P. Compo and M.A. Alexander. *ENSO-Forced Variability of the Pacific Decadal Oscillation*. Journal of Climate, vol. 16, no. 23, pages 3853–3857, 2003. 26

[Newman 2007] M. Newman. *Interannual to Decadal Predictability of Tropical and North Pacific Sea Surface Temperatures*. Journal of climate, vol. 20, pages 2333–2356, 2007. 54, 79, 142

[Orgeville and Peltier 2007] M. Orgeville and W.R. Peltier. *On the Pacific Decadal Oscillation and the Atlantic Multidecadal Oscillation: Might they be related?* Geophysical Research Letters, vol. 34, no. 23, page L23705, 2007. 19, 92, 94, 103, 105

[Otterå et al. 2010] O.H. Otterå, M. Bentsen, H. Drange and L. Suo. *External forcing as a metronome for Atlantic multidecadal variability*. Nature Geoscience, vol. 3, pages 688–694, 2010. 27, 109, 125, 128, 132, 135

[Penland and Matrosova 1994] C. Penland and L. Matrosova. *A Balance Condition for Stochastic Numerical Models with Application to the ENSO.* Journal of Climate, vol. 7, 1994. 47, 53

[Penland and Matrosova 2006] C. Penland and L. Matrosova. *Studies of El Niño and Interdecadal Variability in Tropical Sea Surface Temperatures Using a Nonnormal Filter.* Journal of Climate, vol. 19, pages 5796–5815, 2006. 52, 58, 59, 62, 63, 90, 91, 100, 104, 105, 140

[Penland and Sardeshmukh 1995] C. Penland and P.D. Sardeshmukh. *The Optimal Growth of SST Anomalies.* Journal of Climate, vol. 8, 1995. 47, 48, 52, 54, 63, 66, 140

[Penland 1989] C. Penland. *Random Forcing and Forecasting Using Principal Oscillation Pattern Analysis.* Monthly Weather Review, vol. 117, no. 10, pages 2165–2185, 1989. 47

[Penland 1996] C. Penland. *A stochastic model of IndoPacific SST anomalies.* Physica D., 1996. 47, 140

[Rahmstorf 2006] S. Rahmstorf. *Thermohaline Ocean Circulation. Encyclopedia of Quaternary Sciences.* Postdam Institute for Climate Impact Research, 2006. 5

[Rayner et al. 2003] N. A. Rayner, D.E. Parker, E.B. Horton, C.K. Folland, L.V. Alexander, D.P. Rowell, E.C. Kent and A. Kaplan. *Global analyses of sea surface temperature, sea ice, and night marine air temperature since the late nineteenth century.* Journal of Geophysical Research (Atmospheres), vol. 108, pages 4407–+, 2003. 3, 18, 64

[Risken 1996] H. Risken. The fokker-planck equation: Methods of solution and applications, volume 18. Springer Verlag, 1996. 47

[Robock 2000] A. Robock. *Volcanic eruptions and climate*. Reviews of Geophysics, vol. 38, pages 191–219, 2000. 27, 108, 131, 132

[Sardeshmukh and Sura 2008] P.D. Sardeshmukh and P. Sura. *Reconciling Non-Gaussian Climate Statistics with Linear Dynamics*. Journal of Climate, vol. 22, pages 1193–1207, 2008. 54

[Schmidt et al. 2010] GA Schmidt, JH Jungclaus, CM Ammann, E. Bard, P. Braconnot, TJ Crowley, G. Delaygue, F. Joos, NA Krivova, R. Muscheler*et al.* *Climate forcing reconstructions for use in PMIP simulations of the last millennium (v1. 0)*. Geoscientific Model Development Discussions, vol. 3, pages 1549–1586, 2010. 110

[Schmittner et al. 2005] A. Schmittner, M. Latif and B. Schneider. *Model projections of the North Atlantic thermohaline circulation for the 21st century assessed by observations*. Geophysical research letters, vol. 32, no. 23, pages L23710–1, 2005. 11

[Schmitz 1996] W.J. Schmitz. *On the world ocean circulation. Volume I, some global features/North Atlantic circulation*. Rapport technique, Woods Hole Oceanographic Institution, 1996. 16

[Schneider and Cornuelle 2005] N. Schneider and B.D. Cornuelle. *The Forcing of the Pacific Decadal Oscillation*. Journal of Climate, vol. 18, no. 21, pages 4355–4373, 2005. 26, 92

[Screen et al. 2009] J.A. Screen, N.P. Gillett, D.P. Stevens, G.J. Marshall and H.K. Roscoe. *The Role of Eddies in the Southern Ocean Temperature Response to the Southern Annular Mode*. Journal of Climate, vol. 22, pages 806–818, 2009. 137

[Sen Gupta and England 2006] A. Sen Gupta and M. H. England. *Coupled Ocean-Atmosphere-Ice Response to Variations in the Southern Annular Mode*. Journal Of Climate, vol. 19, pages 4457–4486, 2006. 137

[Sijp and England 2009] Willem P. Sijp and Matthew England. *Southern Hemisphere Westerly Wind Control over the Ocean's Thermohaline Circulation*. Journal of Climate, vol. 22, pages 1277–1286, 2009. 15, 17

[Stenchikov et al. 2009] G. Stenchikov, TL Delworth, V. Ramaswamy, RJ Stouffer, A. Wittenberg and F. Zeng. *Volcanic signals in oceans*. J. Geophys. Res, vol. 114, 2009. 108

[Sutton and Hodson 2003] RT Sutton and DLR Hodson. *Influence of the ocean on North Atlantic climate variability 1871-1999*. Journal of Climate, vol. 16, no. 20, pages 3296–3313, 2003. 89, 105

[Sutton and Hodson 2005] R.T. Sutton and D.L.R. Hodson. *Atlantic ocean forcing of American and European summer climate*. Science, vol. 309, pages 115–118, 2005. 17, 18, 58

[Talley et al. 2003] L.D. Talley, J.L. Reid and P.E. Robbins. *Data-based meridional overturning streamfunctions for the global ocean*. Journal of Climate, vol. 16, no. 19, pages 3213–3226, 2003. 6

[Taylor et al. 2011] KE Taylor, R.J. Stouffer and G.A. Meehl. *A Summary of the CMIP5 Experiment Design*. $http://cmip-pcmdi.llnl.gov/cmip5/docs/Taylor_CMIP5_design.pdf(lastaccess : 22January2011)$, 2011. 72

[Thompson and Solomon 2002] D.W.J. Thompson and S. Solomon. *Interpretation of recent Southern Hemisphere climate change*. Science, vol. 296, no. 5569, page 895, 2002. 139

[Thompson et al. 2009] D.W.J. Thompson, J.M. Wallace, P.D. Jones and J.J. Kennedy. *Identifying signatures of natural climate variability in time series of global-mean surface temperature: methodology and insights*. Journal of Climate, vol. 22, no. 22, pages 6120–6141, 2009. 107, 108, 116

[Timmreck et al. 2009] C. Timmreck, S.J. Lorenz, T.J. Crowley, S. Kinne, T.J. Raddatz, M.A. Thomas and J.H. Jungclaus. *Limited temperature response to the very large AD 1258 volcanic eruption*. Geophysical Research Letters, vol. 36, no. 21, page L21708, 2009. 111

[Ting et al. 2009] M. Ting, Y. Kushnir, R. Seager and C. Li. *Forced and Internal Twentieth-Century SST Trends in the North Atlantic*. Journal of Climate, vol. 22, no. 6, pages 1469–1481, 2009. 19, 21, 22, 58, 76, 98

[Toggweiler and Russell 2008] J. R. Toggweiler and J. Russell. *Ocean Circulation in a warming climate*. Nature, vol. 451, 2008. 16

[Toggweiler and Samuels 1995] J. R. Toggweiler and B. Samuels. *Effect of drake passage on the global thermohaline circulation*. Deep Sea Research Part I: Oceanographic Research Papers, vol. 42, 1995. 9, 15, 139

[Treguier et al. 2010] A.M. Treguier, J. Le Sommer, J.M. Molines and B. De Cuevas. *Response of the Southern Ocean to the Southern Annular Mode: interannual variability and multidecadal trend*. Journal of Physical Oceanography, vol. 40, no. 7, pages 1659–1668, 2010. 137

[Trenberth and Caron 2001] K.E. Trenberth and J.M. Caron. *Estimates of meridional atmosphere and ocean heat transports*. Journal of Climate, vol. 14, no. 16, pages 3433–3443, 2001. 5

[Trenberth and Shea 2006] K.E. Trenberth and D.J. Shea. *Atlantic hurricanes and natural variability in 2005*. Geophysical Research Letters, vol. 33, no. 12, page L12704, 2006. 19, 58, 77, 99, 140

[Trenberth et al. 1998] K. Trenberth, G. Branstator and D. Karoly. *Progress during TOGA in understanding and modeling global teleconnections associated with tropical*. Journal of Geophysical Research, vol. 103, pages 14–291, 1998. 24

[Trenberth et al. 2007] KE Trenberth, PD Jones, P. Ambenje, R. Bojariu, D. Easterling, A.K. Tank, D. Parker, F. Rahimzadeh, JA Renwick, M. Rusticucci*et al. Observations: Surface and Atmospheric Climate Change*. IPCC Fourth Assessment Report, 2007. 21

[Tziperman et al. 2008] E. Tziperman, L. Zanna and C. Penland. *Nonnormal Thermohaline Circulation Dynamics in a Coupled Ocean Atmosphere GCM*. Journal of Physical Oceanography, vol. 38, no. 3, pages 588–604, 2008. 51

[Valcke 2006] S. Valcke. *OASIS3 User Guide (prism-2-5)*. Rapport technique, PRISM support initiative 3, 2006. 110

[Vellinga and Wu 2004] M. Vellinga and P. Wu. *Low-Latitude Freshwater Influence on Centennial Variability of the Atlantic Thermohaline Circulation*. Journal of Climate, vol. 17, pages 4498–4511, 2004. 17, 69, 95, 123

[Vieira and Solanki 2009] L.E.A. Vieira and S. Solanki. *Evolution of the solar magnetic flux on time scales of years to millenia*. Arxiv preprint arXiv:0911.4396, 2009. 110

[Wallace and Gutzler 1981] J.M. Wallace and D.S. Gutzler. *Téléconnexions in the geopotential height field during the Northern Hemisphere winter*. Mon. Wea. Rev., 109, 784, vol. 812, pages 17–43, 1981. 25, 88

[Winkler et al. 2001] C.R. Winkler, M. Newman and P.D. Sardeshmukh. *A linear model of wintertime low-frequency variability. Part 1: Formulation and forecast skill*. Journal of climate, vol. 14, no. 24, pages 4474–4494, 2001. 54

[Zhang and Delworth 2007] R. Zhang and T.L. Delworth. *Impact of the Atlantic Multidecadal Oscillation on North Pacific climate variability.* Geophysical Research Letters, vol. 34, pages 23708–+, 2007. 94, 141